Cooperative Lateral Vehicle Guidance Control for Automated Vehicles with Steer-by-Wire Systems

DISSERTATION

submitted in partial fulfillment
of the requirements for the degree

Doktor-Ingenieur
(Doctor of Engineering)

at the

Faculty of Electrical Engineering and Information Technology
TU Dortmund University

by

Robert Gonschorek, M.Eng.

Halle (Saale), Germany

Date of submission: April 17, 2023
Place of submission: Dortmund, Germany

First examiner: Univ.-Prof. Dr.-Ing. Prof. h.c. Dr. h.c. Torsten Bertram
Second examiner: Univ.-Prof. Dr.-Ing. Steffen Müller

Date of approval: October 20, 2023

Preface

This dissertation was written during my position as a doctoral researcher at the ZF Automotive Germany GmbH Tech Center Düsseldorf. The success of this work results from the support of various persons, who I would like to gratefully thank at this point.

First, I would like to thank Univ.-Prof. Dr.-Ing. Prof. h.c. Dr. h.c. Torsten Bertram, head of the Institute of Control Theory and Systems Engineering at TU Dortmund University, for making the scientific research possible and excellently supporting my work. I am very thankful for his valuable feedback, confidence, interest, and inspiring thoughts. He has continuously given me room for developing scientific knowledge and presenting it to a broad audience at national and international conferences. I would also like to thank Univ.-Prof. Dr.-Ing. Steffen Müller for taking over the review of my dissertation as a second examiner. I greatly appreciate his valuable feedback and expertise. Furthermore, I would like to thank all staff members of the Institute of Control Theory and Systems Engineering for the pleasant working atmosphere, cooperativeness, and fellowship.

My special thanks is directed to Dr. Heinz-Dieter Heitzer, head of the research and development department of ZF Automotive Germany GmbH Düsseldorf, for enabling this work and continuously supporting me throughout my career. I am also very thankful to technical specialist Thomas Schubert for the significant amount of time we spent on in-depth discussions of control theoretical topics. These discussions inspired me to generate new ideas and develop novel control concepts for cooperative lateral vehicle guidance. Also, I would like to thank Dr. Andreas de Moll, Sven Fischer, and Rainer Engel for their great work on the hardware installations of the Steer-by-Wire demonstrator vehicle.

Moreover, words of gratitude are dedicated to my friends for the welcome distraction on the weekends, which helped me to find relaxation. Lastly, I am very grateful to my parents Heide and René Gonschorek for their unconditional support and continuous encouragement throughout my life.

Düsseldorf, October 2023 Robert Gonschorek

Contents

Nomenclature

Abbreviations and Acronyms

ADAS	Advanced Driver Assistance Systems
ADC	Analog-to-Digital Converter
CAN	Controller Area Network
CLS	Constrained Least Squares
CVGC	Cooperative Lateral Vehicle Guidance Control
DAC	Digital-to-Analog Converter
DGPS	Differential Global Positioning System
DOF	Degrees of Freedom
FAA	Front Axle Actuator
FFW	Feedforward
HWA	Handwheel Actuator
IDOB	Inverse Disturbance Observer
IL	Inverse Linearity (Control)
INL	Inverse Nonlinearity (Control)
LIDAR	Light Detection and Ranging
LQG	Linear Quadratic Gaussian
LTI	Linear Time-Invariant
LTR	Loop Transfer Recovery
MABX II	dSPACE MicroAutoBox II
MIMO	Multiple Input Multiple Output
MPC	Model Predictive Control
QP	Quadratic Programming
RCP	Rapid Control Prototyping
SbW	Steer-by-Wire
SISO	Single Input Single Output
SRTG	Steering Reference Torque Generator
VCL	Virtual Control Loop
VDA	Vehicle Dynamics Area
VM	Vector Margin

Greek Symbols

α	Road Inclination Angle
α_{f}	Front Slip Angle
α_{r}	Rear Slip Angle
α_{x}	Longitudinal Acceleration
α_{y}	Lateral Acceleration
β	Side Slip Angle
δ	System Difference Order
δ_{f}	Road Wheel Position Front

θ	Course Angle
$\boldsymbol{\theta}$	Polynomial Coefficient Vector of Regression Spline
κ_{ref}	Reference Path Curvature
$\kappa_{\mathrm{ref,max}}$	Maximum Reference Path Curvature at Constant Vehicle Speed
κ_{unk}	Unknown Curvature
$\overline{\boldsymbol{\kappa}}_{\mathbf{ref}}$	Reference Path Curvature Sequence
$\boldsymbol{\lambda}$	Lagrange Multipliers
μ	Road Friction Coefficient
μ_{max}	Maximum Road Friction Coefficient (Dry Asphalt)
$p(s)$	Characteristic Polynomial
ρ_a	Air Density
$p_{des}(s)$	Desired Characteristic Polynomial
σ^2	Variance of Quantization Noise
φ^*_{AD}	Reference Angular Position – Automated Driving
φ_{EM}	Angular Position - Electric Motor
φ_{FA}	Angular Position - Pinion (Front Axle Actuator)
φ^*_{FA}	Reference Angular Position - Pinion (Front Axle Actuator)
φ^*_{MD}	Reference Angular Position – Manual Driving
φ_{PN}	Angular Position - Pinion
φ_{SW}	Angular Position - Steering Wheel
ϕ	Banked Road Angle
$\dot{\psi}$	Yaw Rate
ψ_{ref}	Reference Path Yaw Angle
ω_{bw}	Control Bandwidth
ω_{o}	Natural Frequency
$\Delta\varphi$	Relative Angular Position
$\Delta\psi$	Heading Angle Error
$\Delta\Omega$	Relative Angular Velocity
Δu	Control Input Change
$\Delta\overline{\mathbf{u}}$	Control Input Change Sequence
Ω_{EM}	Angular Velocity – Electric Motor
Ω_{FA}	Angular Velocity – Pinion (Front Axle Actuator)
Ω_{PN}	Angular Velocity – Pinion
Ω_{SW}	Angular Velocity – Steering Wheel

Latin Symbols

$\mathbf{A}_{\mathrm{a}}$	System Matrix – Discrete-Time Augmented Plant
$\mathbf{A}_{\mathrm{d}}$	System Matrix – Discrete-Time Disturbance Model
$\mathbf{A}^{\mathrm{c}}_{\mathrm{p}}$	System Matrix – Continuous-Time Plant
$\mathbf{A}^{\mathrm{c}}_{\mathrm{pa}}$	System Matrix – Continuous-Time Partial Plant
$\mathbf{A}^{\mathrm{c}*}_{\mathrm{pa}}$	System Matrix – Continuous-Time Inverted Partial Plant
$\mathbf{A}_{\mathrm{p}}$	System Matrix – Discrete-Time Plant
$\mathbf{A}^{\mathrm{c}}_{\mathrm{re}}$	System Matrix – Continuous-Time Remaining Plant
$\mathbf{A}_{\mathrm{re}}$	System Matrix – Discrete-Time Remaining Plant

A_{x}	Longitudinal Effective Flow Surface
A_{y}	Lateral Effective Flow Surface
$\mathbf{B}_{\mathrm{a}}$	Input Matrix – Discrete-Time Augmented Plant
$\mathbf{B}_{\mathrm{c,p}}^{\mathrm{c}}$	Control Input Matrix – Continuous-Time Plant
$\mathbf{B}_{\mathrm{c,p}}$	Control Input Matrix – Discrete-Time Plant
$\mathbf{B}_{\mathrm{d}}$	Input Matrix – Discrete-Time Disturbance Model
$\mathbf{B}_{\mathrm{d,p}}^{\mathrm{c}}$	Disturbance Input Matrix – Continuous-Time Plant
$\mathbf{B}_{\mathrm{d,p}}$	Disturbance Input Matrix – Discrete-Time Plant
$\mathbf{B}_{\mathrm{pa}}^{\mathrm{c}}$	Input Matrix – Continuous-Time Partial Plant
$\mathbf{B}_{\mathrm{pa}}^{\mathrm{c}\,*}$	Input Matrix – Continuous-Time Inverted Partial Plant
$\mathbf{B}_{\mathrm{re}}^{\mathrm{c}}$	Input Matrix – Continuous-Time Remaining Plant
$\mathbf{B}_{\mathrm{re}}$	Input Matrix – Discrete-Time Remaining Plant
$\mathbf{C}_{\mathrm{a}}$	Output Matrix – Discrete-Time Augmented Plant
$\mathbf{C}_{\mathrm{coop}}^{\mathrm{c}}$	Output Matrix for Cooperative Dynamic Feedforward Control Synthesis – Continuous-Time Remaining Plant
$\mathbf{C}_{\mathrm{coop}}$	Output Matrix for Cooperative Dynamic Feedforward Control Synthesis – Discrete-Time Remaining Plant
$\mathbf{C}_{\mathrm{d}}$	Output Matrix – Discrete-Time Disturbance Model
$\mathbf{C}_{\mathrm{est}}^{\mathrm{c}}$	Output Matrix for Estimator Synthesis – Continuous-Time Remaining Plant
$\mathbf{C}_{\mathrm{est}}$	Output Matrix for Estimator Synthesis – Discrete-Time Remaining Plant
c_{f}	Cornering Stiffness Front
$\mathbf{C}_{\mathrm{m,p}}^{\mathrm{c}}$	Measurement Output Matrix – Continuous-Time Plant
$\mathbf{C}_{\mathrm{m,p}}$	Measurement Output Matrix – Discrete-Time Plant
$\mathbf{C}_{\mathrm{mpc}}^{\mathrm{c}}$	Output Matrix for MPC Synthesis – Continuous-Time Remaining Plant
$\mathbf{C}_{\mathrm{mpc}}$	Output Matrix for MPC Synthesis – Discrete-Time Remaining Plant
$\mathbf{C}_{\mathrm{pa}}^{\mathrm{c}}$	Output Matrix – Continuous-Time Partial Plant
$\mathbf{C}_{\mathrm{pa}}^{\mathrm{c}\,*}$	Output Matrix – Continuous-Time Inverted Partial Plant
$\mathbf{C}_{\mathrm{pos}}^{\mathrm{c}}$	Position Output Matrix – Continuous-Time Plant
$\mathbf{C}_{\mathrm{pos}}$	Position Output Matrix – Discrete-Time Plant
c_{r}	Cornering Stiffness Rear
$\mathbf{C}_{\mathrm{trq}}^{\mathrm{c}}$	Torque Output Matrix – Continuous-Time Plant
$\mathbf{C}_{\mathrm{trq}}$	Torque Output Matrix – Discrete-Time Plant
c_{TS}	Stiffness of the Torsion Bar
c_{x}	Longitudinal Air Drag Coefficient
c_{y}	Lateral Air Drag Coefficient
d_{EM}	Viscous Friction Coefficient - Electric Motor
d_{PN}	Viscous Friction Coefficient - Pinion
$d_{\overline{\mathrm{PN}}}$	Lumped Viscous Friction Coefficient - Pinion
$d_{\mathrm{ref}}, d_{\mathrm{unk}}$	Virtual Disturbances
d_{SW}	Viscous Friction Coefficient - Steering Wheel
d_{TS}	Material Damping of the Torsion Bar
D	Damping Coefficient

$\mathbf{D}_{\mathrm{coop}}^{\mathrm{c}}$	Feedthrough Matrix for Cooperative Dynamic Feedforward Control Synthesis – Continuous-Time Remaining Plant
$\mathbf{D}_{\mathrm{coop}}$	Feedthrough Matrix for Cooperative Dynamic Feedforward Control Synthesis – Discrete-Time Remaining Plant
$\mathbf{D}_{\mathrm{pa}}^{\mathrm{c}}$	Feedthrough Matrix – Continuous-Time Partial Plant
$\mathbf{D}_{\mathrm{pa}}^{\mathrm{c}\,*}$	Feedthrough Matrix – Continuous-Time Inverted Partial Plant
$\mathbf{F}, \mathbf{G}, \mathbf{H}, \mathbf{E}$	Prediction Model Matrices
F_{f}	Front Axle Force
F_{n}	Normal Force
F_{r}	Rear Axle Force
F_{x}	Longitudinal Force
$F_{\mathrm{x,d}}$	Longitudinal Disturbance Force
F_{y}	Lateral Force
$F_{\mathrm{y,d}}$	Lateral Disturbance Force
g	Gravitational Constant
$G_{\mathrm{n}}(s)$	Transfer Function of the Nominal Plant Model
$\mathbf{G}(\mathrm{s})$	Transfer Function Matrix
i_{Mot}	Gear Ratio – Motor to Pinion
i_{s}	Gear Ratio – Steering Wheel to Road Wheel Position
J	Performance Index of Quadratic Cost Function
J_{EM}	Electric Motor plus Gear Inertia
J_{PN}	Pinion Inertia
$J_{\overline{\mathrm{PN}}}$	Lumped Pinion Inertia
J_{SW}	Steering Wheel Inertia
J_{z}	Vehicle Inertia about the z-Axis
k	Sample Index
$\mathbf{K}$	Model Predictive Controller Gains (Unconstrained)
$\mathbf{K}_{\mathrm{d}}$	Feedforward Gains for Steady-State Disturbance Rejection
$\mathbf{K}_{\mathrm{p}}$	Optimal State-Feedback Gain Matrix
K_{r}	Feedforward Gain for Steady-State Reference Tracking
l_{f}	Distance - Front Axle to the Center of Gravity
l_{r}	Distance - Rear Axle to the Center of Gravity
l_{wind}	Distance - Side Wind Force to the Center of Gravity
$\mathbf{L}$	Estimator Feedback Gain Matrix
$L_{\mathrm{a}}^{0}\mathrm{c}(\mathbf{x}), L_{\mathrm{a}}^{1}\mathrm{c}(\mathbf{x}), L_{\mathrm{b}}^{1}\mathrm{c}(\mathbf{x})$	Lie-derivatives
m	Vehicle Mass
n	System Order
n_{c}	Control Horizon
n_{p}	Prediction Horizon
$\mathbf{P}_{\mathrm{e}}^{*}$	Steady-State Solution of the Discrete Algebraic Riccati Equation for Kalman Filter Design
q	Quantization Interval
$\mathbf{Q}$	Objective Output Vector Weighting Matrix
r_{pos}	Reference Steering Position
R	Radius

R_{ref}	Reference Path Radius
r_{trq}	Reference Steering Torque
$Q(s)$	Transfer Function of the Q-Filter for the Inverse Disturbance Observer
$\mathbf{Q}_{\mathrm{ctrb}}$	Controllability Matrix
r	Reference Variable
$\mathbf{R}$	Control Input Vector Weighting Matrix
s	Laplace Transform Variable
$\mathbf{S}$	Steady-State Solution of the Discrete Algebraic Riccati Equation for State-Feedback Controller Design
$S(s)$	Sensitivity Function
$\mathbf{T}$	Transformation Matrix
T_{DR}	Driver Torque
$\hat{T}_{\mathrm{DR}}$	Estimated Driver Torque
T_{EM}	Motor Output Torque
T_{EM}^{*}	Reference Motor Torque
$T_{\mathrm{fric,EM}}$	Coulomb Friction Torque of Motor Bearing and Gear
$T_{\mathrm{fric,PN}}$	Coulomb Friction Torque - Pinion
T_{React}	Internal Reaction Torque
T_{RK}	External Rack Torque - Pinion
$\mathrm{T_s}$	Sampling Time
T_{TB}	Torsion Bar Torque
T_{TS}	Torque Sensor Torque
$T_{\mathrm{z,d}}$	Disturbance Torque about the Vehicle z-Axis
$\mathbf{u}_{\mathrm{a}}$	Augmented Plant Input Vector
$u_{\mathrm{c,p}}$	Plant Control Input
$\mathbf{u}_{\mathrm{d,p}}$	Plant Disturbance Input Vector
$u_{\mathrm{min}}, u_{\mathrm{max}}$	Control Input Limits
$\overline{\mathbf{u}}_{\mathrm{min}}, \overline{\mathbf{u}}_{\mathrm{max}}$	Control Input Limit Sequence
u_{opt}	Optimal Control Input
u_{pa}	Partial Plant Input
u_{pa}^{*}	Inverted Partial Plant Input
$\overline{\mathbf{u}}_{\mathrm{pd}}$	Disturbance Input Sequence
$\mathbf{u}_{\mathrm{re}}$	Remaining Plant Input Vector
v	Vehicle Speed
v_{wind}	Side Wind Speed
v_{x}	Longitudinal Vehicle Speed
v_{y}	Lateral Vehicle Speed
$\mathbf{v}$	Measurement Noise Vector
$\mathbf{V}$	Measurement Noise Covariance
v_0	Zero Frequency
$\mathbf{w}$	Process Noise Vector
$\mathbf{W}$	Process Noise Covariance
$\mathbf{x}_{\mathrm{a}}$	Augmented Plant State Vector
$\hat{\mathbf{x}}_{\mathrm{a}}$	Estimated Augmented Plant State Vector
$\mathbf{x}_{\mathrm{d}}$	Disturbance State Vector

$\hat{\mathbf{x}}_{\mathrm{d}}$	Estimated Disturbance State Vector
$x_{\mathrm{g}}, y_{\mathrm{g}}$	Global Coordinates
$\mathbf{x}_{\mathrm{p}}$	Plant State Vector
$\hat{\mathbf{x}}_{\mathrm{p}}$	Estimated Plant State Vector
$\mathbf{x}_{\mathrm{pa}}$	Partial Plant State Vector
$\mathbf{x}_{\mathrm{pa}}^{*}$	Inverted Partial Plant State Vector
$x_{\mathrm{r}}, y_{\mathrm{r}}$	Road Coordinates
$\mathbf{x}_{\mathrm{re}}$	Remaining Plant State Vector
$x_{\mathrm{v}}, y_{\mathrm{v}}$	Vehicle-Fixed Coordinates
$\mathbf{y}_{\mathrm{a}}$	Augmented Plant Output Vector
$\mathbf{y}_{\mathrm{coop}}$	Remaining Plant Output Vector for Cooperative Dynamic Feedforward Control Synthesis
y_{est}	Remaining Plant Output for Estimator Synthesis
$\mathbf{y}_{\mathrm{m,p}}$	Measurement Output Vector - Plant
$\mathbf{y}_{\mathrm{mpc}}$	Remaining Plant Output Vector for MPC Synthesis
y_{pa}	Partial Plant Output
y_{pa}^{*}	Inverted Partial Plant Output
y_{pos}	Steering Position Output - Plant
y_{r}	Lateral Deviation between the Vehicle's Center of Gravity and Reference Path
y_{trq}	Steering Torque Output - Plant
$\overline{\mathbf{y}}$	Objective Output Sequence
z	z-Transform Variable
$\mathbf{z}$	State Vector in Nonlinear Control Canonical Form

Abstract

With the global trend towards automated driving, fault-tolerant onboard power supply systems are introduced into modern vehicles and the level of driving automation is continuously increasing. These advancements contribute to the applicability of Steer-by-Wire systems and the development of automated lateral vehicle guidance control functions. For the market acceptance of automated driving, the lateral vehicle guidance control function must hereby be cooperative, that is it must accept driver interventions. Existing approaches for automated lateral vehicle guidance commonly do not consider driver interventions. If unconsidered in the control loop, the driver intervention is interpreted as an external disturbance that is actively compensated by feedback. This thesis addresses the development of a cooperative lateral vehicle guidance control concept, which enables a true coexistence between manual steering control by the driver and automated steering control. To this end, the subordinate controls of the Steer-by-Wire system for the manual and automated driving mode are initially presented. These include the steering feel generation and steering torque control of the Steer-by-Wire Handwheel Actuator for the manual driving mode, which is structurally extended to a cascade steering position control for the automated driving mode. Subsequently, a superposition control is introduced, which fuses steering torque and position control. The resulting cooperative Handwheel Actuator control achieves precise tracking of the reference steering position in automated driving mode but accepts driver interventions. Thus, the driver can override the active control and experiences a natural steering feel. The transitions hereby are seamless as no blending, gain scheduling or controller output saturation is required. Subsequently, the superimposed lateral vehicle guidance controller for the automated driving mode is described, which computes the reference steering position for the respective Steer-by-Wire controls. In contrast to existing approaches, the plant model equations are rearranged to isolate the vehicle speed dependent dynamics. Thereafter, the concept of inverse nonlinearity control is employed, using a virtual control loop and feedback linearization for an online inversion of the nonlinear plant dynamics. The remaining plant is fully linear and independent of vehicle speed. Consequently, one controller can be synthesized that is valid for all vehicle speeds. The closed and open loop system thereby have the same dynamics independent of vehicle speed, which significantly simplifies control synthesis, analysis, and performance tuning in the vehicle. For considering the future reference path information and constraints on the maximum steering position within the control law, a linear Model Predictive Controller synthesis is selected. The combination of inverse nonlinearity control and linear Model Predictive Controller thus results in a Nonlinear Adaptive Model Predictive Control concept, which makes commonly applied gain scheduling fully obsolete. The controller is structurally extended by a cooperative dynamic feedforward control for considering driver interventions within the control loop. Consequently, the driver can override the active control and seamlessly modify the lateral vehicle motion. A variety of nonlinear simulation analyses and real vehicle tests demonstrate the effectiveness of the proposed control concept.

1 Introduction

1.1 Motivation

Upcoming vehicle generations will provide fault-tolerant onboard power supply systems and an increasing level of driving automation. These changes contribute to the applicability of Steer-by-Wire (SbW) systems and the development of automated lateral vehicle guidance control functions. For the market acceptance of automated driving, the lateral vehicle guidance control function must be cooperative, that is it must permit driver interventions.
Cooperative lateral vehicle guidance control (CVGC) enables a true coexistence between manual steering control by the driver and automated steering control by the automation system. Advanced driver assistance systems (ADAS) like enhance lane guidance will drive the need for CVGC (ADAS with driver intervention, Level 2+). CVGC is relevant for Level 3 autonomous driving, where a human driver must intervene in the driving task in case of a system limitation. Furthermore, it is relevant for Level 4 automated driving, where in most circumstances the driver must not intervene but must still be given the option to intervene in the driving task. Examples of application are the driver steering the vehicle away from construct work or road narrowings, keeping a safe lateral distance to trucks, overtaking a slowly moving vehicle on a single lane road and avoiding obstacles undetected by the automation system.
The primary actuators for the lateral vehicle guidance control of future vehicles are SbW systems. These systems are considered a key technology for highly automated driving as they allow eliminating the mechanical coupling between the steering wheel and road wheels for the sake of permitting: (1) steering control by the driver and (2) steering control by the automation system. Moreover, these systems provide advantages in terms of packaging, vibration, and noise transfer to the cockpit, enhanced occupant safety during crashes, and variable ratio functionality. A direct consequence, which arises from the mechanical decoupling is that the driver does not receive any road feedback. The missing torque feedback must therefore be simulated by an additional actuator at the steering wheel. This actuator is called the Handwheel Actuator (HWA). A second actuator at the front axle of the vehicle (Front Axle Actuator, FAA) moves the road wheels according to the steering commands of the driver. In this context, the steering commands are measured by an angle sensor at the steering wheel and electrically transmitted to the FAA.

Figure 1 shows a schematic diagram of the SbW prototype system architecture. The prototype system consists of a Column Drive Electric Power Steering System (used as HWA) and a Rack Drive Electric Power Steering System (used as FAA). Both systems are electrically connected to a dSPACE MicroAutoBox II (MABX II) control unit, which is a real-time system for performing rapid control prototyping (RCP). In the event of actuator or sensor failures, it must be ensured that the vehicle remains manually steerable by the driver. Therefore, the prototype system is equipped with an electromagnetic clutch between HWA and FAA, which is engaged in the event of system failures and provides an instantaneous mechanical coupling between the steering wheel and road wheels (fail-safe strategy).

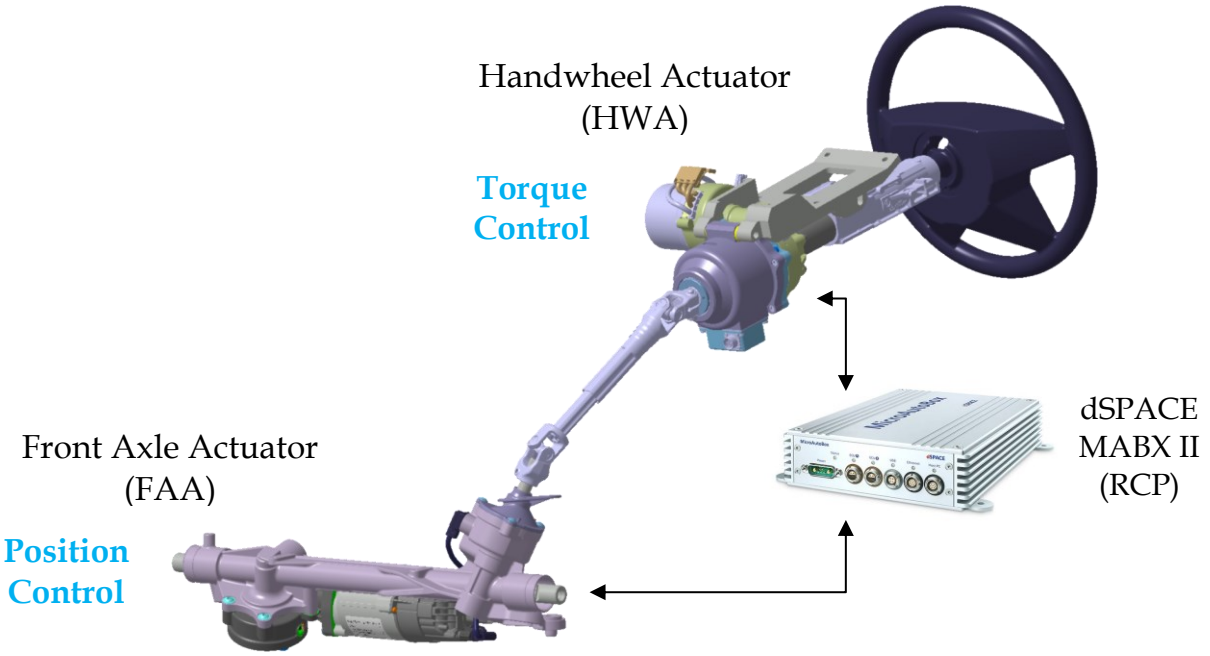

Figure 1: SbW Prototype System Architecture (Source: ZF)

In order to achieve that the road wheels dynamically track the steering wheel inputs of the driver, the FAA must be operated in closed-loop steering position control mode. For this purpose, the measured steering wheel angle serves as the reference signal for position control as it directly captures the driver's steering intent. Alternatively, a reference signal provided by an automated lateral vehicle guidance controller can be supplied. The forces at the front axle are estimated based on the actual vehicle driving state conditions and converted into a reference steering torque. This reference steering torque represents the torque feedback that is expected by the driver during manual driving. To provide this information at the steering wheel, a closed-loop steering torque control of the HWA is required.

1.2 State of the Art

Driven by the progressive development of automated driving functions, the control synthesis for lateral vehicle guidance is subject to various current research. This chapter aims at presenting the state of the art by outlining existing approaches from literature for cooperative and automated lateral vehicle guidance control.

1.2.1 Existing Concepts for Automated Lateral Vehicle Guidance

Several control concepts for automated lateral vehicle guidance were developed, which can be generally structured in:

- Classical Control Methods: Cascade control, PID control, PD plus feedforward control, etc., are often applied for lateral vehicle guidance (see [Ise22], [Zin+12], [Kri12], [Kra+16], [Tal+11], [Kel+15], [Keh07], [Rat+14], [Mou+97], [Mei+04]). As linear dynamic vehicle models are used, the controller design is rather simple. The controller is however only valid for a constant vehicle speed, so that multiple designs for selected vehicle speed breakpoints are required, and gain scheduling is introduced. This is a disadvantage, particularly for the applicability in series production vehicles.

- State-Feedback Control Methods: Reveal the advantage of an extended design freedom as the eigenvalues can be arbitrarily assigned assuming that the plant is fully controllable (see [Mou+97], [Jeo+19], [Lu+18], [Kön+07], [Men+14], [Sni09]). The design is typically based on linear vehicle models. Therefore, multiple controllers for a family of plants must be designed and gain scheduling is required.

- Model Predictive Control (MPC) Methods: Allow considering physical constraints and have previewing capability, which makes them excellently suitable for automated lateral vehicle guidance. However, as the plant dynamics change as a function of vehicle speed, the MPC cost function weights, prediction model, and Kalman Filter are still subject to gain scheduling (see [Gal+17], [Kat+11], [Kat+13], [Sch19], [Kel17], [Yos+08], [Gal21]).

- Feedback Linearization Methods: Pursue the design of one controller that achieves the same dynamics of the closed-loop system independent of vehicle speed. These methods are typically applied to lower order systems as otherwise the complexity of the expressions from the Lie derivatives cannot be handled. Consequently, to reduce the system order parts of the plant dynamics, such as actuator dynamics or lateral vehicle dynamics, are neglected (see [Kor+19], [Rat16], [Wer+12], [Kön09]).

Common approaches in literature make use of an adaptive control, as the lateral vehicle dynamics strongly vary with vehicle speed. Classical and state-feedback control methods thereby perform an offline controller design followed by gain scheduling. Model predictive control methods use an online controller design, but the cost function weights, prediction model and Kalman Filter are still subject to gain scheduling. This implies a large effort in controller design, analysis, tuning, and vehicle performance evaluation. Feedback linearization methods can avoid this but typically require some

sort of model order reduction. Otherwise, the complexity of the resulting control law is not manageable. To avoid the extensive effort of gain scheduling and shortcomings of feedback linearization, a novel approach is pursued in this thesis. The approach has the objective to design one controller that is valid for all vehicle speeds. Hereby the closed and open loop system should have the same dynamics independent of vehicle speed. For incorporating future course information, the controller should further have preview capability. In this contribution, a Nonlinear Adaptive MPC concept is presented, which provides these properties.

1.2.2 Existing Concepts for Cooperative Lateral Vehicle Guidance

Cooperative lateral vehicle guidance control requires that the outer lateral vehicle guidance control loop and the inner steering position control loop accept driver interventions. Since the topic is subject to current research in the automotive industry, only a few works are published that focus on either one of these control levels. These are outlined in the following.

In [Wal+14] a steering position control for assisted to highly automated driving is presented. The position controller is a cascade control with disturbance observer. Moreover, a rack force feedforward is used to unburden the feedback controller. For highly automated driving, large controller gains are selected to ensure accurate reference tracking and strong disturbance rejection. For cooperative driving, weak controller gains are chosen, so that the driver can override the active steering position control. Additionally, the integral action of the controller, which is realized by the disturbance observer, is disabled in the event of a driver intervention.

A similar approach is pursued by [Sch19], who applies a PID steering position control with disturbance feedforward. In highly automated driving mode, large controller gains are used. In cooperative driving mode, weak controller gains are selected, and the integrator is disabled. Furthermore, the position controller output is saturated to a maximum level. Therefore, the driver can override the active position control.

The work of [Fuc+19] adopts a blending strategy between steering position and torque control. Thereby the blending variable is the position control error induced by the driver. This has the advantage that the full control performance is available in the absence of a driver intervention whereas in the event of a driver intervention a natural steering feel is perceived. However, the blending process causes undesirable transitions that are noticeable by the driver.

A lateral vehicle guidance control for assisted to highly automated driving is synthesized in [Rat16]. The integral action of the controller is provided by a disturbance observer. This observer is designed in a specific structure so that the driver torque is not considered as a disturbance. Consequently, the integral controller part reveals a cooperative behavior with respect to driver interventions. For the proportional-derivative controller parts, a gain reduction is proposed. The approach builds on the assumption that for a holistic cooperative control behavior, the inner steering position control loop must also expose a cooperative behavior and shall not compensate the driver torque.

The majority of existing concepts in literature hence adopt a blending, gain scheduling, or controller output saturation strategy on either the lateral vehicle guidance control or steering position control level for realizing a cooperative control behavior. This implies that cooperative behavior is achieved at the expense of control performance degradation. Furthermore, the steering feel is modified as weak control actions are impacting the driver's steering torque. A blending strategy prevents these deficits but involves transitions that are undesirable and noticeable by the driver.
In this thesis, a cooperative HWA control for the Steer-by-Wire system is presented, which enables a true coexistence between steering torque and position control. Thus, the driver can override the active position control while experiencing a natural steering feel. The transitions hereby are smooth as no manual switching involving discontinuities is required. Moreover, a cooperative lateral vehicle guidance control is proposed, which fuses manual steering control by the driver and automated steering control. Thereby, the driver can modify the lateral vehicle motion during automated driving without transitions.

1.3 Problem Description and Objective

Existing approaches for automated lateral vehicle guidance do not consider driver interventions. If unconsidered in the control loop, the driver intervention is interpreted as an external disturbance that is actively compensated by feedback. These automated lateral vehicle guidance control functions therefore expose no cooperative control behavior. Existing approaches for cooperative lateral vehicle guidance commonly rely on gain scheduling, controller output saturation, or blending strategies. Hereby transitions occur that are undesirable as they negatively impact the steering feel, and the control performance is temporarily degraded.
For exploiting the full potential of cooperative lateral vehicle guidance control, a true coexistence between the driver and automation system is pursued. Hereby the driver can override the automation system and experiences a desired steering feel. The transitions during a driver intervention must be seamless. The intervention process must furthermore be intuitive in the sense that the driver can simply hold, steer, and release the steering wheel. Thus, the driver workload is reduced while improving comfort and safety.
The objective of this thesis is to develop a novel control concept for the cooperative lateral vehicle guidance of automated vehicles with Steer-by-Wire systems, which possesses the outlined properties. Thereby different control modes of the vehicle, that is manual driving, automated driving, and cooperative driving, are explicitly considered, and their underlying control structures are systematically designed.

1.4 Outline

This thesis is structured into the following chapters: **Chapter 2** provides an overview of the dynamic models for the Steer-by-Wire system and the lateral vehicle motion. These models are used as a basis for controller synthesis.

In **Chapter 3** the control synthesis for the HWA and FAA of the Steer-by-Wire system is detailed. Hereby the systematic design of the steering torque and the steering position control is presented.

Subsequently, **Chapter 4** describes the synthesis of a Nonlinear Adaptive MPC for automated lateral vehicle guidance. The concept employs an Inverse Nonlinearity Control to cancel the vehicle speed-dependent plant dynamics. For the remaining linear plant, one controller is designed that is valid over the complete operating range. To consider future course information and physical constraints, an MPC design is chosen.

Chapter 5 covers the extension of the control concept for cooperative lateral vehicle guidance. Hereby a superposition control is introduced to fuse steering position and torque control of the HWA. Thereafter, a 2DOF Nonlinear Adaptive MPC is presented, which makes use of a dynamic feedforward control to fuse manual and automated lateral vehicle guidance. The overall control concept thus accepts driver interventions.

Chapter 6 addresses the practical realization and experimental validation of the control concept in a Steer-by-Wire VW Golf 7 prototype vehicle.

Finally, in **Chapter 7** the results of this work are summarized, and an outlook on future research is given.

2

Mathematical Modeling, Identification, and Evaluation

In this chapter, the derivation of mathematical models for the SbW system and lateral vehicle motion is described. Hereby the former is subdivided into HWA and FAA. The applied modeling process is strongly systematic and includes the following sequential steps. On the basis of a schematic diagram of the system a physical replacement model is obtained. From this model, the free-body diagrams are drawn, and the nonlinear differential equations are derived. System identification and model evaluation are conducted to ensure that the nonlinear model accurately reflects the dynamics of the real system. Subsequently, the nonlinear equations are linearized, transformed to state-space representation, and discretized for a sampling time corresponding to the measurement update. The linearized plant model is then analyzed in the frequency domain regarding its essential dynamic properties given by the eigenvalues and transmission zeros. Finally, the developed models provide a suitable basis for control synthesis.

2.1 Steer-by-Wire Handwheel Actuator

Figure 2 shows the schematic diagram of the HWA for the SbW system.

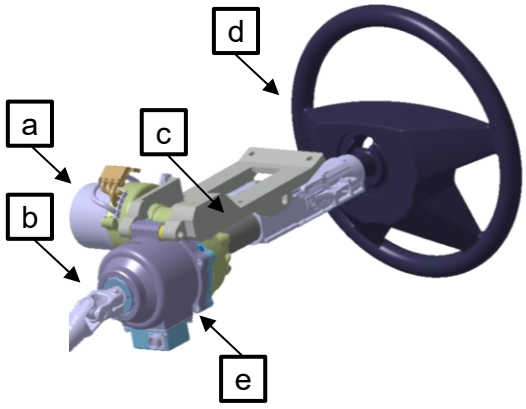

Figure 2: Steer-by-Wire HWA (Source: ZF)

The HWA consists of an interior permanent magnet synchronous motor (a) that is connected over a worm gear assembly to the steering column (b), a flexible torsion bar with finite stiffness (c), and the steering wheel (d). Moreover, the upper half of an electromagnetic clutch (e) is mounted to the steering column. The clutch is disengaged

during normal system operation and provides a mechanical fallback in failure mode. The worm gear assembly translates the torque of the electric motor to a torque at the steering column that is felt by the driver. Due to the finite stiffness of the torsion bar, a structural resonance is introduced to the system at low frequency. This resonance can be easily excited by the motor and cause unwanted torsional oscillations in the control system if not adequately considered. Therefore, it is important to include this flexibility in the nonlinear dynamic plant model [Fra+14]. Besides the described mechanical components, the system is furthermore equipped with a motor position encoder and a steering torque and angle sensor. The latter is measuring the torque of the flexible shaft via a differential angle measurement and the upper torsion bar angle [Pfe+17].

2.1.1 Nonlinear Plant Model

For deriving a physically motivated model, which describes the dynamic behavior of the system with sufficient accuracy, the mechanical components are modeled by spring, mass, damper, and gear elements [Fra+14]. Therewith, the following physical replacement system results

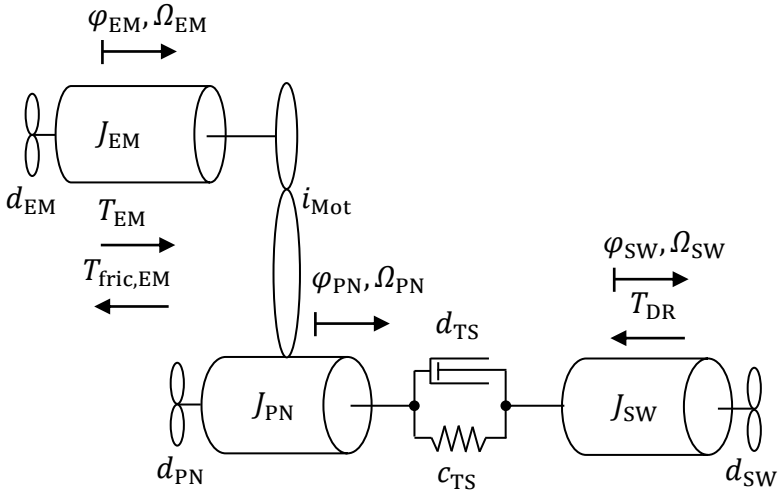

Figure 3: Physical Replacement System – HWA

In this context, the inertias of the electric motor and the worm screw are considered by a lumped inertia (J_{EM}), which is rigidly connected over the worm drive to the steering column inertia (J_{PN}). The steering column inertia is elastically coupled to the steering wheel inertia (J_{SW}) through a flexible torsion bar. For modeling the elasticity of the torsion bar, a spring-damper mechanism with linear stiffness c_{TS} and linear damping constant d_{TS} (i.e. material damping) is considered. The rotational motion of the inertias is described by the state variables angular position (φ_i) and angular velocity (Ω_i) with respect to inertial reference frames (see Figure 3). The mechanical system is driven by the motor output torque (T_{EM}). The driver torque (T_{DR}) as well as the nonlinear gear friction torque ($T_{fric,EM}$) act as disturbance variables. For considering bearing friction, viscous damping elements are further added to the respective inertias (d_{EM}, d_{PN}, d_{SW}). By drawing the free-body diagrams for each inertia and deriving the equations of motion (Newton's Law), the nonlinear differential equations of the plant are obtained[1]

[1] For reasons of readability, the time variable t is omitted in the further course of this work.

$$J_{\mathrm{EM}}\dot{\Omega}_{\mathrm{EM}}(t) = T_{\mathrm{EM}}(t) - d_{\mathrm{EM}}\Omega_{\mathrm{EM}}(t) - T_{\mathrm{fric,EM}}(t) - T_{\mathrm{React}}(t) \tag{2.1}$$

$$J_{\mathrm{PN}}\dot{\Omega}_{\mathrm{PN}}(t) = T_{\mathrm{React}}(t)i_{\mathrm{Mot}} + T_{\mathrm{TB}}(t) - d_{\mathrm{PN}}\Omega_{\mathrm{PN}}(t) \tag{2.2}$$

$$J_{\mathrm{SW}}\dot{\Omega}_{\mathrm{SW}}(t) = -T_{\mathrm{DR}}(t) - T_{\mathrm{TB}}(t) - d_{\mathrm{SW}}\Omega_{\mathrm{SW}}(t) \tag{2.3}$$

with

$$T_{\mathrm{TB}}(t) = c_{\mathrm{TS}}[\varphi_{\mathrm{SW}}(t) - \varphi_{\mathrm{PN}}(t)] + d_{\mathrm{TS}}[\Omega_{\mathrm{SW}}(t) - \Omega_{\mathrm{PN}}(t)]. \tag{2.4}$$

These are further simplified by eliminating the internal reaction torques (T_{React}) in (2.1) and (2.2). In addition, the inertia of the electric motor and the steering column are lumped to a substitute inertia ($J_{\overline{\mathrm{PN}}}$). This gives the simplified nonlinear plant equations

$$J_{\overline{\mathrm{PN}}}\dot{\Omega}_{\mathrm{PN}} = T_{\mathrm{EM}}i_{\mathrm{Mot}} + T_{\mathrm{TB}} - T_{\mathrm{fric,PN}} - d_{\overline{\mathrm{PN}}}\Omega_{\mathrm{PN}} \tag{2.5}$$

$$J_{\mathrm{SW}}\dot{\Omega}_{\mathrm{SW}} = -T_{\mathrm{DR}} - T_{\mathrm{TB}} - d_{\mathrm{SW}}\Omega_{\mathrm{SW}} \tag{2.6}$$

with

$$J_{\overline{\mathrm{PN}}} = J_{\mathrm{PN}} + i_{\mathrm{Mot}}^2 J_{\mathrm{EM}} \tag{2.7}$$

$$d_{\overline{\mathrm{PN}}} = d_{\mathrm{PN}} + i_{\mathrm{Mot}}^2 d_{\mathrm{EM}} \tag{2.8}$$

$$T_{\mathrm{fric,PN}} = i_{\mathrm{Mot}} T_{\mathrm{fric,EM}}. \tag{2.9}$$

The dynamics of the controlled electric motor are approximated by a first-order lag element with ω_{bw} reflecting the control bandwidth and T_{EM}^* the reference motor torque

$$\dot{T}_{\mathrm{EM}} = -\omega_{\mathrm{bw}} T_{\mathrm{EM}} + \omega_{\mathrm{bw}} T_{\mathrm{EM}}^*. \tag{2.10}$$

The physical model parameters are determined experimentally through detailed parameter identification tests on subcomponent level. By this proceeding accurate initial values for the inertias, stiffness, damping coefficients, and nonlinear friction are found. These are subsequently further refined by frequency response analysis between model and real system. Figure 4 shows the frequency response identification and model evaluation results.

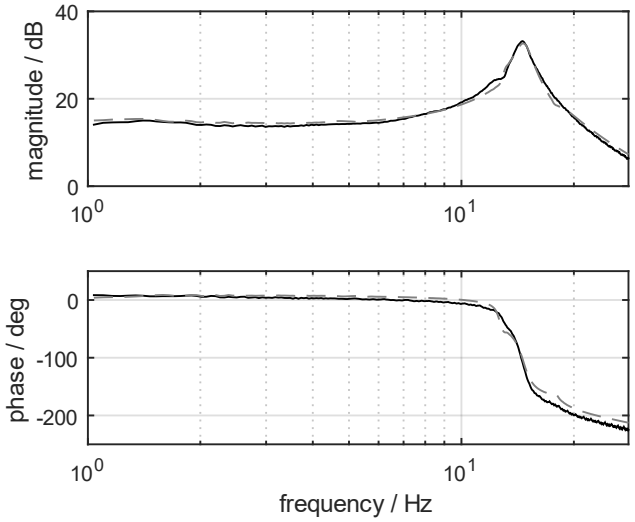

Figure 4: Comparison of Frequency Response Measurement (black) and Nonlinear Model (grey dashed) from Reference Motor Torque T_{EM}^* to Steering Torque T_{TS}

For system identification a sine sweep excitation signal with frequencies from 1 to 30 Hz is injected as the reference motor torque and the steering torque is measured. From the recorded time series of excitation and response signal the cross power spectral density and auto power spectral density are computed. Based on these quantities, the frequency responses of the model and the real system are calculated (refer to [Ise+10]). If the frequency response was computed directly from the discrete Fourier transform of the input and output signal, the result would be rather noisy. The reason for this is the variance of the disturbing noise that is contained in the measurement. To overcome this problem an average of multiple estimates can be taken to reduce the standard deviation of the result. This averaging requires the computation of the power spectral density and cannot be done with the linear spectrum (refer to [Hei+02]). Therefore, the frequency response computation is based on power spectral densities in this work.

The performance evaluation of the identified model as illustrated in Figure 4 reveals a maximum error of 2 dB in magnitude (at frequency = 12.2 Hz) and 10 deg in phase (at frequency = 30 Hz). Thus, the model accurately reflects the dynamics of the real system.

2.1.2 Linearized Plant Model

For deriving a linearized plant model from (2.5) to (2.10) that is suitable for controller synthesis, the nonlinear and external terms ($T_{\mathrm{fric,PN}}$, T_{DR}) are dropped and treated as unknown disturbance inputs. Furthermore, the position φ_{PN}, velocity Ω_{PN}, difference position $\Delta\varphi = \varphi_{\mathrm{SW}} - \varphi_{\mathrm{PN}}$, difference velocity $\Delta\Omega = \Omega_{\mathrm{SW}} - \Omega_{\mathrm{PN}}$, and motor output torque T_{EM} are selected as state variables. Thereby the equations can be transformed into the following state-space representation[2]

$$\dot{\mathbf{x}}_{\mathrm{p}} = \mathbf{A}_{\mathrm{p}}^{\mathrm{c}}\,\mathbf{x}_{\mathrm{p}} + \mathbf{B}_{\mathrm{c,p}}^{\mathrm{c}} u_{\mathrm{c,p}} + \mathbf{B}_{\mathrm{d,p}}^{\mathrm{c}} \mathbf{u}_{\mathrm{d,p}} \tag{2.11}$$

$$y_{\mathrm{trq}} = \mathbf{C}_{\mathrm{trq}}^{\mathrm{c}}\,\mathbf{x}_{\mathrm{p}} \tag{2.12}$$

$$y_{\mathrm{pos}} = \mathbf{C}_{\mathrm{pos}}^{\mathrm{c}}\,\mathbf{x}_{\mathrm{p}} \tag{2.13}$$

$$\mathbf{y}_{\mathrm{m,p}} = \mathbf{C}_{\mathrm{m,p}}^{\mathrm{c}}\,\mathbf{x}_{\mathrm{p}} \tag{2.14}$$

with

$$\mathbf{A}_{\mathrm{p}}^{\mathrm{c}} = \begin{bmatrix} 0 & 1 & 0 & 0 & 0 \\ 0 & -\frac{d_{\overline{\mathrm{PN}}}}{J_{\overline{\mathrm{PN}}}} & \frac{c_{\mathrm{TS}}}{J_{\overline{\mathrm{PN}}}} & \frac{d_{\mathrm{TS}}}{J_{\overline{\mathrm{PN}}}} & \frac{i_{\mathrm{Mot}}}{J_{\overline{\mathrm{PN}}}} \\ 0 & 0 & 0 & 1 & 0 \\ 0 & -\frac{d_{\mathrm{SW}}}{J_{\mathrm{SW}}} + \frac{d_{\overline{\mathrm{PN}}}}{J_{\overline{\mathrm{PN}}}} & -\frac{c_{\mathrm{TS}}}{J_{\mathrm{SW}}} - \frac{c_{\mathrm{TS}}}{J_{\overline{\mathrm{PN}}}} & -\frac{d_{\mathrm{SW}} + d_{\mathrm{TS}}}{J_{\mathrm{SW}}} - \frac{d_{\mathrm{TS}}}{J_{\overline{\mathrm{PN}}}} & -\frac{i_{\mathrm{Mot}}}{J_{\overline{\mathrm{PN}}}} \\ 0 & 0 & 0 & 0 & -\omega_{\mathrm{bw}} \end{bmatrix},$$

$$u_{\mathrm{c,p}} = T_{\mathrm{EM}}^{*},\quad \mathbf{u}_{\mathrm{d,p}} = \begin{bmatrix} T_{\mathrm{fric,PN}} \\ T_{\mathrm{DR}} \end{bmatrix},\quad \mathbf{x}_{\mathrm{p}} = \begin{bmatrix} \varphi_{\mathrm{PN}} \\ \Omega_{\mathrm{PN}} \\ \Delta\varphi \\ \Delta\Omega \\ T_{\mathrm{EM}} \end{bmatrix},\quad \mathbf{B}_{\mathrm{c,p}}^{\mathrm{c}} = \begin{bmatrix} 0 \\ 0 \\ 0 \\ 0 \\ \omega_{bw} \end{bmatrix},\quad \mathbf{B}_{\mathrm{d,p}}^{\mathrm{c}} = \begin{bmatrix} 0 & 0 \\ -\frac{1}{J_{\overline{\mathrm{PN}}}} & 0 \\ 0 & 0 \\ \frac{1}{J_{\overline{\mathrm{PN}}}} & \frac{1}{J_{\mathrm{SW}}} \\ 0 & 0 \end{bmatrix},$$

[2] For reasons of simple notation, the same subscript p is used for all linearized plant models in this work.

$$\mathbf{C}_{\mathrm{trq}}^{\mathrm{c}} = [0 \quad 0 \quad c_{\mathrm{TS}} \quad 0 \quad 0], \quad y_{\mathrm{trq}} = T_{\mathrm{TS}},$$
$$\mathbf{C}_{\mathrm{pos}}^{\mathrm{c}} = [1 \quad 0 \quad 0 \quad 0 \quad 0], \quad y_{\mathrm{pos}} = \varphi_{\mathrm{PN}},$$
$$\mathbf{C}_{\mathrm{m,p}}^{\mathrm{c}} = \begin{bmatrix} 1 & 0 & 0 & 0 & 0 \\ 0 & 0 & c_{\mathrm{TS}} & 0 & 0 \end{bmatrix}, \quad \mathbf{y}_{\mathrm{m,p}} = \begin{bmatrix} \varphi_{\mathrm{PN}} \\ T_{\mathrm{TS}} \end{bmatrix}.$$

The continuous-time linearized plant model is transformed to discrete time using a step invariant discretization. Hereby a sampling time of $\mathrm{T_s} = 0.001$ sec corresponding to the measurement update is selected for allowing a fast response to disturbances [Ise89]

$$\mathbf{x}_{\mathrm{p}}(k+1) = \mathbf{A}_{\mathrm{p}}\mathbf{x}_{\mathrm{p}}(k) + \mathbf{B}_{\mathrm{c,p}}u_{\mathrm{c,p}}(k) + \mathbf{B}_{\mathrm{d,p}}\mathbf{u}_{\mathrm{d,p}}(k) \tag{2.15}$$
$$y_{\mathrm{trq}}(k) = \mathbf{C}_{\mathrm{trq}}\mathbf{x}_{\mathrm{p}}(k) \tag{2.16}$$
$$y_{\mathrm{pos}}(k) = \mathbf{C}_{\mathrm{pos}}\mathbf{x}_{\mathrm{p}}(k) \tag{2.17}$$
$$\mathbf{y}_{\mathrm{m,p}}(k) = \mathbf{C}_{\mathrm{m,p}}\mathbf{x}_{\mathrm{p}}(k) \tag{2.18}$$

with

$$\mathbf{A}_{\mathrm{p}} = \mathrm{e}^{\mathbf{A}_{\mathrm{p}}^{\mathrm{c}}\mathrm{T_s}}, \quad \mathbf{B}_{\mathrm{c,p}} = \left(\int_0^{\mathrm{T_s}} \mathrm{e}^{\mathbf{A}_{\mathrm{p}}^{\mathrm{c}}\eta}\,\mathrm{d}\eta\right)\mathbf{B}_{\mathrm{c,p}}^{\mathrm{c}}, \quad \mathbf{B}_{\mathrm{d,p}} = \left(\int_0^{\mathrm{T_s}} \mathrm{e}^{\mathbf{A}_{\mathrm{p}}^{\mathrm{c}}\eta}\,\mathrm{d}\eta\right)\mathbf{B}_{\mathrm{d,p}}^{\mathrm{c}},$$
$$\mathbf{C}_{\mathrm{m,p}} = \mathbf{C}_{\mathrm{m,p}}^{\mathrm{c}}, \quad \mathbf{C}_{\mathrm{trq}} = \mathbf{C}_{\mathrm{trq}}^{\mathrm{c}}, \quad \mathbf{C}_{\mathrm{pos}} = \mathbf{C}_{\mathrm{pos}}^{\mathrm{c}}.$$

2.2 Steer-by-Wire Front Axle Actuator

Figure 5 illustrates the schematic diagram of the SbW FAA.

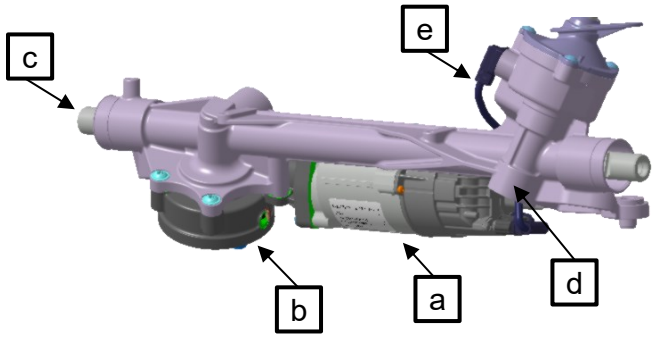

Figure 5: Steer-by-Wire FAA (Source: ZF)

The FAA consists of an interior permanent magnet synchronous motor (a) that is rigidly connected over a worm gear assembly (b) to the steering rack (c), a pinion shaft (d), and an absolute steering angle sensor (e). Moreover, the lower half of an electromagnetic clutch is mounted to the pinion. The relative motor position and absolute steering position are available as measurements and acquired by respective sensors.

2.2.1 Nonlinear Plant Model

For deriving a mathematical model, which accurately reflects the essential plant dynamics, the system components are modeled by spring, damper, mass, and gear elements. This leads to the following physical replacement model

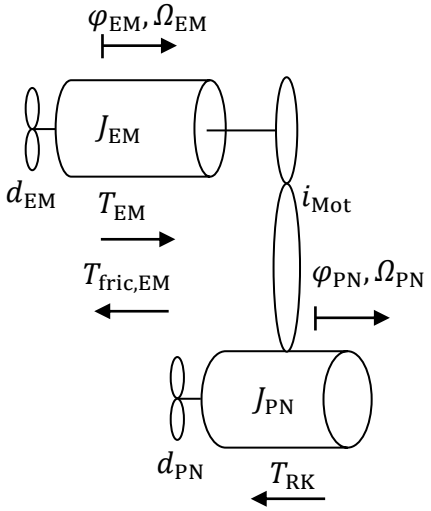

Figure 6: Physical Replacement System – FAA

It consists of an electric motor inertia (J_{EM}) that is rigidly coupled to the pinion inertia (J_{PN}) via the worm gear and a rack and pinion gear mechanism. For model simplification, the rack mass is lumped to the pinion inertia. The pinion inertia itself is coupled to the lower half of the clutch inertia. The rotatory motion of the inertias is described by the state variables angular position (φ_i) and angular velocity (Ω_i) regarding inertial reference frames. The mechanical system model is driven by the output torque of the electric motor (T_{EM}). Hereby the external load torque (T_{RK}) and the nonlinear friction torque ($T_{fric,EM}$) act as disturbances. To consider viscous friction the inertias are augmented by linear damping elements (d_{EM}, d_{PN}). By drawing the free-body diagrams of the inertias and deriving the equations of motion (Newton's Law), the differential equations of the system are derived as [Fra+14]

$$J_{EM}\dot{\Omega}_{EM} = T_{EM} - d_{EM}\Omega_{EM} - T_{fric,EM} - T_{React} \tag{2.19}$$

$$J_{PN}\dot{\Omega}_{PN} = T_{React}i_{Mot} - d_{PN}\Omega_{PN} - T_{RK}. \tag{2.20}$$

These are further simplified through the elimination of the internal reaction torques (T_{React}) in (2.19) and (2.20). Moreover, the electric motor and pinion inertia are lumped into a substitute inertia ($J_{\overline{PN}}$), which yields

$$J_{\overline{PN}}\dot{\Omega}_{PN} = T_{EM}i_{Mot} - T_{fric,PN} - T_{RK} - d_{\overline{PN}}\Omega_{PN} \tag{2.21}$$

with

$$J_{\overline{PN}} = J_{PN} + i_{Mot}^2 J_{EM} \tag{2.22}$$

$$d_{\overline{PN}} = d_{PN} + i_{Mot}^2 d_{EM} \tag{2.23}$$

$$T_{fric,PN} = i_{Mot}T_{fric,EM}. \tag{2.24}$$

The dynamics of electric motor control are approximated by a first-order lag

$$\dot{T}_{\mathrm{EM}} = -\omega_{\mathrm{bw}} T_{\mathrm{EM}} + \omega_{\mathrm{bw}} T_{\mathrm{EM}}^{*} \tag{2.25}$$

with ω_{bw} reflecting the actuator control bandwidth and T_{EM}^{*} the reference motor torque. The physical model parameters are determined experimentally through system identification. Figure 7 shows the system identification and model evaluation results for sine sweep excitation from 1 to 30 Hz. The frequency response from reference motor torque to measured pinion position shows a good correspondence between the model and real system for frequencies up to 30 Hz. The maximum error in magnitude is 0.6 dB and in phase is 3 deg at a frequency of 30 Hz. Thus, it is ensured that the model accurately reflects the dynamics of the system.

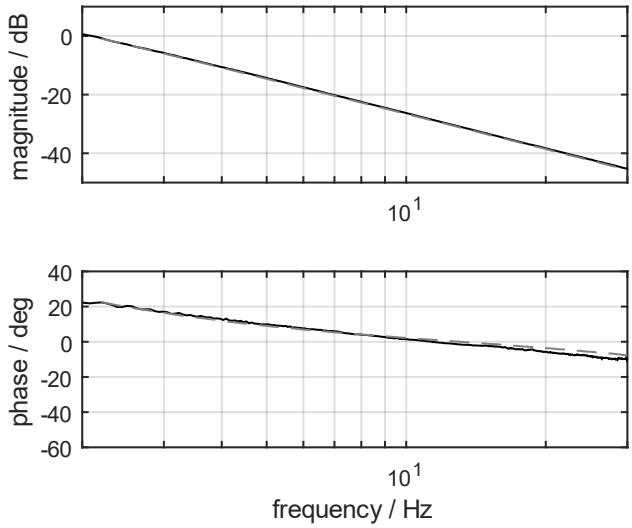

Figure 7: Comparison of Frequency Response Measurement (black) and Nonlinear Model (grey dashed) from Reference Motor Torque T_{EM}^{*} to Pinion Position φ_{PN}

2.2.2 Linearized Plant Model

For deriving a linearized plant model from (2.21) to (2.25) that is suitable for controller synthesis, the nonlinear terms ($T_{\mathrm{RK}}, \mathrm{T}_{\mathrm{fric,PN}}$) are dropped and treated as an unknown disturbance input. Furthermore, the pinion position φ_{PN}, pinion velocity Ω_{PN} and motor output torque T_{EM} are selected as states. Thereby the equations can be transformed into the following state-space representation where for consistency the same subscripts for the plant are used

$$\dot{\mathbf{x}}_{\mathrm{p}} = \mathbf{A}_{\mathrm{p}}^{\mathrm{c}}\, \mathbf{x}_{\mathrm{p}} + \mathbf{B}_{\mathrm{c,p}}^{\mathrm{c}} u_{\mathrm{c,p}} + \mathbf{B}_{\mathrm{d,p}}^{\mathrm{c}} u_{\mathrm{d,p}} \tag{2.26}$$

$$y_{\mathrm{pos}} = \mathbf{C}_{\mathrm{pos}}^{\mathrm{c}}\, \mathbf{x}_{\mathrm{p}} \tag{2.27}$$

with

$$\mathbf{A}_{\mathrm{p}}^{\mathrm{c}} = \begin{bmatrix} 0 & 1 & 0 \\ 0 & -\dfrac{d_{\overline{\mathrm{PN}}}}{J_{\overline{\mathrm{PN}}}} & \dfrac{i_{\mathrm{Mot}}}{J_{\overline{\mathrm{PN}}}} \\ 0 & 0 & -\omega_{\mathrm{bw}} \end{bmatrix},$$

$$u_{\mathrm{c,p}} = T_{\mathrm{EM}}^{*},\ u_{\mathrm{d,p}} = \left[T_{\mathrm{fric,PN}} + T_{\mathrm{RK}}\right],\ \mathbf{x}_{\mathrm{p}} = \begin{bmatrix} \varphi_{\mathrm{PN}} \\ \Omega_{\mathrm{PN}} \\ T_{\mathrm{EM}} \end{bmatrix},\ \mathbf{B}_{\mathrm{c,p}}^{\mathrm{c}} = \begin{bmatrix} 0 \\ 0 \\ \omega_{\mathrm{bw}} \end{bmatrix},\ \mathbf{B}_{\mathrm{d,p}}^{\mathrm{c}} = \begin{bmatrix} 0 \\ -\dfrac{1}{J_{\overline{\mathrm{PN}}}} \\ 0 \end{bmatrix},$$

$\mathbf{C}_{\mathrm{pos}}^{\mathrm{c}} = [1 \quad 0 \quad 0],\ \ y_{\mathrm{pos}} = \varphi_{\mathrm{PN}}.$

To allow a direct discrete controller synthesis, the continuous-time linearized plant is transformed to discrete time using a step invariant discretization and a sampling time of $T_\mathrm{s} = 0.001$ sec

$$\mathbf{x}_\mathrm{p}(k+1) = \mathbf{A}_\mathrm{p}\mathbf{x}_\mathrm{p}(k) + \mathbf{B}_\mathrm{c,p}u_\mathrm{c,p}(k) + \mathbf{B}_\mathrm{d,p}u_\mathrm{d,p}(k) \tag{2.28}$$

$$y_\mathrm{pos}(k) = \mathbf{C}_\mathrm{pos}\mathbf{x}_\mathrm{p}(k) \tag{2.29}$$

with

$$\mathbf{A}_\mathrm{p} = \mathrm{e}^{\mathbf{A}_\mathrm{p}^\mathrm{c}T_\mathrm{s}}, \quad \mathbf{B}_\mathrm{c,p} = \left(\int_0^{T_\mathrm{s}} \mathrm{e}^{\mathbf{A}_\mathrm{p}^\mathrm{c}\eta}\,\mathrm{d}\eta\right)\mathbf{B}_\mathrm{c,p}^\mathrm{c}, \quad \mathbf{B}_\mathrm{d,p} = \left(\int_0^{T_\mathrm{s}} \mathrm{e}^{\mathbf{A}_\mathrm{p}^\mathrm{c}\eta}\,\mathrm{d}\eta\right)\mathbf{B}_\mathrm{d,p}^\mathrm{c}, \quad \mathbf{C}_\mathrm{pos} = \mathbf{C}_\mathrm{pos}^\mathrm{c}.$$

2.3 Dynamics for Lateral Vehicle Guidance

In this chapter, a nonlinear dynamic plant model for lateral vehicle guidance is derived, which consists of the position-controlled FAA, lateral vehicle dynamics, and error equations relative to the reference path. To ensure that the model accurately reflects the dynamics of the real system, the physical parameters are experimentally identified, and the model is evaluated using vehicle measurements. Lastly, linearization is applied to derive a system formulation in state-space representation, which can be analyzed in terms of its essential dynamic properties.

2.3.1 Steering Position Controlled Front Axle Actuator

For ensuring an accurate lateral vehicle guidance control, the actuator dynamics must be modeled with sufficient accuracy. It should be noted that an exact modeling is not reasonable, as this would considerably increase model complexity and complicate controller design. The essential dynamics of the closed loop steering position controlled FAA (refer to [Gon+22]) are determined by a dominant pole pair. Hence, the transfer behavior can be approximated by a second-order lag element with Butterworth damping D and natural frequency ω_o selected to match the control bandwidth

$$\begin{bmatrix}\dot{\varphi}_\mathrm{FA}\\ \dot{\Omega}_\mathrm{FA}\end{bmatrix} = \begin{bmatrix}0 & 1\\ -\omega_\mathrm{o}^2 & -2D\omega_\mathrm{o}\end{bmatrix}\begin{bmatrix}\varphi_\mathrm{FA}\\ \Omega_\mathrm{FA}\end{bmatrix} + \begin{bmatrix}0\\ \omega_\mathrm{o}^2\end{bmatrix}\varphi_\mathrm{FA}^* \tag{2.30}$$

$$\varphi_\mathrm{FA} = \begin{bmatrix}1 & 0\end{bmatrix}\begin{bmatrix}\varphi_\mathrm{FA}\\ \Omega_\mathrm{FA}\end{bmatrix}.$$

Figure 8 shows a comparison between the step response measured at the real system and the linear model. The absolute error at the steepest gradient between model and real system is 0.7 deg and the essential dynamics are adequately represented. Therefore, the model provides an accurate fit and hence a sufficient approximation.

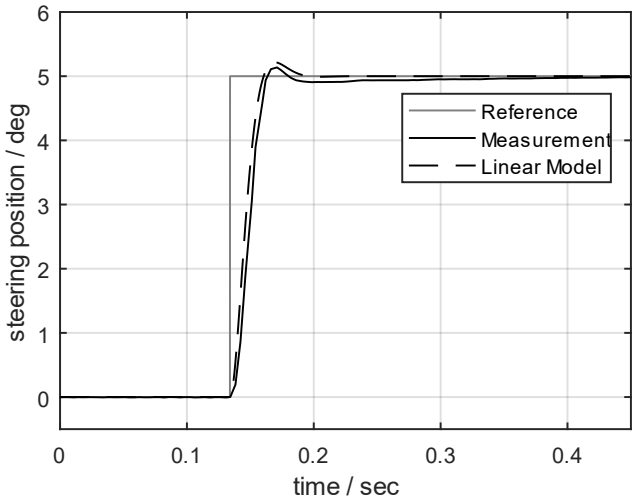

Figure 8: Step Response of the Steering Position Controlled FAA

2.3.2 Coordinate Systems

In the following, the fundamentals for modeling the vehicle motion are described. For this purpose, coordinate systems are first introduced in which the vehicle motion is defined. These are based on the norm DIN ISO 8855 that is currently used in automotive industry and are graphically illustrated in Figure 9.

Global Coordinate System

The global coordinate system $\mathcal{F}_\mathrm{g} = \{x_\mathrm{g}, y_\mathrm{g}\}$ is an earth fixed inertial reference frame with arbitrary origin. It must be chosen such that the z_g-axis lies parallel to the gravitational vector.

Vehicle Coordinate System

The vehicle coordinate system $\mathcal{F}_\mathrm{v} = \{x_\mathrm{v}, y_\mathrm{v}\}$ has its origin in the orthogonal projection of the vehicle's center of gravity on the road surface. Hereby the x_v-axis is directed towards the longitudinal vehicle axis and the y_v-axis is perpendicular to it. The z_v-axis is perpendicular to the road surface.

Road Coordinate System

The global vehicle position is unsuitable for describing the vehicle motion relative to the reference path. The decisive measure for lateral vehicle guidance is instead the lateral deviation to the reference path. For this reason, a road coordinate system $\mathcal{F}_\mathrm{r} = \{x_\mathrm{r}, y_\mathrm{r}\}$ is introduced. This coordinate system has its origin on the reference path. The x_r-axis is tangential to the reference path and the z_r-axis orthogonal to the road surface. Thus, the x_r-axis represents a measure for the distance driven by the vehicle and the y_r-axis a measure for the lateral deviation with respect to the reference path. In the literature, this coordinate system is also known as the Frénet-Serret coordinate system [Wer11].

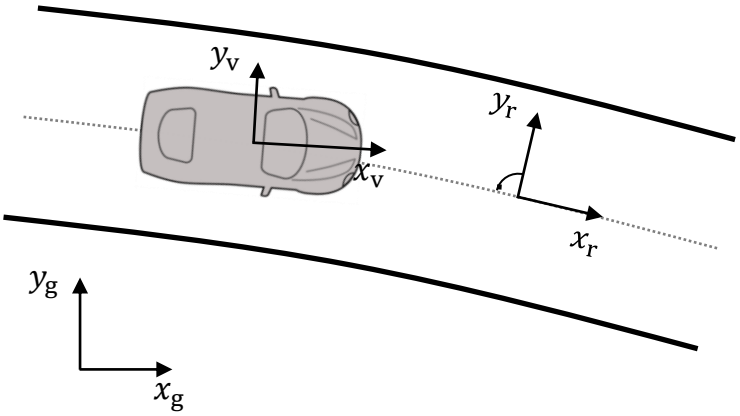

Figure 9: Overview on the Different Coordinate Systems Used in this Work

2.3.3 Lateral Vehicle Dynamics

For describing the fundamental vehicle dynamics, different models are suitable. The available models in the literature can be distinguished with increasing complexity into point mass model, kinematic single-track model, linear single-track model, nonlinear single-track model, and nonlinear two-track model (see [Raj12], [Sch+16]).
The selection of an adequate model for lateral vehicle guidance control requires considering that the lateral dynamics are described with sufficient precision and that the validity of the model over the entire vehicle speed range is given. The point mass model and kinematic single-track model do not include the lateral dynamics. In contrast, the linear single-track model considers the lateral dynamics, but it is exclusively valid for the linear driving range. Hence, the nonlinear models are remaining. With this regard, work by [Kon+15] suggests using a nonlinear single-track model for controller design in automated driving applications. The nonlinear two-track model is also providing the desired degree of precision. However, due to its six degrees of freedom and hence considerably increased complexity, it is not seen as an alternative.

For accurately describing the essential lateral vehicle dynamics, the nonlinear single-track model with magic formula tire model is thus used in the following. The model is valid for large steering positions δ_f and lateral accelerations $a_y > 4\ \mathrm{m/sec^2}$. It is assumed that the wheels of the front and rear axle are lumped to a single wheel and that the vehicle is moving in a horizontal plane (see Figure 10). The vehicle's center of gravity is located on the plane and roll, and pitch motion are neglected. Furthermore, it is assumed that the wheels are freely spinning so that the longitudinal wheel forces become zero. The lateral vehicle dynamics are described in vehicle fixed coordinates and are subsequently derived.

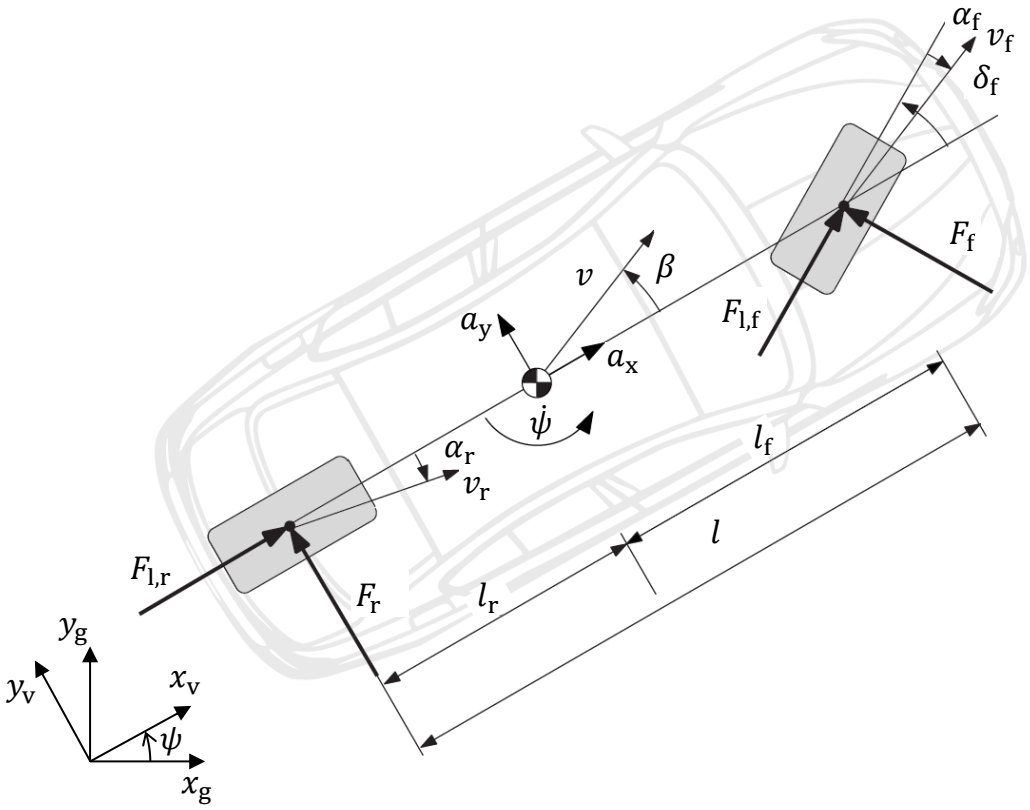

Figure 10: Free-Body Diagram of the Nonlinear Single-Track Model [Rat+15]

From the equilibrium of forces in x_v and y_v direction and the equilibrium of torques about the vehicle vertical axis, the equations of motion of the nonlinear single-track model are obtained

$$ma_x = -F_f \sin(\delta_f) + F_{x,d} \tag{2.31}$$

$$ma_y = F_f \cos(\delta_f) + F_r + F_{y,d} \tag{2.32}$$

$$J_z\ddot{\psi} = F_f l_f \cos(\delta_f) - F_r l_r + T_{z,d} \tag{2.33}$$

with $F_{x,d}$, $F_{y,d}$ and $T_{z,d}$ being external disturbance forces and torques from air resistance, road inclination, side wind and road camber. These disturbances are modeled by [Lug19]

$$F_{x,d} = -\tfrac{1}{2} c_x \rho_a A_x v_x^2 - mg \sin(\alpha) \tag{2.34}$$

$$F_{y,d} = -\tfrac{1}{2} c_y \rho_a A_y v_{wind}^2 - mg \sin(\phi) \tag{2.35}$$

$$T_{z,d} = -\tfrac{1}{2} c_y \rho_a A_y v_{wind}^2 \, l_{wind}. \tag{2.36}$$

The acceleration vector components are calculated from [Ers+11]

$$a_x = -(\dot{\beta} + \dot{\psi}) v \sin(\beta) + \dot{v} \cos(\beta) \tag{2.37}$$

$$a_y = (\dot{\beta} + \dot{\psi}) v \cos(\beta) + \dot{v} \sin(\beta). \tag{2.38}$$

Substituting (2.37) and (2.38) into (2.31) and (2.32) respectively yields

$$-\left(\dot{\beta}+\dot{\psi}\right)v\sin(\beta)+\dot{v}\cos(\beta)=-\frac{F_{\mathrm{f}}}{m}\sin(\delta_{\mathrm{f}})+\frac{1}{m}F_{\mathrm{x,d}} \tag{2.39}$$

$$\left(\dot{\beta}+\dot{\psi}\right)v\cos(\beta)+\dot{v}\sin(\beta)=\frac{F_{\mathrm{f}}}{m}\cos(\delta_{\mathrm{f}})+\frac{F_{\mathrm{r}}}{m}+\frac{F_{\mathrm{y,d}}}{m}. \tag{2.40}$$

By eliminating the vehicle acceleration $\dot{v}$ this gives [Ers+11]

$$v\left(\dot{\beta}+\dot{\psi}\right)\left[\frac{\sin^2(\beta)+\cos^2(\beta)}{\sin(\beta)\cos(\beta)}\right]=\frac{F_{\mathrm{f}}}{m\sin(\beta)}\cos(\delta_{\mathrm{f}})+\frac{F_{\mathrm{r}}}{m\sin(\beta)}+\frac{F_{\mathrm{f}}}{m\cos(\beta)}\sin(\delta_{\mathrm{f}})+ \\ -\frac{F_{\mathrm{x,d}}}{m\cos(\beta)}+\frac{F_{\mathrm{y,d}}}{m\sin(\beta)}. \tag{2.41}$$

Through the exploitation of the trigonometric identities

$$\cos(\alpha\pm\beta)=\cos(\alpha)\cos(\beta)\mp\sin(\alpha)\sin(\beta) \tag{2.42}$$

$$\cos^2(\alpha)+\sin^2(\alpha)=1 \tag{2.43}$$

the equation can be further transformed into

$$v\left(\dot{\beta}+\dot{\psi}\right)=\frac{1}{m}\left[F_{\mathrm{f}}\cos(\delta_{\mathrm{f}}-\beta)+F_{\mathrm{r}}\cos(\beta)-F_{\mathrm{x,d}}\sin(\beta)+F_{\mathrm{y,d}}\cos(\beta)\right] \tag{2.44}$$

respectively

$$\dot{\beta}=\frac{1}{mv}\left[F_{\mathrm{f}}\cos(\delta_{\mathrm{f}}-\beta)+F_{\mathrm{r}}\cos(\beta)-F_{\mathrm{x,d}}\sin(\beta)+F_{\mathrm{y,d}}\cos(\beta)\right]-\dot{\psi}. \tag{2.45}$$

The equilibrium of torques yields

$$\ddot{\psi}=\frac{1}{J_{\mathrm{z}}}\left[F_{\mathrm{f}}l_{\mathrm{f}}\cos(\delta_{\mathrm{f}})-F_{\mathrm{r}}l_{\mathrm{r}}+T_{\mathrm{z,d}}\right]. \tag{2.46}$$

In addition, the kinematic relationship between steering and road wheel position is given by [Ers+11]

$$\delta_{\mathrm{f}}=i_{\mathrm{s}}\varphi_{\mathrm{FA}}. \tag{2.47}$$

By substituting (2.47) into (2.45) and (2.46) respectively, this finally gives the nonlinear differential equations

$$\dot{\beta}=\frac{1}{mv}\left[F_{\mathrm{f}}\cos(i_{\mathrm{s}}\varphi_{\mathrm{FA}}-\beta)+F_{\mathrm{r}}\cos(\beta)-F_{\mathrm{x,d}}\sin(\beta)+F_{\mathrm{y,d}}\cos(\beta)\right]-\dot{\psi} \tag{2.48}$$

$$\ddot{\psi}=\frac{1}{J_{\mathrm{z}}}\left[F_{\mathrm{f}}l_{\mathrm{f}}\cos(i_{\mathrm{s}}\varphi_{\mathrm{FA}})-F_{\mathrm{r}}l_{\mathrm{r}}+T_{\mathrm{z,d}}\right]. \tag{2.49}$$

2.3.4 Nonlinear Tire Force Model

The assumption of a direct proportional relationship between slip angle and lateral force (see e.g. [Rat16]) is only valid for the linear driving range. In the nonlinear driving range, the nonlinear tire behavior has a decisive impact on the control performance and must hence be explicitly considered in the plant model. For an accurate modeling of the

nonlinear tire characteristics, the magic formula tire model by Pacejka [Pac12] is introduced, which is illustrated in Figure 11 and defined as

$$F_\mathrm{f} = D_\mathrm{f} \sin[C_\mathrm{f} \arctan(B_\mathrm{f} \tan(\alpha_\mathrm{f}) - E_\mathrm{f}(B_\mathrm{f} \tan(\alpha_\mathrm{f}) - \arctan(B_\mathrm{f} \tan(\alpha_\mathrm{f}))))] \tag{2.50}$$

$$F_\mathrm{r} = D_\mathrm{r} \sin[C_\mathrm{r} \arctan(B_\mathrm{r} \tan(\alpha_\mathrm{r}) - E_\mathrm{r}(B_\mathrm{r} \tan(\alpha_\mathrm{r}) - \arctan(B_\mathrm{r} \tan(\alpha_\mathrm{r}))))] \tag{2.51}$$

with

$C_{\mathrm{f,r}}$ Shape factor
$B_{\mathrm{f,r}}$ Stiffness factor $\left(B_{\mathrm{f,r}} = c_{\mathrm{f,r}}/C_{\mathrm{f,r}}D_{\mathrm{f,r}}\right)$
$D_{\mathrm{f,r}}$ Peak value
$E_{\mathrm{f,r}}$ Curvature factor.

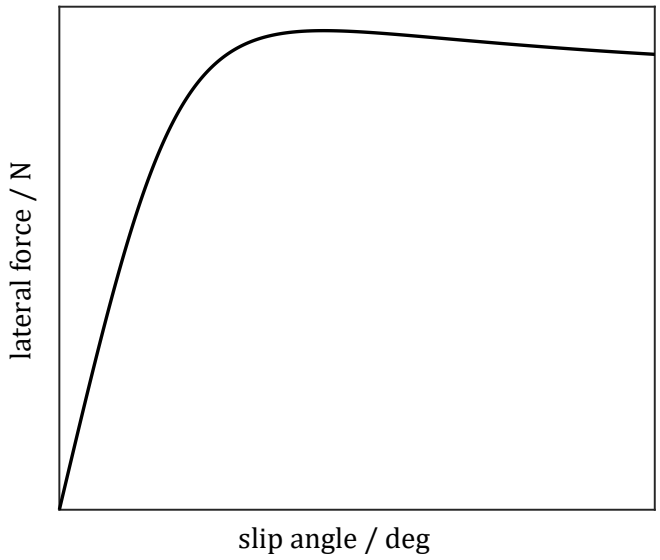

Figure 11: Nonlinear Tire Force Characteristic

With this regard, the slip angles are computed from the kinematic relationships of the nonlinear single-track model given by [Ers+11]

$$\alpha_\mathrm{f} = i_\mathrm{s}\varphi_\mathrm{FA} - \beta - \frac{l_\mathrm{f}\dot{\psi}}{v} \tag{2.52}$$

$$\alpha_\mathrm{r} = -\beta + \frac{l_\mathrm{r}\dot{\psi}}{v}. \tag{2.53}$$

For this purpose, the state variables of the nonlinear single-track model and the steering position of the FAA serve as inputs.

2.3.5 Vehicle Motion Relative to the Reference Path

The nonlinear dynamic single-track model describes the essential lateral vehicle dynamics. For modeling the vehicle motion, the equations must be further extended. In this context, the vehicle motion is typically modeled in global coordinates or in road coordinates as explained below.

The global vehicle position results from the direction in which the vehicle is moving at a given vehicle speed. Hence, it is defined by the integral of the vehicle speed vector components

$$x_{\mathrm{g}} = \int v \cos(\theta)\, dt + x_0 \tag{2.54}$$

$$y_{\mathrm{g}} = \int v \sin(\theta)\, dt + y_0 \tag{2.55}$$

with (x_0, y_0) representing the coordinates of the initial position and θ describing the course angle [Raj12]. The latter is given by the sum of yaw angle and side slip angle

$$\theta = \psi + \beta. \tag{2.56}$$

The global vehicle position proves itself to be unsuitable for automated driving applications. It is only measurable by special sensors at a sufficient degree of accuracy. These are generally not available in a series production car. Moreover, the global vehicle position is not relevant for guiding the vehicle along a reference path. The relevant measures here are the lateral deviation y_{r} and heading angle error $\Delta\psi = \psi - \psi_{\mathrm{ref}}$ with respect to the point of the closest distance between the vehicle and reference path (refer to Figure 12).

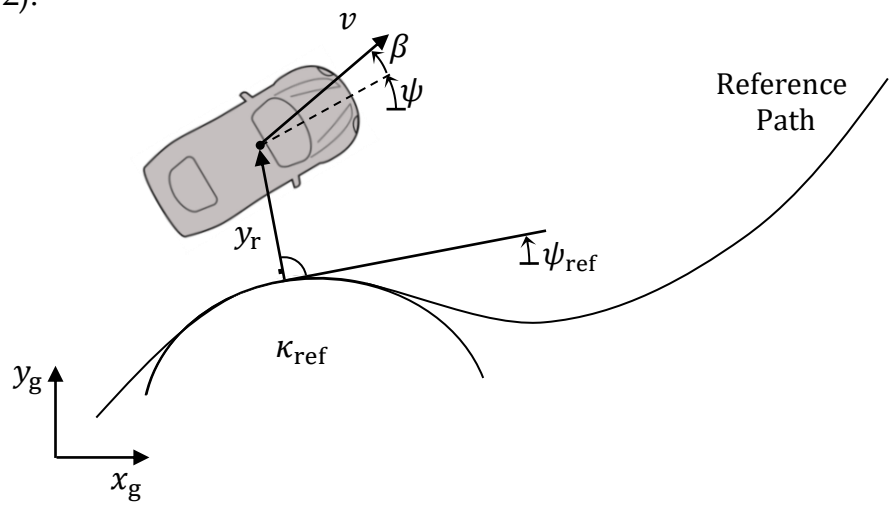

Figure 12: Vehicle Position Relative to the Reference Path

It is supposed that the reference path is locally approximated by circular segments, whose curvature is given by the reciprocal value of the radius $\kappa_{\mathrm{ref}} = 1/R_{\mathrm{ref}}$. Using geometrical relationships and assuming small angle errors, the dynamic equations for the lateral deviation and heading angle error of the vehicle relative to the reference path are derived as [Ack+95]

$$\dot{y}_{\mathrm{r}} = v \sin(\Delta\psi + \beta) \approx v(\Delta\psi + \beta) \tag{2.57}$$

$$\Delta\dot{\psi} = \dot{\psi} - v\kappa_{\mathrm{ref}}\,. \tag{2.58}$$

2.3.6 Nonlinear Dynamic Plant Model

By combining (2.30), (2.48), (2.49), (2.50), (2.51), (2.52), (2.53), (2.57) and (2.58) the nonlinear plant model for lateral vehicle guidance is derived. Figure 13 shows a block diagram

of the complete model. The three model parts are given by the actuator controls, nonlinear single-track model, and the error equations relative to the reference path. These parts are independent of each other. The independency of the actuator controls from the lateral vehicle dynamics bases on the assumption that external disturbance rack forces are effectively compensated by the underlying control.

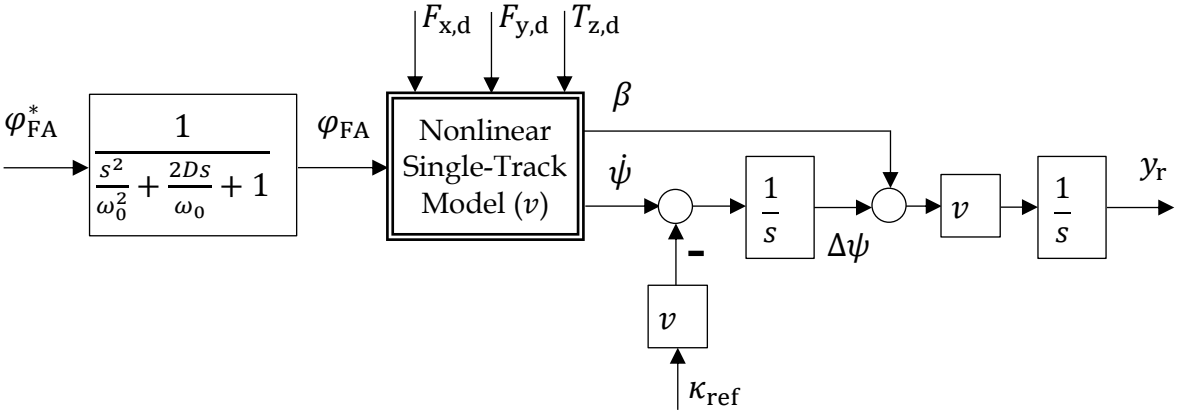

Figure 13: Nonlinear Plant Model for Lateral Vehicle Guidance

The physical parameters of the nonlinear plant model are determined experimentally through system identification. With this regard the vehicle mass, wheelbase and steering ratio are obtained by direct measurement. The center of gravity is identified by measuring the vehicle weight at the front and rear axle respectively. Subsequently, a torque balance around the vehicle's center of gravity is used to compute the distance between the front axle and the center of gravity. The vehicle's yaw moment of inertia is directly requested from the vehicle manufacturer. For identifying the remaining model parameters, quasi stationary circular test drives are conducted on a vehicle dynamics area. Hereby the vehicle is driven at a constant speed, and the steering position is slowly increased. The measured vehicle speed and reference steering position are then used as inputs to the nonlinear plant model. The outputs are selected as yaw rate and lateral acceleration to allow a direct comparison between the nonlinear model and vehicle measurements. By this proceeding, the tire parameters are identified (refer to [Ise22]).
For model evaluation extensive vehicle testing using different driving maneuvers and vehicle speeds is performed. Figure 14 exemplarily shows the model evaluation results for sinusoidal steering at a constant vehicle speed of 50, 70, and 100 km/h. Furthermore, Figure 15 depicts the model evaluation results for vehicle acceleration and deceleration with a constant steering position. The results demonstrate that the time responses of the model accurately match the dynamics of the real system up to the nonlinear driving range (i.e. $a_y > 4$ m/sec^2). Therefore, the nonlinear plant model provides a suitable basis for control synthesis.

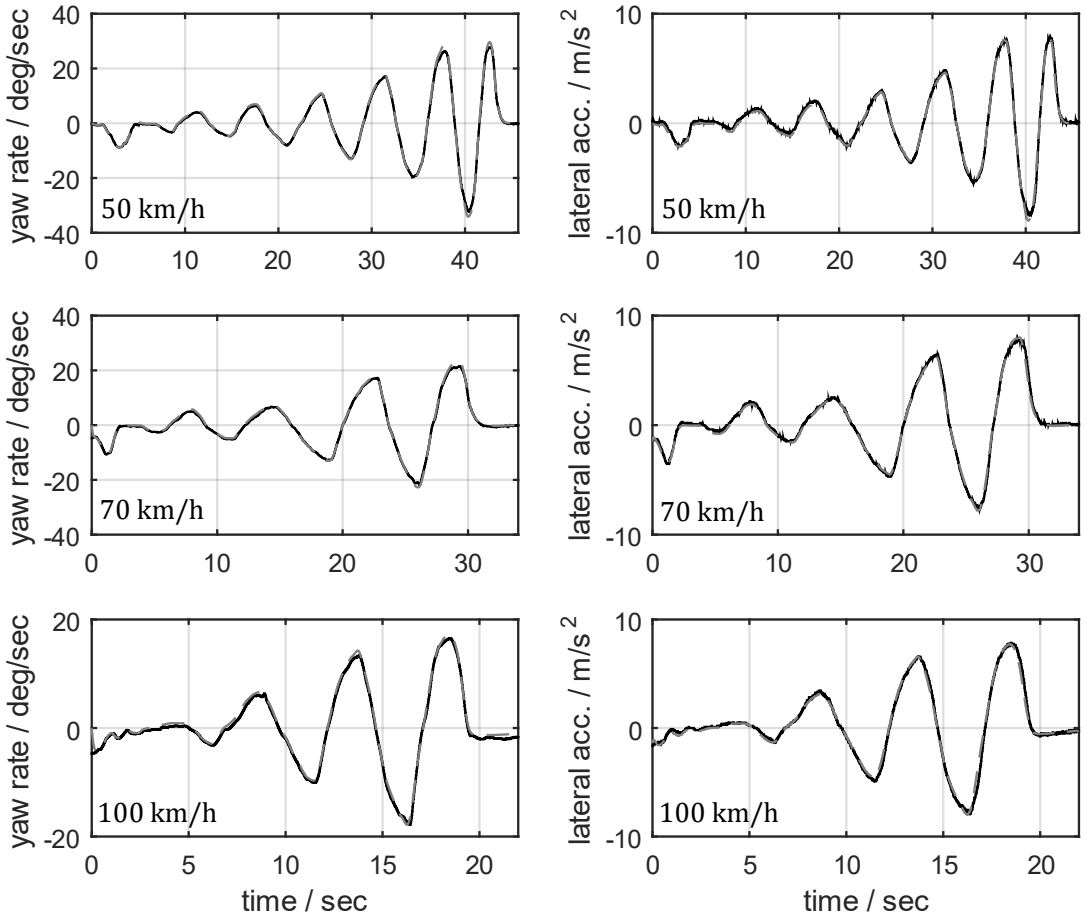

Figure 14: Comparison of Vehicle (black) and Model Results (grey dashed) showing the Yaw Rate and Lateral Acceleration for Sinusoidal Steering at Constant Speeds

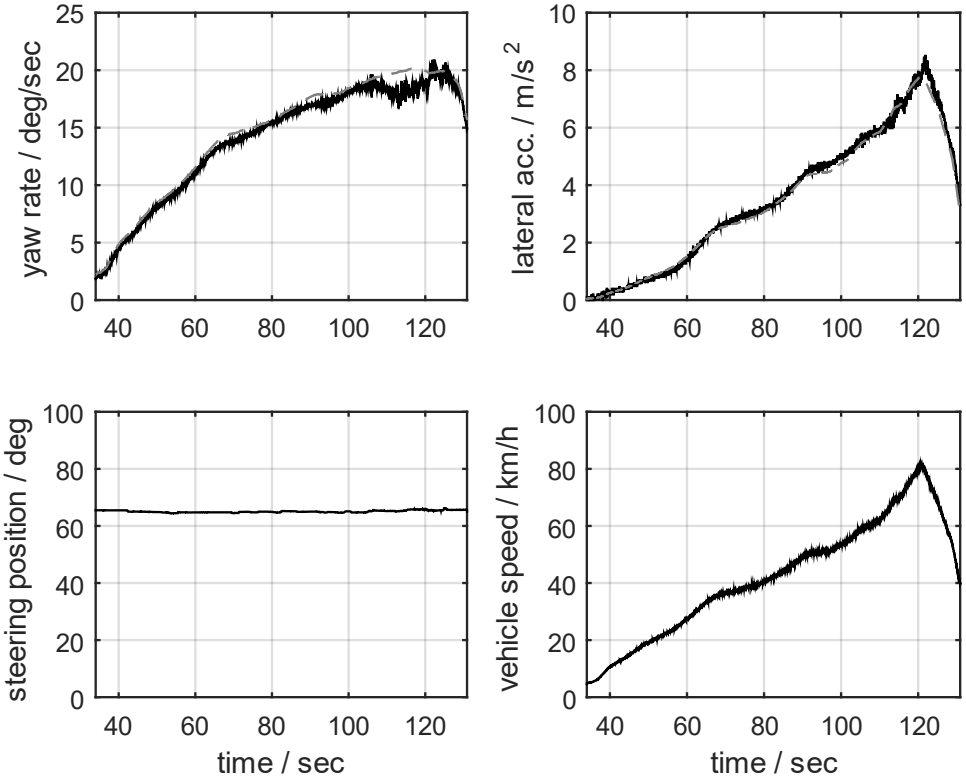

Figure 15: Comparison of Vehicle (black) and Model Results (grey dashed) for Vehicle Acceleration and Deceleration at a Constant Steering Position of 65 deg

2.3.7 Linearized Dynamic Plant Model

For model analysis in frequency domain, the nonlinear plant equations are linearized using small angle assumptions and transformed to state-space representation. This results in

$$\dot{\mathbf{x}}_\mathrm{p} = \mathbf{A}_\mathrm{p}^\mathrm{c}\mathbf{x}_\mathrm{p} + \mathbf{B}_\mathrm{c,p}^\mathrm{c}u_\mathrm{c,p} + \mathbf{B}_\mathrm{d,p}^\mathrm{c}u_\mathrm{d,p} \tag{2.59}$$

$$y_\mathrm{p} = \mathbf{C}_\mathrm{p}^\mathrm{c}\,\mathbf{x}_\mathrm{p} \tag{2.60}$$

where

$$\mathbf{A}_\mathrm{p}^\mathrm{c} = \begin{bmatrix} -\frac{(c_\mathrm{f}+c_\mathrm{r})}{mv} & \left(\frac{c_\mathrm{r}l_\mathrm{r}-c_\mathrm{f}l_\mathrm{f}}{mv^2}-1\right) & 0 & 0 & \frac{c_\mathrm{f}i_\mathrm{s}}{mv} & 0 \\ \frac{(-l_\mathrm{f}c_\mathrm{f}+l_\mathrm{r}c_\mathrm{r})}{J_\mathrm{z}} & -\left(\frac{c_\mathrm{f}{l_\mathrm{f}}^2+c_\mathrm{r}{l_\mathrm{r}}^2}{vJ_\mathrm{z}}\right) & 0 & 0 & \frac{l_\mathrm{f}c_\mathrm{f}i_\mathrm{s}}{J_\mathrm{z}} & 0 \\ 0 & 1 & 0 & 0 & 0 & 0 \\ v & 0 & v & 0 & 0 & 0 \\ 0 & 0 & 0 & 0 & 0 & 1 \\ 0 & 0 & 0 & 0 & -\omega_o^2 & -2D\omega_o \end{bmatrix}, \mathbf{B}_\mathrm{c,p}^\mathrm{c} = \begin{bmatrix} 0 \\ 0 \\ 0 \\ 0 \\ 0 \\ \omega_o^2 \end{bmatrix}, \mathbf{B}_\mathrm{d,p}^\mathrm{c} = \begin{bmatrix} 0 \\ 0 \\ -v \\ 0 \\ 0 \\ 0 \end{bmatrix},$$

$\mathbf{C}_\mathrm{p}^\mathrm{c} = [0 \quad 0 \quad 0 \quad 1 \quad 0 \quad 0],\ \mathbf{x}_\mathrm{p}^\mathrm{T} = \begin{bmatrix}\beta & \dot{\psi} & \Delta\psi & y_\mathrm{r} & \varphi_\mathrm{FA} & \Omega_\mathrm{FA}\end{bmatrix},$

$u_\mathrm{c,p} = \varphi_\mathrm{FA}^*,\ u_\mathrm{d,p} = \kappa_\mathrm{ref},\ y_\mathrm{p} = y_\mathrm{r},$

and the unknown disturbance inputs were neglected for simplicity [Ack+93].

2.4 Plant Model Analysis

To get a general understanding of the plant dynamics, the eigenvalues and transmission zeroes of the linearized system plant models are analyzed. For this purpose, system representations in frequency domain using transfer function matrices $\mathbf{G}(s)$ are considered that are resulting from [Sko+05]

$$\mathbf{G}(s) = \frac{\mathbf{Y}(s)}{\mathbf{U}(s)} = \mathbf{C}(s\mathbf{I}-\mathbf{A})^{-1}\mathbf{B} = \frac{\mathbf{C}\,\mathrm{adj}(s\mathbf{I}-\mathbf{A})\,\mathbf{B}}{\det(s\mathbf{I}-\mathbf{A})}. \tag{2.61}$$

The eigenvalues are the roots of the denominator polynomial of the system transfer function matrix $\mathbf{G}(s)$, which is given by $\det(s\mathbf{I}-\mathbf{A})$. They are identical for all transfer paths and provide detailed information regarding the time constants, damping ratios and natural frequencies of the dynamics that compose the overall system response. The transmission zeros are the complex numbers $s = v_0$ that fulfill $\mathbf{G}(v_0)\mathbf{u}_0 = \mathbf{0}$ for $\mathbf{u}_0 \neq \mathbf{0}$. This implies that the output vector becomes zero for an arbitrary input vector $\mathbf{u}(t) = \mathbf{u}_0 e^{v_0 t}$ at the zero frequency v_0. Complex numbers, which fulfill this condition result in a rank drop of the system transfer function matrix $\mathbf{G}(s)$. Similar to the SISO case, transmission zeros of MIMO systems determine the asymptotic properties of control system design. This is due to the fact, that the finite closed loop poles approach the transmission zeros as the feedback gain increases. Thus, they bring a natural performance limit to the design. With respect to the state-feedback controller and estimator design, transmission zeros are hence from central importance. For example, if the

linear plant model used for state-feedback controller design has m transmission zeros and n eigenvalues in the left half of the s-plane, m eigenvalues will tend towards transmission zeros and (n-m) eigenvalues towards infinity as the controller gain increases. For transmission zeros on or near the imaginary axis, these asymptotic properties can cause unwanted slow dynamics in the closed loop system response and must therefore be carefully considered [Fra+14].

In the following, the fundamental plant dynamics of the HWA, the FAA, and the lateral vehicle motion are analyzed. Figure 16 illustrates the eigenvalues and transmission zeros of the linearized plant model for the Steer-by-Wire HWA. Hereby the transfer paths from control input to steering torque output and from control input to steering position output are separately considered. These are of central importance for steering torque and position controller design.

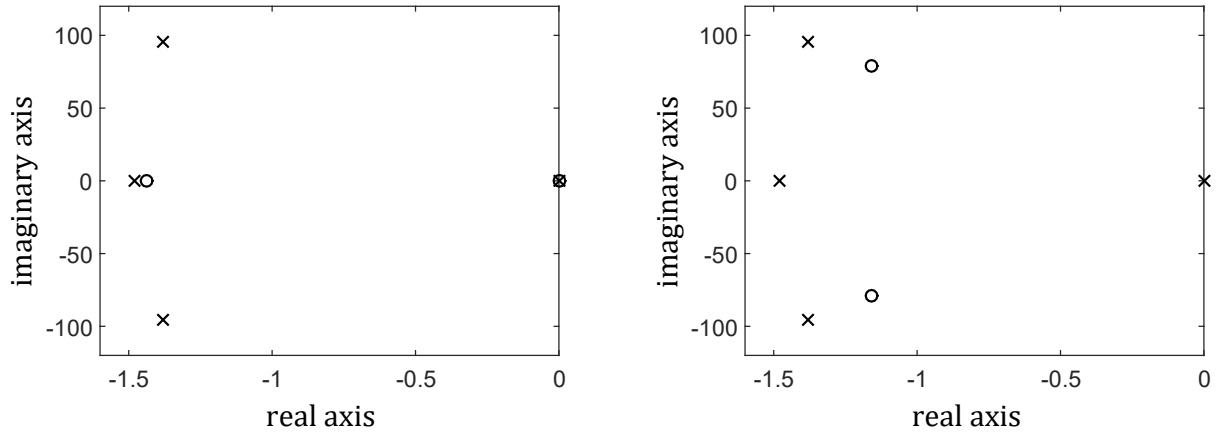

Figure 16: Eigenvalues and Transmission Zeros of the HWA Plant Model for the Steering Torque Output (left) and Steering Position Output (right) (5th eigenvalue not illustrated)

The 5th-order system consists of four eigenvalues that are originating from the mechanical system. They describe the rigid body motion of the inertias and the elasticity of the torsion bar. The rigid part has two real-valued eigenvalues, which describe the integration of the steering velocity to the position and the first-order lag characteristic between the driving torque and the velocity. The elastic part is reflected by a poorly damped conjugate complex eigenvalue pair and hence introduces a structural resonance to the system. This conjugate complex eigenvalue pair has a low natural frequency and a large time constant, thus exposing a dominant behavior. For classical control system design methods, the resonance leads to stability issues and limits the dynamic performance that can be achieved. In order to realize control bandwidths above resonance frequency, the designed controller must therefore provide active torsional damping. The last eigenvalue originates from the dynamics of electric motor control. Due to its very small time constant it is not visible in the plots and only has a minor impact on the overall system response.
The transmission zeros differ for the selected transfer paths. As the steering torque output is defined by $T_{\mathrm{TS}} = c_{\mathrm{TS}}\Delta\varphi$, it is effectively the scaled difference position $\Delta\varphi$ that describes the relative position of the inertias. Due to the fact, that no absolute position is defined as an output, the integrator eigenvalue cancels, and the model reduces to a

4th-order system. The motion of the steering wheel inertia furthermore introduces an additional transmission zero.
For the steering position output, an absolute position signal is defined as the output and thus the integrator eigenvalue persists. Due to the fact that the steering wheel inertia is passively coupled to the pinion inertia, the motion of the steering wheel can oppose the motion of the pinion. Hence, an anti-resonance is introduced, which is revealed by a conjugate complex zero pair with weak damping. A detailed analytical derivation of the corresponding transfer functions can be found in [Gon18].

Figure 17 depicts the eigenvalues and transmission zeroes of the linearized plant model for the Steer-by-Wire FAA. With this regard, the transfer path from control input to steering position output is considered, which is relevant for position controller synthesis.

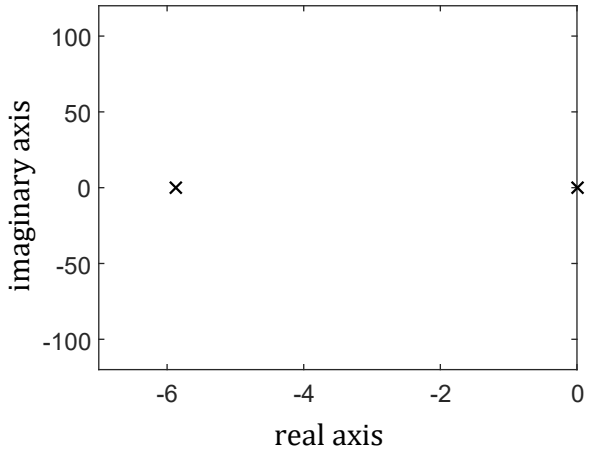

Figure 17: Eigenvalues and Transmission Zeros of the FAA Plant Model (3rd eigenvalue not illustrated)

The 3rd-order system possesses two real-valued eigenvalues that are associated to the steering mechanics and describe the rigid body motion of the inertias. They reflect the integration of the steering velocity to the position and the first-order lag characteristic between the driving torque and the steering velocity. The remaining eigenvalue results from the dynamics of electric motor control. Due to the small time constant, it is not shown in the plot and provides a minor contribution to the overall system response. Furthermore, the system has no transmission zeros.

Figure 18 depicts the eigenvalues and transmission zeros of the linearized plant model for lateral vehicle guidance. Due to the vehicle speed dependency of the lateral dynamics, a family of linearized plant models for vehicle speeds between 20 and 100 km/h is illustrated. Hereby the transfer path from the control input to lateral deviation output is considered, which is of importance for lateral vehicle guidance controller synthesis. The 6th-order system has six eigenvalues that are assignable to the following subsystems:

- 1 conjugate complex eigenvalue pair of the FAA position control
- 2 time-variant eigenvalues of the lateral vehicle dynamics
- 2 integrator eigenvalues of the error dynamics

The conjugate complex eigenvalue pair of the FAA steering position control has a very small time constant, thus contributing little to the overall system response. For the sake of visibility, it is not shown in the plot. The double integrator eigenvalue of the error dynamics reveals an unstable plant behavior for all vehicle speeds [Raj12]. Therefore, stabilization via feedback control is required. Moreover, the two eigenvalues of the lateral vehicle dynamics are time-variant and change as a function of vehicle speed. For low vehicle speeds two real-valued eigenvalues and for high vehicle speeds a conjugate complex eigenvalue pair exists. The latter asymptotically approaches a fixed location in the *s*-plane as the vehicle speed increases. Similarly, the transmission zeros that are introduced by the lateral vehicle dynamics vary as a function of vehicle speed. At low vehicle speeds two real-valued zeros and at high vehicle speeds a conjugate complex zero pair are exposed. This implies the necessity for a vehicle speed adaptive control.

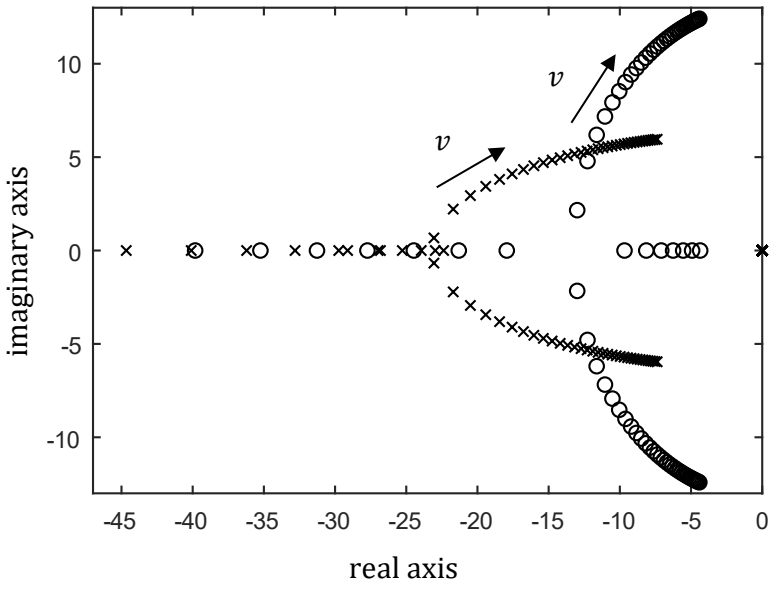

Figure 18: Eigenvalues and Transmission Zeros for Lateral Vehicle Guidance
(conjugate complex eigenvalue pair of FAA position control not depicted)

The findings obtained in this subchapter are essential for the Steer-by-Wire and lateral vehicle guidance control synthesis and will be specifically taken into consideration. For estimator synthesis additional inputs and outputs of the linear plant models are needed, such that the transmission zeros will change. Therefore, additional system analyses are required and conducted in the relevant sections of this thesis.

3

Control Synthesis for the Steer-by-Wire System

In this chapter, the control requirements for the SbW system are defined, and the control synthesis is presented. Depending on the current driving situation the SbW HWA is operated in different control modes. During manual driving, it is operated in steering torque control mode to provide the required torque feedback to the driver for the desired steering feel. During automated driving, it is steering position-controlled to ensure that the steering wheel accurately tracks the position of the road wheels. Suitable control structures for covering both modes are systematically derived in the following. Thereafter the FAA steering position control is described that is active in all driving modes. It solely differs in the source of the reference steering position. This can be either the steering wheel position applied by the driver or the output of a lateral vehicle guidance controller.

3.1 Requirements for the Control System

For the definition of fundamental control requirements to the SbW system, the manual driving mode and automated driving mode are successively considered.

Manual Driving Mode

In manual driving mode, the HWA is steering torque controlled for providing the desired steering feel and the FAA is steering position controlled for dynamic tracking of the steering wheel motion. Hereby the following requirements must be fulfilled:

Table 1: Steer-by-Wire Control Requirements for Manual Driving

Handwheel Actuator - Steering Torque Control
- Reference tracking bandwidth: ≥ 20 Hz - Steady-state disturbance rejection (nonlinear friction, driver torque) - Stability (Vector Margin): 0.5 - Robustness to parameter uncertainty/neglected dynamics
Front Axle Actuator - Steering Position Control
- Reference tracking bandwidth: ≥ 20 Hz - Steady-state disturbance rejection (nonlinear friction, rack force) - Stability (Vector Margin): 0.5 - Robustness to parameter uncertainty/neglected dynamics

As the steering wheel and road wheels are mechanically decoupled, the torque and position transfer in the SbW system is realized by means of control. Besides providing the basic steering torque from the classical assist curves, damping, hysteresis, and active return, high frequent disturbance torques from the tire-road contact must be additionally fed back to the driver. This information is considered as useful for safe vehicle guidance and required for producing an authentic and natural steering feel ([Koc10], [Fan+14]). Therefore, the HWA steering torque control must provide a reference tracking bandwidth of at least 20 Hz. The steering torque control is hereby affected by nonlinear friction and driver torque, which act as disturbances. These must be fully rejected in the steady state. Similarly, disturbances from plant parameter uncertainty and neglected dynamics must be robustly compensated. For ensuring the stability of the control loop a Vector Margin (VM), which defines the closest distance between the Nyquist curve and critical point and represents a stability measure for simultaneous gain and phase variations, of at least 0.5 is required. According to common literature recommendations and considering the fit between the model and measurement, this is rated as acceptable ([Fra+14], [Sko+05]).
The FAA steering position control must provide a reference tracking bandwidth of at least 20 Hz. This high bandwidth requirement is mandatory for realistically emulating the mechanical coupling between the steering wheel and road wheels. Hereby the steering position control is disturbed by external rack forces resulting from tire side forces and nonlinear friction. Moreover, parameter uncertainty and neglected plant dynamics are sources of disturbance. These unknown disturbances must be actively compensated and rejected in steady state. For robust stability a VM of 0.5 is further required.

Automated Driving Mode

In automated driving mode the HWA and FAA are both steering position controlled. In this context, the reference steering position is provided as an output of the automated lateral vehicle guidance controller. The obvious approach would be to synthesize a HWA steering position control with the same bandwidth requirement as the FAA steering position control. However, this introduces a problem that is well known from the development of automated lateral vehicle guidance control functions for conventional Electric Power Steering (EPS) systems. That is the conflict of objectives between precise lateral vehicle guidance and smooth steering wheel motions [Ise22]. An aggressively designed lateral vehicle guidance controller accurately follows the reference path at the expense of permanent and abrupt steering wheel motions. This behavior is undesirable and disturbing to the driver. In contrast, a weak lateral vehicle guidance controller outputs a smooth reference variable for steering position control. This results in gentle steering wheel motions at the expense of degraded control performance.
For fully exploiting the SbW system advantages, the HWA steering position control is synthesized for a reduced reference tracking bandwidth. For the FAA, the previously defined high bandwidth steering position control is maintained. Using this approach, precise lateral vehicle guidance control with smooth steering wheel motions is realizable for automated driving. The occurring phase delay between the steering wheel and road wheels is unproblematic and generally not noticeable by the driver. Table 2 gives an overview of the control requirements to the SbW system for the automated driving mode.

Table 2: Steer-by-Wire Control Requirements for Automated Driving

Handwheel Actuator - Steering Position Control
- Reference tracking bandwidth: ≤ 4 Hz - Steady-state disturbance rejection (nonlinear friction, driver torque) - Stability (Vector Margin): 0.5 - Robustness to parameter uncertainty/neglected dynamics
Front Axle Actuator - Steering Position Control
- Reference tracking bandwidth: ≥ 20 Hz - Steady-state disturbance rejection (nonlinear friction, rack force) - Stability (Vector Margin): 0.5 - Robustness to parameter uncertainty/neglected dynamics

To ensure smooth steering wheel motions, a reference tracking bandwidth of up to 4Hz is adequate for the HWA steering position control. Hereby disturbances from nonlinear friction and driver torque must be rejected in steady state. Furthermore, plant parameter uncertainty and neglected dynamics introduce model error that must be robustly compensated. The requirement for an arbitrary reference tracking bandwidth while maintaining good disturbance rejection properties must be considered in the selection of the controller structure. With this regard, the possibility for an independent design of the command and the disturbance response is desirable. Moreover, for robust stability a VM of at least 0.5 is compulsory. The requirements for the FAA steering position control remain unchanged as the control persists throughout the manual and automated driving mode.

3.2 LQG Steering Torque Control for the Handwheel Actuator

The main challenge in the development of SbW systems is to provide a natural and authentic steering feel to the driver. In order to meet this challenge, an accurate control of the steering torque is required. The objective of this section is therefore to synthesize a closed-loop steering torque controller for the HWA of the SbW system. Due to the high control performance requirements and the necessity to dampen the structural resonance of the mechanical system, a Linear Quadratic Gaussian (LQG) controller design is employed. With this regard, a direct discrete controller synthesis is performed in the following for the discrete linear plant model in state-space representation given by (2.15), (2.16), and (2.18).

The general control structure is illustrated in Figure 19. It results from combining an optimal state-feedback controller with static reference and disturbance feedforward and an extended optimal state-estimator. By inclusion of an integrator disturbance model inside the estimator, the resulting LQG controller receives integral action and is robust against plant parameter uncertainty as well as unknown disturbances. Furthermore, because the plant model is fully controllable and state-feedback control is applied, the complete system dynamics can be arbitrarily designed ([Föl22], [Sko+05]).

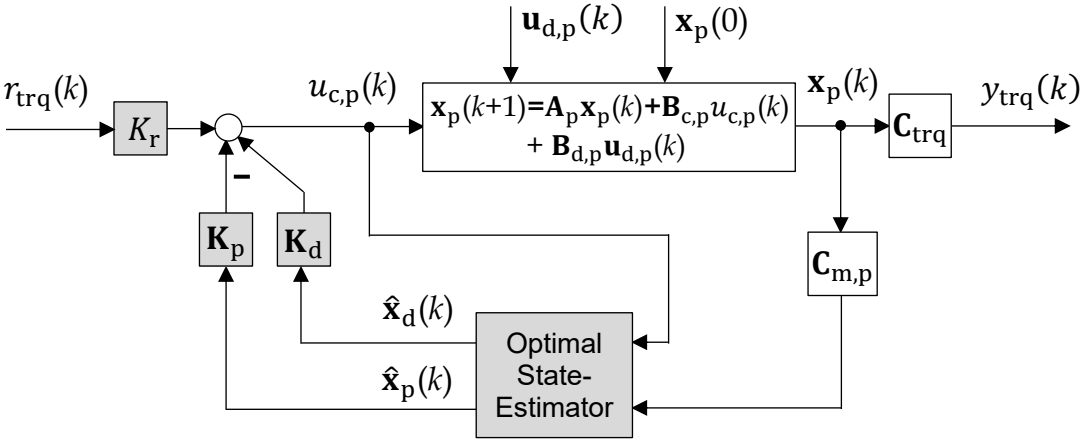

LQG Steering Torque Controller

Figure 19: HWA – LQG Steering Torque Control

In the following sections, the synthesis of an optimal state-feedback controller is initially described, which defines the dynamics and the stability of the closed-loop system. Thereafter, static feedforward controls for steady-state reference tracking and disturbance rejection are introduced. For the reconstruction of the unmeasurable plant states and unknown disturbances, an extended optimal state-estimator (Kalman Filter) with integrator disturbance model is synthesized. The interconnection of feedback controller, static feedforward control, and state-estimator ultimately results in the LQG steering torque controller.

3.2.1 Optimal State-Feedback Controller

For the discrete linear plant model with objective output equation as given by (2.15) and (2.16)

$$\begin{aligned}\mathbf{x}_{\mathrm{p}}(k+1) &= \mathbf{A}_{\mathrm{p}}\mathbf{x}_{\mathrm{p}}(k) + \mathbf{B}_{\mathrm{c,p}}u_{\mathrm{c,p}}(k) \;\text{ with }\; \mathbf{u}_{\mathrm{d,p}} = \mathbf{0} \\ y_{\mathrm{trq}}(k) &= \mathbf{C}_{\mathrm{trq}}\mathbf{x}_{\mathrm{p}}(k)\end{aligned} \tag{3.1}$$

an optimal control $u_{\mathrm{c,p}}$ is needed, which drives the state vector $\mathbf{x}_{\mathrm{p}}$ from any initial state to the zero state, such that the value of a performance index is minimized. For the performance index, a quadratic cost function J build by the weighted control input and objective output is used [Fri05]

$$J = \sum_{k=0}^{\infty}\left[y_{\mathrm{trq}}^{\mathrm{T}}(k)\mathbf{Q}\,y_{\mathrm{trq}}(k) + u_{\mathrm{c,p}}^{\mathrm{T}}(k)\mathbf{R}\,u_{\mathrm{c,p}}(k)\right] \quad \text{with } \mathbf{Q} \geq \mathbf{0},\ \mathbf{R} > \mathbf{0}\,. \tag{3.2}$$

The weighting matrices $\mathbf{Q}$ and $\mathbf{R}$ are diagonal matrices whose elements penalize large values of the respective signals in the minimization of the cost function. The state-feedback

$$u_{\mathrm{c,p}}(k) = -\mathbf{K}_{\mathrm{p}}\mathbf{x}_{\mathrm{p}}(k) \tag{3.3}$$

is the optimal control, which minimizes the quadratic cost function over an infinite time horizon $[0, \infty]$. Hereby the controller gains $\mathbf{K}_{\mathrm{p}}$ follow from [Kwa+05]

$$\mathbf{K}_\mathrm{p} = \left(\mathbf{B}_{\mathrm{c,p}}^\mathrm{T}\mathbf{S}\mathbf{B}_{\mathrm{c,p}} + \mathbf{R}\right)^{-1}\mathbf{B}_{\mathrm{c,p}}^\mathrm{T}\mathbf{S}\mathbf{A}_\mathrm{p} \tag{3.4}$$

where $\mathbf{S}$ is the steady-state solution of the discrete algebraic Riccati equation

$$\mathbf{A}_\mathrm{p}^\mathrm{T}\left[\mathbf{S} - \mathbf{S}\mathbf{B}_{\mathrm{c,p}}\left(\mathbf{B}_{\mathrm{c,p}}^\mathrm{T}\mathbf{S}\mathbf{B}_{\mathrm{c,p}} + \mathbf{R}\right)^{-1}\mathbf{B}_{\mathrm{c,p}}^\mathrm{T}\mathbf{S}\right]\mathbf{A}_\mathrm{p} + \mathbf{C}_\mathrm{trq}^\mathrm{T}\mathbf{Q}\,\mathbf{C}_\mathrm{trq} - \mathbf{S} = \mathbf{0}. \tag{3.5}$$

Selection of Physically Meaningful Weighting Matrices

The weighting matrices $\mathbf{Q}$ and $\mathbf{R}$ can be treated as design parameters, which allow penalizing large control error and too extensive use of the control input. Since the selection of these matrices is only weakly connected to the control performance requirements, an iterative trial and error process is typically employed until satisfactory results are obtained.
However, a simple and physically meaningful choice for these design parameters is given by Bryson's rule [Fra+98], which suggests selecting $\mathbf{Q}$ and $\mathbf{R}$ diagonal with

$$q_{ii} = \frac{1}{\text{max. acceptable value of } y_i^2} \qquad i \in \{1,2,\dots,\mathrm{l}\} \tag{3.6}$$

$$r_{jj} = \frac{1}{\text{max. acceptable value of } u_j^2} \qquad j \in \{1,2,\dots,\mathrm{k}\}. \tag{3.7}$$

Following this rule, the variables that appear in the cost function J are scaled so that the maximum acceptable value of each term is 1. Since the plant model for optimal state-feedback controller synthesis is a SISO system, the weighting matrices reduce to scalar factors. Their maximum acceptable values are defined according to the control input range and tolerable dynamic control error. By application of this method, good starting values for the optimal controller design are obtained, which are further refined by additional iterations.

3.2.2 Static Reference Feedforward

The optimal state-feedback controller determines the dynamics and the stability of the closed loop system. For steady-state reference tracking, a static reference feedforward is further introduced. The extended control law thus yields

$$u_{\mathrm{c,p}}(k) = -\mathbf{K}_\mathrm{p}\mathbf{x}_\mathrm{p}(k) + K_\mathrm{r} r_\mathrm{trq}(k). \tag{3.8}$$

To determine the feedforward gain K_r, the extended control law (3.8) is substituted into the discrete linear plant model given by (2.15) and (2.16) to obtain the closed loop system

$$\begin{aligned}\mathbf{x}_\mathrm{p}(k+1) &= \left[\mathbf{A}_\mathrm{p} - \mathbf{B}_{\mathrm{c,p}}\mathbf{K}_\mathrm{p}\right]\mathbf{x}_\mathrm{p}(k) + \mathbf{B}_{\mathrm{c,p}}K_\mathrm{r}\, r_\mathrm{trq}(k) \quad \text{with } \mathbf{u}_{\mathrm{d,p}}(k) = \mathbf{0} \\ y_\mathrm{trq}(k) &= \mathbf{C}_\mathrm{trq}\mathbf{x}_\mathrm{p}(k).\end{aligned} \tag{3.9}$$

For analyzing the transfer behavior of the closed loop system from reference input r_trq to objective output y_trq, z-Transformation is applied (with $\mathbf{x}_\mathrm{p}(0)$ set to zero)

$$z\mathbf{X}_\mathrm{p}(z) = \left[\mathbf{A}_\mathrm{p} - \mathbf{B}_{\mathrm{c,p}}\mathbf{K}_\mathrm{p}\right]\mathbf{X}_\mathrm{p}(z) + \mathbf{B}_{\mathrm{c,p}}K_\mathrm{r}\, R_\mathrm{trq}(z) \tag{3.10}$$

$$Y_{\mathrm{trq}}(z) = \mathbf{C}_{\mathrm{trq}}\mathbf{X}_{\mathrm{p}}(z)$$

and thus, it follows for the reference transfer function

$$Y_{\mathrm{trq}}(z) = \mathbf{C}_{\mathrm{trq}}\left(z\mathbf{I} - \left[\mathbf{A}_{\mathrm{p}} - \mathbf{B}_{\mathrm{c,p}}\mathbf{K}_{\mathrm{p}}\right]\right)^{-1}\mathbf{B}_{\mathrm{c,p}}K_{\mathrm{r}}\, R_{\mathrm{trq}}(z). \tag{3.11}$$

For stationary conditions $z \to 1$, which results in

$$Y_{\mathrm{trq}}(z) = \mathbf{C}_{\mathrm{trq}}\left(\mathbf{I} - \left[\mathbf{A}_{\mathrm{p}} - \mathbf{B}_{\mathrm{c,p}}\mathbf{K}_{\mathrm{p}}\right]\right)^{-1}\mathbf{B}_{\mathrm{c,p}}K_{\mathrm{r}}\, R_{\mathrm{trq}}(z). \tag{3.12}$$

Consequently, for steady-state reference tracking it is required that

$$\mathbf{C}_{\mathrm{trq}}\left(\mathbf{I} - \left[\mathbf{A}_{\mathrm{p}} - \mathbf{B}_{\mathrm{c,p}}\mathbf{K}_{\mathrm{p}}\right]\right)^{-1}\mathbf{B}_{\mathrm{c,p}}K_{\mathrm{r}} = 1 \tag{3.13}$$

from which the feedforward gain K_{r} is determined as

$$K_{\mathrm{r}} = \left[\mathbf{C}_{\mathrm{trq}}\left(\mathbf{I} - \left[\mathbf{A}_{\mathrm{p}} - \mathbf{B}_{\mathrm{c,p}}\mathbf{K}_{\mathrm{p}}\right]\right)^{-1}\mathbf{B}_{\mathrm{c,p}}\right]^{-1}. \tag{3.14}$$

3.2.3 Static Disturbance Feedforward

The requirement for steady-state disturbance rejection can be fulfilled by introducing an additional feedforward term to the control law

$$u_{\mathrm{c,p}}(k) = -\mathbf{K}_{\mathrm{p}}\mathbf{x}_{\mathrm{p}}(k) + K_{\mathrm{r}}r_{\mathrm{trq}}(k) + \mathbf{K}_{\mathrm{d}}\mathbf{u}_{\mathrm{d,p}}(k) \tag{3.15}$$

and necessitates that the disturbance variables can be measured or estimated. To determine the feedforward gain vector $\mathbf{K}_{\mathrm{d}}$, the extended control law (3.15) is inserted into the linear plant model given by (2.15) and (2.16), which yields for the closed loop system

$$\begin{aligned}\mathbf{x}_{\mathrm{p}}(k+1) &= \left[\mathbf{A}_{\mathrm{p}} - \mathbf{B}_{\mathrm{c,p}}\mathbf{K}_{\mathrm{p}}\right]\mathbf{x}_{\mathrm{p}}(k) + \left[\mathbf{B}_{\mathrm{c,p}}\mathbf{K}_{\mathrm{d}} + \mathbf{B}_{\mathrm{d,p}}\right]\mathbf{u}_{\mathrm{d,p}}(k) \quad \text{with } r_{\mathrm{trq}}(k) = 0 \\ y_{\mathrm{trq}}(k) &= \mathbf{C}_{\mathrm{trq}}\mathbf{x}_{\mathrm{p}}(k).\end{aligned} \tag{3.16}$$

Under application of z-Transformation, the disturbance transfer function matrix from disturbance input vector to objective output is derived as

$$Y_{\mathrm{trq}}(z) = \mathbf{C}_{\mathrm{trq}}\left[z\mathbf{I} - \left[\mathbf{A}_{\mathrm{p}} - \mathbf{B}_{\mathrm{c,p}}\mathbf{K}_{\mathrm{p}}\right]\right]^{-1}\left[\mathbf{B}_{\mathrm{c,p}}\mathbf{K}_{\mathrm{d}} + \mathbf{B}_{\mathrm{d,p}}\right]\mathbf{U}_{\mathrm{d,p}}(z). \tag{3.17}$$

For stationary conditions $z \to 1$, which further gives

$$\begin{aligned}Y_{\mathrm{trq}}(z) &= \boldsymbol{\phi}\left[\mathbf{B}_{\mathrm{c,p}}\mathbf{K}_{\mathrm{d}} + \mathbf{B}_{\mathrm{d,p}}\right]\mathbf{U}_{\mathrm{d,p}}(z) \\ \text{with } \boldsymbol{\phi} &= \mathbf{C}_{\mathrm{trq}}\left[\mathbf{I} - \left[\mathbf{A}_{\mathrm{p}} - \mathbf{B}_{\mathrm{c,p}}\mathbf{K}_{\mathrm{p}}\right]\right]^{-1}.\end{aligned} \tag{3.18}$$

Thus, for steady-state disturbance rejection it is required that

$$\boldsymbol{\phi}\left[\mathbf{B}_{\mathrm{c,p}}\mathbf{K}_{\mathrm{d}} + \mathbf{B}_{\mathrm{d,p}}\right] = \mathbf{0} \tag{3.19}$$

from which the feedforward gain vector $\mathbf{K}_{\mathrm{d}}$ is directly found [Rop09]

$$\mathbf{K}_{\mathrm{d}} = -\left[\boldsymbol{\phi}\mathbf{B}_{\mathrm{c,p}}\right]^{-1}\boldsymbol{\phi}\mathbf{B}_{\mathrm{d,p}}. \tag{3.20}$$

3.2.4 Extended Optimal State-Estimator

For optimal state-feedback controller and static disturbance feedforward design, it was assumed that the plant state vector and the disturbance input vector are known. However, this is not the case in the practical implementation. The objective of this section is therefore to design an extended optimal state-estimator that provides estimates of the plant states $\hat{\mathbf{x}}_\mathrm{p}$ and reconstructs unknown disturbance variables $\hat{\mathbf{x}}_\mathrm{d}$.
For the design of the state-estimator, the discrete linear plant model with measurement output equation given by (2.15) and (2.18)

$$\mathbf{x}_\mathrm{p}(k+1) = \mathbf{A}_\mathrm{p}\mathbf{x}_\mathrm{p}(k) + \mathbf{B}_\mathrm{c,p}u_\mathrm{c,p}(k) + \mathbf{B}_\mathrm{d,p}\mathbf{u}_\mathrm{d,p}(k)$$
$$\mathbf{y}_\mathrm{m,p}(k) = \mathbf{C}_\mathrm{m,p}\mathbf{x}_\mathrm{p}(k)$$

is augmented by unknown input integrator disturbance models

$$\mathbf{x}_\mathrm{d}(k+1) = \mathbf{A}_\mathrm{d}\mathbf{x}_\mathrm{d}(k) + \mathbf{B}_\mathrm{d}\mathbf{u}_\mathrm{d}(k) \quad \text{with } \mathbf{A}_\mathrm{d} = \mathbf{I}_{2\times2}, \mathbf{B}_\mathrm{d} = \mathrm{T_s}\mathbf{I}_{2\times2}, \mathbf{C}_\mathrm{d} = \mathbf{I}_{2\times2} \tag{3.21}$$
$$\mathbf{y}_\mathrm{d}(k) = \mathbf{C}_\mathrm{d}\mathbf{x}_\mathrm{d}(k).$$

These disturbance models are suitable for the reconstruction of piece-wise constant disturbances such as for example load torque or Coulomb friction ([Fra+98], [Hen97], [Irm+20]). Using the substitution $\mathbf{u}_\mathrm{d,p} = \mathbf{y}_\mathrm{d}$, the linear plant model and disturbance model are combined to an augmented plant model, that is

$$\begin{bmatrix}\mathbf{x}_\mathrm{p}(k+1)\\ \mathbf{x}_\mathrm{d}(k+1)\end{bmatrix} = \begin{bmatrix}\mathbf{A}_\mathrm{p} & \mathbf{B}_\mathrm{d,p}\mathbf{C}_\mathrm{d}\\ \mathbf{0} & \mathbf{A}_\mathrm{d}\end{bmatrix}\begin{bmatrix}\mathbf{x}_\mathrm{p}(k)\\ \mathbf{x}_\mathrm{d}(k)\end{bmatrix} + \begin{bmatrix}\mathbf{B}_\mathrm{c,p} & \mathbf{0}\\ \mathbf{0} & \mathbf{B}_\mathrm{d}\end{bmatrix}\begin{bmatrix}u_{c,p}(k)\\ \mathbf{u}_\mathrm{d}(k)\end{bmatrix} \tag{3.22}$$
$$\mathbf{y}_\mathrm{m,p}(k) = [\mathbf{C}_\mathrm{m,p} \quad \mathbf{0}]\begin{bmatrix}\mathbf{x}_\mathrm{p}(k)\\ \mathbf{x}_\mathrm{d}(k)\end{bmatrix}$$

respectively written in compact vector-matrix notation

$$\mathbf{x}_\mathrm{a}(k+1) = \mathbf{A}_\mathrm{a}\mathbf{x}_\mathrm{a}(k) + \mathbf{B}_\mathrm{a}\mathbf{u}_\mathrm{a}(k) \tag{3.23}$$
$$\mathbf{y}_\mathrm{a}(k) = \mathbf{C}_\mathrm{a}\mathbf{x}_\mathrm{a}(k).$$

Based on the augmented plant model, an extended optimal state-estimator (Kalman Filter) is designed. For the optimal estimation problem, it is assumed that the augmented plant is disturbed by process noise **w** and measurement noise **v.** These are modelled as white, Gaussian random noise processes, which are uncorrelated and their respective noise covariances are given by

$$E[\mathbf{w}(k)\ \mathbf{w}^\mathrm{T}(k)] = \mathbf{W} \quad E[\mathbf{v}(k)\mathbf{v}^\mathbf{T}(k)] = \mathbf{V} \quad \text{with } \mathbf{W} \geq \mathbf{0}\ \ \mathbf{V} > \mathbf{0}. \tag{3.24}$$

In this context, the process noise is modeled additive to the inputs for penalizing the unknown disturbance model inputs and preparing for input Loop Transfer Recovery (LTR). The latter is essentially a Kalman Filter adjustment procedure, which asymptotically recovers the excellent robustness properties of the optimal state-feedback controller for full-state feedback. Thereby it contributes to the robust design of the LQG steering torque controller ([Fra+14], [Hen97], [Bru+19], [Doy+79]). The measurement noise is modeled additive to the outputs, which are reflecting the available measurements in the system. For the augmented plant model subject to process and

measurement noise an optimal state estimate $\hat{\mathbf{x}}_\mathrm{a}$ is needed, which minimizes the steady-state value of the sum of the squared estimation errors

$$J = \lim_{k\to\infty} \mathrm{tr}[E\{\mathbf{x}_\mathrm{a}(k) - \hat{\mathbf{x}}_\mathrm{a}(k)\}\{\mathbf{x}_\mathrm{a}(k) - \hat{\mathbf{x}}_\mathrm{a}(k)\}^\mathrm{T}] \quad \text{respectively} \tag{3.25}$$
$$J = \lim_{k\to\infty} \mathrm{tr}[\mathbf{P}_\mathrm{e}] = \mathrm{tr}[\mathbf{P}_\mathrm{e}^*].$$

The optimal solution to the problem is given by the state-estimator [Dut+97]

$$\hat{\mathbf{x}}_\mathrm{a}(k+1) = (\mathbf{A}_\mathrm{a} - \mathbf{L}\,\mathbf{C}_\mathrm{a})\hat{\mathbf{x}}_\mathrm{a}(k) + \mathbf{B}_\mathrm{a}\,\mathbf{u}_\mathrm{a}(k) + \mathbf{L}\,\mathbf{y}_\mathrm{a}(k) \tag{3.26}$$

which minimizes the quadratic cost function over an infinite time interval $[0, \infty]$. In this context, the optimal feedback gain matrix $\mathbf{L}$ is given by ([Lew+08], [Lew+12])

$$\mathbf{L} = \mathbf{A}_\mathrm{a}\mathbf{P}_\mathrm{e}^*\mathbf{C}_\mathrm{a}^\mathrm{T}(\mathbf{C}_\mathrm{a}\mathbf{P}_\mathrm{e}^*\mathbf{C}_\mathrm{a}^\mathrm{T} + \mathbf{V})^{-1} \tag{3.27}$$

where $\mathbf{P}_\mathrm{e}^*$ is the steady-state solution of the discrete algebraic Riccati equation

$$\mathbf{A}_\mathrm{a}[\mathbf{P}_\mathrm{e}^* - \mathbf{P}_\mathrm{e}^*\mathbf{C}_\mathrm{a}^\mathrm{T}(\mathbf{C}_\mathrm{a}\mathbf{P}_\mathrm{e}^*\mathbf{C}_\mathrm{a}^\mathrm{T} + \mathbf{V})^{-1}\mathbf{C}_\mathrm{a}\mathbf{P}_\mathrm{e}^*]\mathbf{A}_\mathrm{a}^\mathrm{T} + \mathbf{B}_\mathrm{a}\mathbf{W}\mathbf{B}_\mathrm{a}^\mathrm{T} - \mathbf{P}_\mathrm{e}^* = \mathbf{0}. \tag{3.28}$$

The plant state and disturbance estimates are provided as an input to the extended control law. By inclusion of the disturbance states, the LQG controller receives integral action and is thus robust against plant uncertainty.

Selection of Physically Meaningful Noise Covariance Matrices

The noise covariance matrices $\mathbf{W}$ and $\mathbf{V}$ can be treated as design parameters for determining the estimator feedback gain matrix $\mathbf{L}$. Under the assumption that the noise processes are uncorrelated, they become diagonal matrices whose elements are the variances of the respective noise vector components. Suitable starting values for the noise variances may be obtained by considering the environment of the estimator in the digital implementation. The control inputs will be fixed point values with a defined quantization that is given by the software scaling. The measurement outputs will also be subject to quantization, which is due to the limited resolution in the AD conversion of these signals. The resulting round-off errors can be modeled as stochastic white noise processes that are added to the respective signals. According to [Fra+14], the variance of quantization noise is defined by

$$\sigma^2 = \frac{1}{12}q^2 \tag{3.29}$$

with q being the signal quantization. Noise that does not originate from signal quantization, such as for example sensor noise, can be directly measured by experiment, and the determined variance value used as a design parameter. By applying this rule to the control input and measurement output signals, suitable estimator design parameters can be found. All that remains is finding appropriate values for the noise variances of the integrator disturbance model input signals. As these inputs are unknown, their noise variances must be selected as high as possible (i.e. high uncertainty) to make the estimator fully rely on the measurements for their reconstruction. Summarizing these design guidelines, physically meaningful initial values for the noise covariances $\mathbf{W}$ and $\mathbf{V}$ are obtained by selecting

W_{ii} = variance of $u_{a,i}(k)$ $\quad i \in \{1,2,\dots,\mathrm{l}\}$

V_{jj} = variance of $y_{a,i}(k)$ $\quad j \in \{1,2,\dots,\mathrm{k}\}$

with the noise variance

- from quantization error computed by $\sigma^2 = q^2/12$,
- from sensor noise identified by experiment,
- for integrator disturbance model inputs selected as high as possible.

3.2.5 Steering Feel Generation and LQG Steering Torque Controller

By combining the optimal state-feedback controller, static reference feedforward, static disturbance feedforward, and extended optimal state-estimator, the LQG steering torque controller according to Figure 20 results. The LQG controller controls the steering torque y_{trq} felt by the driver. In this context, a reference steering torque r_{trq} is provided by the Steering Reference Torque Generator (SRTG). The SRTG includes all steering feel generation functions such as the inverted assist curves, linear damping, active return, hysteresis, rack end stop emulation, oversteer and understeer detection, banked road correction and low μ-adaption [Koc10].

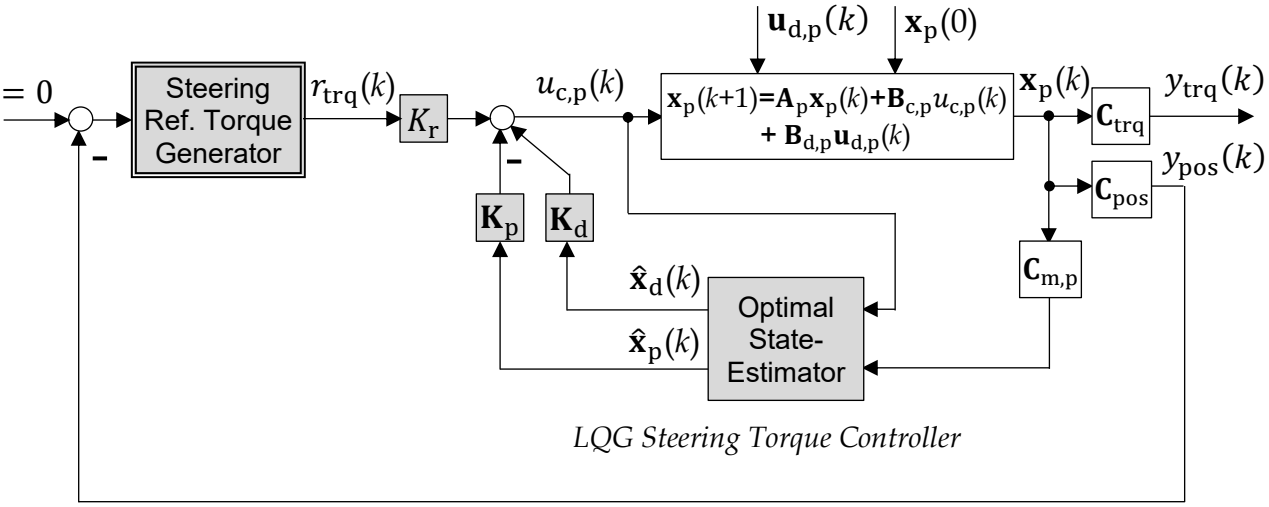

Figure 20: HWA – Steering Feel Generation and Steering Torque Controller

The reference steering torque is provided mainly as a function of steering position and steering velocity. Therefore, the SRTG can be abstracted as a nonlinear PD steering position controller where the proportional and derivative gains are tuned for the desired steering feel. When the driver turns the steering wheel, the position increases, and the SRTG provides a reference steering torque, which counteracts the driver. The LQG steering torque controller accurately tracks this reference steering torque.

3.3 Cascade 2DOF LQG Steering Position Control for the Handwheel Actuator

For automated driving, the HWA must be operated in steering position control mode to ensure that the steering wheel motion corresponds to the road wheel motion. This gives the driver an indication on where the automation system is heading. Hereby the reference steering position is provided by an automated lateral vehicle guidance controller. To fulfill the requirement of precise lateral vehicle guidance while having smooth steering wheel motions, the reference tracking bandwidth of the HWA steering position control is reduced in order to attenuate high-frequency content of the lateral vehicle guidance controller output. For allowing a reduced reference tracking bandwidth but preserving strong disturbance rejection, a 2 Degrees-of-Freedom (2DOF) controller structure is selected. This structure provides the possibility for an independent design of the command and the disturbance response that is useful in this application. Moreover, due to the requirement to dampen the mechanical resonance of the system, a LQG controller design is employed. An elegant way for designing this controller is to consider the existing steering torque control loop as the virtual plant for position controller synthesis. Thereby, the same state variables and disturbance variables can be used, which are directly supplied by the existing optimal state-estimator. Figure 21 depicts the general structure of the resulting cascade 2DOF LQG steering position controller. In the following, the synthesis of an optimal state-feedback steering position controller for the virtual plant is initially described. Thereafter, a static feedforward control for steady-state disturbances rejection is added. Lastly, for an independent design of the command and the disturbance response, a model-based dynamic reference feedforward is introduced.

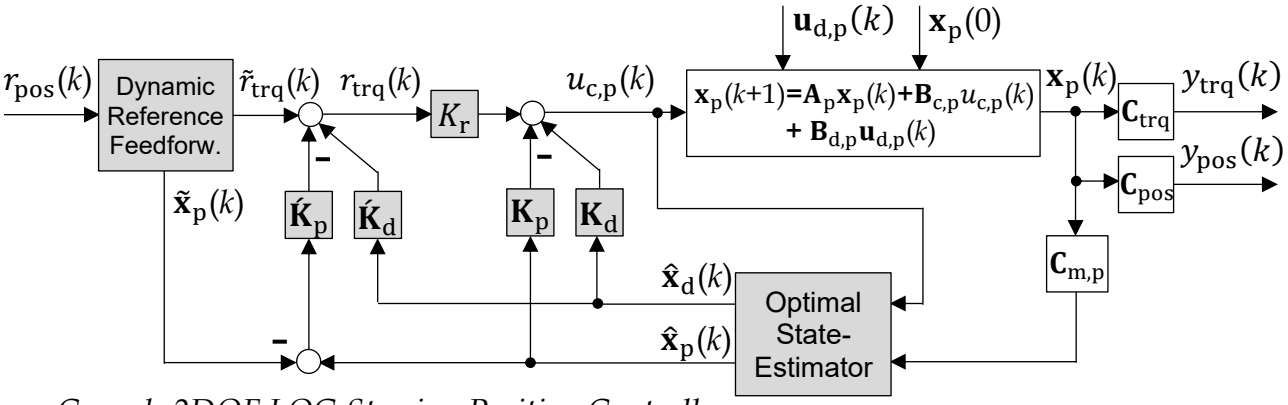

Figure 21: HWA – Cascade 2DOF LQG Steering Position Controller

The developed control structure has the advantage that the torque control loop persists as an inner control loop for steering position control. This is similar to the control structure from the previous section. Therefore, effectively two steering position controllers, which are pursuing different control objectives, are employed. These objectives are reference steering position tracking and steering feel generation. This essential finding is further exploited in chapter 5 where a superposition control is synthesized that allows fusing both structures. Hereby a cooperative HWA control is realized, which enables a true coexistence between steering position and steering torque control.

3.3.1 Derivation of the Virtual Plant Model for Controller Synthesis

The control law and plant model of the steering torque control loop corresponding to (3.15) and (2.15) are given by

$$\left.\begin{aligned} u_{\mathrm{c,p}}(k) &= -\mathbf{K}_{\mathrm{p}}\mathbf{x}_{\mathrm{p}}(k) + K_{\mathrm{r}} r_{\mathrm{trq}}(k) + \mathbf{K}_{\mathrm{d}}\mathbf{u}_{\mathrm{d,p}}(k) \quad &\} \text{ Control Law} \\ \mathbf{x}_{\mathrm{p}}(k+1) &= \mathbf{A}_{\mathrm{p}}\mathbf{x}_{\mathrm{p}}(k) + \mathbf{B}_{\mathrm{c,p}} u_{\mathrm{c,p}}(k) + \mathbf{B}_{\mathrm{d,p}}\mathbf{u}_{\mathrm{d,p}}(k) \quad &\} \text{ Plant} \end{aligned}\right.$$

Substituting the control law into the plant yields for the closed loop system

$$\mathbf{x}_{\mathrm{p}}(k+1) = \underbrace{\left[\mathbf{A}_{\mathrm{p}} - \mathbf{B}_{\mathrm{c,p}}\mathbf{K}_{\mathrm{p}}\right]}_{\acute{\mathbf{A}}_{\mathrm{p}}} \mathbf{x}_{\mathrm{p}}(k) + \underbrace{\mathbf{B}_{\mathrm{c,p}}}_{\acute{\mathbf{B}}_{\mathrm{c,p}}} \underbrace{K_{\mathrm{r}} r_{\mathrm{trq}}(k)}_{\acute{u}_{\mathrm{c,p}}(k)} + \underbrace{\left[\mathbf{B}_{\mathrm{d,p}} + \mathbf{B}_{\mathrm{c,p}}\mathbf{K}_{\mathrm{d}}\right]}_{\acute{\mathbf{B}}_{\mathrm{d,p}}} \mathbf{u}_{\mathrm{d,p}}(k). \tag{3.30}$$

Considering this as the virtual plant model for steering position controller synthesis with position output equation finally gives

$$\begin{aligned} \mathbf{x}_{\mathrm{p}}(k+1) &= \acute{\mathbf{A}}_{\mathrm{p}}\mathbf{x}_{\mathrm{p}}(k) + \acute{\mathbf{B}}_{\mathrm{c,p}}\acute{u}_{\mathrm{c,p}}(k) + \acute{\mathbf{B}}_{\mathrm{d,p}}\mathbf{u}_{\mathrm{d,p}}(k) \\ y_{\mathrm{pos}}(k) &= \mathbf{C}_{\mathrm{pos}}\mathbf{x}_{\mathrm{p}}(k). \end{aligned} \tag{3.31}$$

3.3.2 Optimal State-Feedback Controller and Static Disturbance Feedforward

For the virtual plant model with position output equation given by (3.31)

$$\begin{aligned} \mathbf{x}_{\mathrm{p}}(k+1) &= \acute{\mathbf{A}}_{\mathrm{p}}\mathbf{x}_{\mathrm{p}}(k) + \acute{\mathbf{B}}_{\mathrm{c,p}}\acute{u}_{\mathrm{c,p}}(k) \;\text{ with }\; \mathbf{u}_{\mathrm{d,p}} = \mathbf{0} \\ y_{\mathrm{pos}}(k) &= \mathbf{C}_{\mathrm{pos}}\mathbf{x}_{\mathrm{p}}(k) \end{aligned} \tag{3.32}$$

an optimal control $\acute{u}_{\mathrm{c,p}}$ is needed, which drives the state vector $\mathbf{x}_{\mathrm{p}}$ from any initial state to the zero state, such that the value of a performance index is minimized. For the performance index, a quadratic cost function J build by the weighted control input and steering position output is used [Dor+11]

$$J = \sum_{k=0}^{\infty} \left[y_{\mathrm{pos}}^{\mathrm{T}}(k)\acute{\mathbf{Q}}\, y_{\mathrm{pos}}(k) + \acute{u}_{\mathrm{c,p}}^{\mathrm{T}}(k)\acute{\mathbf{R}}\, \acute{u}_{\mathrm{c,p}}(k) \right] \quad \text{with } \acute{\mathbf{Q}} \geq \mathbf{0},\ \acute{\mathbf{R}} > \mathbf{0}\,. \tag{3.33}$$

The weighting matrices $\acute{\mathbf{Q}}$ and $\acute{\mathbf{R}}$ are thereby diagonal matrices whose elements penalize large values of the respective signals in the minimization of the cost function. The state-feedback

$$\acute{u}_{\mathrm{c,p}}(k) = -\acute{\mathbf{K}}_{\mathrm{p}}\mathbf{x}_{\mathrm{p}}(k) \tag{3.34}$$

is the optimal control, which minimizes the quadratic cost function over an infinite time horizon $[0, \infty]$. Hereby the controller gains $\acute{\mathbf{K}}_{\mathrm{p}}$ follow from ([Kwa+05], [Ant+07])

$$\acute{\mathbf{K}}_{\mathrm{p}} = \left(\acute{\mathbf{B}}_{\mathrm{c,p}}^{\mathrm{T}}\acute{\mathbf{S}}\acute{\mathbf{B}}_{\mathrm{c,p}} + \acute{\mathbf{R}}\right)^{-1}\acute{\mathbf{B}}_{\mathrm{c,p}}^{\mathrm{T}}\acute{\mathbf{S}}\acute{\mathbf{A}}_{\mathrm{p}} \tag{3.35}$$

with $\acute{\mathbf{S}}$ being the steady-state solution of the discrete algebraic Riccati equation

$$\acute{\mathbf{A}}_{\mathrm{p}}^{\mathrm{T}}\left[\acute{\mathbf{S}}-\acute{\mathbf{S}}\acute{\mathbf{B}}_{\mathrm{c,p}}\left(\acute{\mathbf{B}}_{\mathrm{c,p}}^{\mathrm{T}}\acute{\mathbf{S}}\acute{\mathbf{B}}_{\mathrm{c,p}}+\acute{\mathbf{R}}\right)^{-1}\acute{\mathbf{B}}_{\mathrm{c,p}}^{\mathrm{T}}\acute{\mathbf{S}}\right]\acute{\mathbf{A}}_{\mathrm{p}}+\mathbf{C}_{\mathrm{pos}}^{\mathrm{T}}\acute{\mathbf{Q}}\,\mathbf{C}_{\mathrm{pos}}-\acute{\mathbf{S}}=\mathbf{0}. \tag{3.36}$$

For steady-state disturbance rejection, a static disturbance feedforward must furthermore be added to the control law and thus it follows

$$\acute{u}_{\mathrm{c,p}}(k)=-\acute{\mathbf{K}}_{\mathrm{p}}\mathbf{x}_{\mathrm{p}}(k)+\acute{\mathbf{K}}_{\mathrm{d}}\mathbf{u}_{\mathrm{d,p}}(k). \tag{3.37}$$

With this regard, through derivation of the disturbance transfer function matrix, it can be shown that the feedforward gains

$$\acute{\mathbf{K}}_{\mathrm{d}}=-\left[\acute{\boldsymbol{\phi}}\acute{\mathbf{B}}_{\mathrm{c,p}}\right]^{-1}\acute{\boldsymbol{\phi}}\acute{\mathbf{B}}_{\mathrm{d,p}} \tag{3.38}$$

$$\text{with } \acute{\boldsymbol{\phi}}=\mathbf{C}_{\mathrm{pos}}\left[\mathbf{I}-\left[\acute{\mathbf{A}}_{\mathrm{p}}-\acute{\mathbf{B}}_{\mathrm{c,p}}\acute{\mathbf{K}}_{\mathrm{p}}\right]\right]^{-1}$$

guarantee steady-state disturbance rejection [Rop09]. For the control law defined by (3.37) the same state variables and disturbance variables can be used, which are directly provided by the existing optimal state-estimator. The connection of this control law to the LQG steering torque controller, as detailly illustrated in Figure 21, hence gives a cascade LQG steering position controller.

3.3.3 Dynamic Reference Feedforward

The previously synthesized cascade LQG steering position controller determines the dynamics of the disturbance response and the stability of the closed loop system. For an independent design of the command response, the control structure is augmented by a model-based dynamic reference feedforward (see Figure 22). It consists of a virtual control loop, which is calculated online to generate a control signal $\tilde{r}_{\mathrm{trq}}$ for command following. The generated control signal is then provided to the real plant. For hiding the effect of the control signal on the system states from LQG feedback control, the virtual state vector $\tilde{\mathbf{x}}_{\mathrm{p}}$ is subtracted from the state estimates $\hat{\mathbf{x}}_{\mathrm{p}}$ (see Figure 21). Following the superposition principle, the LQG feedback controller thus accepts any intervention from dynamic reference feedforward [Rop09].

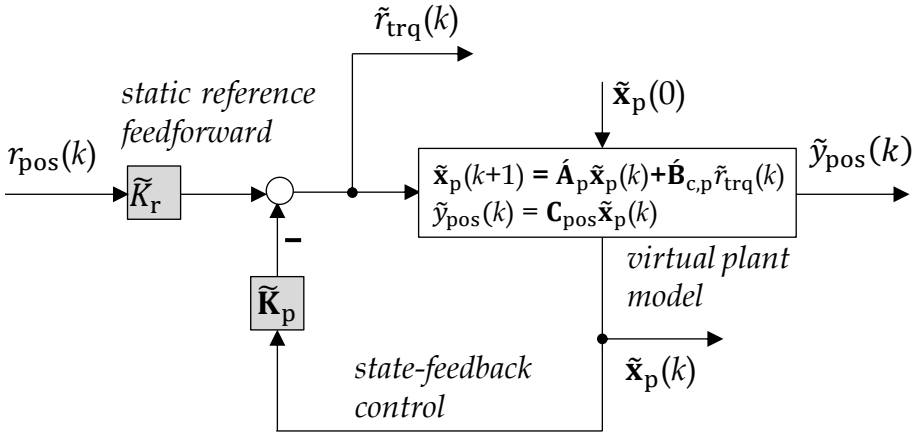

Figure 22: HWA – Model-based Dynamic Reference Feedforward

Consequently, in the absence of model error, disturbances, or different initial conditions, the command response of the virtual control loop propagates to the real system.

In the presence of model error, disturbances, or different initial conditions, the LQG feedback controller becomes active and determines the disturbance response.

The virtual control loop is designed for a desired command response. For this purpose, the synthesis of an optimal state-feedback controller with static reference feedforward is suitable as the state vector of the virtual plant model is directly accessible [Deu12]. The control law is hence defined as

$$\tilde{r}_{\mathrm{trq}}(k) = -\tilde{\mathbf{K}}_{\mathrm{p}}\tilde{\mathbf{x}}_{\mathrm{p}}(k) + \tilde{K}_{\mathrm{r}} r_{\mathrm{pos}}(k). \tag{3.39}$$

Hereby the optimal feedback gain matrix $\tilde{\mathbf{K}}_{\mathrm{p}}$ is similar to section 3.3.2 synthesized by minimization of a quadratic cost function. The static reference feedforward $\tilde{K}_{\mathrm{r}}$ is according to [Rop09] analytically computed from

$$\tilde{K}_{\mathrm{r}} = \left[\mathbf{C}_{\mathrm{pos}}\left(\mathbf{I} - \left[\acute{\mathbf{A}}_{\mathrm{p}} - \acute{\mathbf{B}}_{\mathrm{c,p}}\tilde{\mathbf{K}}_{\mathrm{p}}\right]\right)^{-1}\acute{\mathbf{B}}_{\mathrm{c,p}}\right]^{-1}. \tag{3.40}$$

3.4 2DOF LQG Steering Position Control for the Front Axle Actuator

For manual and automated lateral vehicle guidance, the SbW FAA is operated in closed-loop steering position control mode and must provide an accurate reference steering position tracking. Thereby, high requirements regarding dynamics, steady-state accuracy, and robustness must be fulfilled, which require an active compensation of external rack forces and nonlinear friction. For meeting these requirements, a 2DOF LQG steering position control is presented in this section. The general control structure is illustrated in Figure 23 and results from combining a model-based dynamic reference feedforward with an LQG feedback control. This structure has the advantage that the dynamics of the command and the disturbance response can be independently designed ([Rop09], [Kre99], [Zei12]). Furthermore, as the model-based dynamic reference feedforward represents a pure feedforward control, the reference tracking bandwidth can be increased without degrading the stability of the control loop.

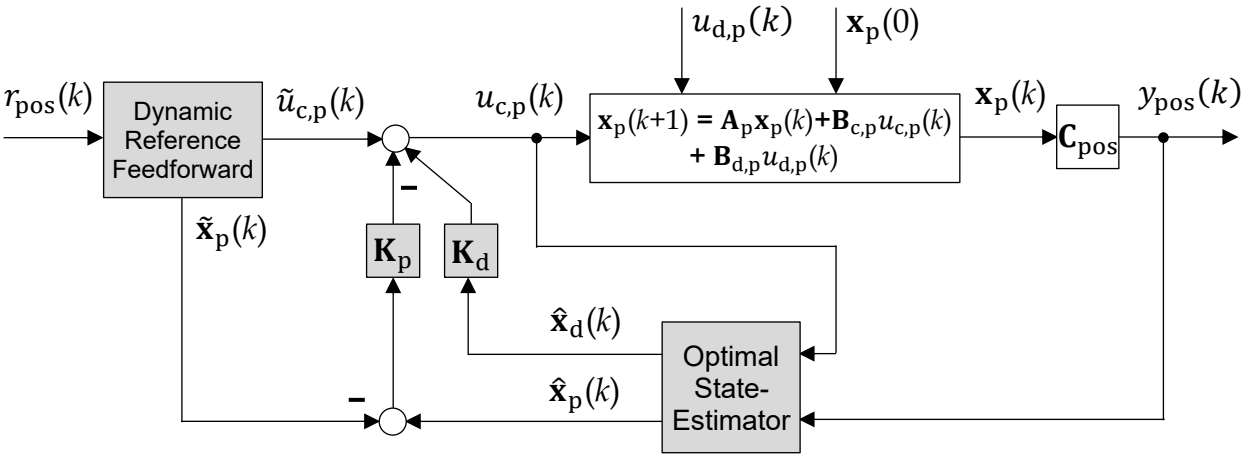

2DOF LQG Steering Position Controller

Figure 23: FAA – 2DOF LQG Steering Position Controller

Hence, superior control performance is achieved, which is decisive for a realistic emulation of the missing mechanical coupling between the steering wheel and road wheels.

The controller synthesis is directly performed for the discrete linear plant model in state-space representation given by (2.28) and (2.29). For this purpose, an optimal state-feedback controller with static disturbance feedforward is first synthesized using the same design methods as described in the previous sections. Thereafter, an extended optimal state-estimator is introduced, which includes an integrator disturbance model for the unknown disturbance input of the plant model. The connection of the optimal state-feedback controller, static disturbance feedforward, and extended optimal state-estimator gives an LQG steering position controller. To ensure an independent design of the command response, the LQG controller is structurally augmented by a model-based dynamic reference feedforward as illustrated in Figure 24. The latter includes a virtual control that is designed for a desired command response and calculated online to generate the required control signal for command following.

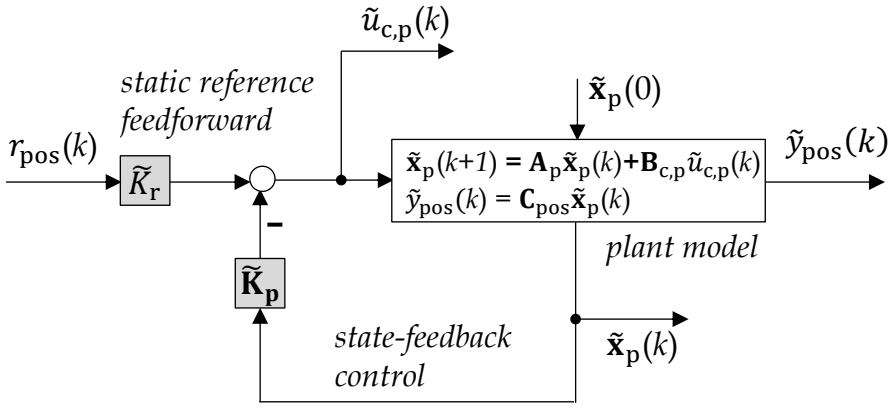

Figure 24: FAA – Model-based Dynamic Reference Feedforward

For a detailed description of the 2DOF LQG steering position controller synthesis for the FAA of the SbW system it is referred to the publications [Gon+22] and [Gon+23a].

3.5 Control System Analysis

After control synthesis, the performance and stability of each of the control systems are analyzed. For this purpose, time and frequency domain analysis is conducted.
Figure 25 to 27 depict the computed frequency response functions of the HWA steering torque and steering position control and the FAA steering position control. With this regard, the closed loop reference and disturbance frequency response and the open loop frequency response are shown. The designed LQG steering torque controller for the HWA of the SbW system achieves a reference tracking bandwidth of 27 Hz (see Figure 25). Furthermore, the frequency responses from the plant disturbance input vector to the measured steering torque are inspected, which reflect the disturbance rejection capability of the control loop. Disturbance torques at pinion are attenuated by at least -12.2 dB and at steering wheel by at least -5 dB. Thereover, steady-state disturbance rejection for both transfer paths is achieved.

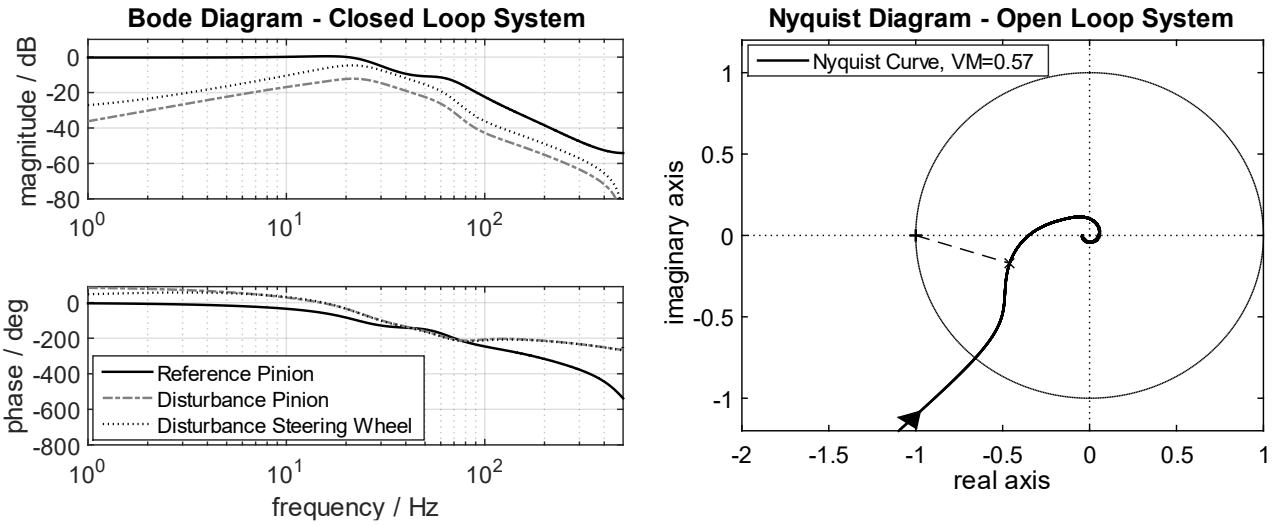

Figure 25: HWA – Frequency Responses of the Steering Torque Control Loop

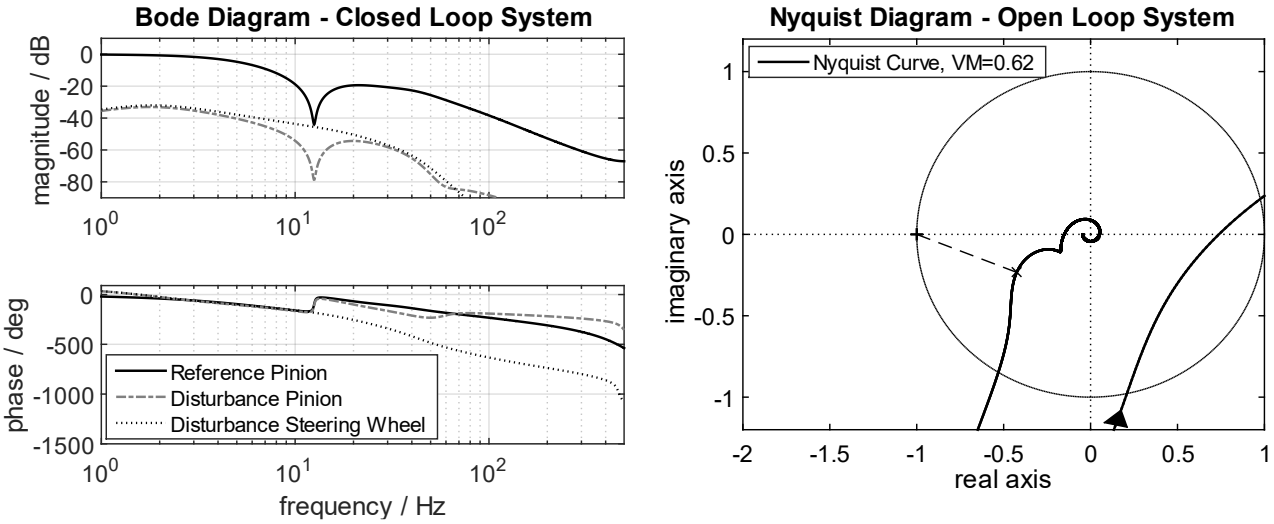

Figure 26: HWA – Frequency Responses of the Steering Position Control Loop

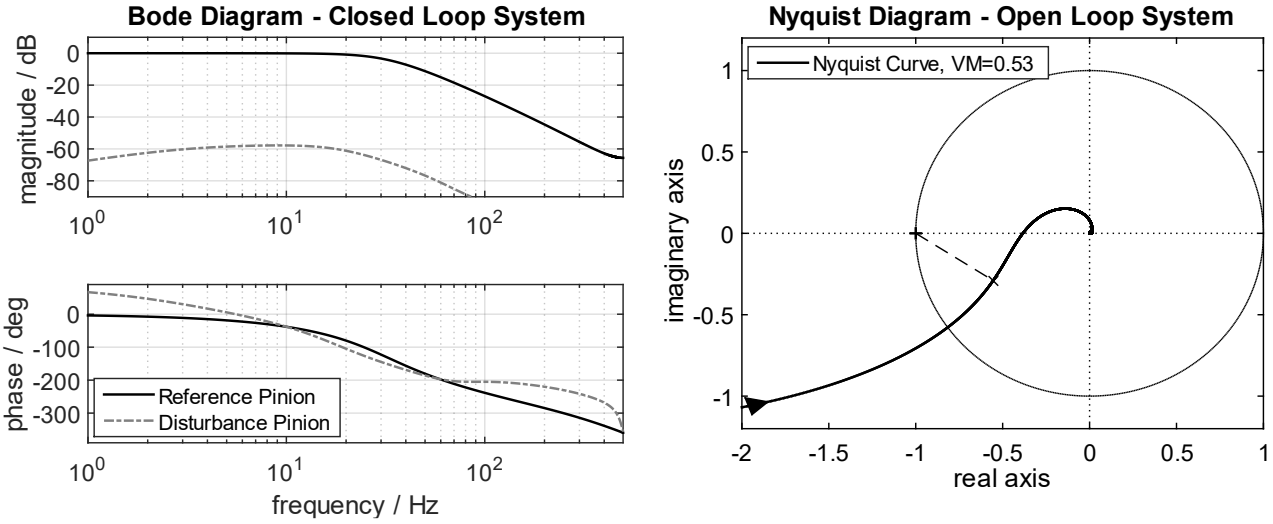

Figure 27: FAA – Frequency Responses of the Steering Position Control Loop

From the Nyquist diagram, which illustrates the frequency response of the open loop system and provides the basis for stability analysis, a vector margin of 0.57 is exposed. Therefore, the LQG controller reveals good robustness, which was essentially achieved by application of the LTR method in the extended optimal-estimator synthesis. In Figure 26 the frequency responses of the cascade 2DOF LQG steering position control for the SbW HWA are further shown. The control possesses a reference tracking bandwidth of 4 Hz. Due to the 2DOF controller structure, the bandwidth can be arbitrarily reduced for ensuring smooth steering wheel motions during automated driving without compromising on disturbance rejection performance. Disturbance torques at the pinion and the steering wheel are attenuated both by at least –32 dB and completely rejected in steady state. Moreover, the control shows a vector margin of 0.62 and is thus robust against plant uncertainty. Lastly, Figure 27 depicts the frequency responses of the 2DOF LQG steering position control for the SbW FAA. The control reveals a reference tracking bandwidth of 30 Hz. Thereover, disturbance torques at pinion are strongly rejected and attenuated by at least -57 dB. Despite the reference tracking and disturbance rejection performance, the control reveals good robustness properties as indicated by a vector margin of 0.52.

Figure 28 to 30 illustrate the step responses of the individual control loops for reference and disturbance excitation, respectively. For a reference torque step of 1 Nm, the LQG steering torque control of the HWA achieves a rise time of 12 msec, an overshoot of 11%, and a settling time of 35 msec (5% error band). A friction torque disturbance step of 1 Nm at pinion shows a maximum steering torque error of 0.15 Nm, which is eliminated within 28 msec. Similarly, a driver torque disturbance step of 1 Nm at steering wheel reveals a maximum torque error of 0.3 Nm, which vanishes after 30 msec. Consequently, the designed control achieves dynamic command following and is robust against unknown disturbances. Moreover, for a reference position step of 10 deg, the cascade 2DOF LQG steering position control of the HWA reveals a rise time of 130 msec, no overshoot, and a settling time of 142 msec. A friction torque disturbance step of 1 Nm at pinion shows a maximum steering position error of 0.7 deg. Similarly, a driver torque disturbance step of 1 Nm at steering wheel reveals a maximum position error of 0.69 deg. Both disturbance torques are eliminated within approximately 336 msec. Lastly, the step responses of the 2DOF LQG steering position control of the FAA are considered. Hereby, for a reference position step of 10 deg, the control exposes a rise time of 12 msec, an overshoot of 4.8%, and a settling time of 18 msec. A rack load disturbance torque step of 10 Nm at pinion gives a maximum steering position error of 0.6 deg, which is fully rejected in steady state. Hence, the 2DOF control shows superior reference tracking performance and good disturbance rejection.

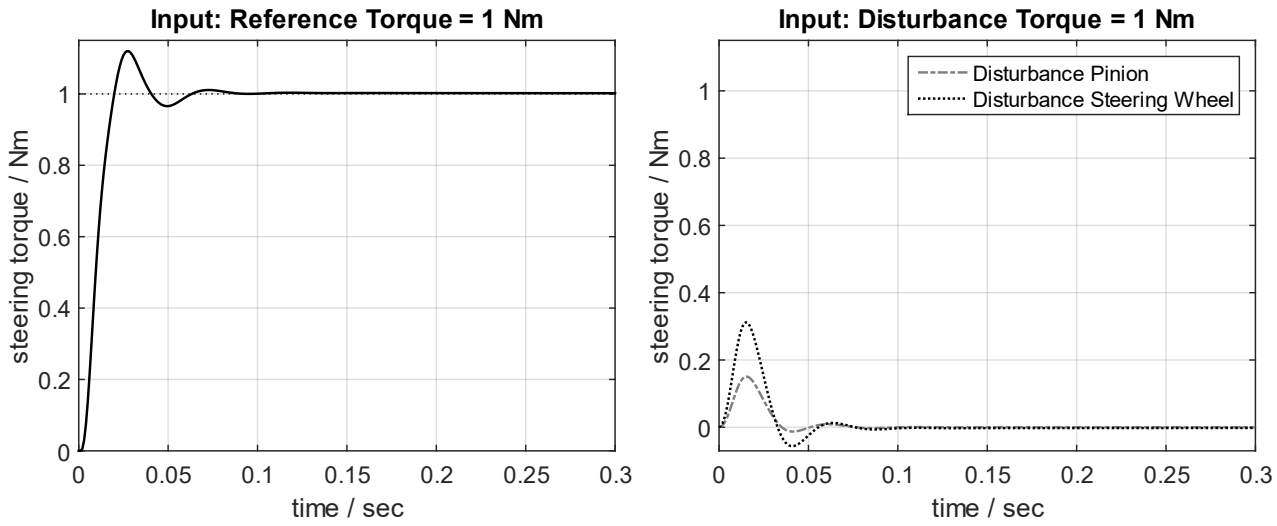

Figure 28: HWA – Step Responses of the Steering Torque Control Loop

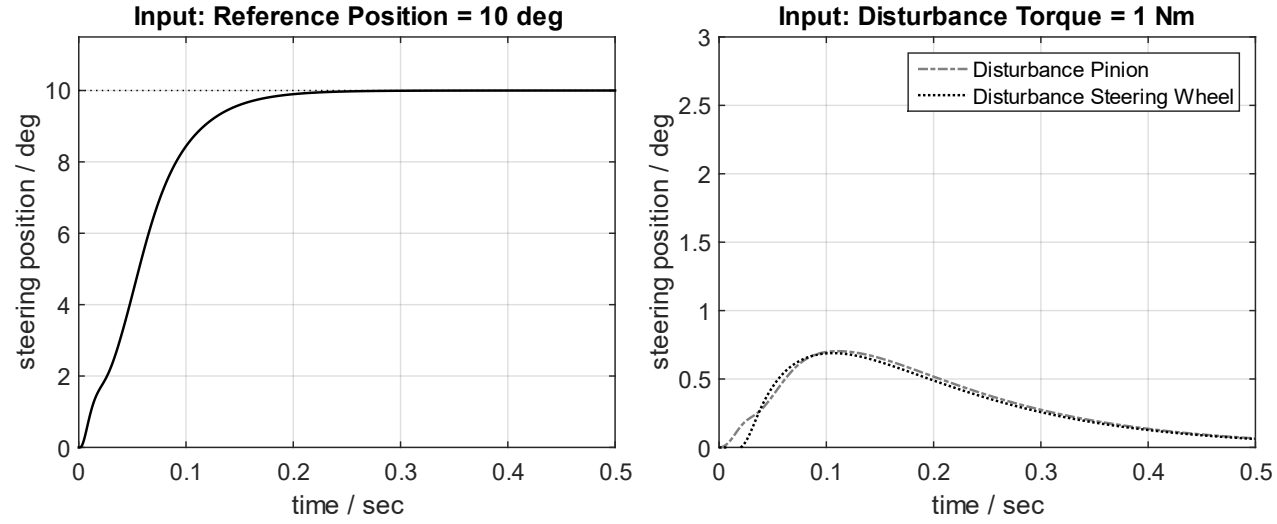

Figure 29: HWA – Step Responses of the Steering Position Control Loop

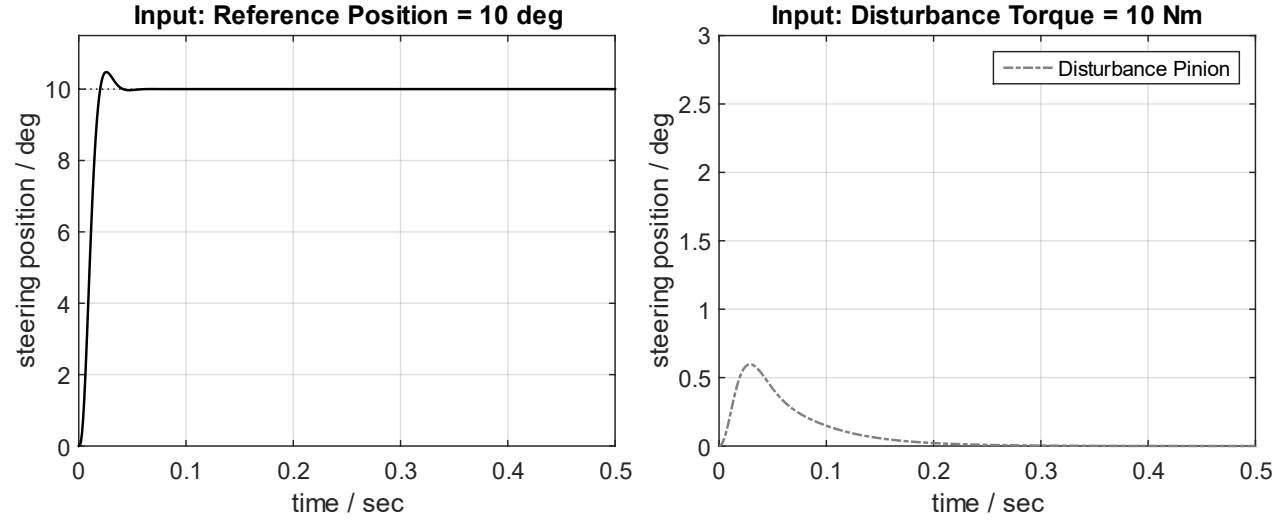

Figure 30: FAA – Step Responses of the Steering Position Control Loop

4

Control Synthesis for Automated Lateral Vehicle Guidance

This chapter presents the control requirements definition and control synthesis of a Nonlinear Adaptive Model Predictive Controller (MPC) for automated lateral vehicle guidance. In contrast to existing approaches, the concept of Inverse Nonlinearity (INL) Control is introduced to cancel the vehicle speed dependent nonlinear plant dynamics. The remaining plant is an LTI system for which one controller can be designed that is valid for all operating points. The resulting closed and open loop system have the same dynamics independent of vehicle speed. This simplifies control system analysis, tuning, and performance evaluation. To explicitly consider the reference path curvature profile and constraints on the steering position within the control law, an MPC controller is synthesized. After a linear analysis of the control performance and stability, a nonlinear simulation analysis is conducted to verify the control performance under plant nonlinearities, measurement signal quantization, and actuator constraints.

4.1 Requirements for the Control System

The primary objective of the lateral vehicle guidance controller is to minimize the lateral deviation y_r between the vehicle's center of gravity and reference path by adjusting the reference steering position φ_{FA}^{*} of the FAA. Hereby, diverse control requirements must be fulfilled, which are outlined in the following table:

Table 3: Lateral Vehicle Guidance Control Requirements for Automated Driving

Automated Lateral Vehicle Guidance Control
- Validity for all vehicle speeds - Validity up to nonlinear driving range ($a_y \geq 4\ \mathrm{m/sec^2}$) - Consideration of actuator constraints ($\varphi_{FA,lim} = 520\ \mathrm{deg}$) - Previewing capability - Reference tracking bandwidth: ≥ 0.1 Hz - Steady-state rejection of curvature, side wind and road camber disturbances - Stability (Vector Margin): 0.5 - Robustness to parameter uncertainty/neglected dynamics

As the eigenvalues and transmission zeros of the lateral vehicle dynamics strongly vary as a function of vehicle speed (refer to chapter 2.4), a vehicle speed adaptive control is required. Hereby, vehicle speeds ranging from standstill (0 km/h) to highway driving (130 km/h) must be covered. Moreover, the control must be valid up to the nonlinear driving range and hence for lateral accelerations $a_y \geq 4\ \mathrm{m/sec^2}$. This requirement arises out of the necessity to support regular driving as well as evasive driving maneuvers within a single control framework. Hereby large steering positions and nonlinear tire characteristics must be specifically taken into consideration. Thereover, the maximum steering position is physically limited to 520 deg. This actuator constraint must be explicitly accounted for in the control law to prevent integral windup. From the perspective of lateral vehicle guidance control, the reference path curvature acts as a disturbance that is known ahead and provided by a path planner. This future disturbance information must be considered in the control law, thereby raising the necessity for a Model Predictive Control concept with measured disturbance previewing.
The previous requirements are focused on general aspects for lateral vehicle guidance control synthesis. Besides these, classical control requirements that are directed to performance and stability are specified. For providing an accurate lateral vehicle guidance, a reference tracking bandwidth of at least 0.1 Hz is required [Rat16]. Hereby, the control is affected by disturbances originating from reference path curvature, side wind, and road camber, which must be fully rejected in steady state. Similarly, unknown disturbances from plant parameter uncertainty and neglected dynamics must be entirely compensated. For robust stability, a VM of at least 0.5 is moreover required [Sko+05].
The additional requirement of gentle control actions for ensuring smooth steering wheel motions (see [Ise22]) is obsolete in this application. This is because in the SbW system the HWA and FAA are mechanically decoupled. Hence, the lateral vehicle guidance controller can be synthesized with the focus on performance. Disturbing noise in the reference steering position is attenuated by a reduced reference tracking bandwidth of the HWA steering position control.

4.2 Nonlinear Adaptive Model Predictive Control Concept

Figure 31 depicts the lateral vehicle guidance control system consisting of the Nonlinear Adaptive MPC and nonlinear dynamic plant model. The inner structure of the controller is detailed, and each module described subsequently. The INL control at the controller output cancels the vehicle speed-dependent nonlinear plant dynamics. The MPC and extended optimal state-estimator are therefore designed for the remaining plant and independent of vehicle speed. The extended optimal state-estimator reconstructs the plant and unknown disturbance states and provides both as an input to the prediction model. Thereby, the controller receives integral action and is robust to unknown disturbances such as model error, side wind and road camber ([Liu+20], [Yan+15]). The MPC uses the prediction model (matrices **E**, **F**, **G**) and constraints on the maximum steering position to compute the optimal control input. By using the reference path curvature sequence $\overline{\boldsymbol{\kappa}}_{\mathrm{ref}}(k)$ that is provided by a path planner as a known disturbance input to the prediction model, a measured disturbance previewing is realized. For unburdening the disturbance estimation, the current disturbance $\kappa_{\mathrm{ref}}(k)$ is given as an

input to the optimal state-estimator. Hence, exclusively the remaining disturbances $\hat{x}_\mathrm{d}(k)$ are estimated.

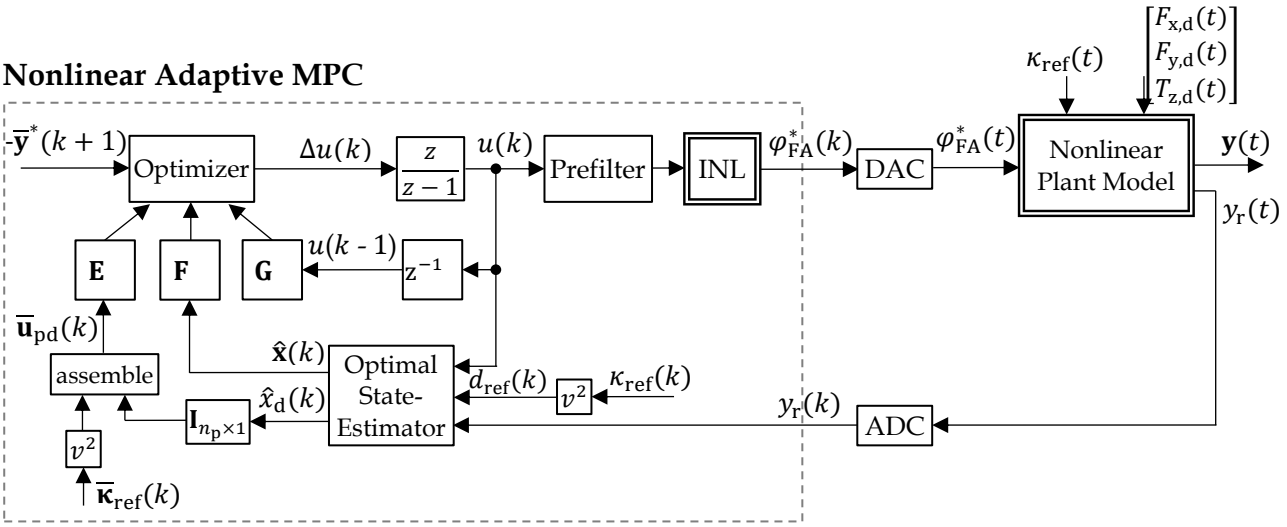

Figure 31: Nonlinear Adaptive MPC for Automated Lateral Vehicle Guidance

The prefilter at the controller output is used to cope with the significant differences in sampling time between lateral vehicle guidance control and FAA steering position control. Thereby, the control actions of the former are smoothed, and unnecessary stress on the mechanical actuator components is avoided. The dynamics of the prefilter are part of the MPC prediction model and plant model for optimal state-estimator synthesis. Consequently, they are directly considered for controller synthesis. The actuator constraints are scaled to controller output coordinates and used as inequality constraints within the optimizer. Hence, it is ensured that the control variable $u(k)$ is correctly limited. By using this limited control variable as an input to the extended optimal state-estimator, integral windup prevention is guaranteed ([Deu12], [Deu+14]). Lastly, for avoiding a singularity in the INL control, a lower vehicle speed limit is introduced. Thereby, control operation from standstill to highway driving is permitted.

4.3 Inverse Nonlinearity Control

In this section, it is demonstrated that the nonlinear dynamic plant model for lateral vehicle guidance can be restructured to isolate the vehicle speed-dependent dynamics. Thereafter, the concepts of inverse linearity (IL) and inverse nonlinearity (INL) control are introduced, to eliminate the vehicle speed-dependent dynamics. The remaining plant model is linear and independent of vehicle speed except for the reference path curvature input κ_ref. However, this is unproblematic as shown in the following. On this foundation, one controller can be synthesized, which is valid for all operating points. This simplifies controller synthesis, analysis, and performance evaluation and makes the necessity for gain scheduling obsolete.

4.3.1 Restructuring of the Nonlinear Dynamic Plant Model

The nonlinear dynamic plant model for lateral vehicle guidance (refer to Figure 13) can be restructured using block diagram algebra to isolate the vehicle speed-dependent dynamics. Thereby, the restructured model, as illustrated in Figure 32, results. All the grey parts are subject to IL control and INL control as detailed in sections 4.3.2 and 4.3.3.

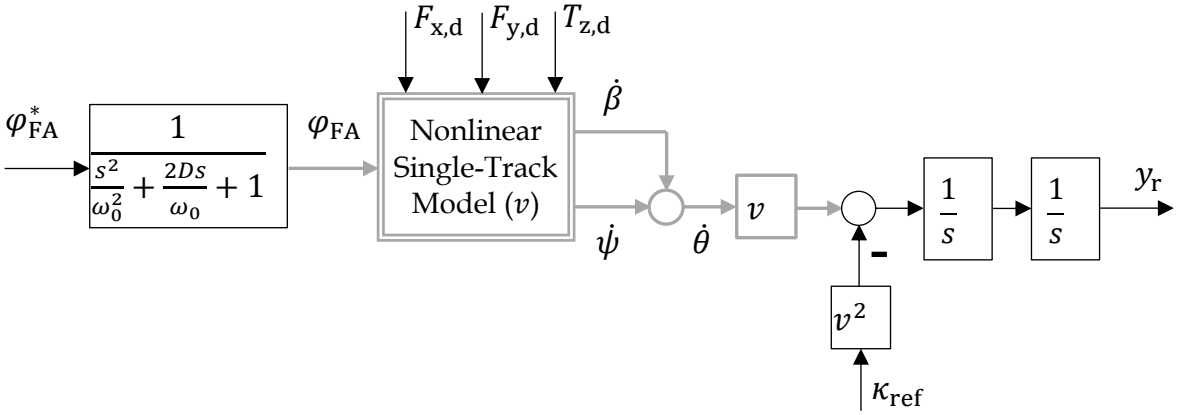

Figure 32: Restructured Nonlinear Plant Model for Lateral Vehicle Guidance

With this regard, the vehicle speed-dependent nonlinear plant dynamics are governed by the equations

$$\dot{\beta} = \frac{1}{mv}\left[F_\mathrm{f}\cos(i_\mathrm{s}\varphi_\mathrm{FA} - \beta) + F_\mathrm{r}\cos(\beta)\right] - \dot{\psi} \tag{4.1}$$

$$\ddot{\psi} = \frac{1}{J_\mathrm{z}}\left[F_\mathrm{f} l_\mathrm{f}\cos(i_\mathrm{s}\varphi_\mathrm{FA}) - F_\mathrm{r} l_\mathrm{r}\right] \tag{4.2}$$

$$v\dot{\theta} = \frac{1}{m}\left[F_\mathrm{f}\cos(i_\mathrm{s}\varphi_\mathrm{FA} - \beta) + F_\mathrm{r}\cos(\beta)\right] \tag{4.3}$$

where F_f, F_r, α_f, α_r are defined by (2.50) to (2.53) and are not substituted here for reasons of readability. The disturbance inputs $F_{x,d}$, $F_{y,d}$ and $T_{z,d}$ are assumed to zero. These are treated as unknown disturbances in the following that are reconstructed by the integrator disturbance model inside the extended optimal state-estimator. By providing the disturbance estimate as an input to the MPC prediction model, steady state disturbance rejection is achieved. Through the application of small-angle approximations $\cos(\phi) \approx 1$ and under the assumption of linear tire behavior, these partial plant dynamics can be further linearized and transformed to state-space representation. This results in

$$\dot{\mathbf{x}}_\mathrm{pa} = \mathbf{A}^\mathrm{c}_\mathrm{pa}\mathbf{x}_\mathrm{pa} + \mathbf{B}^\mathrm{c}_\mathrm{pa}u_\mathrm{pa} \tag{4.4}$$

$$y_\mathrm{pa} = \mathbf{C}^\mathrm{c}_\mathrm{pa}\mathbf{x}_\mathrm{pa} + \mathbf{D}^\mathrm{c}_\mathrm{pa}u_\mathrm{pa} \tag{4.5}$$

where

$$\mathbf{A}^\mathrm{c}_\mathrm{pa} = \begin{bmatrix} -\frac{c_\mathrm{f}+c_\mathrm{r}}{mv} & \frac{c_\mathrm{r}l_\mathrm{r}-c_\mathrm{f}l_\mathrm{f}}{mv^2} - 1 \\ \frac{c_\mathrm{r}l_\mathrm{r}-c_\mathrm{f}l_\mathrm{f}}{J_\mathrm{z}} & -\frac{c_\mathrm{f}{l_\mathrm{f}}^2+c_\mathrm{r}{l_\mathrm{r}}^2}{J_\mathrm{z}v} \end{bmatrix}, \quad \mathbf{B}^\mathrm{c}_\mathrm{pa} = \begin{bmatrix} \frac{c_\mathrm{f}i_\mathrm{s}}{mv} \\ \frac{c_\mathrm{f}l_\mathrm{f}i_\mathrm{s}}{J_\mathrm{z}} \end{bmatrix}, \quad \mathbf{x}^\mathrm{T}_\mathrm{pa} = [\beta \quad \dot{\psi}],$$

$$\mathbf{C}_{\mathrm{pa}}^{\mathrm{c}} = \left[-\frac{c_\mathrm{f}+c_\mathrm{r}}{m} \quad \frac{c_\mathrm{r}l_\mathrm{r}-c_\mathrm{f}l_\mathrm{f}}{mv}\right],\ \mathbf{D}_{\mathrm{pa}}^{\mathrm{c}} = \left[\frac{c_\mathrm{f}i_\mathrm{s}}{m}\right],\ u_\mathrm{pa} = \varphi_\mathrm{FA},\ y_\mathrm{pa} = v\dot{\theta}.$$

4.3.2 Inverse Linearity Control (IL Control)

The Inverse Linearity Control pursues a dynamic inversion of the linearized single-track model with output $v\dot{\theta}$. As the partial plant dynamics (4.4) and (4.5) to be inverted represent a minimum phase SISO system whose corresponding transfer function possesses two poles and two zeros, an analytic inversion is directly possible. The inverse is hereby stable for all vehicle speeds, and no realizing filter is required. For avoiding a singularity at 0 km/h a lower vehicle speed limit is introduced.

The analytic inversion of the linearized partial plant dynamics is obtained by [Buc+08]

$$\mathbf{D}_{\mathrm{pa}}^{\mathrm{c}\,*} = \mathbf{D}_{\mathrm{pa}}^{\mathrm{c}\,-1} \tag{4.6}$$

$$\mathbf{C}_{\mathrm{pa}}^{\mathrm{c}\,*} = -\mathbf{D}_{\mathrm{pa}}^{\mathrm{c}\,-1}\mathbf{C}_{\mathrm{pa}}^{\mathrm{c}} = -\mathbf{D}_{\mathrm{pa}}^{\mathrm{c}\,*}\mathbf{C}_{\mathrm{pa}}^{\mathrm{c}} \tag{4.7}$$

$$\mathbf{B}_{\mathrm{pa}}^{\mathrm{c}\,*} = \mathbf{B}_{\mathrm{pa}}^{\mathrm{c}}\mathbf{D}_{\mathrm{pa}}^{\mathrm{c}\,-1} = \mathbf{B}_{\mathrm{pa}}^{\mathrm{c}}\mathbf{D}_{\mathrm{pa}}^{\mathrm{c}\,*} \tag{4.8}$$

$$\mathbf{A}_{\mathrm{pa}}^{\mathrm{c}\,*} = \mathbf{A}_{\mathrm{pa}}^{\mathrm{c}} - \mathbf{B}_{\mathrm{pa}}^{\mathrm{c}}\mathbf{D}_{\mathrm{pa}}^{\mathrm{c}\,-1}\mathbf{C}_{\mathrm{pa}}^{\mathrm{c}} = \mathbf{A}_{\mathrm{pa}}^{\mathrm{c}} - \mathbf{B}_{\mathrm{pa}}^{\mathrm{c}\,*}\mathbf{C}_{\mathrm{pa}}^{\mathrm{c}} \tag{4.9}$$

which gives

$$\begin{aligned}\dot{\mathbf{x}}_{\mathrm{pa}}^{*} &= \mathbf{A}_{\mathrm{pa}}^{\mathrm{c}\,*}\mathbf{x}_{\mathrm{pa}}^{*} + \mathbf{B}_{\mathrm{pa}}^{\mathrm{c}\,*}u_{\mathrm{pa}}^{*} \\ y_{\mathrm{pa}}^{*} &= \mathbf{C}_{\mathrm{pa}}^{\mathrm{c}\,*}\mathbf{x}_{\mathrm{pa}}^{*} + \mathbf{D}_{\mathrm{pa}}^{\mathrm{c}\,*}u_{\mathrm{pa}}^{*}\end{aligned} \tag{4.10}$$

where

$$\mathbf{A}_{\mathrm{pa}}^{\mathrm{c}\,*} = \begin{bmatrix} 0 & -1 \\ \dfrac{c_\mathrm{r}(l_\mathrm{f}+l_\mathrm{r})}{J_\mathrm{z}} & \dfrac{-c_\mathrm{r}l_\mathrm{r}l_\mathrm{f}-c_\mathrm{r}l_\mathrm{r}^2}{J_\mathrm{z}v} \end{bmatrix},\ \mathbf{B}_{\mathrm{pa}}^{\mathrm{c}\,*} = \begin{bmatrix} \dfrac{1}{v} \\ \dfrac{l_\mathrm{f}m}{J_\mathrm{z}} \end{bmatrix},\ \mathbf{C}_{\mathrm{pa}}^{\mathrm{c}\,*} = \left[\frac{c_\mathrm{f}+c_\mathrm{r}}{c_\mathrm{f}i_\mathrm{s}} \quad \frac{c_\mathrm{f}l_\mathrm{f}-c_\mathrm{r}l_\mathrm{r}}{c_\mathrm{f}i_\mathrm{s}v}\right],$$

$$\mathbf{D}_{\mathrm{pa}}^{\mathrm{c}\,*} = \left[\frac{m}{c_\mathrm{f}i_\mathrm{s}}\right],\ \mathbf{x}_{\mathrm{pa}}^{*\,\mathrm{T}} = [x_1 \quad x_2],\ u_{\mathrm{pa}}^{*} = v\dot{\theta}^{*},\ y_{\mathrm{pa}}^{*} = \varphi_\mathrm{FA}.$$

The continuous-time inverted linearized partial plant dynamics are discretized symbolically using the Tustin approximation and a sampling time of $\mathrm{T_s} = 0.001$ sec through

$$\mathbf{A}_{\mathrm{pa}}^{*} = (\mathbf{I} - \mathbf{A}_{\mathrm{pa}}^{\mathrm{c}\,*}\mathrm{T_s}/2)^{-1}(\mathbf{I} + \mathbf{A}_{\mathrm{pa}}^{\mathrm{c}\,*}\mathrm{T_s}/2) \tag{4.11}$$

$$\mathbf{B}_{\mathrm{pa}}^{*} = (\mathbf{I} - \mathbf{A}_{\mathrm{pa}}^{\mathrm{c}\,*}\mathrm{T_s}/2)^{-1}\mathbf{B}_{\mathrm{pa}}^{\mathrm{c}\,*}\mathrm{T_s} \tag{4.12}$$

$$\mathbf{C}_{\mathrm{pa}}^{*} = \mathbf{C}_{\mathrm{pa}}^{\mathrm{c}\,*}(\mathbf{I} - \mathbf{A}_{\mathrm{pa}}^{\mathrm{c}\,*}\mathrm{T_s}/2)^{-1} \tag{4.13}$$

$$\mathbf{D}_{\mathrm{pa}}^{*} = \mathbf{D}_{\mathrm{pa}}^{\mathrm{c}\,*} + \mathbf{C}_{\mathrm{pa}}^{\mathrm{c}\,*}(\mathbf{I} - \mathbf{A}_{\mathrm{pa}}^{\mathrm{c}\,*}\mathrm{T_s}/2)^{-1}\mathbf{B}_{\mathrm{pa}}^{\mathrm{c}\,*}\mathrm{T_s}/2. \tag{4.14}$$

Thereby, the possibility for an online discretization is provided as the vehicle speed is updated [Tot+10]. By using this as an adaptive prefilter at the control input of the complete plant model, the vehicle speed-dependent partial plant dynamics are eliminated. The remaining plant is hence independent of vehicle speed for the transfer path from control input to objective output. Since the IL control is only valid for the linear driving range, an advanced approach is presented in the next section.

4.3.3 Inverse Nonlinearity Control (INL Control)

The IL control presented in the last section provides an effective method for canceling the vehicle speed-dependent plant dynamics by dynamic inversion of the linearized single-track model. As the latter is solely valid for small steering positions and lateral accelerations $a_y \leq 4\ \mathrm{m/sec^2}$, its application is exclusively limited to the linear driving range. To overcome this problem, an INL control is synthesized in the following using two different approaches, which pursue a dynamic inversion of the nonlinear single-track model. The advanced approaches are valid for large steering positions and lateral accelerations $a_y > 4\ \mathrm{m/sec^2}$. Hereby, the nonlinear tire behavior is explicitly considered in the design. Therefore, a significant improvement in control performance is achievable in the nonlinear driving range.

Approach I: Virtual Control Loop and Feedback Linearization (VCL)

The analytic inversion of the nonlinear single-track model given by (4.1) to (4.3) is not possible. However, at least an approximate inversion using techniques for online inversion can be pursued. For the online inversion of the nonlinear vehicle speed-dependent plant dynamics, a virtual control loop and feedback linearization control, as shown in Figure 33, are applied. The application of feedback linearization requires a linear affine input and no direct feedthrough of the nonlinear plant [Ada22]. Both prerequisites are not fulfilled but can be achieved by extending the plant equations by a first-order lag element to a virtual plant. Thereby, the dynamics of the first-order lag are also part of the inversion, which is unproblematic as shown below. For avoiding a singularity, a lower vehicle speed limit is additionally introduced. The virtual plant is obtained as

$$\dot{\varphi}_{\mathrm{FA}} = -\omega_{\mathrm{c}}\varphi_{\mathrm{FA}} + \omega_{\mathrm{c}}\varphi_{\mathrm{FA}}^{*} \tag{4.15}$$

$$\dot{\beta} = \frac{1}{mv}\left[F_{\mathrm{f}}\cos(i_{\mathrm{s}}\varphi_{\mathrm{FA}} - \beta) + F_{\mathrm{r}}\cos(\beta)\right] - \dot{\psi} \tag{4.16}$$

$$\ddot{\psi} = \frac{1}{J_{\mathrm{z}}}\left[F_{\mathrm{f}}l_{\mathrm{f}}\cos(i_{\mathrm{s}}\varphi_{\mathrm{FA}}) - F_{\mathrm{r}}l_{\mathrm{r}}\right] \tag{4.17}$$

$$v\dot{\theta} = \frac{1}{m}\left[F_{\mathrm{f}}\cos(i_{\mathrm{s}}\varphi_{\mathrm{FA}} - \beta) + F_{\mathrm{r}}\cos(\beta)\right] \tag{4.18}$$

with F_{f}, F_{r}, α_{f}, α_{r} given by (2.50) to (2.53) and is under selection of the state vector $\mathbf{x}^{\mathrm{T}} = [\varphi_{\mathrm{FA}}\ \ \beta\ \ \dot{\psi}]$ brought into the following standard form

$$\dot{\mathbf{x}} = \mathbf{a}(\mathbf{x}) + \mathbf{b}(\mathbf{x})u \tag{4.19}$$

$$y = \mathbf{c}(\mathbf{x})$$

for which a feedback linearization controller can be designed. For feedback linearization controller synthesis, the output y must be derived with respect to time until the input $u \neq 0$ appears. Hereby, Lie-derivatives $L_{\mathrm{a}}^{0}\mathrm{c}(\mathbf{x})$, $L_{\mathrm{a}}^{1}\mathrm{c}(\mathbf{x})$ and $L_{\mathrm{b}}^{1}\mathrm{c}(\mathbf{x})$ are employed that are computed as ([Ada22], [Slo+91], [Kha14])

$$L_{\mathrm{a}}^{0}\mathrm{c}(\mathbf{x}) = y = \mathbf{c}(\mathbf{x}) \tag{4.20}$$

$$L_{\mathrm{a}}^{1}\mathrm{c}(\mathbf{x}) = \frac{\partial L_{\mathrm{a}}^{0}\mathrm{c}(\mathbf{x})}{\partial \mathbf{x}}\mathbf{a}(\mathbf{x}) \tag{4.21}$$

$$L_{\mathrm{b}}^{1}\mathrm{c}(\mathbf{x}) = \frac{\partial L_{\mathrm{a}}^{0}\mathrm{c}(\mathbf{x})}{\partial \mathbf{x}}\mathbf{b}(\mathbf{x}) \neq 0\,. \tag{4.22}$$

From (4.22) it can be shown that the input u appears after the first derivative, thus implying a difference order of $\delta = 1$. Consequently, a first-order command response with arbitrary bandwidth can be enforced to the virtual control loop. Moreover, as the difference order is smaller than the system order ($\delta < n$) internal dynamics occur for which stability analysis is required [Ada22]. The original system states $\mathbf{x}$ are now transformed into the new system states $\mathbf{z}$ using the diffeomorphism [Sch+17]

$$\mathbf{z} = \mathrm{T}(\mathbf{x}) = \begin{bmatrix} z_1 \\ z_2 \\ z_3 \end{bmatrix} = \begin{bmatrix} L_\mathrm{a}^0 \mathrm{c}(\mathbf{x}) \\ T_2(\mathbf{x}) \\ T_3(\mathbf{x}) \end{bmatrix} \tag{4.23}$$

where $T_2(\mathbf{x})$ and $T_3(\mathbf{x})$ must still be defined and can be arbitrarily selected. For simplicity these are selected as

$$T_2(\mathbf{x}) = x_2 \tag{4.24}$$

$$T_3(\mathbf{x}) = x_3 \tag{4.25}$$

such that

$$L_\mathrm{b} T_2(\mathbf{x}) = \frac{\partial T_2(\mathbf{x})}{\partial \mathbf{x}} \mathbf{b}(\mathbf{x}) = [0 \quad 1 \quad 0] \begin{bmatrix} \omega_\mathrm{c} \\ 0 \\ 0 \end{bmatrix} = 0 \tag{4.26}$$

$$L_\mathrm{b} T_3(\mathbf{x}) = \frac{\partial T_3(\mathbf{x})}{\partial \mathbf{x}} \mathbf{b}(\mathbf{x}) = [0 \quad 0 \quad 1] \begin{bmatrix} \omega_\mathrm{c} \\ 0 \\ 0 \end{bmatrix} = 0 \tag{4.27}$$

and thus, the dependency of the internal dynamics on the input u becomes obsolete. The diffeomorphism herewith takes the form

$$\mathbf{z} = \mathrm{T}(\mathbf{x}) = \begin{bmatrix} z_1 \\ z_2 \\ z_3 \end{bmatrix} = \begin{bmatrix} L_\mathrm{a}^0 \mathrm{c}(\mathbf{x}) \\ x_2 \\ x_3 \end{bmatrix}. \tag{4.28}$$

Hereby it must be considered that $\mathrm{T}(\mathbf{x})$ is continuously differentiable and that the inverse transformation $\mathbf{x} = \mathrm{T}^{-1}(\mathbf{z})$ exists. The latter is ensured if the Jacobian matrix $\partial \mathrm{T}(\mathbf{x}) / \partial \mathbf{x}$ is regular, which is the case if [Ada22]

$$\det\left(\frac{\partial \mathrm{T}}{\partial \mathbf{x}}\right) \neq 0. \tag{4.29}$$

For the selected diffeomorphism the Jacobian matrix is for $v \neq 0$ always regular. The transformation of the original system (4.19) results in the following system representation in nonlinear control canonical form [Isi95]

$$\begin{bmatrix} \dot{z}_1 \\ \dot{z}_2 \\ \dot{z}_3 \end{bmatrix} = \begin{bmatrix} L_\mathrm{a}^1 \mathrm{c}(\mathbf{x}) \\ \dot{T}_2(\mathbf{x}) \\ \dot{T}_3(\mathbf{x}) \end{bmatrix} + \begin{bmatrix} L_\mathrm{b}^1 \mathrm{c}(\mathbf{x}) \\ 0 \\ 0 \end{bmatrix} u \quad \begin{matrix} \} \text{ External Dynamics} \\ \} \text{ Internal Dynamics} \end{matrix} \tag{4.30}$$

$$y = z_1$$

with

$$\dot{T}_2(\mathbf{x}) = \frac{\partial T_2(\mathbf{x})}{\partial \mathbf{x}} \mathbf{a}(\mathbf{x}) \tag{4.31}$$

$$\dot{T}_3(\mathbf{x}) = \frac{\partial T_3(\mathbf{x})}{\partial \mathbf{x}} \mathbf{a}(\mathbf{x}). \tag{4.32}$$

For the purpose of compensating the nonlinearity in the first row of the transformed system (4.30) and controlling the remaining integrator system by state-feedback control with static reference feedforward, the following control law is defined [Ada22]

$$u = -\frac{L_\mathrm{a}^1 \mathrm{c}(\mathbf{x}) + \mathbf{K}_\mathrm{p}\mathbf{z}}{L_\mathrm{b}^1 \mathrm{c}(\mathbf{x})} + \frac{K_\mathrm{r} r}{L_\mathrm{b}^1 \mathrm{c}(\mathbf{x})} \tag{4.33}$$

where

$$\mathbf{K}_\mathrm{p} = [a_0 \quad 0 \quad 0], \;\; K_\mathrm{r} = a_0.$$

Consequently, the dynamics of the virtual control loop for the transfer path from r to y are given by a first-order lag with cut-off frequency a_0[3]

$$G_{\mathrm{cl},yr}(s) = \frac{a_0}{s + a_0}. \tag{4.34}$$

The cut-off frequency a_0 is under consideration of digital implementation constraints as given by the sampling time selected as high as possible. Hence, the transfer path of the virtual control loop from r to φ_FA gives the desired inversion of the nonlinear vehicle speed-dependent plant dynamics plus the dynamics of the command response corresponding to (4.34). Thus, the online inversion obtains an approximate dynamic inverse:

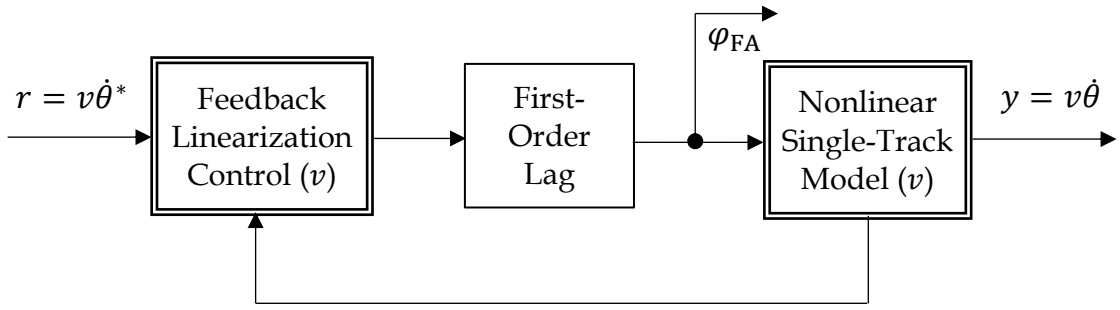

Figure 33: Inverse Nonlinearity Control (INL Control) – Virtual Control Loop

As the difference order is smaller than the system order ($\delta < n$), internal dynamics occur for which stability analysis is required. Since no analytic transformation rule for the state x_1 can be found this is not trivial. A simple solution is given by introducing small angle assumptions, which linearizes the plant equations and simplifies the diffeomorphism. In this case, the internal dynamics can be analytically derived and expressed as a function of the transformed states. For analyzing its stability, the case $z_1 = 0$ is considered to obtain the differential equations of the zero dynamics, which yields [Sva06]

$$\begin{bmatrix} \dot{z}_2 \\ \dot{z}_3 \end{bmatrix} = \begin{bmatrix} 0 & -1 \\ c_\mathrm{r}(l_\mathrm{f} + l_\mathrm{r})/J_\mathrm{z} & -c_\mathrm{r} l_\mathrm{r}(l_\mathrm{f} + l_\mathrm{r})/(J_\mathrm{z} v) \end{bmatrix} \begin{bmatrix} z_2 \\ z_3 \end{bmatrix}. \tag{4.35}$$

[3] For reasons of readability, the complex Laplace variable s is omitted in the further course of this work.

Thereby, the eigenvalues of the zero dynamics (4.35) reflect the zeros of the linear dynamic single-track model. The latter are for all vehicle speeds located in the left half of the *s*-plane. Hence, stability in the linear operating range is guaranteed. The nonlinear operating range was extensively tested by simulation analysis. Thereby, no instabilities were found that are not associated with nonlinear tire saturation. As the trajectory planner considers vehicle physics, such saturation phenomena can be safely excluded (refer to [Wer+12]).
The virtual control loop is discretized for a sampling time of $T_s = 0.001$ sec. By using the INL control as a nonlinear adaptive prefilter at the control input of the complete plant, the nonlinear vehicle speed-dependent partial plant dynamics are effectively compensated. Hence, the remaining plant is independent of vehicle speed in the transfer path from control input to objective output.

Approach II: Inverse Disturbance Observer (IDOB)

As mentioned in the previous section, an analytic inversion of the nonlinear single-track model given by (4.1) to (4.3) is not possible. However, at least an approximate inversion using the concept of a virtual control loop and feedback linearization for online inversion can be conducted. An alternative approach is given by the concept of the Inverse Disturbance Observer (IDOB), which is illustrated in Figure 34 and synthesized in the following ([Bün+05], [Baj+05a], [Baj+05b]). Similarly to the former approach, the IDOB performs an online inversion of the nonlinear single-track model that is denoted as G in the sequel. For this purpose, feedforward control including an inverted nominal model of the plant and high gain feedback control are combined into an integrated structure while preserving the advantages of each. In the IDOB structure, G_n^{-1} is the approximate inverse of the nonlinear plant model G and serves as a feedforward control. The expression $G_n^{-1}r$ thus provides the main portion of the output u. The feedback loop computes the deviation between the nominal plant model G_n and the nonlinear plant model G and feeds back the error signal over the Q-Filter to the input. The latter is selected as a lowpass filter with unity gain. Thereby, the approximate inversion of the

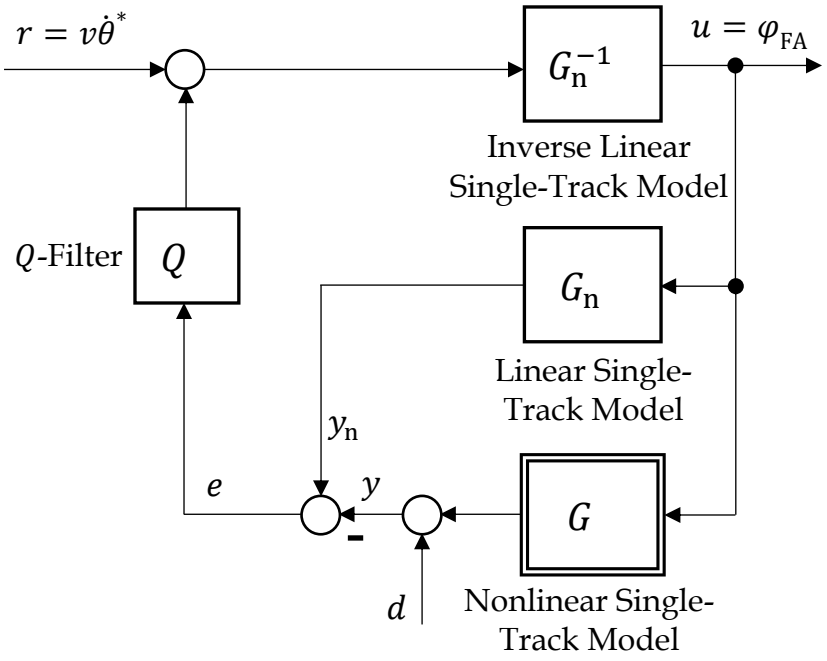

Figure 34: Inverse Nonlinearity Control (INL Control) – IDOB Basic Approach

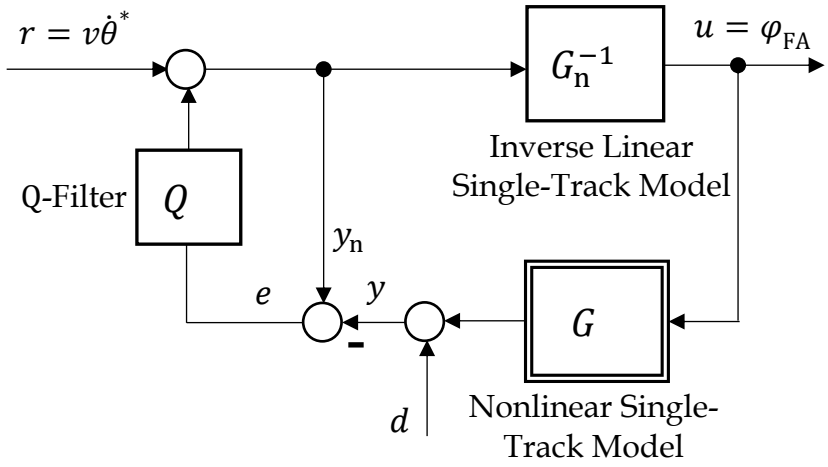

Figure 35: Inverse Nonlinearity Control (INL Control) – IDOB Implementation Structure

feedforward path is forced to converge to the exact inversion. By application of block diagram algebra, the IDOB structure is further simplified, which gives the final structure for implementation as depicted in Figure 35.

For its synthesis, the nonlinear single-track model G given by (2.50) to (2.53) and (4.1) to (4.3), the inverted linearized single-track model G_n^{-1} given by (4.10), and a first-order lowpass filter Q with unity gain are used. To avoid a singularity a lower vehicle speed limit is once more introduced. The objective of the IDOB is to match the closed loop dynamics to G^{-1}. The IDOB structure thereby serves as an approximate model inversion approach, which is directly evident when considering the transfer behavior from the input r to the output u [Baj+05b]

$$\frac{u}{r} = \frac{1}{G_n(1-Q) + GQ}. \tag{4.36}$$

The frequency range from zero to the cut-off frequency of the Q-Filter is defined as the operating range of the IDOB. Thus, in the IDOB operating range $Q \to 1$ and hence $u \to G^{-1}r$, which provides the inverse of the nonlinear single-track model. Outside the operating range $Q \to 0$ and consequently $u \to G_\mathrm{n}^{-1}r$, which is at least the inverse linearized single-track model. For practical application Q is selected as a compromise between performance and stability. For the exact model inversion, one of the following two conditions must hold

$$Q \to 1 \ \text{ or } \ G_n \to G. \tag{4.37}$$

The IDOB combines the properties of both conditions that is high gain feedback control (feedback loop with $Q \to 1$) and inversion by feedforward control ($G_n \to G$) in a single structure. In the linear driving range, the feedback error e is zero and an exact inversion is instantly obtained. In the nonlinear driving range, feedforward control provides the main portion of the inversion, and a corrective term is supplied by feedback. Based on this approach, an approximate inversion of the nonlinear single-track model G is obtained without analytically inverting the model.

From Figure 35 the sensitivity function S of the IDOB structure is further derived, which provides the basis for stability analysis [Baj+05b]

$$S = \frac{y}{d} = \frac{1 - Q}{1 - Q(1 - G_n^{-1}G)}. \tag{4.38}$$

By linearization of G for selected operating points, a family of sensitivity functions can be derived. With this regard, the poles of the sensitivity functions, which are obtained as the roots of the denominator polynomial of S, must be located in the left half s-plane. For all the tested operating points this was successfully confirmed.

For the digital implementation, the discrete IL control from section 4.3.2 is used for G_{n}^{-1}. Furthermore, the nonlinear single-track model G given by (2.50) to (2.53) and (4.1) to (4.3) as well as the Q-Filter are discretized using feedforward Euler approximations for a sampling time of $\mathrm{T_s} = 0.001$ sec.

4.3.4 Performance Evaluation

For a performance evaluation of the synthesized dynamic inversion approaches, the simulation environment illustrated in Figure 36 is employed. Hereby, a signal generator, the IL/INL control, and the nonlinear single-track model are arranged in series connection. The signal generator produces a step-shaped synthetic excitation signal for the input r, which is reconstructed at the output y. For an exact inversion, the condition $r = y$ must be satisfied.

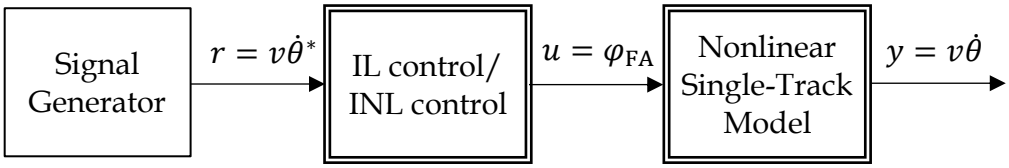

Figure 36: Simulation Environment for IL and INL Control Performance Evaluation

In Figure 37 and 38 reference step inputs of $r = 1$ and $r = 6$ are considered respectively, to evaluate the performance of the dynamic inversion approaches in the linear and nonlinear driving range. With this regard, results for the output y and the generated input u are illustrated for the inverse linearity control (IL), virtual control loop based inverse nonlinearity control (INL VCL), and inverse disturbance observer-based inverse nonlinearity control (INL IDOB). Thereby, a vehicle speed of 70 km/h is exemplarily selected.

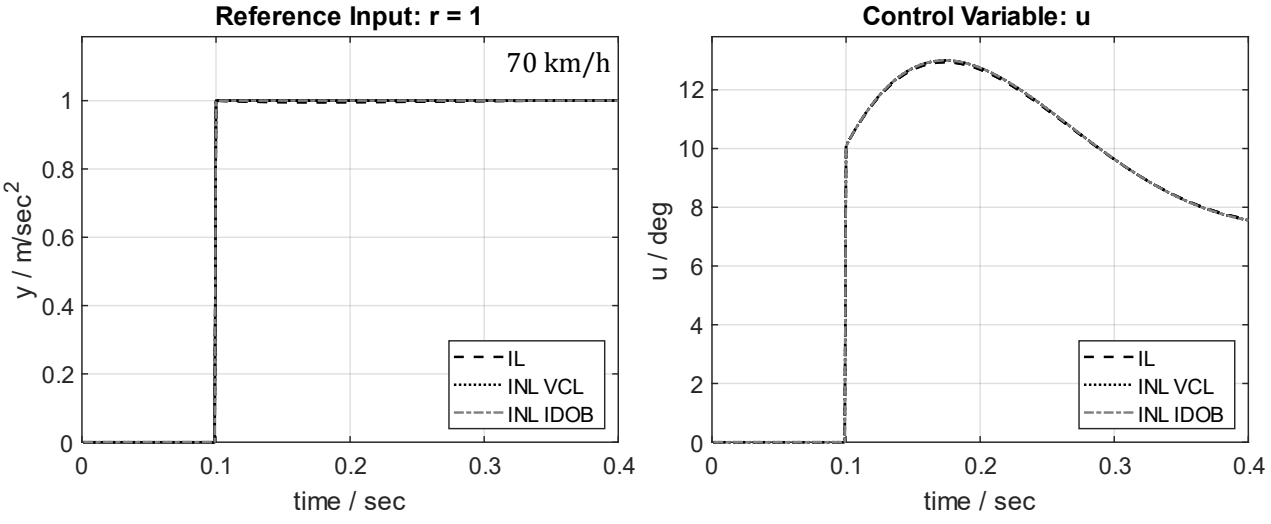

Figure 37: Performance Evaluation - Linear Driving Range

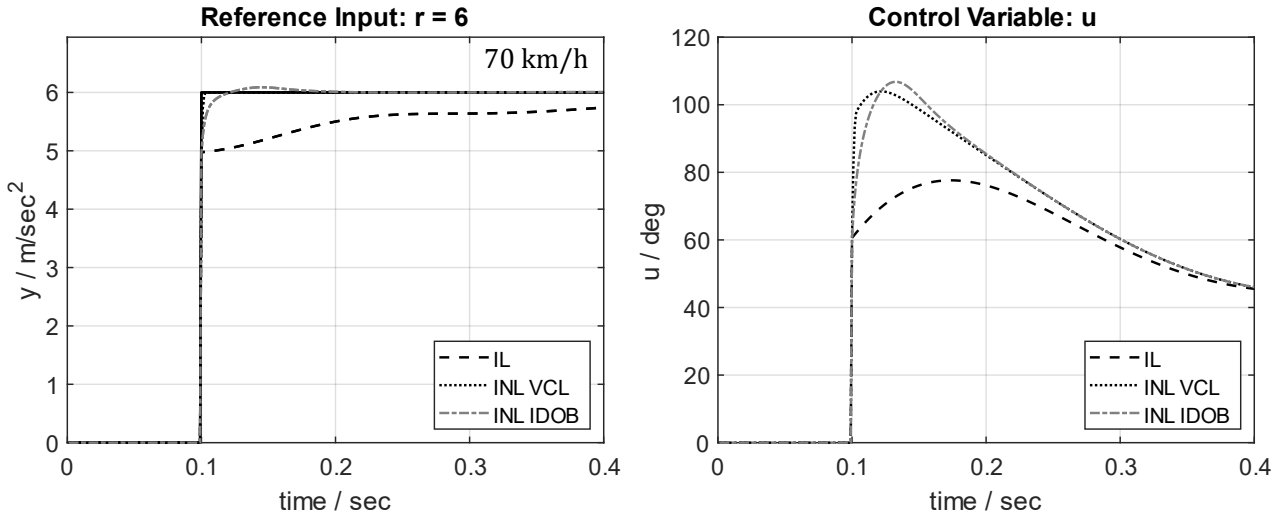

Figure 38: Performance Evaluation - Nonlinear Driving Range

Figure 37 depicts the performance results in the linear driving range for a reference step in lateral acceleration of 1 $\mathrm{m/sec^2}$. The IL, INL VCL, and INL IDOB approach are almost identical and achieve an exact inversion of the vehicle speed-dependent plant dynamics. In Figure 38 the performance results in the nonlinear driving range are shown for a reference step of 6 $\mathrm{m/sec^2}$. With this regard, the IL control reveals significant deviations, which are due to the assumption of linear tire behavior and small angle approximations that are not valid. Thereby, it shows a rise time of 0.08 sec, a settling time of 0.274 sec (5 % error band), and zero overshoot. In contrast, the INL controls expose an accurate inversion. The INL IDOB approach achieves a rise time of 0.002 sec, a settling time of 0.005 sec, and a 1.5 % overshoot. This excellent inversion of the nonlinear lateral vehicle dynamics is outperformed by the INL VCL approach. The latter reveals a rise time of 0.001 sec, a settling time of 0.001 sec, and no overshoot. The generated control input u of both approaches is thereby well within the actuator saturation bounds, which are given by a maximum steering position of 520 deg. Hence, the physical realizability of the required control actions is guaranteed.
In the next section the remaining plant model that is obtained from the interconnection of INL VCL control and the complete plant model is presented. The remaining plant model provides the basis for lateral vehicle guidance controller synthesis.

4.3.5 Remaining Plant Model

For eliminating the nonlinear vehicle speed-dependent plant dynamics, the INL VCL control is connected to the plant control input as illustrated in Figure 39. The new control input, which is provided as the output of a lateral vehicle guidance controller for automated driving, is denoted as $\varphi_{\mathrm{AD}}^{*}$ in the sequel. In addition, the driver steering input for manual driving is introduced. The latter is moved to the INL control input using block diagram algebra and denoted as $\varphi_{\mathrm{MD}}^{*}$ in the following. Under the assumption of an exact compensation, the grey model parts cancel, and the remaining plant model, as depicted in Figure 40, is obtained.

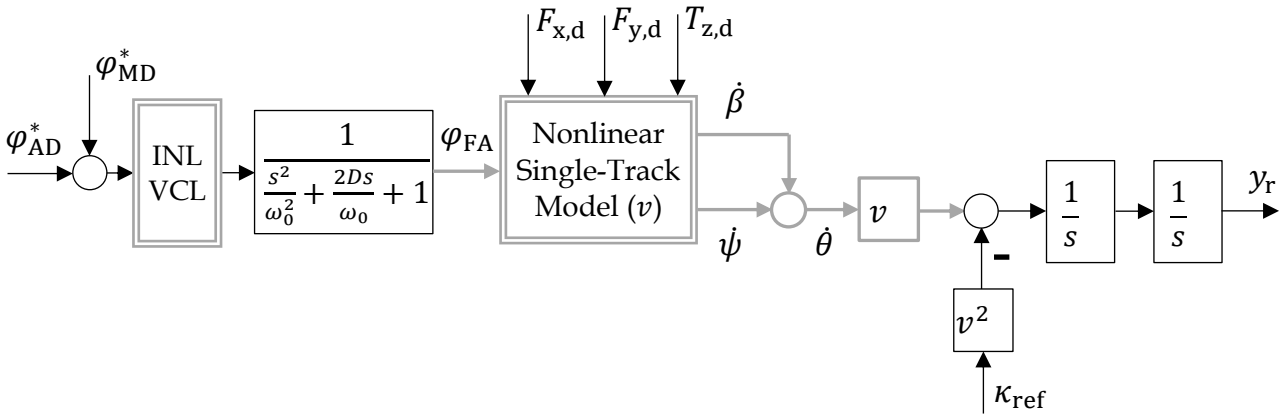

Figure 39: Combining INL Control and Nonlinear Plant for Lateral Vehicle Guidance

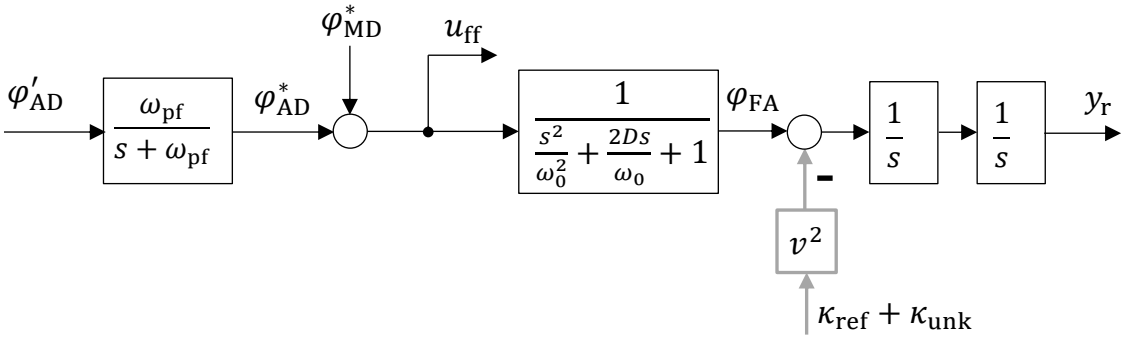

Figure 40: Remaining Plant Model for Lateral Vehicle Guidance

Thereby, a prefilter with cut-off frequency ω_{pf} was added to the control input of the remaining plant model to cope with differences in sampling time between lateral vehicle guidance control and FAA steering position control (refer to section 4.2). This results in a smoothing of the control actions of the former and prevents unnecessary stress on the mechanical actuator components. Moreover, the unknown disturbance inputs $F_{x,d}$, $F_{y,d}$ and $T_{z,d}$ are replaced by a lumped unknown disturbance input κ_{unk}. To avoid a vehicle speed-dependency of the reference path curvature and unknown disturbance input, virtual disturbances $d_{ref} = v^2\kappa_{ref}$ and $d_{unk} = v^2\kappa_{unk}$ are further introduced. By this proceeding, the vehicle speed-dependency is moved outside the remaining plant model and treated as a nonlinear input (see Figure 41).

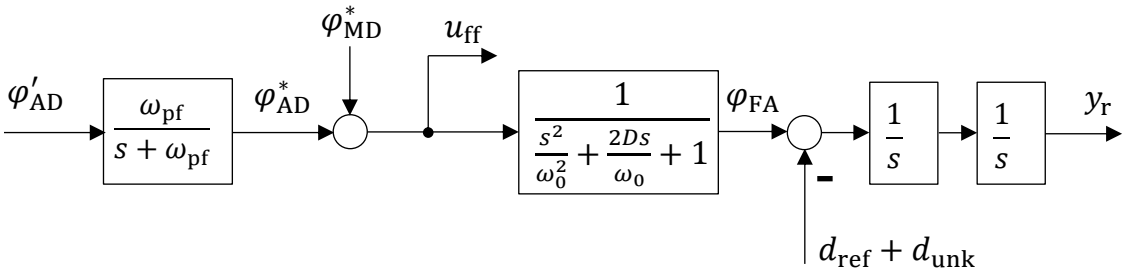

Figure 41: Remaining Plant Model for Lateral Vehicle Guidance with Virtual Disturbance

Thus, the remaining plant model becomes linear and fully independent of vehicle speed. Consequently, it is represented by an LTI system for which one controller can be synthesized that is valid over the complete operating range.

The derived model provides the basis for MPC, extended optimal state-estimator, and cooperative dynamic feedforward control synthesis that are presented in the upcoming sections. For this purpose, a state-space representation of the remaining plant model is employed, which is obtained as

$$\dot{\mathbf{x}}_{\mathrm{re}} = \mathbf{A}_{\mathrm{re}}^{\mathrm{c}}\mathbf{x}_{\mathrm{re}} + \mathbf{B}_{\mathrm{re}}^{\mathrm{c}}\mathbf{u}_{\mathrm{re}} \tag{4.39}$$

$$\mathbf{y}_{\mathrm{mpc}} = \mathbf{C}_{\mathrm{mpc}}^{\mathrm{c}}\mathbf{x}_{\mathrm{re}} \tag{4.40}$$

$$y_{\mathrm{est}} = \mathbf{C}_{\mathrm{est}}^{\mathrm{c}}\mathbf{x}_{\mathrm{re}} \tag{4.41}$$

$$\mathbf{y}_{\mathrm{coop}} = \mathbf{C}_{\mathrm{coop}}^{\mathrm{c}}\mathbf{x}_{\mathrm{re}} + \mathbf{D}_{\mathrm{coop}}^{\mathrm{c}}\mathbf{u}_{\mathrm{re}} \tag{4.42}$$

with

$$\mathbf{A}_{\mathrm{re}}^{\mathrm{c}} = \begin{bmatrix} 0 & 0 & 1 & 0 & 0 \\ 1 & 0 & 0 & 0 & 0 \\ 0 & 0 & 0 & 1 & 0 \\ 0 & 0 & -\omega_{\mathrm{o}}^2 & -2D\omega_{\mathrm{o}} & \omega_{\mathrm{o}}^2 \\ 0 & 0 & 0 & 0 & -\omega_{\mathrm{pf}} \end{bmatrix}, \mathbf{x}_{\mathrm{re}} = \begin{bmatrix} \dot{y}_{\mathrm{r}} \\ y_{\mathrm{r}} \\ \varphi_{\mathrm{FA}} \\ \Omega_{\mathrm{FA}} \\ x_{\mathrm{pf}} \end{bmatrix}, \mathbf{B}_{\mathrm{re}}^{\mathrm{c}} = \begin{bmatrix} 0 & 0 & -1 & -1 \\ 0 & 0 & 0 & 0 \\ 0 & 0 & 0 & 0 \\ 0 & \omega_{\mathrm{o}}^2 & 0 & 0 \\ \omega_{\mathrm{pf}} & 0 & 0 & 0 \end{bmatrix}, \mathbf{u}_{\mathrm{re}} = \begin{bmatrix} \varphi'_{\mathrm{AD}} \\ \varphi^{*}_{\mathrm{MD}} \\ d_{\mathrm{ref}} \\ d_{\mathrm{unk}} \end{bmatrix},$$

$$\mathbf{y}_{\mathrm{mpc}} = \begin{bmatrix} y_{\mathrm{r}} \\ \dot{y}_{\mathrm{r}} \end{bmatrix}, \ \mathbf{C}_{\mathrm{mpc}}^{\mathrm{c}} = \begin{bmatrix} 0 & 1 & 0 & 0 & 0 \\ 1 & 0 & 0 & 0 & 0 \end{bmatrix},$$

$$y_{\mathrm{est}} = y_{\mathrm{r}}, \ \mathbf{C}_{\mathrm{est}}^{\mathrm{c}} = [0 \quad 1 \quad 0 \quad 0 \quad 0],$$

$$\mathbf{y}_{\mathrm{coop}} = \begin{bmatrix} u_{\mathrm{ff}} \\ \dot{y}_{\mathrm{r}} \\ y_{\mathrm{r}} \\ \varphi_{\mathrm{FA}} \\ \Omega_{\mathrm{FA}} \\ x_{\mathrm{pf}} \end{bmatrix}, \ \mathbf{C}_{\mathrm{coop}}^{\mathrm{c}} = \begin{bmatrix} 0 & 0 & 0 & 0 & 1 \\ 1 & 0 & 0 & 0 & 0 \\ 0 & 1 & 0 & 0 & 0 \\ 0 & 0 & 1 & 0 & 0 \\ 0 & 0 & 0 & 1 & 0 \\ 0 & 0 & 0 & 0 & 1 \end{bmatrix}, \ \mathbf{D}_{\mathrm{coop}}^{\mathrm{c}} = \begin{bmatrix} 0 & 1 & 0 & 0 \\ 0 & 0 & 0 & 0 \\ 0 & 0 & 0 & 0 \\ 0 & 0 & 0 & 0 \\ 0 & 0 & 0 & 0 \\ 0 & 0 & 0 & 0 \end{bmatrix}.$$

The continuous-time remaining plant model is transformed to discrete time using a step invariant discretization and a sampling time of $\mathrm{T_s} = 0.05$ sec corresponding to the measurement update [Fra+98]

$$\mathbf{x}_{\mathrm{re}}(k+1) = \mathbf{A}_{\mathrm{re}}\mathbf{x}_{\mathrm{re}}(k) + \mathbf{B}_{\mathrm{re}}\mathbf{u}_{\mathrm{re}}(k) \tag{4.43}$$

$$\mathbf{y}_{\mathrm{mpc}}(k) = \mathbf{C}_{\mathrm{mpc}}\mathbf{x}_{\mathrm{re}}(k) \tag{4.44}$$

$$y_{\mathrm{est}}(k) = \mathbf{C}_{\mathrm{est}}\mathbf{x}_{\mathrm{re}}(k) \tag{4.45}$$

$$\mathbf{y}_{\mathrm{coop}}(k) = \mathbf{C}_{\mathrm{coop}}\mathbf{x}_{\mathrm{re}}(k) + \mathbf{D}_{\mathrm{coop}}\mathbf{u}_{\mathrm{re}}(k) \tag{4.46}$$

with

$$\mathbf{A}_{\mathrm{re}} = \mathrm{e}^{\mathbf{A}_{\mathrm{re}}^{\mathrm{c}}\mathrm{T_s}}, \quad \mathbf{B}_{\mathrm{re}} = \left(\int_0^{\mathrm{T_s}} \mathrm{e}^{\mathbf{A}_{\mathrm{re}}^{\mathrm{c}}\eta}\,\mathrm{d}\eta\right)\mathbf{B}_{\mathrm{re}}^{\mathrm{c}},$$

$$\mathbf{C}_{\mathrm{mpc}} = \mathbf{C}_{\mathrm{mpc}}^{\mathrm{c}},$$

$$\mathbf{C}_{\mathrm{est}} = \mathbf{C}_{\mathrm{est}}^{\mathrm{c}},$$

$$\mathbf{C}_{\mathrm{coop}} = \mathbf{C}_{\mathrm{coop}}^{\mathrm{c}}, \quad \mathbf{D}_{\mathrm{coop}} = \mathbf{D}_{\mathrm{coop}}^{\mathrm{c}}.$$

4.4 Model Predictive Controller Synthesis

This section gives a brief introduction to the functional principle of Model Predictive Control. Thereafter, the synthesis of a Model Predictive Controller for automated lateral vehicle guidance is detailed. Under the assumption of no active constraints, the MPC control law is linear, which gives rise to a linear analysis of the control system in time and frequency domain. Furthermore, nonlinear simulation analysis is conducted to verify the control performance in the presence of nonlinear plant behavior and actuator constraints.

4.4.1 Functional Principle

Model Predictive Control is a nonlinear control approach that allows considering constraints and has previewing capability. For this reason, it is excellently suited for automated lateral vehicle guidance control since the reference path is known ahead and physical limits on the steering position must be respected. The starting point is the previously derived discrete-time remaining plant model given by (4.43) and (4.44), which is used to make predictions about the future plant behavior

$$\mathbf{x}(k+1) = \mathbf{A}\mathbf{x}(k) + \mathbf{B}u(k) + \mathbf{B}_{\mathrm{pd}}\mathbf{u}_{\mathrm{pd}}(k) \tag{4.47}$$

$$\mathbf{y}(k) = \mathbf{C}\mathbf{x}(k) \tag{4.48}$$

with

$\mathbf{B} = \mathbf{B}_{\mathrm{re}(l,m)}$ where $l = 1, 2, \ldots, 5$ and $m = 1$

$\mathbf{B}_{\mathrm{pd}} = \mathbf{B}_{\mathrm{re}(l,m)}$ where $l = 1, 2, \ldots, 5$ and $m = 3, 4$

$u(k) = \mathbf{u}_{\mathrm{re}(l,m)}(k)$ where $l = 1$ and $m = 1$

$\mathbf{u}_{\mathrm{pd}}(k) = \mathbf{u}_{\mathrm{re}(l,m)}(k)$ where $l = 3, 4$ and $m = 1$

$\mathbf{A} = \mathbf{A}_{\mathrm{re}}$

$\mathbf{x}(k) = \mathbf{x}_{\mathrm{re}}(k)$

$\mathbf{C} = \mathbf{C}_{\mathrm{mpc}}$

$\mathbf{y}(k) = \mathbf{y}_{\mathrm{mpc}}(k)$.

In this context, l and m denote the row and column indices respectively of the required submatrices and vector components. By separation of the disturbance inputs $\mathbf{u}_{\mathrm{pd}}(k)$, it is ensured that $u(k)$ exclusively includes the control input whose sequence of present and future values is subject to optimization.

Based on the prediction model, an online optimization of the objective output sequence using the control input sequence is performed, such that the value of a quadratic cost function is minimized. The optimization hereby varies the future control input sequence $u(k+i)$ beginning from time step k for $i = 0 \ldots n_{\mathrm{c}} - 1$ control steps. With this regard, the value n_{c} is called the control horizon [Grü+17]. Typically, the following quadratic cost function is employed

$$J = \sum_{i=1}^{n_{\mathrm{p}}} \|\mathbf{Q}^*[\mathbf{y}(k+i) - \mathbf{y}^*(k+i)]\|^2 + r^* \sum_{i=1}^{n_{\mathrm{c}}} \|[u(k+i-1) - u(k+i-2)]\|^2 \tag{4.49}$$

where n_p is called the prediction horizon as the future plant behavior is predicted for n_p time steps ahead. In the cost function, the first term is reflecting the weighted deviation between the objective output sequence and reference sequence, whereas the second term is expressing the weighted control input change sequence. The weighting matrices $\mathbf{Q}^*$ and r^* are diagonal matrices whose elements penalize large values of the respective signals in the minimization of the cost function. Thereby, a compromise between control performance and control effort is required. The prediction is done over n_p time steps, where $n_\mathrm{c} \leq n_\mathrm{p}$ holds. This implies that the prediction horizon is always greater than or at least equal to the control horizon. To ensure that for time steps $i \geq n_\mathrm{c}$ control inputs $u(k+i)$ are available for predicting $\mathbf{y}(k+i)$, the respective control inputs are set to a constant value $u(k+n_\mathrm{c}-1)$. Figure 42 illustrates the fundamental functional principle of Model Predictive Control.

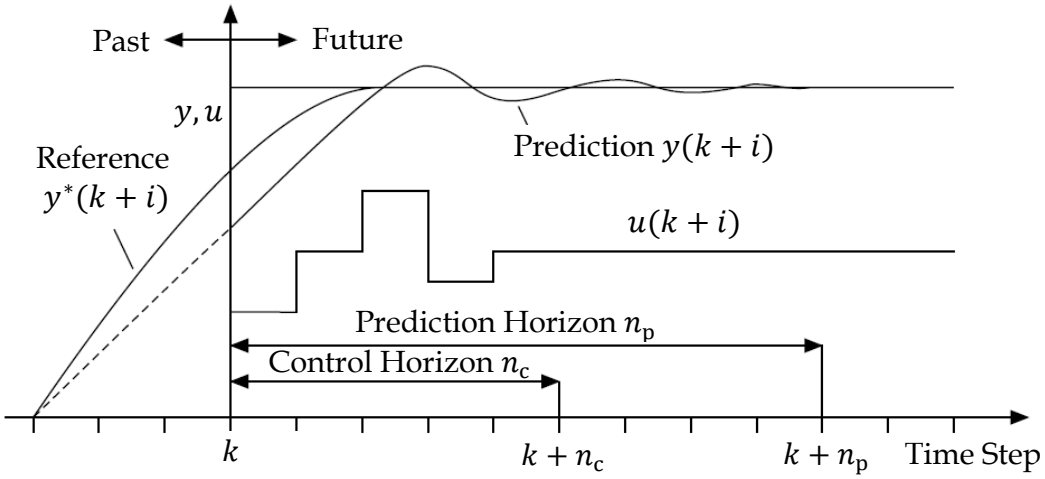

Figure 42: Functional Principle of Model Predictive Control [Ada22]

After the optimization has found the optimal control input sequence $u_\mathrm{opt}(k+i)$ with $i = 0 \ldots n_\mathrm{c}-1$, only the first value is applied to the real plant, that is $u(k) = u_\mathrm{opt}(k)$. Thereafter, one-time step is moved ahead, and the entire process is repeated. This mechanism is known as the receding horizon principle. It allows the model predictive control to react to external disturbances. For this purpose, the current plant state vector $\mathbf{x}(k)$ and disturbance inputs $\mathbf{u}_\mathrm{pd}(k)$ must be known at the beginning of the optimization to allow an exact prediction. Since the direct measurement of the plant states and unknown disturbances is often not possible, an extended optimal state-estimator is employed.

For computing the optimal control input sequence based on the quadratic cost function given by (4.49) it is distinguished between an optimization problem without constraints and with constraints. In the following, the solution to the unconstrained optimization problem is first detailed. It will be shown that the results obtained can be directly used for the constrained optimization problem.

4.4.2 Model Predictive Control without Constraints

To determine the optimal control input sequence that minimizes the quadratic cost function (4.49), the objective output sequence in the cost function must be expressed as a function of the optimization variable. For this purpose, the control input $u(k)$ in the remaining plant model given by (4.47) and (4.48) is first substituted by

$$u(k) = u(k-1) + \Delta u(k) \tag{4.50}$$

which yields

$$\mathbf{x}(k+1) = \mathbf{A}\mathbf{x}(k) + \mathbf{B}u(k-1) + \mathbf{B}\Delta u(k) + \mathbf{B}_{\mathrm{pd}}\mathbf{u}_{\mathrm{pd}}(k) \tag{4.51}$$

$$\mathbf{y}(k) = \mathbf{C}\mathbf{x}(k). \tag{4.52}$$

Subsequently, all output vectors $\mathbf{y}(k+i)$ for $i = 1 \ldots n_{\mathrm{p}}$, that is over the entire prediction horizon, are considered.
For $i \leq n_{\mathrm{c}}$ and employing (4.50) to (4.52) this gives ([Ada22], [Mac00])

$$\mathbf{y}(k+1) = \mathbf{C}\mathbf{x}(k+1) = \mathbf{C}\mathbf{A}\mathbf{x}(k) + \mathbf{C}\mathbf{B}u(k-1) + \mathbf{C}\mathbf{B}\Delta u(k) + \mathbf{C}\mathbf{B}_{\mathrm{pd}}\mathbf{u}_{\mathrm{pd}}(k) \tag{4.53}$$

$$\begin{aligned}\mathbf{y}(k+2) = \mathbf{C}\mathbf{x}(k+2) = {} & \mathbf{C}\mathbf{A}^{\mathbf{2}}\mathbf{x}(k) + \mathbf{C}[\mathbf{A}+\mathbf{I}]\mathbf{B}u(k-1) + \mathbf{C}[\mathbf{A}+\mathbf{I}]\mathbf{B}\Delta u(k) + \\ & + \mathbf{C}\mathbf{B}\Delta u(k+1) + \mathbf{C}\mathbf{A}\mathbf{B}_{\mathrm{pd}}\mathbf{u}_{\mathrm{pd}}(k) + \mathbf{C}\mathbf{B}_{\mathrm{pd}}\mathbf{u}_{\mathrm{pd}}(k+1)\end{aligned} \tag{4.54}$$

$$\vdots$$

$$\begin{aligned}\mathbf{y}(k+i) = {} & \mathbf{C}\mathbf{A}^{i}\mathbf{x}(k) + \mathbf{C}\left(\mathbf{A}^{i-1} + \cdots + \mathbf{A} + \mathbf{I}\right)\mathbf{B}u(k-1) + \\ & + \textstyle\sum_{j=1}^{i} \mathbf{C}(\mathbf{A}^{i-j} + \cdots + \mathbf{A} + \mathbf{I})\mathbf{B}\Delta u(k+j-1) + \\ & + \textstyle\sum_{j=1}^{i} \mathbf{C}(\mathbf{A}^{i-j})\mathbf{B}_{\mathrm{pd}}\mathbf{u}_{\mathrm{pd}}(k+j-1)\end{aligned} \tag{4.55}$$

$$\vdots$$

$$\begin{aligned}\mathbf{y}(k+n_{\mathrm{c}}) = {} & \mathbf{C}\mathbf{A}^{n_{\mathrm{c}}}\mathbf{x}(k) + \mathbf{C}(\mathbf{A}^{n_{\mathrm{c}}-1} + \cdots + \mathbf{A} + \mathbf{I})\mathbf{B}u(k-1) + \\ & + \textstyle\sum_{j=1}^{n_{\mathrm{c}}} \mathbf{C}(\mathbf{A}^{n_{\mathrm{c}}-j} + \cdots + \mathbf{A} + \mathbf{I})\mathbf{B}\Delta u(k+j-1) + \\ & + \textstyle\sum_{j=1}^{n_{\mathrm{c}}} \mathbf{C}(\mathbf{A}^{n_{\mathrm{c}}-j})\mathbf{B}_{\mathrm{pd}}\mathbf{u}_{\mathrm{pd}}(k+j-1).\end{aligned} \tag{4.56}$$

The equations above describe the objective output sequence up to the time step n_{c}. Thereafter, the control input remains constant and hence $\Delta u(k+i-1) = 0$ for $i > n_{\mathrm{c}}$. Consequently, it follows that

$$\begin{aligned}\mathbf{y}(k+n_{\mathrm{c}}+1) = {} & \mathbf{C}\mathbf{A}^{n_{\mathrm{c}}+1}\mathbf{x}(k) + \mathbf{C}(\mathbf{A}^{n_{\mathrm{c}}} + \cdots + \mathbf{A} + \mathbf{I})\mathbf{B}u(k-1) + \\ & + \textstyle\sum_{j=1}^{n_{\mathrm{c}}} \mathbf{C}(\mathbf{A}^{n_{\mathrm{c}}+1-j} + \cdots + \mathbf{A} + \mathbf{I})\mathbf{B}\Delta u(k+j-1) + \\ & + \textstyle\sum_{j=1}^{n_{\mathrm{c}}+1} \mathbf{C}(\mathbf{A}^{n_{\mathrm{c}}+1-j})\mathbf{B}_{\mathrm{pd}}\mathbf{u}_{\mathrm{pd}}(k+j-1)\end{aligned} \tag{4.57}$$

$$\vdots$$

$$\begin{aligned}\mathbf{y}\left(k+n_{\mathrm{p}}\right) = {} & \mathbf{C}\mathbf{A}^{n_{\mathrm{p}}}\mathbf{x}(k) + \mathbf{C}(\mathbf{A}^{n_{\mathrm{p}}-1} + \cdots + \mathbf{A} + \mathbf{I})\mathbf{B}u(k-1) + \\ & + \textstyle\sum_{j=1}^{n_{\mathrm{c}}} \mathbf{C}\left(\mathbf{A}^{n_{\mathrm{p}}-j} + \cdots + \mathbf{A} + \mathbf{I}\right)\mathbf{B}\Delta u(k+j-1) + \\ & + \textstyle\sum_{j=1}^{n_{\mathrm{p}}} \mathbf{C}(\mathbf{A}^{n_{\mathrm{p}}-j})\mathbf{B}_{\mathrm{pd}}\mathbf{u}_{\mathrm{pd}}(k+j-1).\end{aligned} \tag{4.58}$$

The objective outputs $\mathbf{y}(k+1)$ to $\mathbf{y}\left(k+n_{\mathrm{p}}\right)$ are now combined in the $2n_{\mathrm{p}} \times 1$ - vector

$$\overline{\mathbf{y}}(k+1) = \begin{bmatrix} \mathbf{y}(k+1) \\ \mathbf{y}(k+2) \\ \vdots \\ \mathbf{y}\left(k+n_{\mathrm{p}}\right) \end{bmatrix}. \tag{4.59}$$

Similarly, the changes in control input $\Delta u(k)$ to $\Delta u(k+n_\mathrm{c}-1)$ are combined in the $n_\mathrm{c} \times 1$ - vector

$$\Delta\overline{\mathbf{u}}(k) = \begin{bmatrix} \Delta u(k) \\ \Delta u(k+1) \\ \vdots \\ \Delta u(k+n_\mathrm{c}-1) \end{bmatrix}. \tag{4.60}$$

Lastly, the measured and unmeasured disturbance inputs $\mathbf{u}_\mathrm{pd}(k)$ to $\mathbf{u}_\mathrm{pd}\big(k+n_\mathrm{p}-1\big)$ are combined in the $2n_\mathrm{p} \times 1$ - vector

$$\overline{\mathbf{u}}_\mathrm{pd}(k) = \begin{bmatrix} \mathbf{u}_\mathrm{pd}(k) \\ \mathbf{u}_\mathrm{pd}(k+1) \\ \vdots \\ \mathbf{u}_\mathrm{pd}\big(k+n_\mathrm{p}-1\big) \end{bmatrix}. \tag{4.61}$$

As the prediction model output is already the lateral deviation and lateral deviation velocity, the vector of future reference values can be set to zero in this application. Here measured disturbance previewing rather than reference previewing is required [Cam+13]. In this context, the measured disturbance $\kappa_\mathrm{ref}(k)$ is provided by a path planner for the entire prediction horizon n_p. The future measured disturbance sequence

$$\overline{\boldsymbol{\kappa}}_\mathbf{ref}(k)^\mathrm{T} = \big[\kappa_\mathrm{ref}(k) \;\; \kappa_\mathrm{ref}(k+1) \;\; \cdots \;\; \kappa_\mathrm{ref}\big(k+n_\mathrm{p}-1\big)\big] \tag{4.62}$$

is thereby estimated assuming that the vehicle follows the reference path at a constant speed and without deviations. The estimate is subsequently multiplied by v^2 to yield the virtual disturbance sequence $\overline{\mathbf{d}}_\mathrm{ref}(k)$ that is directly used for (4.61). The unknown disturbance $d_\mathrm{unk}(k)$ is reconstructed by an extended optimal state-estimator and assumed to be constant over the prediction horizon. Both parts are then assembled to the final disturbance input sequence $\overline{\mathbf{u}}_\mathrm{pd}(k)$ (refer to Figure 31).

From (4.53) to (4.58) it hence follows in compact vector-matrix notation [Mac00]

$$\overline{\mathbf{y}}(k+1) = \mathbf{F}\mathbf{x}(k) + \mathbf{G}u(k-1) + \mathbf{H}\Delta\overline{\mathbf{u}}(k) + \mathbf{E}\overline{\mathbf{u}}_\mathrm{pd}(k) \tag{4.63}$$

with

$$\mathbf{F} = \begin{bmatrix} \mathbf{CA} \\ \mathbf{CA}^2 \\ \vdots \\ \mathbf{CA}^{n_\mathrm{p}} \end{bmatrix}, \quad \mathbf{G} = \begin{bmatrix} \mathbf{CB} \\ \mathbf{C}(\mathbf{A}+\mathbf{I})\mathbf{B} \\ \vdots \\ \mathbf{C}(\mathbf{A}^{n_\mathrm{p}-1}+\cdots+\mathbf{A}+\mathbf{I})\mathbf{B} \end{bmatrix},$$

$$\mathbf{H} = \begin{bmatrix} \mathbf{CB} & 0 & \cdots & 0 \\ \mathbf{C}(\mathbf{A}+\mathbf{I})\mathbf{B} & \mathbf{CB} & \cdots & 0 \\ \mathbf{C}(\mathbf{A}^2+\mathbf{A}+\mathbf{I})\mathbf{B} & \mathbf{C}(\mathbf{A}+\mathbf{I})\mathbf{B} & \cdots & 0 \\ \vdots & \vdots & \ddots & \vdots \\ \mathbf{C}(\mathbf{A}^{n_\mathrm{c}-1}+\cdots+\mathbf{I})\mathbf{B} & \mathbf{C}(\mathbf{A}^{n_\mathrm{c}-2}+\cdots+\mathbf{I})\mathbf{B} & \cdots & \mathbf{CB} \\ \mathbf{C}(\mathbf{A}^{n_\mathrm{c}}+\cdots+\mathbf{I})\mathbf{B} & \mathbf{C}(\mathbf{A}^{n_\mathrm{c}-1}+\cdots+\mathbf{I})\mathbf{B} & \cdots & \mathbf{C}(\mathbf{A}+\mathbf{I})\mathbf{B} \\ \vdots & \vdots & \ddots & \vdots \\ \mathbf{C}(\mathbf{A}^{n_\mathrm{p}-1}+\cdots+\mathbf{I})\mathbf{B} & \mathbf{C}(\mathbf{A}^{n_\mathrm{p}-2}+\cdots+\mathbf{I})\mathbf{B} & \cdots & \mathbf{C}(\mathbf{A}^{n_\mathrm{p}-n_\mathrm{c}}+\cdots+\mathbf{I})\mathbf{B} \end{bmatrix},$$

$$\mathbf{E} = \begin{bmatrix} \mathbf{CB}_{\mathrm{pd}} & 0 & \cdots & 0 \\ \mathbf{CAB}_{\mathrm{pd}} & \mathbf{CB}_{\mathrm{pd}} & \cdots & 0 \\ \mathbf{CA}^2\mathbf{B}_{\mathrm{pd}} & \mathbf{CAB}_{\mathrm{pd}} & \cdots & 0 \\ \vdots & \vdots & \ddots & \vdots \\ \mathbf{C}(\mathbf{A}^{n_{\mathrm{p}}-1})\mathbf{B}_{\mathrm{pd}} & \mathbf{C}(\mathbf{A}^{n_{\mathrm{p}}-2})\mathbf{B}_{\mathrm{pd}} & \cdots & \mathbf{CB}_{\mathrm{pd}} \end{bmatrix}.$$

By inspection of (4.63), it is revealed that the term

$$\mathbf{g}(k) = \mathbf{F}\mathbf{x}(k) + \mathbf{G}u(k-1) + \mathbf{E}\overline{\mathbf{u}}_{\mathrm{pd}}(k) \tag{4.64}$$

is constant and given by the current state vector, past control actions, and future disturbance input sequence all of which are known. Substituting (4.64) into (4.63), the equation is more compactly written as

$$\overline{\mathbf{y}}(k+1) = \mathbf{g}(k) + \mathbf{H}\Delta\overline{\mathbf{u}}(k). \tag{4.65}$$

The summation terms in the cost function (4.49) can now be alternatively expressed by vector-matrix multiplications

$$J\big(\Delta\overline{\mathbf{u}}(k)\big) = \big[\overline{\mathbf{y}}(k+1) - \overline{\mathbf{y}}^*(k+1)\big]^{\mathrm{T}}\mathbf{Q}\big[\overline{\mathbf{y}}(k+1) - \overline{\mathbf{y}}^*(k+1)\big] + \Delta\overline{\mathbf{u}}^{\mathrm{T}}(k)\mathbf{R}\Delta\overline{\mathbf{u}}(k). \tag{4.66}$$

Hereby the weighting matrices $\mathbf{Q}$ and $\mathbf{R}$ are diagonal matrices, whose main diagonal is composed of the previous weighting matrices with the appropriate dimension. Inserting (4.65) into (4.66) gives

$$\begin{aligned} J\big(\Delta\overline{\mathbf{u}}(k)\big) = {} & \big[\mathbf{g}(k) + \mathbf{H}\Delta\overline{\mathbf{u}}(k) - \overline{\mathbf{y}}^*(k+1)\big]^{\mathrm{T}}\mathbf{Q}\big[\mathbf{g}(k) + \mathbf{H}\Delta\overline{\mathbf{u}}(k) - \overline{\mathbf{y}}^*(k+1)\big] + \\ & + \Delta\overline{\mathbf{u}}^{\mathrm{T}}(k)\mathbf{R}\Delta\overline{\mathbf{u}}(k). \end{aligned} \tag{4.67}$$

Through the introduction of the definition

$$\mathbf{e}(k) = \mathbf{g}(k) - \overline{\mathbf{y}}^*(k+1) \tag{4.68}$$

and by expanding the expression, it is obtained that

$$J\big(\Delta\overline{\mathbf{u}}(k)\big) = \Delta\overline{\mathbf{u}}^{\mathrm{T}}(k)[\mathbf{H}^{\mathrm{T}}\mathbf{Q}\mathbf{H} + \mathbf{R}]\Delta\overline{\mathbf{u}}(k) + 2\Delta\overline{\mathbf{u}}^{\mathrm{T}}(k)\mathbf{H}^{\mathrm{T}}\mathbf{Q}\mathbf{e}(k) + \mathbf{e}^{\mathrm{T}}(k)\mathbf{Q}\mathbf{e}(k). \tag{4.69}$$

For computing the minimum of the cost function J, the gradient is calculated, set to zero and solved for $\Delta\overline{\mathbf{u}}(k)$, that is

$$\frac{\partial J\big(\Delta\overline{\mathbf{u}}(k)\big)}{\partial\Delta\overline{\mathbf{u}}(k)} = 2[\mathbf{H}^{\mathrm{T}}\mathbf{Q}\mathbf{H} + \mathbf{R}]\Delta\overline{\mathbf{u}}(k) + 2\mathbf{H}^{\mathrm{T}}\mathbf{Q}\mathbf{e}(k) = \mathbf{0} \tag{4.70}$$

which results in

$$\Delta\overline{\mathbf{u}}(k) = -[\mathbf{H}^{\mathrm{T}}\mathbf{Q}\mathbf{H} + \mathbf{R}]^{-1}\mathbf{H}^{\mathrm{T}}\mathbf{Q}\mathbf{e}(k). \tag{4.71}$$

As only the first value of the optimal control input sequence is applied to the plant input, it follows that

$$\Delta u(k) = -\mathbf{K}\mathbf{e}(k) \tag{4.72}$$

with

$$\mathbf{K} = [\mathbf{I} \quad 0 \quad \cdots \quad 0][\mathbf{H}^{\mathrm{T}}\mathbf{Q}\mathbf{H} + \mathbf{R}]^{-1}\mathbf{H}^{\mathrm{T}}\mathbf{Q}.$$

Consequently, the MPC control law without constraints is fully linear and defined as

$$\begin{aligned} u(k) &= u(k-1) - \mathbf{K}\mathbf{e}(k) \\ \mathbf{e}(k) &= \mathbf{F}\mathrm{x}(k) + \mathbf{G}\mathrm{u}(k-1) + \mathbf{E}\overline{\mathbf{u}}_{\mathrm{pd}}(k) - \overline{\mathbf{y}}^{*}(k+1). \end{aligned} \tag{4.73}$$

This form gives rise to all linear analysis methods from classical controls theory and is therefore particularly useful. Figure 43 shows the inner structure of the resulting MPC without constraints.

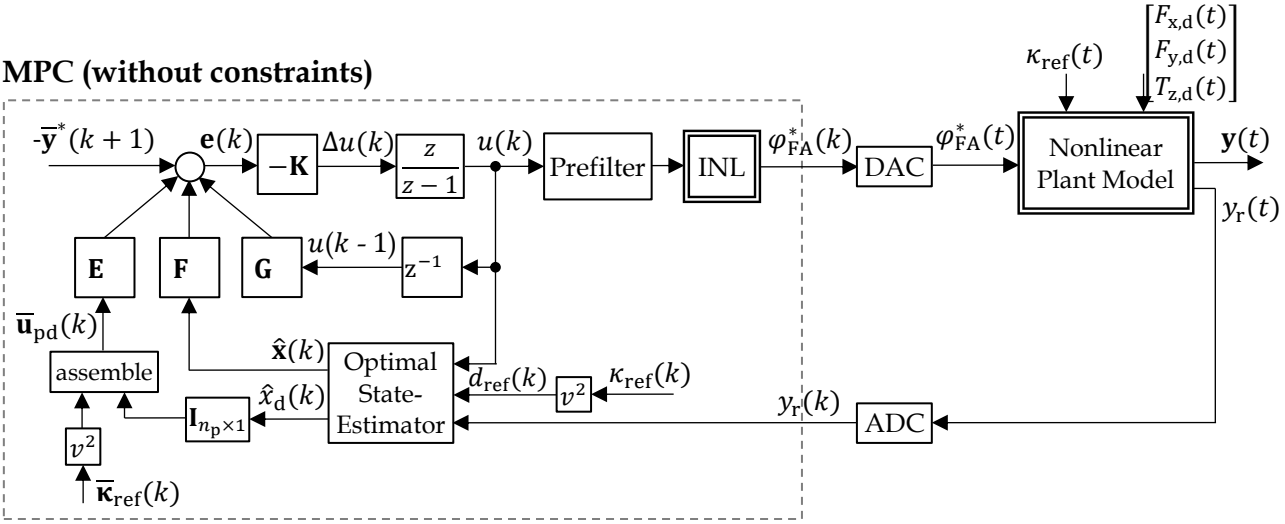

Figure 43: MPC Structure without Constraints

The selection of physically meaningful weighting matrices **Q** and **R** is achieved identically to the proceeding described in section 3.2.1. Since an online synthesis is employed, the weighting matrices can be adjusted during runtime, which significantly facilitates the tuning process in the vehicle. The prediction horizon and control horizon are selected to $n_{\mathrm{p}} = 15$ and $n_{\mathrm{c}} = 3$. This provides a compromise between adequate previewing and computational complexity for the present application (refer to [Gal21], [Erl15], [Gao+10]). For the sampling time $\mathrm{T_s} = 0.05\,\mathrm{sec}$ is chosen, which corresponds to the measurement update and thus provides the fastest response to external disturbances.

4.4.3 Model Predictive Control with Constraints

For the practical application, constraints on the control input $u(k)$ must be considered by the MPC. These are resulting from the physical limits of the steering position, which implies that

$$u_{\min} \leq u(k) \leq u_{\max}. \tag{4.74}$$

The constraints on the control input sequence are rewritten as a function of the control input changes $\Delta u(k)$, which leads to

$$\begin{aligned} u_{\min} \leq u(k) \quad &= u(k-1) + \Delta u(k) \quad &\leq u_{\max} \\ u_{\min} \leq u(k+1) \quad &= u(k-1) + \Delta u(k) + \Delta u(k+1) \quad &\leq u_{\max} \end{aligned} \tag{4.75}$$

$$
\begin{aligned}
u_{\min} \le u(k+2) &= u(k-1) + \Delta u(k) + \Delta u(k+1) + \Delta u(k+2) &\le u_{\max} \\
&\vdots \\
u_{\min} \le u(k+n_c-1) &= u(k-1) + \Delta u(k) + \cdots + \Delta u(k+n_c-1) &\le u_{\max}.
\end{aligned}
$$

The physical limits are then combined in the $n_c \times 1$ - vectors

$$\overline{\mathbf{u}}_{\min} = \begin{bmatrix} 1 \\ \vdots \\ 1 \end{bmatrix} u_{\min}, \quad \overline{\mathbf{u}}_{\max} = \begin{bmatrix} 1 \\ \vdots \\ 1 \end{bmatrix} u_{\max}. \tag{4.76}$$

This allows expressing (4.75) in compact vector-matrix notation

$$\overline{\mathbf{u}}_{\min} \le \quad \mathbf{m}u(k-1) + \mathbf{N}\Delta\overline{\mathbf{u}}(k) \quad \le \overline{\mathbf{u}}_{\max} \tag{4.77}$$

with the $n_c \times 1$ - vector $\mathbf{m}$ and the $n_c \times n_c$ - matrix $\mathbf{N}$ given by

$$\mathbf{m} = \begin{bmatrix} 1 \\ 1 \\ \vdots \\ 1 \end{bmatrix}, \quad \mathbf{N} = \begin{bmatrix} 1 & 0 & 0 & \cdots & 0 \\ 1 & 1 & 0 & \cdots & 0 \\ \vdots & \vdots & \vdots & \ddots & \vdots \\ 1 & 1 & 1 & \cdots & 1 \end{bmatrix}. \tag{4.78}$$

These inequality constraints can now be brought into the following form

$$\mathbf{W}\Delta\overline{\mathbf{u}}(k) \le \mathbf{w} \tag{4.79}$$

with

$$\mathbf{W} = \begin{bmatrix} -\mathbf{N} \\ \mathbf{N} \end{bmatrix}, \quad \mathbf{w} = \begin{bmatrix} -\overline{\mathbf{u}}_{\min} + \mathbf{m}u(k-1) \\ \overline{\mathbf{u}}_{\max} - \mathbf{m}u(k-1) \end{bmatrix}.$$

Finally, this gives the constrained optimization problem with quadratic cost function

$$
\begin{aligned}
&\min_{\Delta\overline{\mathbf{u}}(k)} J\left(\Delta\overline{\mathbf{u}}(k)\right) \\
&s.t.: \quad \mathbf{W}\Delta\overline{\mathbf{u}}(k) \le \mathbf{w}.
\end{aligned} \tag{4.80}
$$

The cost function J is given in a positive definite quadratic form, which results in a convex quadratic optimization problem with linear inequality constraints. In this case, the optimization problem has a unique minimum. The minimum can typically not be analytically found and must be determined by numerical methods. In this context, safely convergent quadratic programming methods (QP methods, Active-Set Solver) are existent, which allow an efficient determination of the solution [Ada22]. The MPC control law can in this case not be explicitly stated and is thus given as illustrated in Figure 31.

4.5 Extended Optimal State-Estimator Synthesis

The MPC uses a model to make predictions about the future plant output. The initial states $\hat{\mathbf{x}}(k)$ and unknown disturbance input $\hat{x}_d(k)$ of the prediction model are hereby provided by an extended optimal state-estimator. The latter includes an integrator

disturbance model, which gives the resulting MPC integral action. Hence, the controller becomes robust against model error, parameter uncertainty, and external disturbances. The starting point for estimator synthesis is the discrete-time remaining plant model with measurement output equation given by (4.43) and (4.45)

$$\begin{aligned} \mathbf{x}(k+1) &= \mathbf{A}\mathbf{x}(k) + \mathbf{B}\mathbf{u}(k) + \mathbf{B}_{\mathrm{pd}} u_{\mathrm{pd}}(k) \\ y(k) &= \mathbf{C}\mathbf{x}(k) \end{aligned} \tag{4.81}$$

with

$\mathbf{B} = \mathbf{B}_{\mathrm{re}(l,m)}$ where $l = 1, 2, \ldots, 5$ and $m = 1, 3$
$\mathbf{B}_{\mathrm{pd}} = \mathbf{B}_{\mathrm{re}(l,m)}$ where $l = 1, 2, \ldots, 5$ and $m = 4$
$\mathbf{u}(k) = \mathbf{u}_{\mathrm{re}(l,m)}(k)$ where $l = 1, 3$ and $m = 1$
$u_{\mathrm{pd}}(k) = \mathbf{u}_{\mathrm{re}(l,m)}(k)$ where $l = 4$ and $m = 1$
$\mathbf{A} = \mathbf{A}_{\mathrm{re}}$
$\mathbf{x}(k) = \mathbf{x}_{\mathrm{re}}(k)$
$\mathbf{C} = \mathbf{C}_{\mathrm{est}}$
$y(k) = y_{\mathrm{est}}(k)$.

With this regard, l and m denote the row and column indices of the required submatrices and vector components. The input vector $\mathbf{u}(k)$ hereby includes the control input $\varphi'_{\mathrm{AD}}(k)$ and the measured disturbance input $d_{\mathrm{ref}}(k)$. The separated input $u_{\mathrm{pd}}(k)$ reflects the unknown disturbance input $d_{\mathrm{unk}}(k)$ that is subject to disturbance estimation. As the measured disturbance $d_{\mathrm{ref}}(k)$ is considered as an input to the estimator, this part of the disturbance is already known. Consequently, the disturbance estimation is unburdened, and exclusively the remaining disturbances are reconstructed.
For disturbance estimation, the discrete-time remaining plant model is augmented by an integrator disturbance model of the following form

$$\begin{aligned} x_{\mathrm{d}}(k+1) &= \mathbf{A}_{\mathrm{d}} x_{\mathrm{d}}(k) + \mathbf{B}_{\mathrm{d}} u_{\mathrm{d}}(k) \quad \text{with} \quad \mathbf{A}_{\mathrm{d}} = 1, \mathbf{B}_{\mathrm{d}} = \mathrm{T_s}, \mathbf{C}_{\mathrm{d}} = 1 \\ y_{\mathrm{d}}(k) &= \mathbf{C}_{\mathrm{d}} x_{\mathrm{d}}(k) \end{aligned} \tag{4.82}$$

which is suitable for the reconstruction of piece-wise constant disturbances such as for example side wind or road camber ([Fra+98], [Hen97], [Irm+20], [Coe+00]). Using the substitution $u_{\mathrm{pd}}(k) = y_{\mathrm{d}}(k)$, the remaining plant model (4.81) and disturbance model (4.82) are combined to an augmented plant model, that is

$$\begin{aligned} \begin{bmatrix} \mathbf{x}(k+1) \\ x_{\mathrm{d}}(k+1) \end{bmatrix} &= \begin{bmatrix} \mathbf{A} & \mathbf{B}_{\mathrm{pd}}\mathbf{C}_{\mathrm{d}} \\ \mathbf{0} & \mathbf{A}_{\mathrm{d}} \end{bmatrix} \begin{bmatrix} \mathbf{x}(k) \\ x_{\mathrm{d}}(k) \end{bmatrix} + \begin{bmatrix} \mathbf{B} & \mathbf{0} \\ \mathbf{0} & \mathbf{B}_{\mathrm{d}} \end{bmatrix} \begin{bmatrix} \mathbf{u}(k) \\ u_{\mathrm{d}}(k) \end{bmatrix} \\ y(k) &= \begin{bmatrix} \mathbf{C} & 0 \end{bmatrix} \begin{bmatrix} \mathbf{x}(k) \\ x_{\mathrm{d}}(k) \end{bmatrix} \end{aligned} \tag{4.83}$$

respectively written in compact vector-matrix notation

$$\begin{aligned} \mathbf{x}_{\mathrm{a}}(k+1) &= \mathbf{A}_{\mathrm{a}}\mathbf{x}_{\mathrm{a}}(k) + \mathbf{B}_{\mathrm{a}}\mathbf{u}_{\mathrm{a}}(k) \\ y_{\mathrm{a}}(k) &= \mathbf{C}_{\mathrm{a}}\mathbf{x}_{\mathrm{a}}(k). \end{aligned} \tag{4.84}$$

Based on the augmented plant model, an extended optimal state-estimator is synthesized. For the optimal estimation problem, it is assumed that the augmented plant is disturbed by process noise $\mathbf{w}$ and measurement noise $\mathbf{v}$. These are modelled as white, Gaussian random noise processes that are uncorrelated and their respective noise covariances given by

$$E[\mathbf{w}(k)\ \mathbf{w}^{\mathrm{T}}(k)] = \mathbf{W} \quad E[\mathbf{v}(k)\mathbf{v}^{\mathbf{T}}(k)] = \mathbf{V} \quad \text{with } \mathbf{W} \geq 0\ \ \mathbf{V} > 0. \tag{4.85}$$

With this regard, the process noise is modeled additive to the inputs for penalizing the unknown disturbance model input in the design. The measurement noise is modeled additive to the output that is reflecting the measured lateral deviation between the vehicle and reference path. For the augmented plant model subject to process and measurement noise an optimal state estimate $\hat{\mathbf{x}}_{\mathrm{a}}$ is needed, which minimizes the steady-state value of the sum of the squared estimation errors

$$J = \lim_{k\to\infty} \mathrm{tr}[E\{\mathbf{x}_{\mathrm{a}}(k) - \hat{\mathbf{x}}_{\mathrm{a}}(k)\}\{\mathbf{x}_{\mathrm{a}}(k) - \hat{\mathbf{x}}_{\mathrm{a}}(k)\}^{\mathrm{T}}] \quad \text{respectively} \tag{4.86}$$

$$J = \lim_{k\to\infty} \mathrm{tr}[\mathbf{P}_{\mathrm{e}}] = \mathrm{tr}[\mathbf{P}_{\mathrm{e}}^{*}].$$

The optimal solution is given by the state-estimator [Dut+97]

$$\hat{\mathbf{x}}_{\mathrm{a}}(k+1) = (\mathbf{A}_{\mathrm{a}} - \mathbf{L}\,\mathbf{C}_{\mathrm{a}})\hat{\mathbf{x}}_{\mathrm{a}}(k) + \mathbf{B}_{\mathrm{a}}\,\mathbf{u}_{\mathrm{a}}(k) + \mathbf{L}\,y_{\mathrm{a}}(k) \tag{4.87}$$

which minimizes the quadratic cost function over an infinite time interval $[0, \infty]$. The optimal feedback gains $\mathbf{L}$ are hereby obtained from ([Lew+08], [Lew+12])

$$\mathbf{L} = \mathbf{A}_{\mathrm{a}}\mathbf{P}_{\mathrm{e}}^{*}\mathbf{C}_{\mathrm{a}}^{\mathrm{T}}(\mathbf{C}_{\mathrm{a}}\mathbf{P}_{\mathrm{e}}^{*}\mathbf{C}_{\mathrm{a}}^{\mathrm{T}} + \mathbf{V})^{-1} \tag{4.88}$$

where $\mathbf{P}_{\mathrm{e}}^{*}$ is the steady-state solution of the discrete algebraic Riccati equation

$$\mathbf{A}_{\mathrm{a}}[\mathbf{P}_{\mathrm{e}}^{*} - \mathbf{P}_{\mathrm{e}}^{*}\mathbf{C}_{\mathrm{a}}^{\mathrm{T}}(\mathbf{C}_{\mathrm{a}}\mathbf{P}_{\mathrm{e}}^{*}\mathbf{C}_{\mathrm{a}}^{\mathrm{T}} + \mathbf{V})^{-1}\mathbf{C}_{\mathrm{a}}\mathbf{P}_{\mathrm{e}}^{*}]\mathbf{A}_{\mathrm{a}}^{\mathrm{T}} + \mathbf{B}_{\mathrm{a}}\mathbf{W}\mathbf{B}_{\mathrm{a}}^{\mathrm{T}} - \mathbf{P}_{\mathrm{e}}^{*} = \mathbf{0}. \tag{4.89}$$

The plant state and disturbance estimates are provided as an input to the prediction model. By inclusion of the disturbance state, the MPC receives integral action.

The selection of physically meaningful noise covariance matrices $\mathbf{W}$ and $\mathbf{V}$ is accomplished identically to the proceeding described in section 3.2.4. Moreover, for an online synthesis of the optimal feedback gains $\mathbf{L}$, the recursive algorithm of the Kalman Filter is employed [Kal60]

$$\begin{aligned} \mathbf{L} &= \mathbf{P}_{\mathrm{prior}}\mathbf{C}_{\mathrm{a}}^{\mathrm{T}}\left(\mathbf{C}_{\mathrm{a}}\mathbf{P}_{\mathrm{prior}}\mathbf{C}_{\mathrm{a}}^{\mathrm{T}} + \mathbf{V}\right)^{-1} \\ \mathbf{P}_{\mathrm{post}} &= (\mathbf{I} - \mathbf{L}\mathbf{C}_{\mathrm{a}})\mathbf{P}_{\mathrm{prior}} \\ \mathbf{P}_{\mathrm{prior}} &= \mathbf{A}_{\mathrm{a}}\mathbf{P}_{\mathrm{post}}\mathbf{A}_{\mathrm{a}}^{\mathrm{T}} + \mathbf{B}_{\mathrm{a}}\mathbf{W}\mathbf{B}_{\mathrm{a}}^{\mathrm{T}}. \end{aligned} \tag{4.90}$$

The algorithm considerably facilitates the tuning process in the real vehicle and is thus particularly useful.

4.6 Control System Analysis

4.6.1 Linear Control System Analysis

After the control synthesis, the performance and stability of the automated lateral vehicle guidance control system are analyzed. For the unconstrained case, the MPC control law can be represented by a linear time-invariant system. Furthermore, by assuming a perfect compensation of the INL control, the remaining plant model is also fully linear. Consequently, frequency domain analysis of the linear control system can be conducted as detailed in the following.

To consider a physically realistic reference path curvature for the analysis, the maximum curvature that can be driven at a constant vehicle speed is examined in the following. The maximum curvature is hereby obtained based on Kamm's Circle relation (refer to Figure 44)

$$\sqrt{F_{\mathrm{x}}^2 + F_{\mathrm{y}}^2} \leq \mu F_{\mathrm{n}} \tag{4.91}$$

with F_{x} being the longitudinal tire force, F_{y} the lateral tire force, F_{n} the normal force and μ the road adhesion coefficient [Abe15].

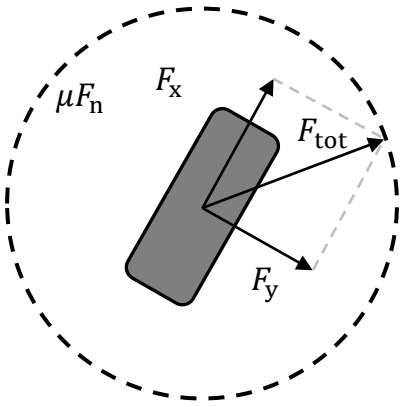

Figure 44: Kamm's Circle Relation

Neglecting the effects of weight transfer and assuming zero longitudinal tire forces, the following relationship holds [Erl15]

$$F_{\mathrm{f,max}} + F_{\mathrm{r,max}} = \mu m \mathrm{g} \tag{4.92}$$

respectively by applying the substitution $F_{\mathrm{f,max}} + F_{\mathrm{r,max}} = m a_{\mathrm{y,max}}$

$$a_{\mathrm{y,max}} = \mu \mathrm{g}. \tag{4.93}$$

Furthermore, for circular cornering at a constant vehicle speed this yields

$$\frac{v^2}{R} = \mu \mathrm{g}. \tag{4.94}$$

By introducing the definition of the curvature $\kappa_{\mathrm{ref,max}} = \frac{1}{R}$, it is obtained that [Ers+11]

$$\kappa_{\mathrm{ref,max}} = \frac{\mu \mathrm{g}}{v^2} \tag{4.95}$$

respectively

$$\kappa_{\mathrm{ref,max}} = \frac{\mu_{\max} \mathrm{g}}{v^2} \quad \text{with} \quad \mu_{\max} \approx 1.16 \quad \text{(dry asphalt)}. \tag{4.96}$$

By using the physically realistic maximum curvature $\kappa_{\mathrm{ref,max}}$ for the computation of the virtual disturbance input, that is

$$d_{\mathrm{ref}} = v^2 \kappa_{\mathrm{ref,max}} = \frac{v^2 \mu_{\max} \mathrm{g}}{v^2} = \mu_{\max} \mathrm{g} \tag{4.97}$$

the vehicle speed dependency cancels (see Figure 39). This implies that the disturbance response of the control loop for a maximum curvature disturbance at each vehicle speed is identical. Thereby, the analysis of the disturbance rejection performance simplifies.

Figure 45 illustrates the frequency responses of the control system for command following and disturbance rejection. Furthermore, the open loop frequency response is shown.

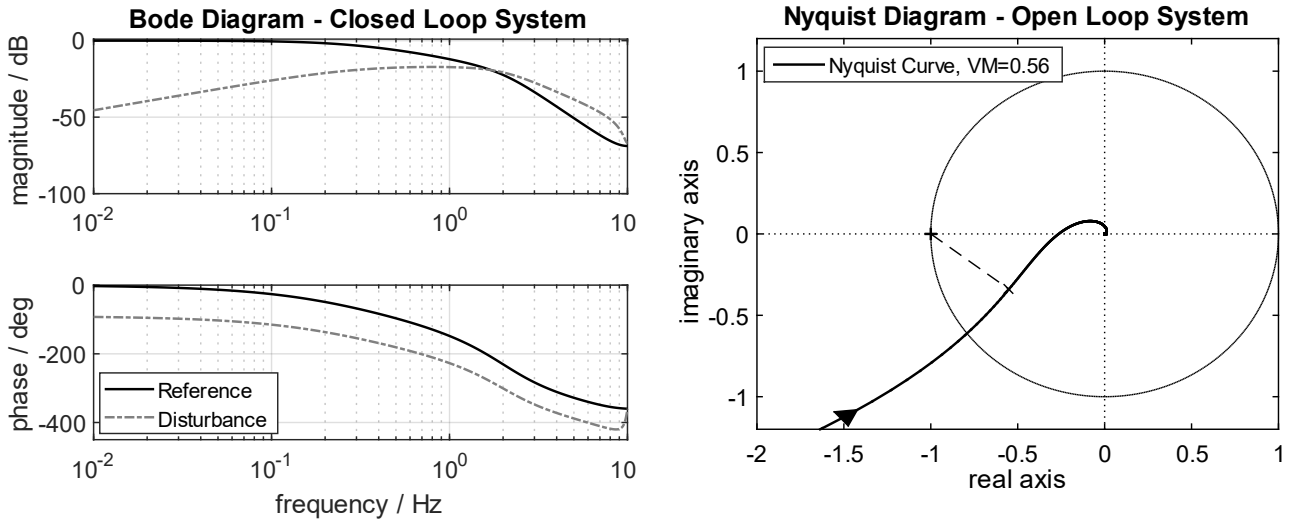

Figure 45: Frequency Responses of the Automated Lateral Vehicle Guidance Control System

The synthesized controller achieves a reference tracking bandwidth of 0.3 Hz. Maximum curvature disturbances are thereby attenuated by at least -17 dB and completely rejected in the steady state. The Nyquist diagram moreover illustrates the open loop frequency response, which gives the basis for stability analysis. The control loop reveals a vector margin of 0.56 and is therefore robustly stable against simultaneous variations in gain and phase, which may originate from plant uncertainty [Sko+05].
These performance and stability properties are valid over the entire operating range, as the closed and open loop system have the same dynamics independent of vehicle speed. This significantly simplifies controller synthesis, analysis, and tuning in the real vehicle.

4.6.2 Nonlinear Simulation Analysis

In this section, the designed control structure is verified using nonlinear simulation analysis. Hereby, the MPC is operated at the nonlinear plant, and curvature disturbance previewing as well as physical constraints on the steering position are taken into consideration.

As a first test, the disturbance step response of the control system for curvature and side wind disturbances at a vehicle speed of 50 km/h is considered. Figure 46 shows the simulation results. The reference path curvature $\kappa_{\mathrm{ref,max}} = 0.059\ 1/\mathrm{m}$ is the maximum curvature that can be driven before the tires lose grip and occurs at a simulation time of 2 seconds. Due to the previewing capability, the MPC controller already starts counteracting the disturbance before that time. Consequently, a maximum lateral deviation of around 0.13 m results. Thereafter, a sudden side wind disturbance of $F_{\mathrm{y,d}} = 500\ \mathrm{N}$ is analyzed, which affects the vehicle perpendicular from the side at a simulation time of 2 seconds. The unknown disturbance is reconstructed by the extended optimal state-estimator and provided as an input to the prediction model for an instantaneous rejection. Hereby, different settings of the process noise intensity $\mathbf{W}_{(3,3)}$ for the unknown disturbance model input are shown. With increasing noise intensity, the disturbance estimation bandwidth increases. Consequently, the disturbance rejection performance is improved. In comparison, without disturbance estimation a constant lateral deviation of 0.063 m is exposed. Hence, the noise intensity for the disturbance model input must be selected as high as possible. Thereby, a compromise between performance and stability must be found.

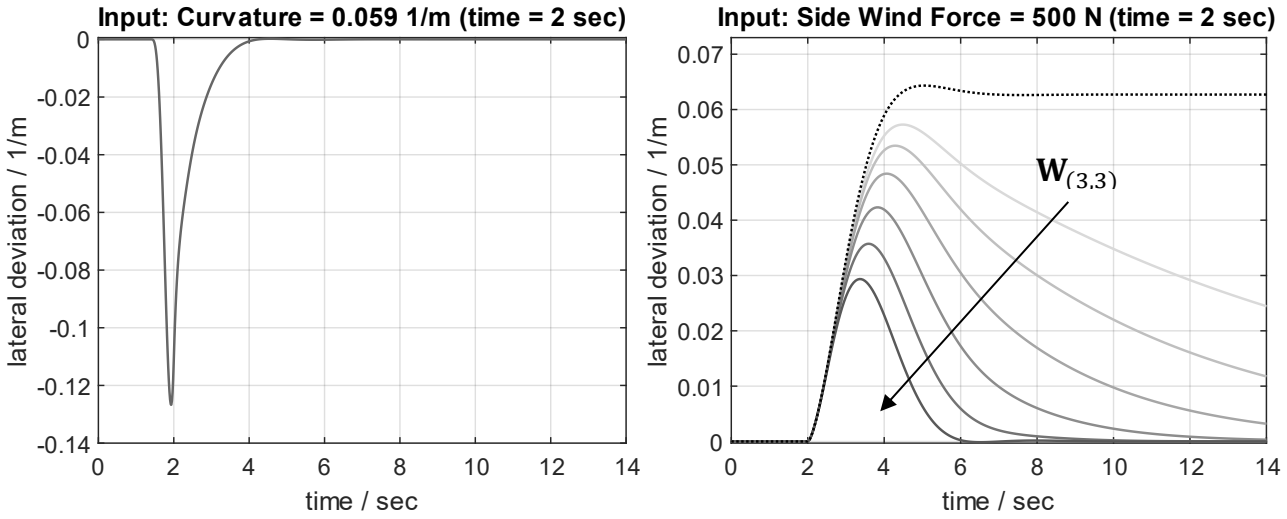

Figure 46: Step Responses of the Automated Lateral Vehicle Guidance Control System

As a next step, virtual test drives in simulation on an oval test track are conducted to verify the performance of the automated lateral vehicle guidance control. Figure 47 illustrates the test track in x-y coordinates with the vehicle starting position marked by a black star. The total track length is approximately 2074 m, and the vehicle is driven at a constant speed of 70 km/h. Figure 48 provides an overview of the nonlinear simulation analysis results by showing the lateral deviation, FAA steering position, and vehicle speed over time. With this regard, it is confirmed that the Nonlinear Adaptive MPC accurately tracks the given reference path. During the test, the vehicle is driven close to the limits of vehicle dynamics. Hereby a maximum lateral deviation of 0.07 meters is found, which occurs at the entry to the tightest curve segment and is thus originating from curvature disturbance. Due to the measured disturbance previewing, the MPC reacts to the disturbance ahead of time and takes the required corrective actions for its instantaneous compensation. Hence, superior path tracking performance is achieved.

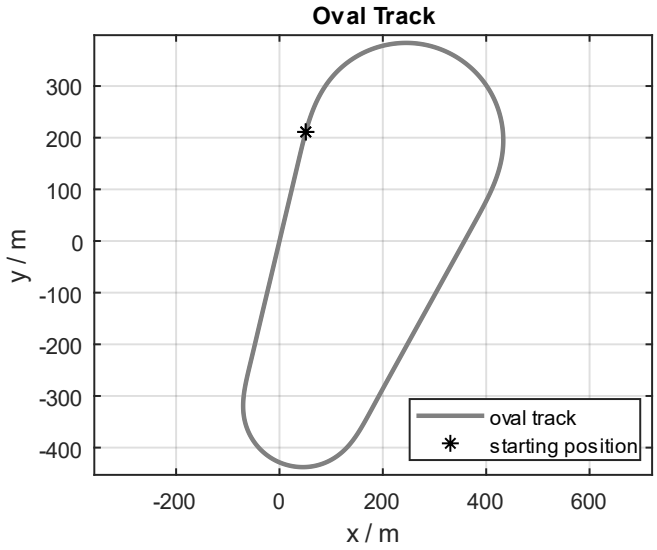

Figure 47: Nonlinear Simulation – Oval Track in x-y Plane
(Direction of Travel Clockwise)

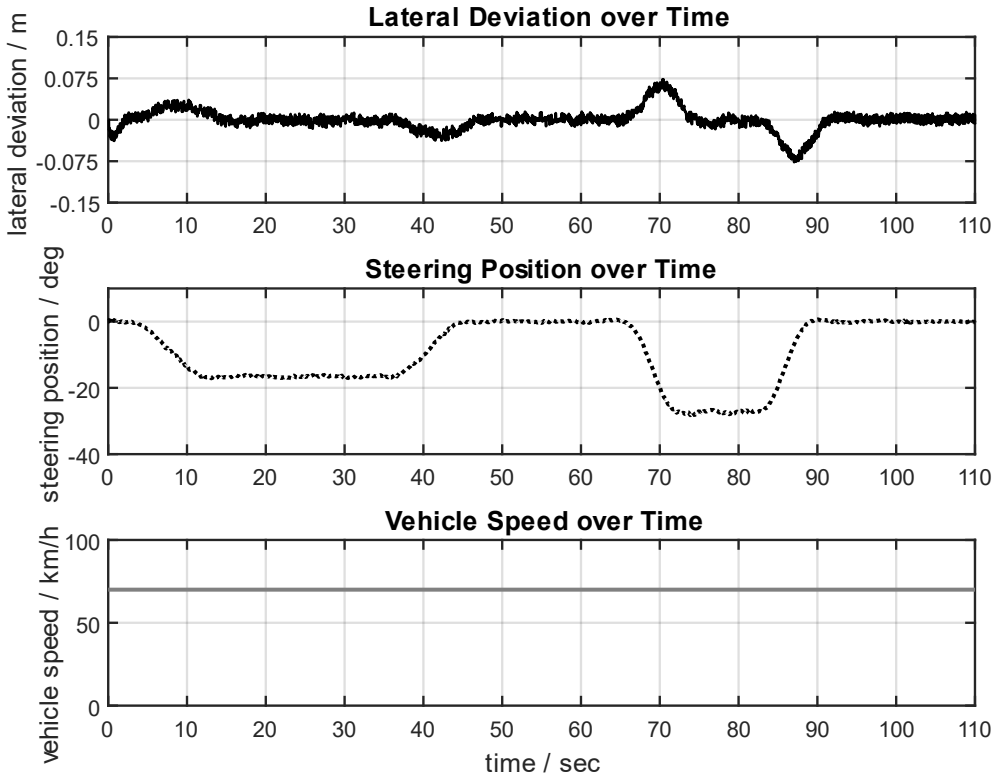

Figure 48: Nonlinear Simulation – Automated Driving on the Oval Track at 70 km/h

5

Extension of the Control Structure for Cooperative Lateral Vehicle Guidance

The previously designed control structure enables a precise automated lateral vehicle guidance. This chapter introduces extensions of the structure for explicitly considering driver interventions and thereby permitting a cooperative lateral vehicle guidance. To this end, the overall control architecture is first presented, and the impact of a driver intervention is exposed. If unconsidered by control, the driver intervention is interpreted as an external disturbance that is compensated by feedback control. Therefore, an extended control architecture is proposed, which supports driver interventions and enables a true coexistence between the driver and automation system. For this purpose, a superposition control concept is introduced, which realizes a cooperative HWA control by fusing steering torque and steering position control. Hence, the driver can override the active position control while experiencing an authentic steering feel. Subsequently, a 2DOF Nonlinear Adaptive MPC concept for cooperative lateral vehicle guidance is employed, which fuses manual steering control by the driver and automated steering control. Thereby the driver can seamlessly modify the lateral vehicle trajectory during automated driving. At the end of the chapter, the performance of the cooperative HWA and lateral vehicle guidance control is verified using nonlinear simulation analysis. Essential results are published in [Gon+23b].

5.1 Control Architecture

5.1.1 Automated Lateral Vehicle Guidance

For an accurate and robust automated lateral guidance of the vehicle along a preplanned reference path, advanced control structures were systematically designed in the preceding chapters. Figure 49 illustrates the overall control architecture for the automated driving mode. It consists of an automated lateral vehicle guidance controller, which is given by the Nonlinear Adaptive MPC, and an automated HWA controller that is reflected by the cascaded 2DOF LQG steering position controller. The output of the automated lateral vehicle guidance controller hereby serves as the reference signal for automated HWA control. Driver interventions in form of a driver torque $T_{\mathrm{DR}}(k)$ applied at steering wheel and a manual steering position $\varphi_{\mathrm{MD}}^{*}(k)$ at FAA are interpreted as external disturbance variables that are compensated by the respective feedback controls. Therefore, the controls expose no cooperative behavior.

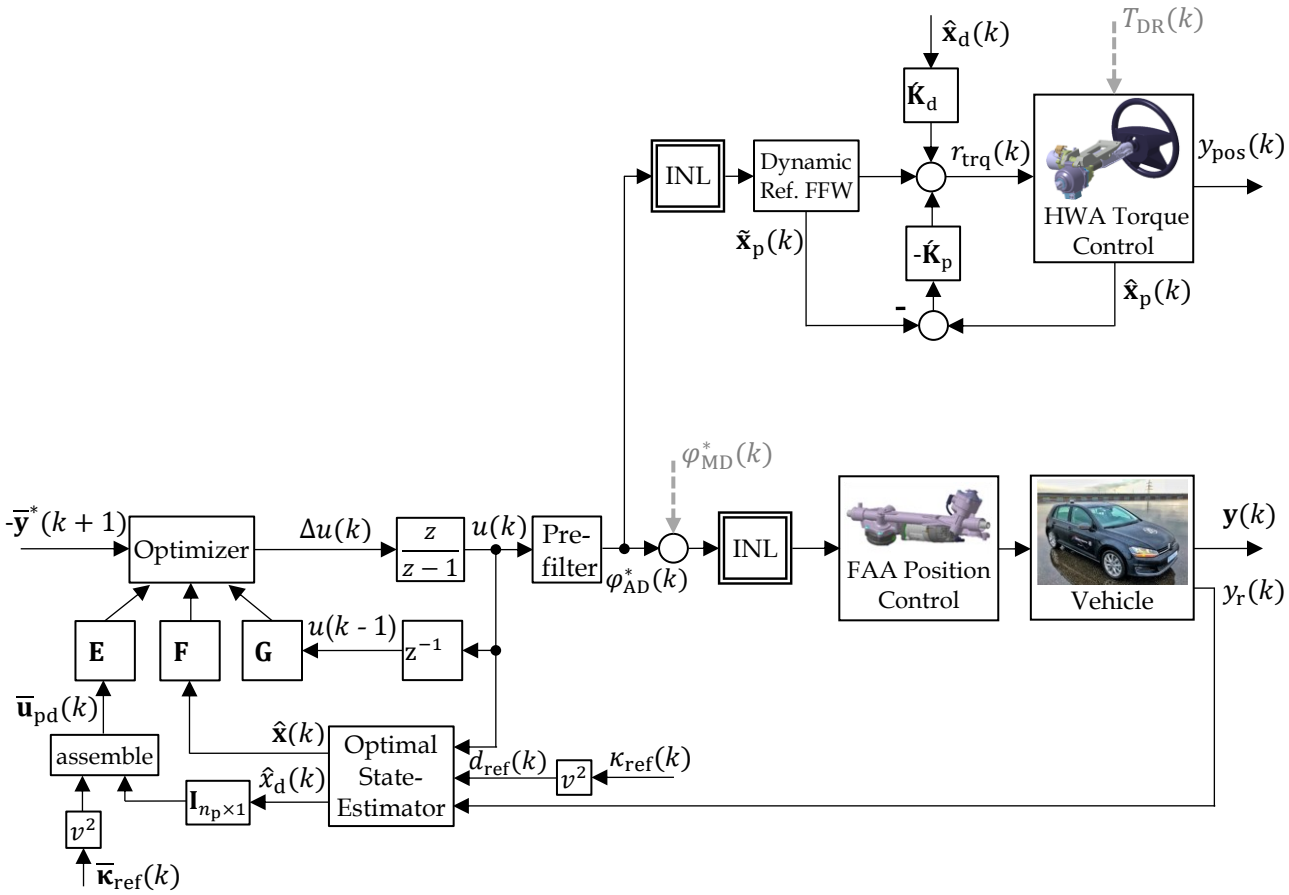

Figure 49: Control Architecture for Automated Driving Mode

With this regard, the driver steering input $\varphi^*_\mathrm{MD}(k)$ must not be interpreted as an external disturbance and accepted by automated lateral vehicle guidance control. Similarly, the driver torque input $T_\mathrm{DR}(k)$ must not be treated as an external disturbance and accepted by automated HWA control. Thereby, the additional challenge arises that the driver must experience a natural steering feel during an intervention. Moreover, the transitions must be seamless. In the following section, extensions to the overall control architecture are introduced for specifically pursuing these objectives.

5.1.2 Cooperative Lateral Vehicle Guidance

For achieving a cooperative control behavior that accepts driver interventions, the extended control architecture shown in Figure 50 is introduced. It comprises a cooperative lateral vehicle guidance controller, which is given by a 2DOF Nonlinear Adaptive MPC. Furthermore, a cooperative HWA controller is used that relies on a superposition control concept for fusing steering torque and steering position control.

The 2DOF Nonlinear Adaptive MPC uses a dynamic cooperative feedforward control. The latter includes a virtual control loop for computing the effect of the driver steering input $\varphi^*_\mathrm{MD}(k)$ on the system states $\check{\mathbf{x}}(k)$ online. By subtraction of $\check{\mathbf{x}}(k)$ from the state estimates $\hat{\mathbf{x}}(k)$, the driver intervention is hidden from feedback control. Thus, the driver can override the lateral vehicle guidance controller and seamlessly modify the lateral vehicle trajectory. For preventing that the driver steering input is subject to disturbance estimation, an additional control input must be considered for the extended optimal state-estimator. Hence, the integral action of the controller permits driver interventions, and a holistic cooperative control behavior is achieved.

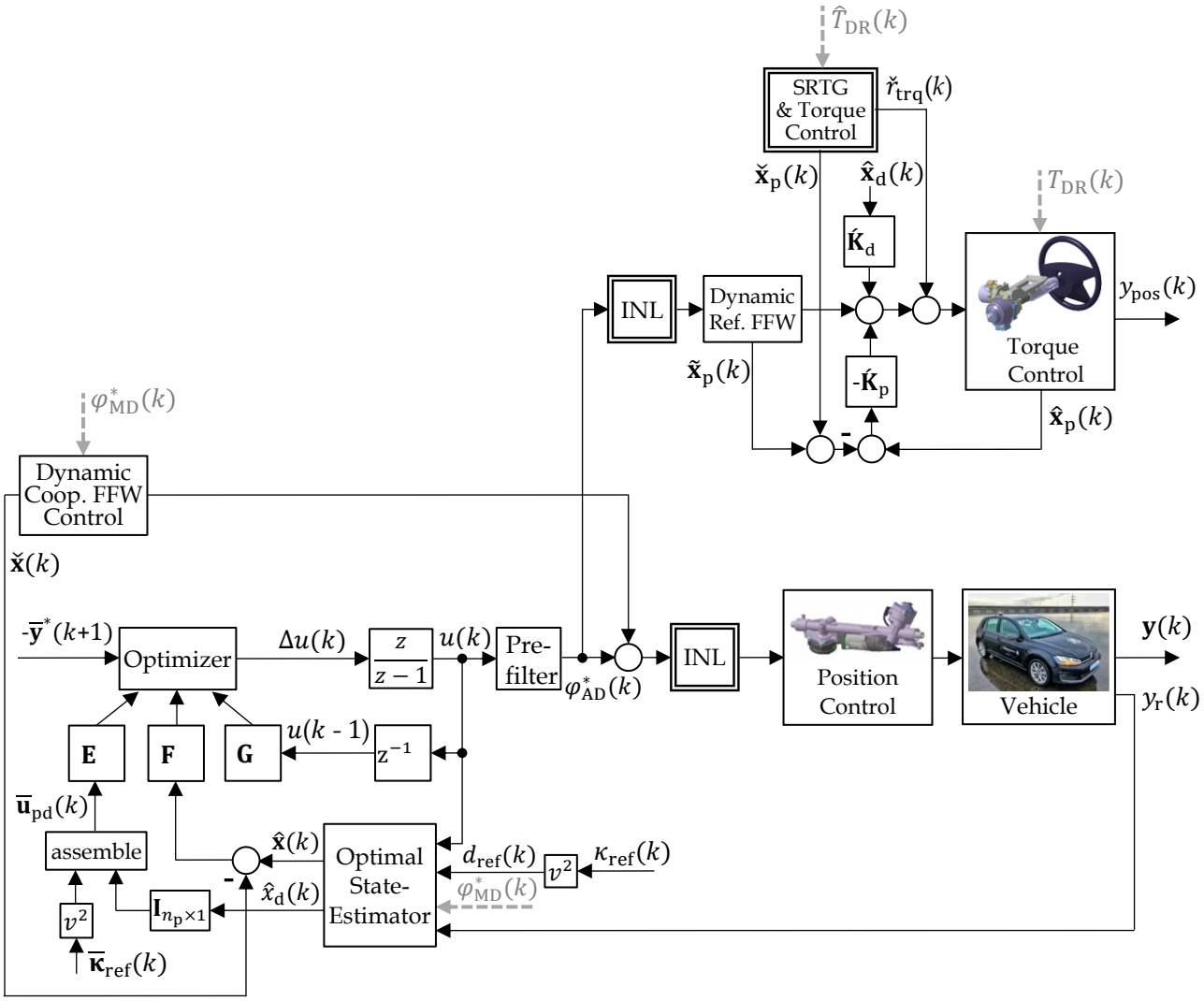

Figure 50: Control Architecture for Cooperative Driving Mode

The cooperative HWA control uses a superposition control concept to elegantly combine steering position and steering torque control. For this purpose, the cascade 2DOF LQG steering position control is extended by a virtual control loop for steering feel generation and steering torque control. The virtual control loop receives the estimated driver torque $\hat{T}_{DR}(k)$ as an input and generates the reference torque $\check{r}_{trq}(k)$ for steering feel generation. By providing this reference torque to the real system, the desired steering feel will propagate. Furthermore, the virtual control loop computes the effect of the driver torque and reference torque on the system states $\check{\mathbf{x}}_p(k)$. According to the superposition principle, by subtraction of $\check{\mathbf{x}}_p(k)$ from the state estimates $\hat{\mathbf{x}}_p(k)$ both torques are accepted by feedback control. Hence, the driver can override the active position control and experiences a desired steering feel. Thereby the transitions are seamless as no blending, gain switching, or controller output saturation is required. To ensure that the integral action of the controller accepts both torques, the reference torque is provided as an additional control input to the extended optimal state-estimator so that exclusively the remaining disturbances are reconstructed. These comprise the nonlinear friction torque and the driver torque estimate, where the disturbance feedforward gain of the latter must be set to zero to prevent its compensation. In the following sections, the inner structure of the cooperative HWA control and cooperative lateral vehicle guidance control is outlined in detail.

5.2 Superposition Control Concept

In chapter 3.2 the steering feel generation and steering torque control of the HWA for the manual driving mode were detailed. Furthermore, in chapter 3.3 the steering position control of the HWA for the automated driving mode was presented. Both control concepts have structural similarities in the sense that the torque control loop persists as an inner control loop and that the outer controller forms a steering position controller. Thereby, the latter serves different purposes, which is either steering feel generation or reference steering position tracking.
These essential properties are exploited in the following by introducing a superposition control concept for fusing steering position and steering torque control. Figure 51 shows the resulting HWA control for the cooperative driving mode. It consists of a cascade 2DOF LQG steering position controller that is extended by a dynamic feedforward control with a virtual control loop for steering reference torque generation and torque control. The input to the virtual control loop is a driver torque estimate that is reconstructed by a separate extended optimal state-estimator for the steering wheel subsystem. The virtual control loop for steering feel generation and torque control as well as the driver torque estimation are outlined in the following sections. Moreover, specific measures for ensuring a cooperative control behavior of the proportional-derivative and integral steering position controller parts are exposed.

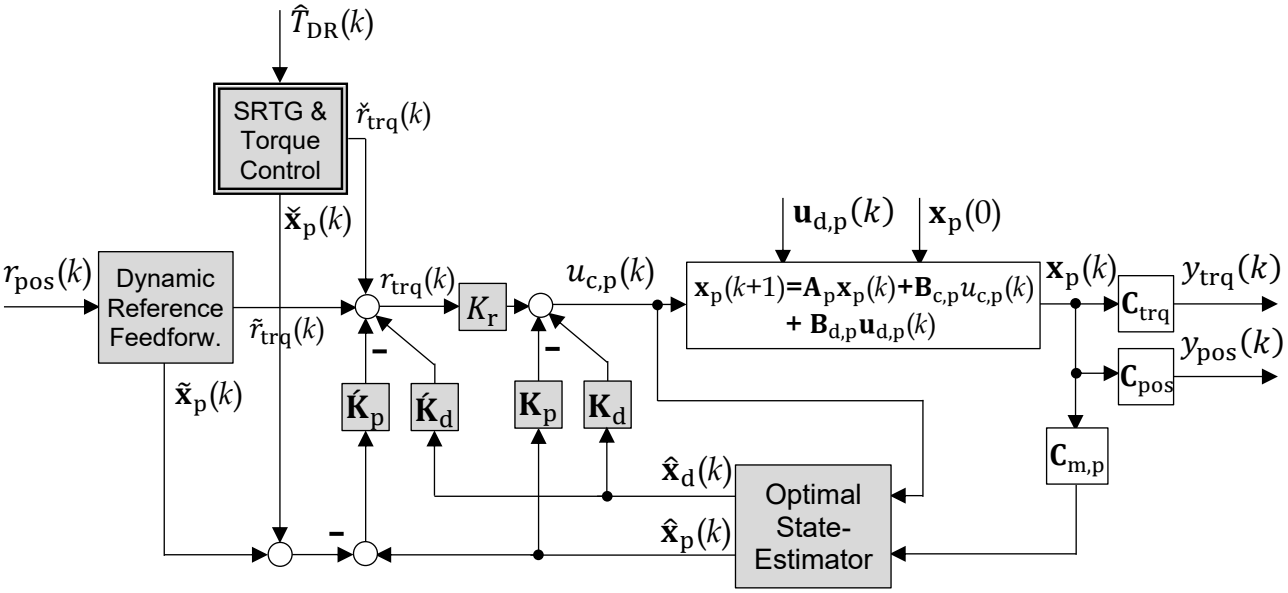

Superposition Control – Fusing Steering Torque and Position Control

Figure 51: Cooperative HWA Control for the Steer-by-Wire System

5.2.1 Dynamic Feedforward for Steer Feel Generation and Torque Control

To ensure that the state-feedback position controller does not consider driver torque as a disturbance and that a desired steering feel is generated, a dynamic feedforward control is introduced. The dynamic feedforward control includes the steering reference torque generator and torque control loop, which constitute a virtual control loop (see Figure 52). As the HWA plant model states $\check{\mathbf{x}}_{\mathrm{p}}(k)$ are already available, they can be directly used for control. Hence, there is no state-estimator needed within the virtual control loop. A driver torque estimate $\hat{T}_{\mathrm{DR}}$ serves as the input for the virtual control loop.

Consequently, in the event of a driver intervention the steering position $\check{y}_{\mathrm{pos}}(k)$ of the HWA plant model increases, and the desired reference steering torque $\check{r}_{\mathrm{trq}}(k)$ is generated. By providing the generated reference steering torque to the real system, the desired steering feel will propagate. Thereover, the effect of the driver torque and reference steering torque on the system states $\check{\mathbf{x}}_{\mathrm{p}}(k)$ is computed. Following the superposition principle, by subtraction of $\check{\mathbf{x}}_{\mathrm{p}}(k)$ from the estimated states $\hat{\mathbf{x}}_{\mathrm{p}}(k)$ (see Figure 51), the state-feedback steering position controller will accept both torques. Hence, the proportional-derivative part of the cascade 2DOF LQG steering position controller receives a cooperative behavior.
For ensuring that the integral part of the cascade 2DOF LQG steering position controller is also cooperative, separate disturbance integrator models for nonlinear friction torque and driver torque are considered. Thereby, a selective disturbance compensation is realizable. This allows compensating the nonlinear friction torque whereas the driver torque is permitted. Therefore, the integral controller part is cooperative towards driver interventions [Gon+21]. Furthermore, the reference steering torque for steering feel generation must be provided as a control input to the extended optimal state-estimator. Hereby, it is excluded from disturbance estimation. Consequently, the driver torque and reference torque are both accepted by the integral part of the steering position control.
The cooperative HWA control performs accurate tracking of the reference steering position while allowing the driver to override the active control. Hereby the driver perceives a natural steering feel that is symmetric about the reference steering position. The transitions during a driver intervention are seamless as steering position and steering torque control coexist and no manual switching involving discontinuities is required.

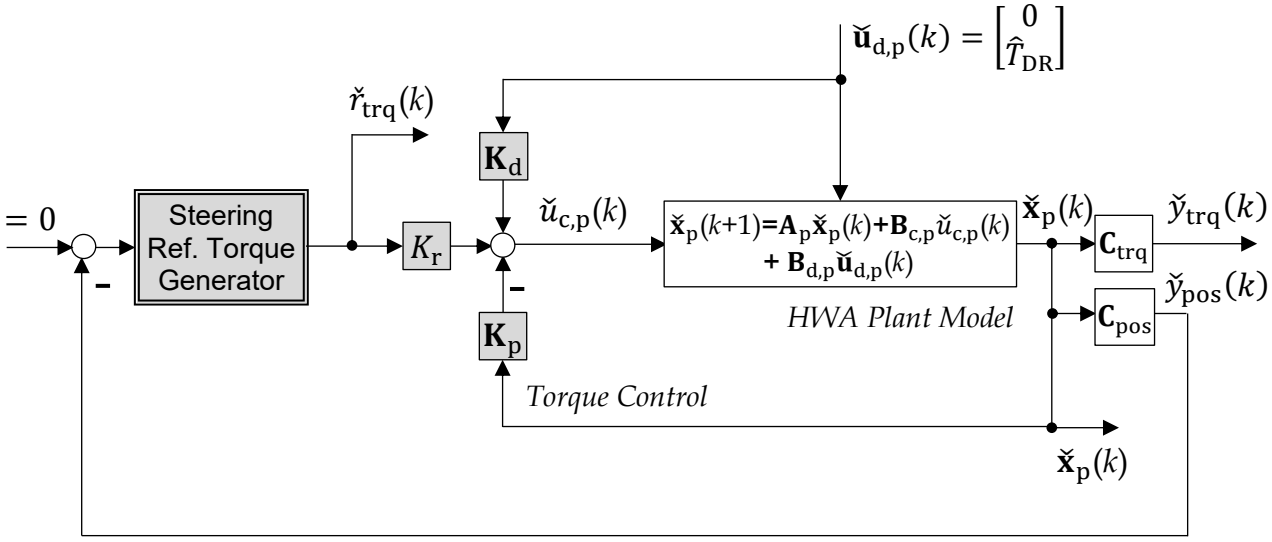

Figure 52: Dynamic Feedforward Control – Steering Feel Generation and Torque Control

5.2.2 Driver Torque Estimation

The effectiveness of the presented superposition control concept presupposes the absence of model error, external disturbances, and the availability of the driver torque as a measurement. As previously outlined, the integral controller action corrects for external disturbances and model error. Thus, the robustness of the control is guaranteed. As the direct measurement of the driver torque is not possible due to the lack of available

sensors, an extended optimal state-estimator for the steering wheel subsystem is designed in the following. Hereby, it is important that the estimation bandwidth is selected as high as possible to approximate the measurement.
For estimator synthesis, the differential equations of the steering wheel subsystem given by (2.3) and (2.4) are transformed to state-space representation. Hence, it is obtained

$$\begin{aligned} \dot{\mathbf{x}}_\mathrm{p} &= \mathbf{A}_\mathrm{p}^\mathrm{c}\mathbf{x}_\mathrm{p} + \mathbf{B}_\mathrm{c,p}^\mathrm{c}u_\mathrm{c,p} + \mathbf{B}_\mathrm{d,p}^\mathrm{c}u_\mathrm{d,p} \\ y_\mathrm{m,p} &= \mathbf{C}_\mathrm{m,p}^\mathrm{c}\mathbf{x}_\mathrm{p} \end{aligned} \tag{5.1}$$

with

$$\mathbf{A}_\mathrm{p}^\mathrm{c} = \begin{bmatrix} -\dfrac{d_\mathrm{TS}+d_\mathrm{SW}}{J_\mathrm{SW}} & -\dfrac{c_\mathrm{TS}}{J_\mathrm{SW}} \\ 1 & 0 \end{bmatrix},\quad \mathbf{x}_\mathrm{p} = \begin{bmatrix} \Omega_\mathrm{SW} \\ \Delta\varphi \end{bmatrix},\quad \mathbf{B}_\mathrm{c,p}^\mathrm{c} = \begin{bmatrix} \dfrac{d_\mathrm{TS}}{J_\mathrm{SW}} \\ -1 \end{bmatrix},\quad u_\mathrm{c,p} = \Omega_\mathrm{PN},$$

$$\mathbf{B}_\mathrm{d,p}^\mathrm{c} = \begin{bmatrix} -\dfrac{1}{J_\mathrm{SW}} \\ 0 \end{bmatrix},\quad u_\mathrm{d,p} = T_\mathrm{DR},\quad \mathbf{C}_\mathrm{m,p}^\mathrm{c} = [0 \quad c_\mathrm{TS}],\quad y_\mathrm{m,p} = T_\mathrm{TS}.$$

The continuous-time plant model is discretized by employing a step invariant discretization and a sampling time of $\mathrm{T_s} = 0.001$ sec, which yields

$$\begin{aligned} \mathbf{x}_\mathrm{p}(k+1) &= \mathbf{A}_\mathrm{p}\mathbf{x}_\mathrm{p}(k) + \mathbf{B}_\mathrm{c,p}u_\mathrm{c,p}(k) + \mathbf{B}_\mathrm{d,p}u_\mathrm{d,p}(k) \\ y_\mathrm{m,p}(k) &= \mathbf{C}_\mathrm{m,p}\mathbf{x}_\mathrm{p}(k) \end{aligned} \tag{5.2}$$

with

$$\mathbf{A}_\mathrm{p} = \mathrm{e}^{\mathbf{A}_\mathrm{p}^\mathrm{c}\mathrm{T_s}},\quad \mathbf{B}_\mathrm{c,p} = \left(\int_0^{\mathrm{T_s}} \mathrm{e}^{\mathbf{A}_\mathrm{p}^\mathrm{c}\eta}\,\mathrm{d}\eta\right)\mathbf{B}_\mathrm{c,p}^\mathrm{c},\quad \mathbf{B}_\mathrm{d,p} = \left(\int_0^{\mathrm{T_s}} \mathrm{e}^{\mathbf{A}_\mathrm{p}^\mathrm{c}\eta}\,\mathrm{d}\eta\right)\mathbf{B}_\mathrm{d,p}^\mathrm{c},\quad \mathbf{C}_\mathrm{m,p} = \mathbf{C}_\mathrm{m,p}^\mathrm{c}.$$

To reconstruct the driver torque, an integrator disturbance model of the following form is introduced

$$\begin{aligned} x_\mathrm{d}(k+1) &= \mathbf{A}_\mathrm{d}x_\mathrm{d}(k) + \mathbf{B}_\mathrm{d}u_\mathrm{d}(k) \quad \text{with } \mathbf{A}_\mathrm{d} = 1, \mathbf{B}_\mathrm{d} = \mathrm{T_s}, \mathbf{C}_\mathrm{d} = 1 \\ y_\mathrm{d}(k) &= \mathbf{C}_\mathrm{d}x_\mathrm{d}(k). \end{aligned} \tag{5.3}$$

This disturbance model is suitable for the estimation of piece-wise constant disturbances such as for example load torque [Hen97]. Using the substitution $u_\mathrm{d,p} = y_\mathrm{d}$, the plant model and disturbance model are combined to an augmented plant model, that is

$$\begin{aligned} \begin{bmatrix} \mathbf{x}_\mathrm{p}(k+1) \\ x_\mathrm{d}(k+1) \end{bmatrix} &= \begin{bmatrix} \mathbf{A}_\mathrm{p} & \mathbf{B}_\mathrm{d,p}\mathbf{C}_\mathrm{d} \\ \mathbf{0} & \mathbf{A}_\mathrm{d} \end{bmatrix}\begin{bmatrix} \mathbf{x}_\mathrm{p}(k) \\ x_\mathrm{d}(k) \end{bmatrix} + \begin{bmatrix} \mathbf{B}_\mathrm{c,p} & \mathbf{0} \\ 0 & \mathbf{B}_\mathrm{d} \end{bmatrix}\begin{bmatrix} u_\mathrm{c,p}(k) \\ u_\mathrm{d}(k) \end{bmatrix} \\ y_\mathrm{m,p}(k) &= [\mathbf{C}_\mathrm{m,p} \quad 0]\begin{bmatrix} \mathbf{x}_\mathrm{p}(k) \\ x_\mathrm{d}(k) \end{bmatrix} \end{aligned} \tag{5.4}$$

respectively written in compact vector-matrix notation

$$\begin{aligned} \mathbf{x}_\mathrm{a}(k+1) &= \mathbf{A}_\mathrm{a}\mathbf{x}_\mathrm{a}(k) + \mathbf{B}_\mathrm{a}\mathbf{u}_\mathrm{a}(k) \\ y_\mathrm{a}(k) &= \mathbf{C}_\mathrm{a}\mathbf{x}_\mathrm{a}(k). \end{aligned} \tag{5.5}$$

Based on the augmented plant, an extended optimal state-estimator (Kalman filter) is designed. For the optimal estimation problem, it is assumed that the augmented plant is disturbed by process noise $\mathbf{w}$ and measurement noise $\mathbf{v}$ with covariances $E[\mathbf{w}\,\mathbf{w}^{\mathrm{T}}] = \mathbf{W}$ and $E[\mathbf{v}\,\mathbf{v}^{\mathrm{T}}] = \mathbf{V}$ (where $\mathbf{W} \geq \mathbf{0}$, $\mathbf{V} > \mathbf{0}$). In this context, the process noise is modeled additive to the inputs for penalizing the unknown disturbance model input. For the augmented plant subject to noise an optimal state estimate $\hat{\mathbf{x}}_{\mathbf{a}}(k)$ is needed, which minimizes the steady-state value of the sum of the squared estimation errors

$$J = \lim_{k\to\infty} \mathrm{tr}[E\{\mathbf{x}_{\mathrm{a}}(k) - \hat{\mathbf{x}}_{\mathrm{a}}(k)\}\{\mathbf{x}_{\mathrm{a}}(k) - \hat{\mathbf{x}}_{\mathrm{a}}(k)\}^{\mathrm{T}}] = \lim_{k\to\infty} \mathrm{tr}[\mathbf{P}_{\mathrm{e}}]\,. \tag{5.6}$$

The optimal solution is given by the state-estimator

$$\hat{\mathbf{x}}_{\mathrm{a}}(k+1) = (\mathbf{A}_{\mathrm{a}} - \mathbf{L}\mathbf{C}_{\mathrm{a}})\hat{\mathbf{x}}_{\mathrm{a}}(k) + \mathbf{B}_{\mathrm{a}}\mathbf{u}_{\mathrm{a}}(k) + \mathbf{L}y_{\mathrm{a}}(k) \tag{5.7}$$

that minimizes the quadratic cost function over an infinite time horizon $[0, \infty]$. In this context, the optimal feedback gains $\mathbf{L}$ are given by

$$\mathbf{L} = \mathbf{A}_{\mathrm{a}}\mathbf{P}_{\mathrm{e}}^{*}\mathbf{C}_{\mathrm{a}}^{\mathrm{T}}(\mathbf{C}_{\mathrm{a}}\mathbf{P}_{\mathrm{e}}^{*}\mathbf{C}_{\mathrm{a}}^{\mathrm{T}} + \mathbf{V})^{-1} \tag{5.8}$$

where $\mathbf{P}_{\mathrm{e}}^{*}$ is the steady-state solution of the discrete algebraic Riccati equation [Lew+12]

$$\mathbf{A}_{\mathrm{a}}[\mathbf{P}_{\mathrm{e}}^{*} - \mathbf{P}_{\mathrm{e}}^{*}\mathbf{C}_{\mathrm{a}}^{\mathrm{T}}(\mathbf{C}_{\mathrm{a}}\mathbf{P}_{\mathrm{e}}^{*}\mathbf{C}_{\mathrm{a}}^{\mathrm{T}} + \mathbf{V})^{-1}\mathbf{C}_{\mathrm{a}}\mathbf{P}_{\mathrm{e}}^{*}]\mathbf{A}_{\mathrm{a}}^{\mathrm{T}} + \mathbf{B}_{\mathrm{a}}\mathbf{W}\mathbf{B}_{\mathrm{a}}^{\mathrm{T}} - \mathbf{P}_{\mathrm{e}}^{*} = \mathbf{0}. \tag{5.9}$$

The synthesis of a separate driver torque estimator for the steering wheel provides the advantage that its performance is designed independently from the extended optimal state-estimator of the feedback controller. This provides enhanced design flexibility in the tuning of the overall controller. The performance of the driver torque estimation is detailly analyzed in chapter 5.4.

5.3 2DOF Nonlinear Adaptive Model Predictive Control Concept

In chapter 4 the Nonlinear Adaptive MPC for automated lateral vehicle guidance was synthesized. The control allows accurate lateral vehicle guidance but interprets the driver steering input $\varphi_{\mathrm{MD}}^{*}(k)$ as an external disturbance. To overcome this problem, a 2DOF Nonlinear Adaptive MPC concept is employed in this chapter, which fuses manual and automated lateral vehicle guidance.

Figure 53 gives an overview on the cooperative lateral vehicle guidance control. It consists of the Nonlinear Adaptive MPC for automated lateral vehicle guidance that is structurally extended by a dynamic cooperative feedforward control. The dynamic cooperative feedforward control includes a virtual control loop that is designed for a desired disturbance response of the lateral vehicle guidance control with respect to driver inputs $\varphi_{\mathrm{MD}}^{*}(k)$. The Nonlinear Adaptive MPC feedback controller is designed for a desired disturbance response of the lateral vehicle guidance control regarding all residual disturbances. The latter comprise reference path curvature, side wind, road camber, and model error. Hence, by employing the 2DOF control structure two contradicting control objectives are simultaneously achievable. That is precise control of the lateral deviation

between vehicle and reference path, but acceptance of lateral deviation induced by the driver.

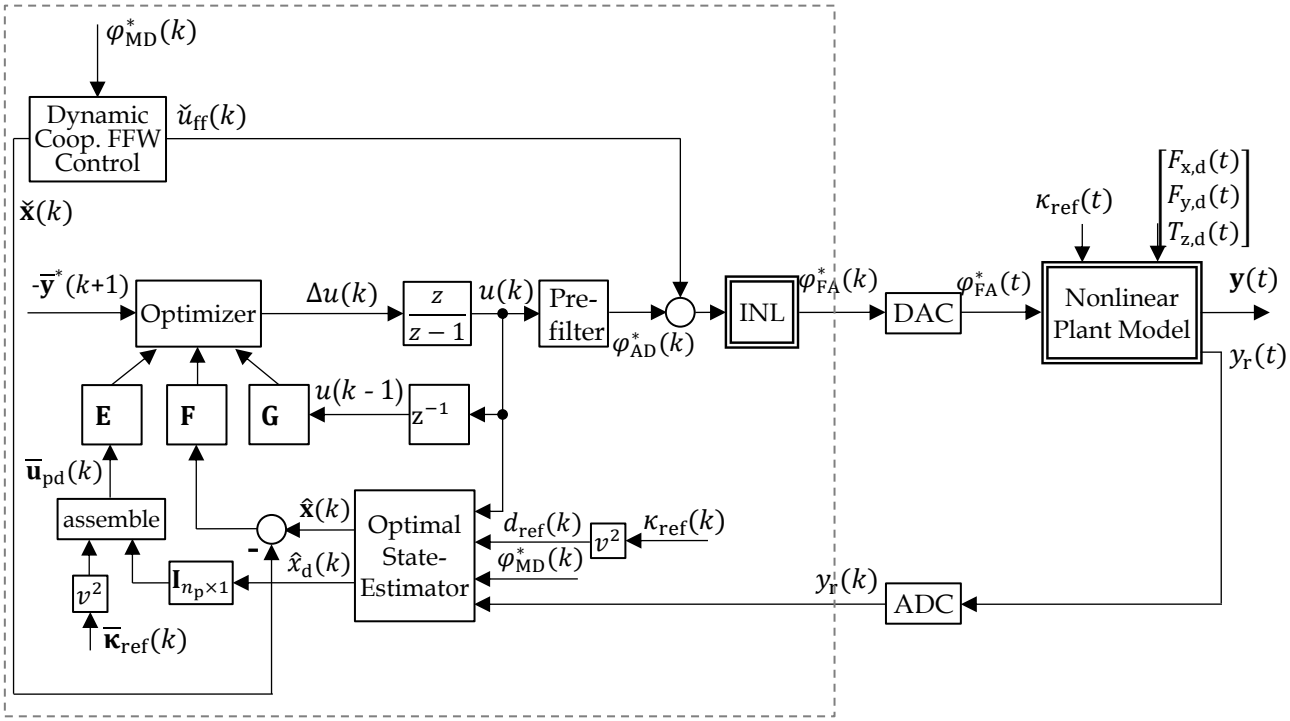

Figure 53: Cooperative Lateral Vehicle Guidance Control

5.3.1 Dynamic Cooperative Feedforward

In Figure 54 the dynamic cooperative feedforward control is shown. It includes a virtual control loop that receives the steering position induced by the driver $\varphi^*_{\mathrm{MD}}(k)$ as an input. The virtual control loop is computed online and generates a control input $\breve{u}_{\mathrm{ff}}(k)$. By supplying the generated control input to the real system, the desired disturbance response with respect to driver inputs propagates [Wur+09]. Furthermore, the effect of the driver steering input on the system states $\breve{\mathbf{x}}(k)$ is calculated. By subtraction of the virtual states $\breve{\mathbf{x}}(k)$ from the state estimates $\hat{\mathbf{x}}(k)$ that enter the prediction model, the effect of the driver intervention is hidden from Nonlinear Adaptive MPC feedback control (see Figure 53). Thus, the driver can override the active control and seamlessly modify the lateral vehicle trajectory. Consequently, the 2DOF Nonlinear Adaptive MPC concept possesses the desired cooperative control behavior.

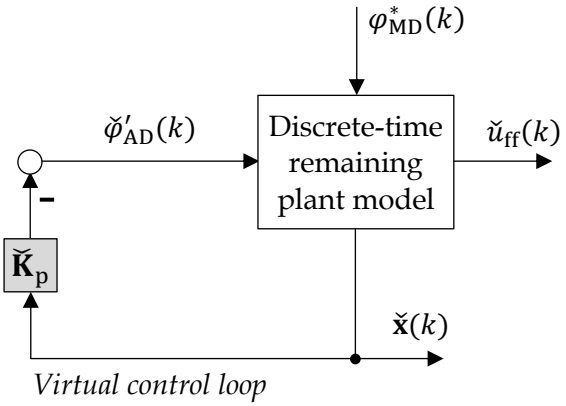

Figure 54: Dynamic Cooperative Feedforward Control

For the synthesis of the virtual control loop, the continuous-time remaining plant model according to (4.39) and (4.42) is considered

$$\begin{aligned}\dot{\check{\mathbf{x}}} &= \mathbf{A}^{\mathrm{c}}\check{\mathbf{x}} + \mathbf{B}^{\mathrm{c}}\check{u} + \mathbf{B}^{\mathrm{c}}_{\mathrm{pd}}\check{u}_{\mathrm{pd}} \\ \check{\mathbf{y}} &= \mathbf{C}^{\mathrm{c}}\check{\mathbf{x}} + \mathbf{D}^{\mathrm{c}}\check{u} + \mathbf{D}^{\mathrm{c}}_{\mathrm{pd}}\check{u}_{\mathrm{pd}}\end{aligned} \tag{5.10}$$

with

$\mathbf{B}^{\mathrm{c}} = \mathbf{B}^{\mathrm{c}}_{\mathrm{re}(l,m)}$ where $l = 1, 2, \dots, 5$ and $m = 1$

$\mathbf{B}^{\mathrm{c}}_{\mathrm{pd}} = \mathbf{B}^{\mathrm{c}}_{\mathrm{re}(l,m)}$ where $l = 1, 2, \dots, 5$ and $m = 2$

$\mathbf{D}^{\mathrm{c}} = \mathbf{D}^{\mathrm{c}}_{\mathrm{coop}(l,m)}$ where $l = 1, 2, \dots, 6$ and $m = 1$

$\mathbf{D}^{\mathrm{c}}_{\mathrm{pd}} = \mathbf{D}^{\mathrm{c}}_{\mathrm{coop}(l,m)}$ where $l = 1, 2, \dots, 6$ and $m = 2$

$\check{u} = \mathbf{u}_{\mathrm{re}(l,m)}$ where $l = 1$ and $m = 1$

$\check{u}_{\mathrm{pd}} = \mathbf{u}_{\mathrm{re}(l,m)}$ where $l = 2$ and $m = 1$

$\mathbf{A}^{\mathrm{c}} = \mathbf{A}^{\mathrm{c}}_{\mathrm{re}}$

$\check{\mathbf{x}} = \mathbf{x}_{\mathrm{re}}$

$\mathbf{C}^{\mathrm{c}} = \mathbf{C}^{\mathrm{c}}_{\mathrm{coop}}$

$\check{\mathbf{y}} = \mathbf{y}_{\mathrm{coop}}$.

With this regard, l and m denote the row and column indices of the required submatrices and vector components. The input $\check{u}$ hereby corresponds to the control input $\check{\varphi}'_{\mathrm{AD}}$. The separated input $\check{u}_{\mathrm{pd}}$ represents the steering input that is induced by the driver $\varphi^{*}_{\mathrm{MD}}$.

The remaining plant model is a 5th-order system whose eigenvalues are given by the prefilter, FAA steering position control, and error equations relative to the reference path, respectively. As the latter introduce a double integrator eigenvalue at $s^2 = 0$, the remaining plant model is unstable and cannot be used for dynamic feedforward control. Hence, stabilization via feedback is required inside the virtual control loop. For this purpose, a full state-feedback controller based on eigenvalue assignment is synthesized in the following. Thereby, the locations of the initial eigenvalues are pre-computed, and exclusively the integrator eigenvalues are assigned to the desired locations. The starting point for controller synthesis is the remaining plant model given by (5.10) that is transformed to control canonical form using the substitution

$$\mathbf{z} = \mathbf{T}\check{\mathbf{x}} \tag{5.11}$$

where $\mathbf{z}$ is the state vector of the transformed system [Föl22]. Hereby the transformation matrix is given by

$$\mathbf{T} = \begin{bmatrix} \mathbf{t}_1^{\mathrm{T}} \\ \mathbf{t}_1^{\mathrm{T}}\mathbf{A}^{\mathrm{c}} \\ \vdots \\ \mathbf{t}_1^{\mathrm{T}}\mathbf{A}^{\mathrm{c}n-1} \end{bmatrix} \tag{5.12}$$

with $\mathbf{t}_1^{\mathrm{T}}$ being the last row of the inverse controllability matrix

$$\mathbf{Q}^{-1}_{\mathrm{ctrb}} = [\mathbf{B}^{\mathrm{c}}, \quad \mathbf{A}^{\mathrm{c}}\mathbf{B}^{\mathrm{c}}, \quad \cdots, \quad \mathbf{A}^{\mathrm{c}n-1}\mathbf{B}^{\mathrm{c}}]^{-1}. \tag{5.13}$$

The remaining plant in control canonical form is hence given by

$$\begin{bmatrix}\dot{z}_1\\ \dot{z}_2\\ \dot{z}_3\\ \dot{z}_4\\ \dot{z}_5\end{bmatrix}=\begin{bmatrix}0 & 1 & 0 & 0 & 0\\ 0 & 0 & 1 & 0 & 0\\ 0 & 0 & 0 & 1 & 0\\ 0 & 0 & 0 & 0 & 1\\ -a_0 & -a_1 & -a_2 & -a_3 & -a_4\end{bmatrix}\begin{bmatrix}z_1\\ z_2\\ z_3\\ z_4\\ z_5\end{bmatrix}+\begin{bmatrix}0\\ 0\\ 0\\ 0\\ 1\end{bmatrix}\breve{u} \tag{5.14}$$

for which a full state-feedback controller using eigenvalue assignment is synthesized. The state-feedback control law in control canonical form is defined as

$$\breve{u}=-\breve{\mathbf{K}}_{\mathrm{pz}}\mathbf{z}=-[k_{pz,1}\quad k_{pz,2}\quad k_{pz,3}\quad k_{pz,4}\quad k_{pz,5}]\begin{bmatrix}z_1\\ z_2\\ z_3\\ z_4\\ z_5\end{bmatrix}. \tag{5.15}$$

Through substitution of the control law (5.15) into the plant (5.14) the closed loop system in control canonical form is obtained

$$\begin{bmatrix}\dot{z}_1\\ \dot{z}_2\\ \dot{z}_3\\ \dot{z}_4\\ \dot{z}_5\end{bmatrix}=\begin{bmatrix}0 & 1 & 0 & 0 & 0\\ 0 & 0 & 1 & 0 & 0\\ 0 & 0 & 0 & 1 & 0\\ 0 & 0 & 0 & 0 & 1\\ -a_0-k_{pz,1} & -a_1-k_{pz,2} & -a_2-k_{pz,3} & -a_3-k_{pz,4} & -a_4-k_{pz,5}\end{bmatrix}\begin{bmatrix}z_1\\ z_2\\ z_3\\ z_4\\ z_5\end{bmatrix} \tag{5.16}$$

from which the characteristic polynomial is directly derived

$$p(s)=s^5+\left(a_4+k_{pz,5}\right)s^4+\left(a_3+k_{pz,4}\right)s^3+\left(a_2+k_{pz,3}\right)s^2+\left(a_1+k_{pz,2}\right)s+a_0+k_{pz,1}. \tag{5.17}$$

For controller synthesis, it is required that the locations of the initial eigenvalues are maintained and exclusively the integrator eigenvalues are assigned. Hereby the latter are assigned to two real-valued eigenvalues at $s_{4,5}=-0.25$ for stabilization. These specifications are included in the following desired characteristic polynomial

$$p_{des}(s)=s^5+p_4s^4+p_3s^3+p_2s^2+p_1s+p_0. \tag{5.18}$$

Coefficient comparison of the characteristic polynomial given by (5.17) and (5.18) yields the controller gains in control canonical form

$$\breve{\mathbf{K}}_{\mathrm{pz}}=[p_0-a_0,\ \ p_1-a_1,\ \ p_2-a_2,\ \ p_3-a_3,\ \ p_4-a_4] \tag{5.19}$$

which are transformed back to the coordinates of the original physical states using (5.11) to obtain the final control law

$$\breve{u}=-\breve{\mathbf{K}}_{\mathrm{pz}}\mathbf{z}=-\breve{\mathbf{K}}_{\mathrm{pz}}\mathbf{T}\breve{\mathbf{x}}=-\breve{\mathbf{K}}_{\mathrm{p}}\breve{\mathbf{x}}. \tag{5.20}$$

For the digital implementation, the virtual control loop consisting of control law and remaining plant model is discretized using a step-invariant discretization and a sampling time of $\mathrm{T_s}=0.001$ sec.

5.3.2 Reference Path Reinitialization

It is recalled that $y_\mathrm{r}(k)$ represents the lateral deviation between the vehicle's center of gravity and the reference path (refer to Figure 12), which is measured and preprocessed by an appropriate vision system. During a lane change, the vision system is subject to a change in the reference path. Before the maneuver, the lateral deviation is measured with respect to the reference path of the current lane, whereas after the maneuver it is measured with respect to the reference path of the new lane. Hence, at the transition point, which is defined as the point where the vehicle crosses the lane boundary, a discontinuity in the lateral deviation occurs. This discontinuity can be handled by applying an offset correction to the state variable $y_\mathrm{r}(k)$ of the dynamic cooperative feedforward control and the extended optimal state-estimator. Thereby the corresponding state variables are reinitialized to the correct values at the time of transition. The other plant state variables continuously evolve over time and thus remain unchanged. Figure 55 depicts a block diagram of the cooperative lateral vehicle guidance control loop with the respective reinitialization interfaces. As the remaining plant model inside the dynamic cooperative feedforward control and the extended optimal state-estimator is implemented in state-variable form, the corresponding states are directly accessible for reinitialization. The same reinitialization interfaces are exploitable for the functional integration with a trajectory planner.

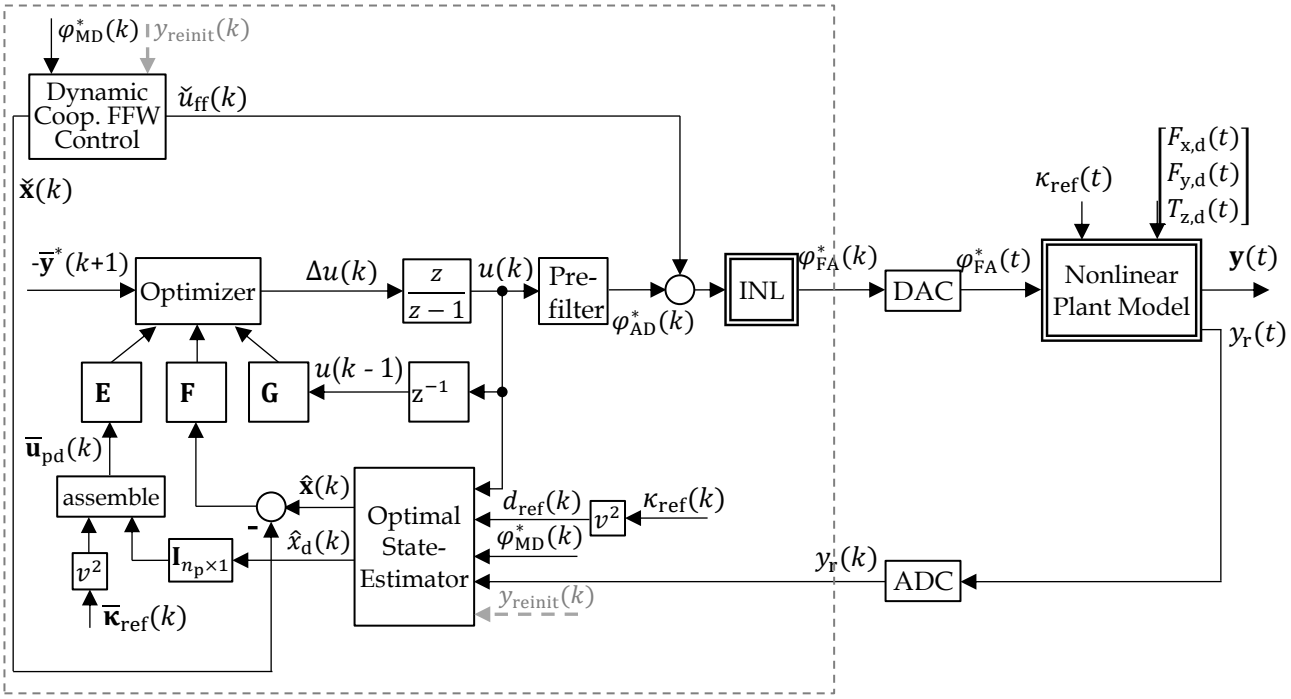

Figure 55: Cooperative Lateral Vehicle Guidance Control with Reinitialization Interfaces

5.4 Control System Analysis

In this section, the performance of the cooperative HWA control and the cooperative lateral vehicle guidance control is verified using nonlinear simulation analysis. For this purpose, realistic driving maneuvers are considered in the following to demonstrate the effect of a driver intervention in cooperative driving mode.

5.4.1 Cooperative Handwheel Actuator Control

For the first scenario, cooperative driving on a winding road at a vehicle speed of 80 km/h is examined. Due to roadwork, the lane narrows on the right side, which forces the driver to intervene in order to keep the vehicle at a safe lateral distance. Figure 56 depicts the simulation results for the cooperative HWA control. Thereby, the steering position control and steering torque control are shown separately. The vehicle initially follows the automated driving trajectory, and the lateral vehicle guidance controller provides the required reference steering position to the HWA and FAA, respectively. The superposition control accurately tracks this reference steering position in the absence of driver intervention. At a simulation time between 4.5 and 16 seconds, the driver intervenes to steer the vehicle away from the construction work. The driver torque input at the steering wheel is reconstructed by the driver torque estimator and provided as an input to the virtual control loop. Consequently, a reference steering torque is generated, which is supplied to the steering torque controller and precisely tracked. Due to the superposition control concept, the driver can override the active steering position control while experiencing a desired steering feel. Hereby, the transitions are seamless as no blending, gain scheduling, or controller output saturation is required, allowing for true coexistence between steering position and torque control.

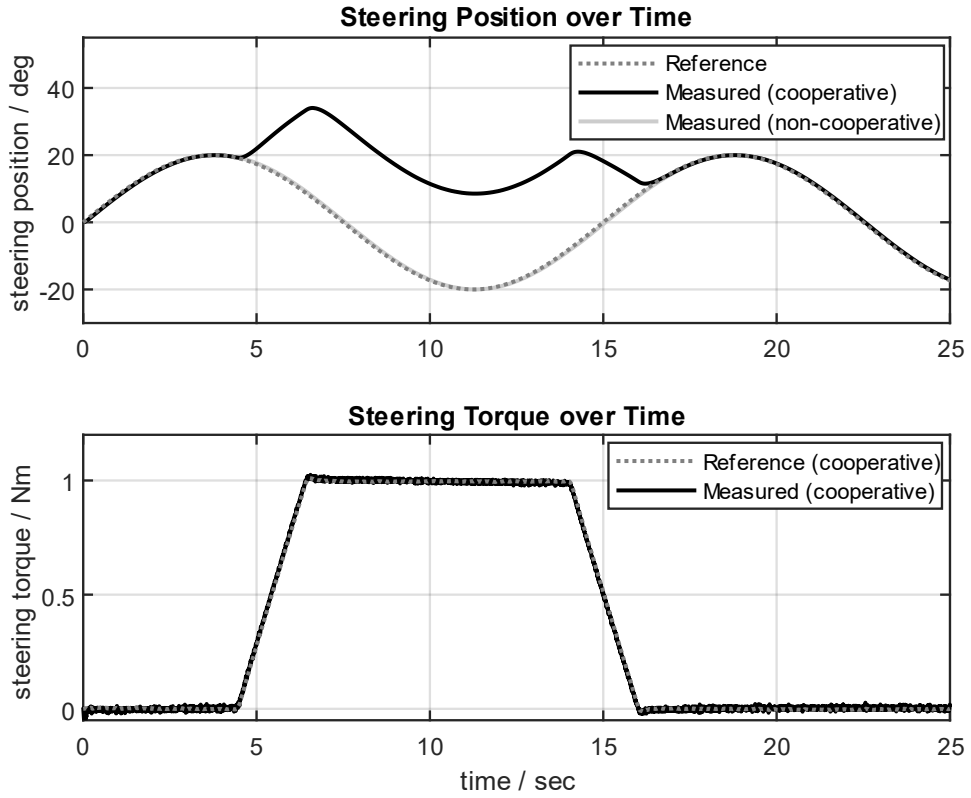

Figure 56: Superposition Control – Fusing Steering Position and Torque Control

For comparison, the results for a non-cooperative control behavior are further illustrated in Figure 56. In this scenario, the steering position controller interprets the driver input as a disturbance that is actively compensated. Hence, the control counteracts the driver to maintain its primary control objective, which is reference steering position tracking. Figure 57 illustrates the performance of the driver torque estimation in time and frequency domain. The estimation bandwidth is 85 Hz and therefore allows a dynamic

reconstruction of the driver input. A driver torque of 1 Nm at the steering wheel is reconstructed within 6 msec and provided as a direct input to the superposition control.

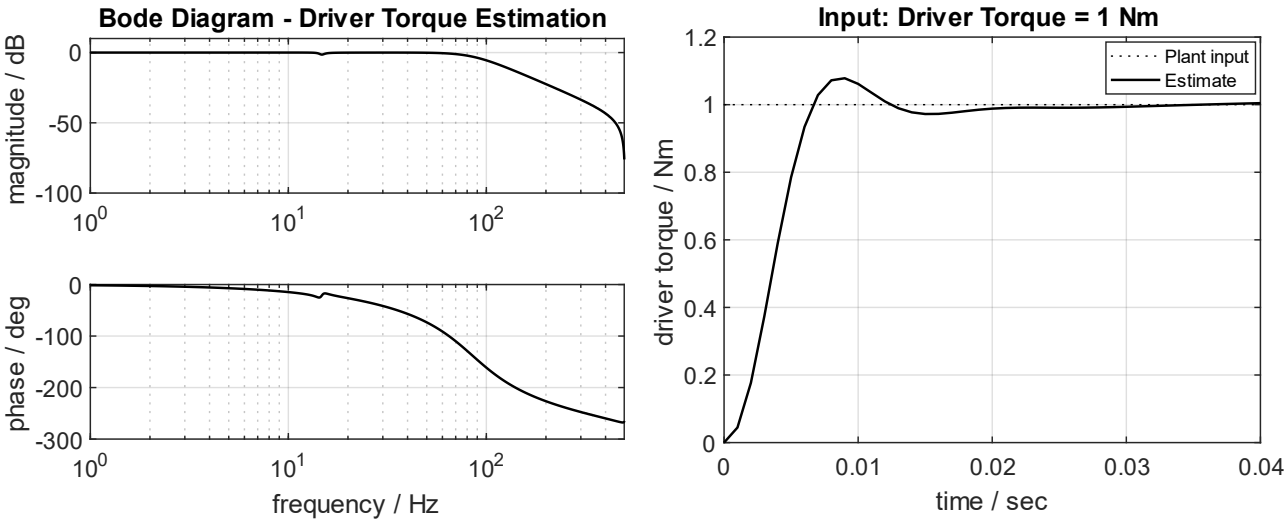

Figure 57: Superposition Control – Driver Torque Estimation Performance

5.4.2 Cooperative Lateral Vehicle Guidance Control

In the second scenario, cooperative driving on a straight road at a vehicle speed of 50 km/h is analyzed. The vehicle initially precisely follows the reference trajectory provided by the automation system, which is exposed by a lateral deviation of zero. Figure 58 depicts the simulation results for the cooperative lateral vehicle guidance control. Due to an obstacle that is undetected by the automation system, the driver intervenes in the driving task at a simulation time between 10 to 14 seconds. For obstacle avoidance, a lateral deviation of 1.5 meters is sufficient. This lateral deviation is induced by the driver steering input as illustrated. Therefore, the 2DOF Nonlinear Adaptive MPC accurately tracks the given reference path in the absence of a driver intervention. In the event of a driver intervention, the driver can override the active control and continuously modify the lateral vehicle trajectory. For reasons of comparison, the results for a non-cooperative control behavior are moreover illustrated. In this case, the lateral vehicle guidance controller counteracts the driver steering input and the lateral vehicle trajectory cannot be modified.

As the last scenario, a lane change in cooperative driving mode at a vehicle speed of 50 km/h is considered. During the lane change, the vision system is subject to a change in the reference path. Hence, a discontinuity in the lateral deviation measurement occurs. The discontinuity is handled by a reinitialization of the corresponding state variables in the dynamic cooperative feedforward control and the extended optimal state-estimator. Consequently, the lane change is smoothly completed, and the control activity is resumed.

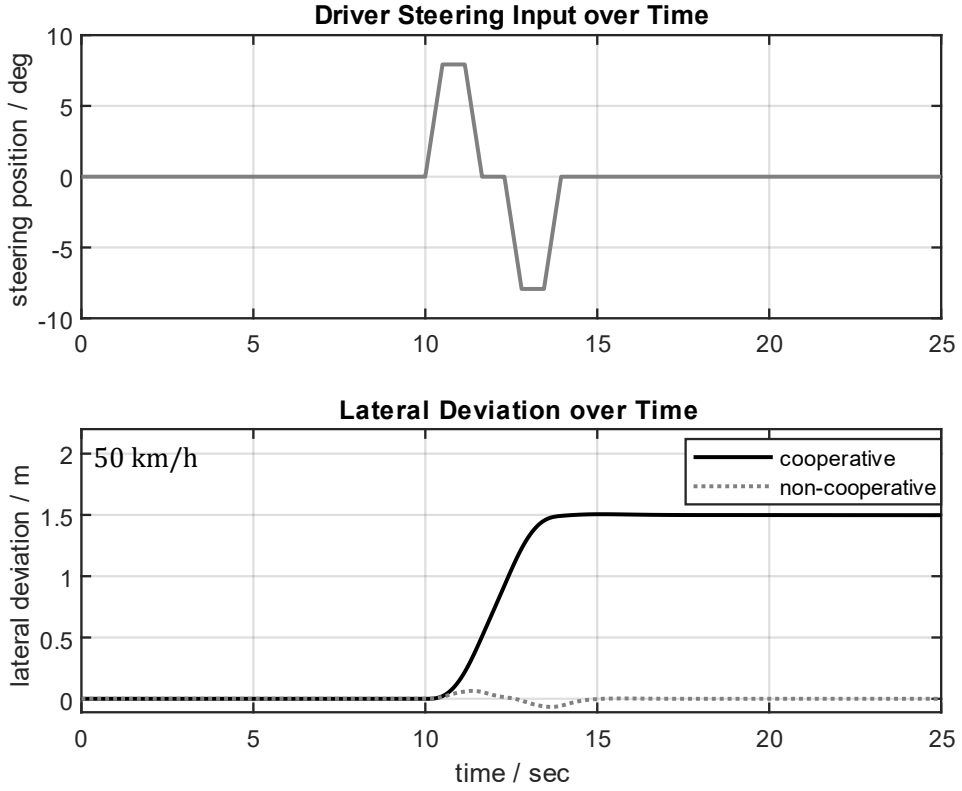

Figure 58: 2DOF Nonlinear Adaptive MPC – Fusing Manual and Automated Lateral Vehicle Guidance

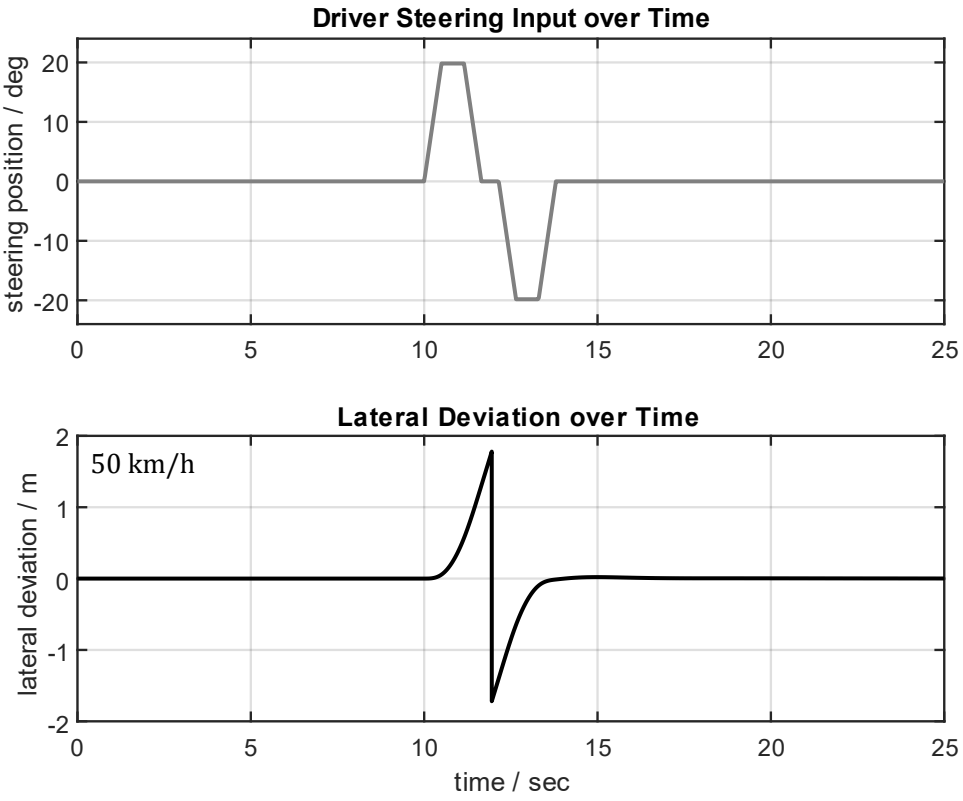

Figure 59: 2DOF Nonlinear Adaptive MPC – Reinitialization during a Lane Change

6

Realization and Validation of the Concept

Besides the preceding theoretical contributions to an integrated control structure for the cooperative lateral vehicle guidance, the practical realization and validation of the concept represent an essential part of this thesis. In this chapter, the performance of the synthesized controls is evaluated using realistic driving scenarios. For this purpose, a sequential proceeding is selected. At first, the Steer-by-Wire prototype vehicle and the installed development hardware are presented. Thereafter, an automated driving emulation for the demonstration of cooperative lateral vehicle guidance control functions is described. Hereby, a spline-based reference path generation and map matching are employed. Subsequently, the performance evaluation of the control concepts is conducted based on real vehicle tests. In this context, the Steer-by-Wire controls for manual and automated driving are first examined. Afterward, the lateral vehicle guidance control for automated driving is detailly tested. Finally, the extensions of the Steer-by-Wire and lateral vehicle guidance controls for cooperative driving are evaluated.

6.1 Steer-by-Wire Prototype Vehicle

The prototype vehicle illustrated in Figure 60 represents a VW Golf 7, which is equipped with a Steer-by-Wire system. As no stereoscopic camera for lane detection is installed in the vehicle, the relevant signals are emulated by a DGPS-based inertial sensor platform.

Figure 60: Steer-by-Wire VW Golf 7 Prototype Vehicle with DGPS System for Localization

For this purpose, the route to be driven is manually recorded, pre-processed, and stored as the reference path. Based on the current vehicle position relative to the reference path, the required error signals for the lateral vehicle guidance control are analytically computed online (refer to [Gon+20]). The cooperative HWA and cooperative lateral vehicle guidance control are autocoded, compiled, and flashed on a dSPACE MicroAutoBox II with DS1007 processor board. The latter communicates with other control units in the vehicle over respective Ethernet and CAN interfaces.

6.2 Spline-based Reference Path Generation and Map Matching

Figure 61 shows a satellite image of the oval test track, which is used for the evaluation of the cooperative lateral vehicle guidance control function. The route to be driven is manually recorded by a professional test driver using a DGPS platform. Thereafter, an advanced algorithm for spline-based reference path generation and map matching is applied. The reference path generation algorithm employs a regularized constrained least-squares method for optimally fitting piece-wise cubic polynomial functions to the scattered DGPS data. Thereby, a smooth, mathematical model for the reference path is obtained (see Figure 61). Based on this model, a map matching algorithm performs an online optimization to search for the minimum distance between the vehicle and the reference path. At the minimum distance point, exact computations of the lateral deviation $y_{\mathrm{r}}(k)$ and reference path curvature $\kappa_{\mathrm{ref}}(k)$ are performed. Furthermore, under the assumption that the vehicle follows the reference path at a constant speed and without deviations, the future reference path curvature sequence $\overline{\boldsymbol{\kappa}}_{\mathbf{ref}}(k)$ is determined over the entire prediction horizon and thus for a lookahead time of 750 msec. By this proceeding, a smooth and continuous calculation of the control error signals for lateral vehicle guidance is obtained, which is decisive for the accuracy and performance of control. The details of the spline-based reference path generation and map matching algorithm are given in Appendix A. Additionally, the derivation of the solution to the regularized constrained least-squares optimization problem for spline regression is provided.

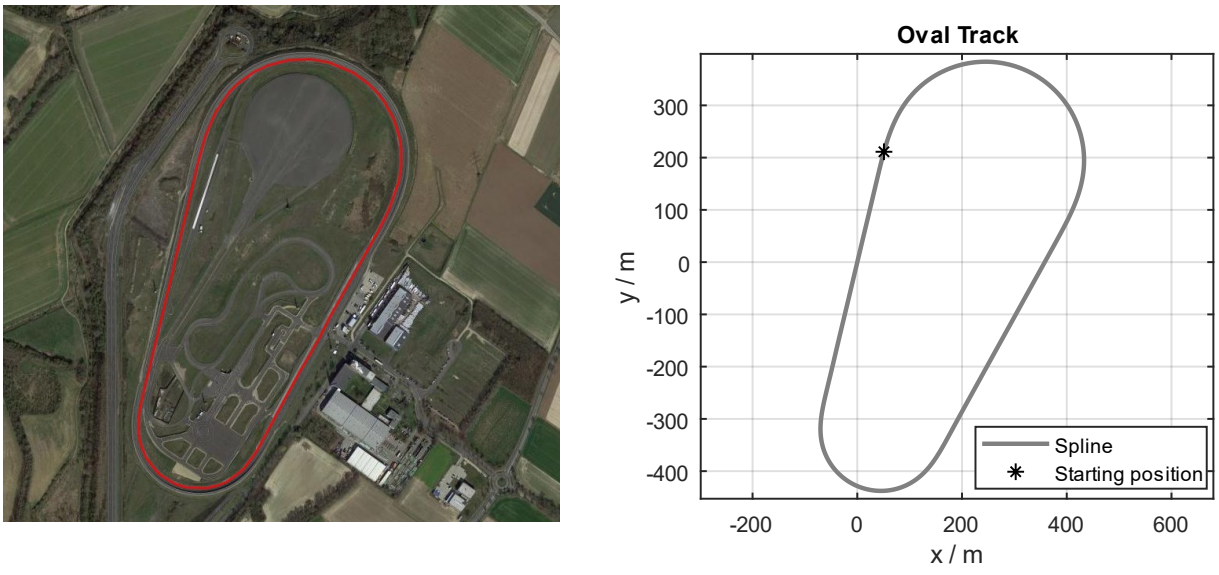

Figure 61: Satellite Image of the Oval Test Track and Spline-based Reference Path

6.3 Performance Evaluation: Steer-by-Wire Control Systems

The performance of the developed overall control system is validated in the following using real vehicle measurements. For this purpose, the performance of the Steer-by-Wire controls for manual driving is first examined. With this regard, the HWA is operated in steering torque control mode and receives a desired reference steering torque for steering feel generation. The FAA is steering position controlled and uses the measured steering wheel position as a reference. Thus, the missing mechanical linkage between the steering wheel and road wheels is emulated by controls. As a first test, the vehicle is driven on a vehicle dynamics area (VDA) at a constant speed of 30 km/h. The driver performs a sweep steering maneuver starting at a frequency of 0.25 Hz that is progressively increasing up to 3.2 Hz. Figure 62 shows the vehicle test results by illustrating the reference steering torque and measured steering torque over time as well as the control error over time. From the measurements, it is revealed that the LQG steering torque controller accurately tracks the given reference torque profile. The control shows zero steady-state error and achieves a strong disturbance rejection. Disturbance torques from nonlinear friction, which are occurring during motion reversals, and driver torque disturbances are rapidly compensated. Moreover, the control is found to be stable over the complete operating range of the Steer-by-Wire system and shows good robustness.

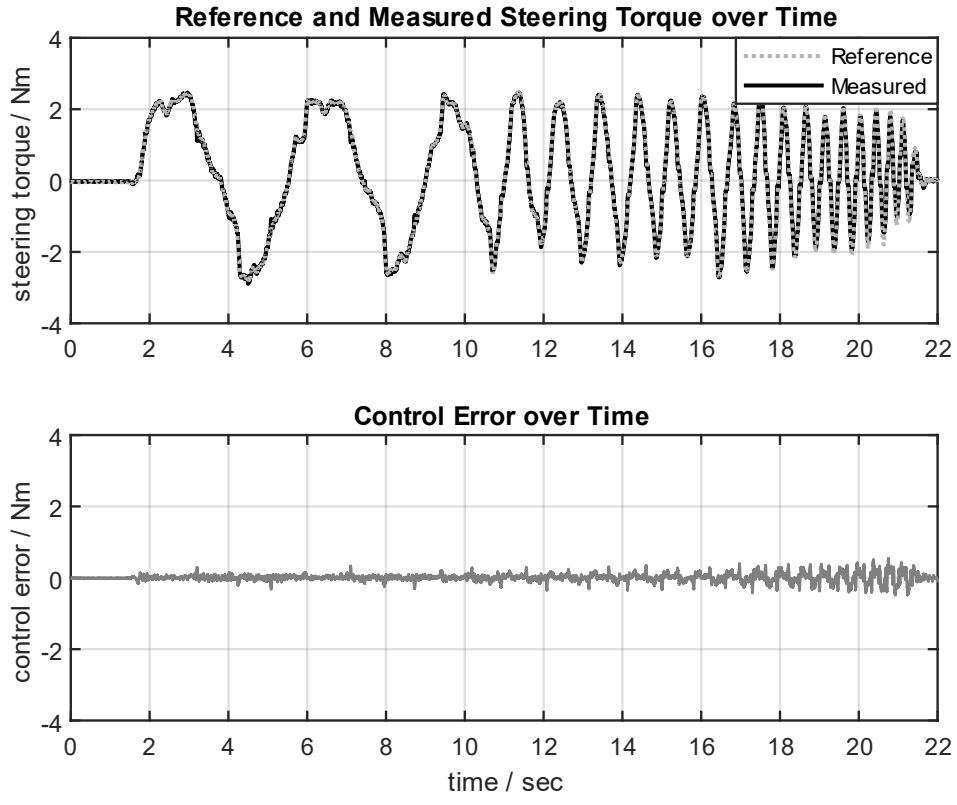

Figure 62: Performance Measurement – HWA Steering Torque Control

For assessing the dynamic performance of the FAA steering position control, the vehicle is driven on a handling track close to the limits of vehicle dynamics. Thereby, vehicle speeds above 90 km/h and steering wheel positions over 135 deg are reached. Figure 63 summarizes the vehicle test results by showing the reference steering position and measured steering position, the control error, and the vehicle speed over time. Even for

this highly dynamic driving maneuver at various vehicle speeds and with large steering wheel positions, the measured position precisely tracks the reference position. The maximum control error is approximately two degrees over the entire time range, thereby providing evidence for an excellent control performance in the real vehicle. Besides an accurate reference tracking performance, the 2DOF LQG steering position control is stable over the entire operating range of the system. A vehicle dynamics expert subjectively rated the vehicle reaction to driver steering inputs as responsive, linear, and dynamic. The NVH performance is also rated acceptable.

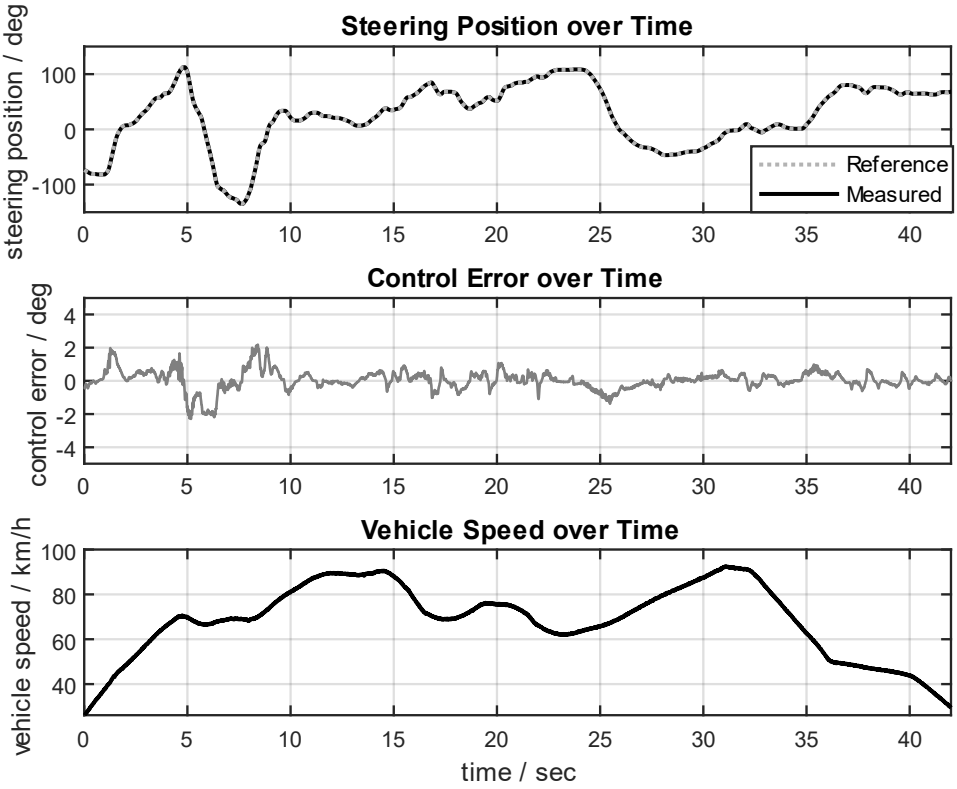

Figure 63: Performance Measurement – FAA Steering Position Control

As the last test, the performance of the HWA steering position control is evaluated, which is used in automated driving mode. For this purpose, the vehicle is driven on the VDA at a constant speed of 30 km/h, and a sine wave signal with a constant frequency of 1 Hz and amplitude of 45 deg is injected as the reference steering position. Figure 64 depicts the vehicle test results for the automated HWA control by showing the reference and measured steering position over time and the control error over time. From the results it is exposed that the cascade 2DOF LQG steering position controller for the HWA precisely tracks the supplied reference steering position. Disturbance torques from nonlinear friction during motion reversals are actively compensated by the controller and completely rejected in steady state. The control bandwidth is hereby selected to 4 Hz, which ensures good reference tracking and smooth steering wheel motions. The latter is particularly important for the integration of the Steer-by-Wire controls and the lateral vehicle guidance control as explained in chapter 3.1. The control was extensively tested for different amplitudes and frequencies of the reference excitation signal. Hereby, a stable behavior was consistently found over the complete

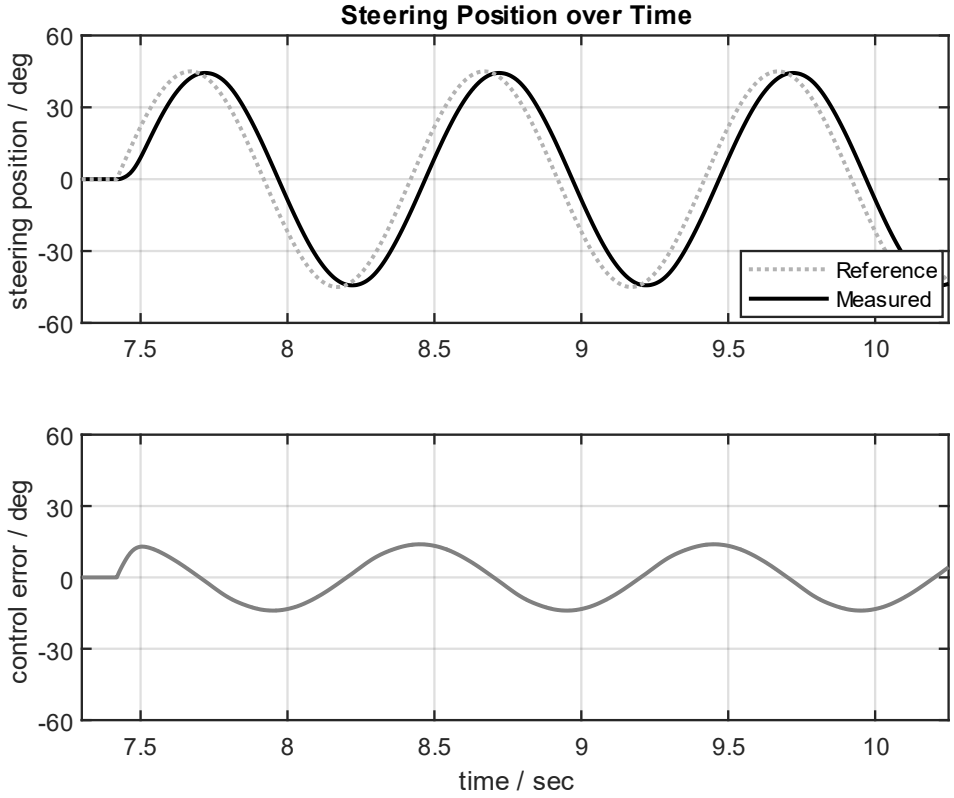

Figure 64: Performance Measurement – HWA Steering Position Control

operating range of the Steer-by-Wire system.

6.4 Performance Evaluation: Automated Lateral Vehicle Guidance

After the experimental validation of the Steer-by-Wire controls, the lateral vehicle guidance control for automated driving is detailly tested. For this purpose, real vehicle tests at different vehicle speeds and steering positions are conducted on the oval test track to get a representative impression of the controller performance. Figure 61 shows the test track in x-y coordinates with the vehicle starting position marked by a black star. The test track was manually recorded by a professional test driver and optimally fitted by a regression spline to generate a fixed reference path. For an accurate localization, the vehicle position is measured using a DGPS-based inertial sensor platform. By comparing the current vehicle position to the reference path, an exact computation of the control error signals for automated lateral vehicle guidance is performed. This automated driving emulation provides a suitable basis for assessing the control performance.
Figure 65 shows the vehicle results for automated lateral vehicle guidance at a constant speed of 70 km/h by illustrating the lateral deviation relative to the reference path, the measured steering position, and the vehicle speed over time. The Nonlinear Adaptive MPC accurately tracks the given reference path, which is exposed by a maximum lateral deviation of 0.16 m that occurs at the entry to the tightest curve segment. Moreover, by

comparison of Figure 48 and 65, a good fit between vehicle results and nonlinear simulation analysis is revealed, thereby confirming the validity of controller design. Minor deviations are due to model error, neglected roll and pitch motion as well as side wind disturbances. The control was further extensively tested for vehicle speeds ranging from standstill up to 130 km/h. Hereby, it has proven a strong tracking performance and stable behavior over the entire vehicle speed range.

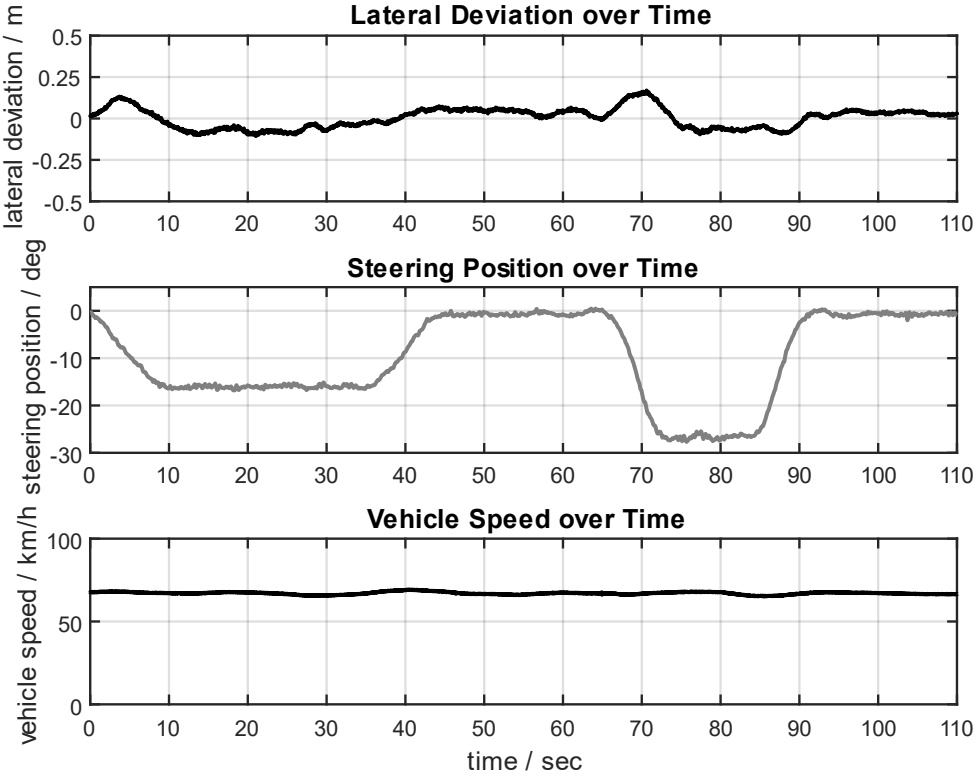

Figure 65: Performance Measurement – Automated Lateral Vehicle Guidance Control

For assessing the real-time capability, the Nonlinear Adaptive MPC algorithm is run on a dSPACE MicroAutoBox II with a 900 MHz PowerPC 750GL processor. The optimizer uses an active set method for a safely convergent and efficient determination of the MPC solution. With a turnaround time of approximately 0.8 msec, the MPC completes the computations within the sampling interval of 50 msec and therefore in real-time.

6.5 Performance Evaluation: Cooperative Lateral Vehicle Guidance

In this chapter, the performance of the complete control system for cooperative lateral vehicle guidance is validated. For this purpose, the extensions of the Steer-by-Wire and lateral vehicle guidance controls for permitting driver interventions are considered. Consequently, the driver can intervene in the driving task and seamlessly modify the lateral vehicle motion while experiencing an authentic steering feel. For the evaluation of the cooperative lateral vehicle guidance control, the following driving maneuvers are examined

- **Maneuver 1:** Avoiding an obstacle that is undetected by the automation system
- **Maneuver 2:** Overtaking a slow-moving vehicle on a single lane road
- **Maneuver 3:** On-center steering within the current lane

which are conducted on the straight sections of the oval test track. Since no stereoscopic camera is installed in the vehicle, the essential signals are, as previously explained, emulated by a DGPS-based inertial sensor platform.

As a first maneuver, cooperative driving on a straight road at a vehicle speed of 70 km/h is considered. Due to an object that is undetected by the automation system, the driver must intervene in the driving task. Figure 66 shows the vehicle results of the cooperative lateral vehicle guidance control for obstacle avoidance by illustrating the reference and measured steering position, the reference and measured steering torque, and the lateral deviation relative to the reference path over time. The vehicle initially precisely follows the reference path, and the cooperative lateral vehicle guidance controller supplies the required reference steering position to the cooperative HWA control and the FAA control respectively. The cooperative HWA control accurately tracks this reference steering position in the absence of a driver intervention. Hereby, the driver torque estimate is zero and hence no reference steering torque is generated by the virtual control loop. At the time between 5.6 and 14.2 seconds, the driver intervenes and overrides the active control for obstacle avoidance. During the intervention, the driver torque is estimated and provided as an input to the virtual control loop, which generates the required reference steering torque for steering feel. This reference steering torque is forwarded to the steering torque controller and accurately tracked. Hence, the driver

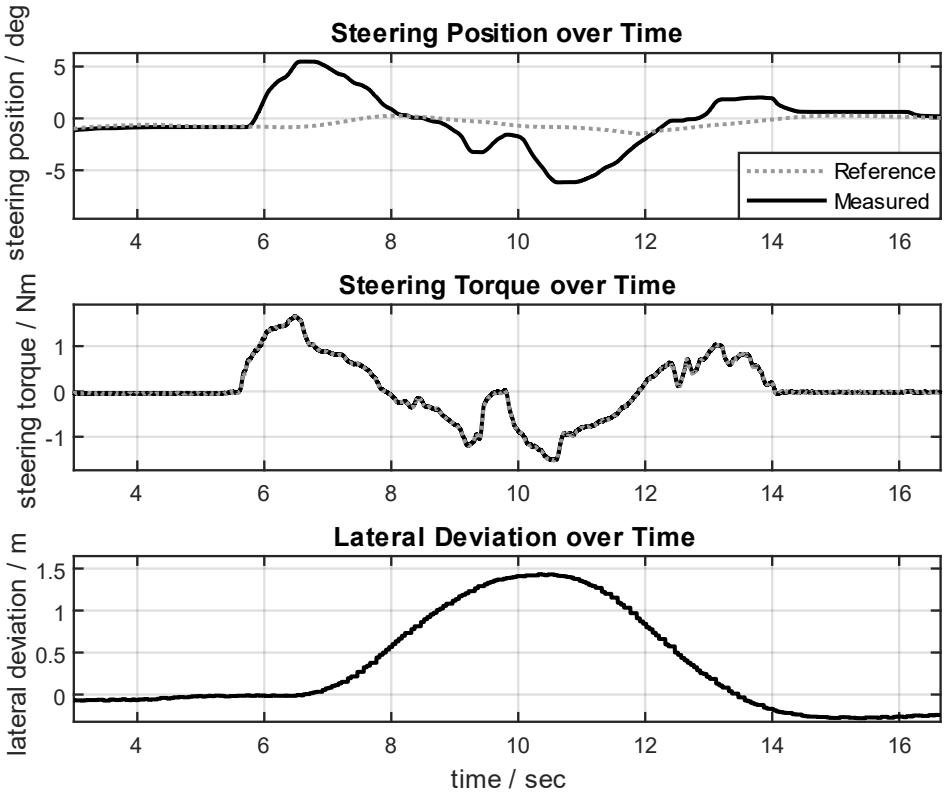

Figure 66: Performance Measurement – Cooperative Lateral Vehicle Guidance Control: Avoiding an Obstacle Undetected by the Automation System at 70 km/h

can override the lateral vehicle guidance control and perceives a desired steering feel that is symmetric about the reference path. For safe obstacle avoidance, a driver-induced lateral deviation of 1.4 m relative to the reference path is sufficient. The transitions hereby are smooth, as no manual switching processes that involve discontinuities are used.

As another maneuver, cooperative driving on a straight road at a vehicle speed of 75 km/h is considered. The driver hereby intervenes in the driving task for overtaking a slow-moving vehicle. Figure 67 depicts the vehicle results of the cooperative lateral vehicle guidance control by illustrating the reference and measured steering position, the reference and measured steering torque, and the lateral deviation with respect to the reference path over time. Before the maneuver, the vehicle precisely follows the reference path as revealed by a lateral deviation near zero. The cooperative lateral vehicle guidance controller outputs the required reference steering position for both the cooperative HWA control and the FAA control. This reference steering position is accurately tracked by the respective HWA and FAA steering position controls in the absence of a driver intervention. The reference torque for steering feel generation is zero. At a time of 2.2 seconds, the driver intervenes in the driving task for initiating the overtaking maneuver. The driver torque at steering wheel is reconstructed by the extended optimal state-estimator and provided as an input to the virtual control loop. Consequently, a reference steering torque is generated and forwarded to the steering torque control for providing the desired steering feel to the driver. The driver intervention is accepted by the cooperative lateral vehicle guidance control. Consequently, the driver can override the active control and induce a lateral deviation of 3.5 m for a lane change. Hereby, a natural steering feel is perceived that is symmetric about the reference path.

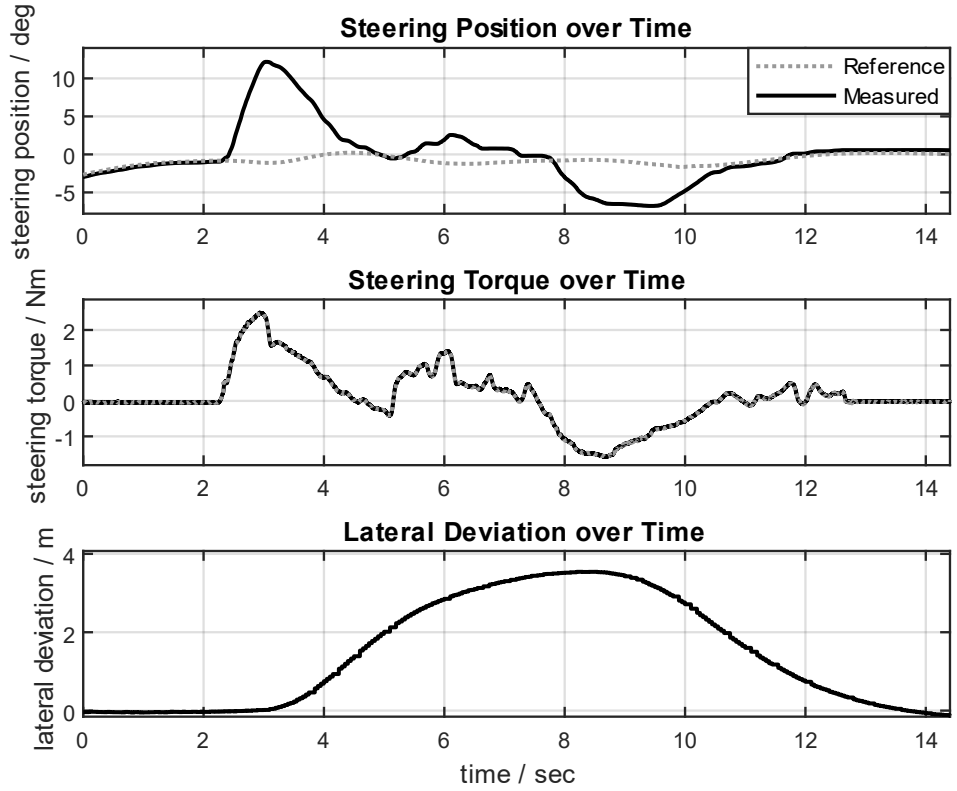

Figure 67: Performance Measurement – Cooperative Lateral Vehicle Guidance Control: Overtaking a Slow-Moving Vehicle on a Single Lane Road at 75 km/h

After successfully passing the slow-moving vehicle, the driver returns to the initial lane and removes his hands from the steering wheel. Hence, the lateral vehicle guidance is resumed, and the vehicle precisely follows the reference path. Thus, cooperative lateral vehicle guidance control enables the driver to modify the lateral vehicle motion continuously and without transitions.

In a last maneuver, cooperative driving on a straight road at a vehicle speed of 60 km/h is examined. The driver performs a sinusoidal steering test within the current lane to evaluate the on-center steering feel and the symmetry of the torque build-up in cooperative driving mode. Figure 68 shows the vehicle results by depicting the reference and measured steering position, the reference and measured steering torque as well as the lateral deviation to the reference path over time. In the absence of a driver intervention, the cooperative lateral vehicle guidance control accurately tracks the reference path. The generated reference steering position is precisely tracked by the cooperative HWA control and the reference steering torque is zero. At the time interval between 2.1 and 15.4 seconds, the driver applies a sinusoidal steering input. The driver torque at the steering wheel is estimated and provided as input to the virtual control loop. Consequently, the reference steering torque for providing a desired steering feel is generated and forwarded to the steering torque control. The cooperative HWA control permits the driver torque and the generated reference steering torque. Hence, the driver can override the active control. Hereby, a natural on-center steering feel is perceived. The torque build-up is consistent and symmetric about the reference steering position (see Figure 69). In addition, the intervention process is intuitive, which reduces the driver workload while improving comfort and safety.

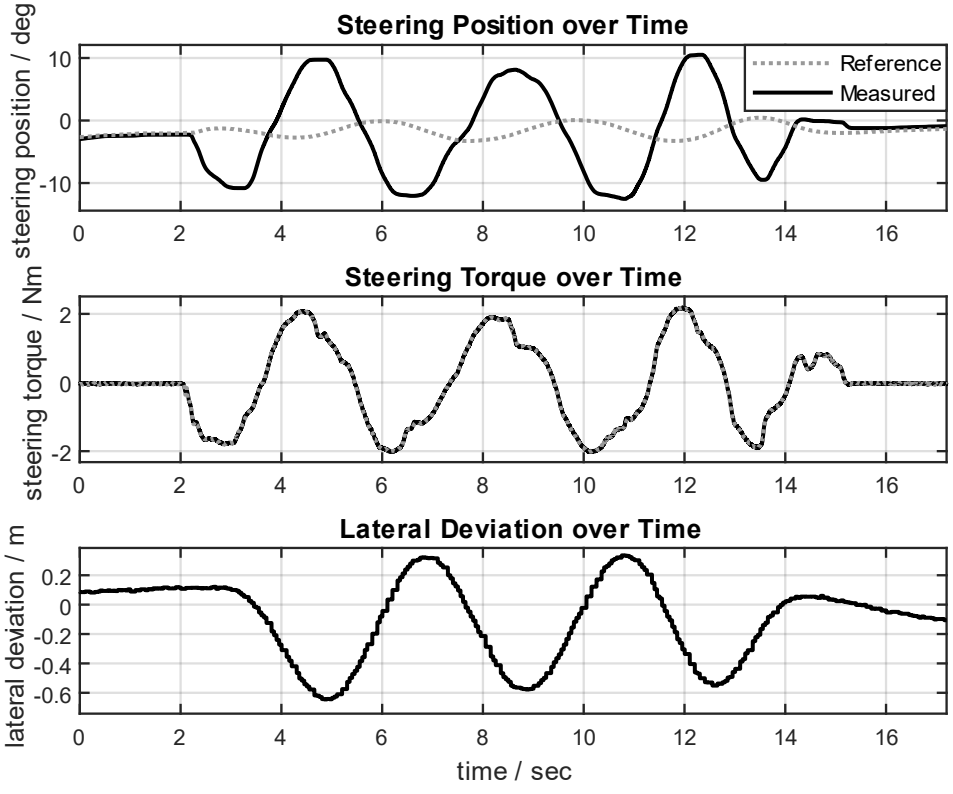

Figure 68: Performance Measurement – Cooperative Lateral Vehicle Guidance Control: On-Center Steering Within the Current Lane at 60 km/h

Figure 69: Performance Measurement – Cooperative Lateral Vehicle Guidance Control: Consistency and Symmetry of the Torque Build-Up at 60 km/h

7

Conclusion and Outlook

With the global trend towards automated driving, fault-tolerant onboard power supply systems are introduced into modern vehicles, and the level of driving automation is continuously increasing. These changes contribute to the applicability of Steer-by-Wire systems and the development of automated lateral vehicle guidance control functions. For the market acceptance of automated driving, the lateral vehicle guidance control function must be cooperative, that is it must accept driver interventions.

On the basis of this motivation, a cooperative lateral vehicle guidance control (CVGC) concept is systematically designed in this thesis, which fuses manual steering control by the driver and automated steering control. To this end, the subordinate controls of the SbW system for the manual and automated driving mode are initially synthesized. These include the steering feel generation and LQG steering torque control of the Steer-by-Wire HWA for the manual driving mode. The latter is structurally extended to a cascade 2DOF LQG steering position control for the automated driving mode. This approach has the advantage that the LQG steering torque control persists as an inner control loop and that the interfaces to the outer steering position controllers are identical. The steering position controllers thereby pursue different objectives, which is either steering feel generation or reference steering position tracking. By exploiting these structural similarities, a superposition control is developed, which fuses steering torque and steering position control. Using this approach, a cooperative HWA control is realized, which ensures accurate tracking of the reference steering position but accepts driver interventions. In the event of a driver intervention, the driver can hence override the active control and perceives a desired steering feel that is symmetric about the reference steering position. The transitions hereby are seamless as no blending, gain scheduling, or controller output saturation is required. The concept furthermore provides the advantage that the steering feel generation and steering position control are independently designed. Thus, the calibration effort regarding potential applications in future series production vehicles is reduced.

Subsequently, the superimposed Nonlinear Adaptive Model Predictive Controller for automated lateral vehicle guidance is synthesized, which computes the required reference steering position for the respective SbW controls. In contrast to existing approaches, the plant equations are rearranged to isolate the vehicle speed-dependent dynamics. Thereafter, the concept of inverse nonlinearity control is employed, using a virtual control loop and feedback linearization control for an online inversion of the nonlinear plant dynamics. The remaining plant is linear and independent of vehicle speed.

Consequently, one controller can be synthesized that is valid for all operating points. The resulting closed and open loop system have the same dynamics independent of vehicle speed. This significantly facilitates control system design, analysis, and performance tuning in the vehicle. For explicitly considering constraints on the maximum steering position within the control law and employing previewing capability, a Model Predictive Controller synthesis is selected. With this regard, the future reference path curvature information is used for computing the optimal control input sequence, thereby providing superior lateral vehicle guidance control performance. Furthermore, by considering the unknown disturbance estimate, which is reconstructed by an extended optimal state-estimator, as an input to the MPC prediction model, the resulting controller receives integral action. Hence, robustness against unknown disturbances such as side wind, road camber, neglected plant dynamics, and parameter variation is guaranteed. The synthesized Nonlinear Adaptive Model Predictive Controller ensures accurate lateral vehicle guidance but interprets the driver induced lateral deviation as an external disturbance. This motivates the synthesis of a 2DOF Nonlinear Adaptive Model Predictive Controller for cooperative lateral vehicle guidance. The latter relies on a structural extension of the original controller by a cooperative dynamic feedforward control for separating the driver induced lateral deviation from the remaining lateral deviation. Under exploitation of the superposition principle, the driver can thus override the active control and seamlessly modify the lateral vehicle motion. The transitions hereby are continuous since no switching operations are required.

The complete control concept for the cooperative lateral vehicle guidance is extensively tested in nonlinear simulation analyses to verify the control performance under actuator constraints and plant nonlinearities. Subsequently, the control concept is practically realized and experimentally validated in a Steer-by-Wire VW Golf 7 prototype vehicle. For this purpose, realistic driving maneuvers are considered that successfully demonstrate the effectiveness of the developed approach in practical application.

The results of this work motivate the continuation of the development activities in the field as part of future research. In this context, the commissioning of CVGC with a stereoscopic camera and other environment sensors such as LIDAR instead of the DGPS system is to be conducted. Furthermore, the integration of the function with a higher-level trajectory planner is subject to future developments. The required interfaces for performing such an integration were already presented in this work. Another aspect is the extension of the inverse nonlinearity control, as an essential component of the CVGC function, for different road friction coefficients. With this regard, an appropriate interface to an external road friction estimation module must be established. As the impact of varying road friction coefficients is exclusively compensated by inverse nonlinearity control, all other components of the CVGC function can remain unchanged. A last point is the extension of the control concept for cooperative longitudinal vehicle guidance. Hereby, the vehicle speed is closed loop controlled to a reference vehicle speed provided by the trajectory planner. The longitudinal vehicle guidance controller precisely tracks the given reference vehicle speed but permits driver interventions in form of accelerator or brake pedal operation. Consequently, a cooperative trajectory tracking controller is realized. The latter improves the driving comfort and safety on the way to highly automated driving and is hence indispensable.

A

Algorithms for Automated Driving Emulation

The availability of a reliable piloted driving environment is crucial for the development of automated and cooperative lateral vehicle guidance control functions tightly integrated with the Steer-by-Wire controls. For this purpose, an advanced method is presented in the following, which allows using offline recorded track data as a reference for lateral vehicle guidance control (refer to Figure 70). Map matching is employed for comparing the actual vehicle position (DGPS localization) to the reference path to determine the lateral deviation and the reference path curvature sequence. These signals are input to the lateral vehicle guidance controller, which actuates the Steer-by-Wire system to guide the vehicle along the desired track. For the accuracy and performance of lateral vehicle guidance control, the quality of the reference and control error signals is essential [Ise22].

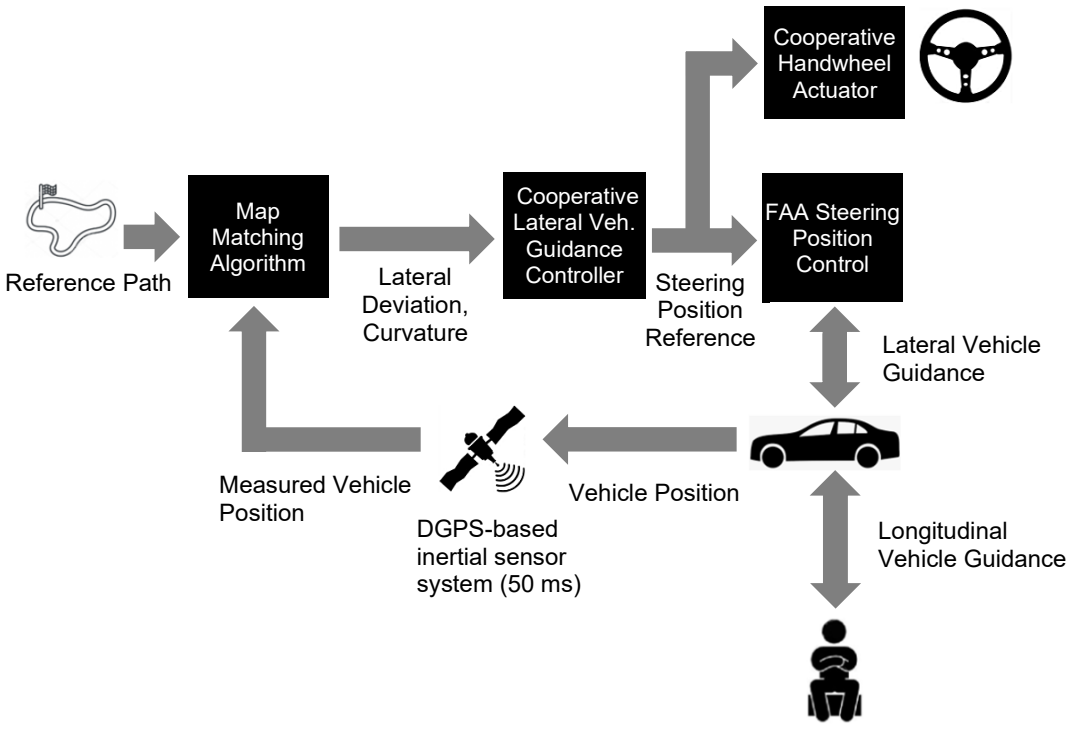

Figure 70: System Architecture for Piloted Driving [Gon+19]

In practice, the offline recorded track data is typically scattered and not equidistant. Moreover, saving a large number of data points for map matching places high memory

requirements. The calculation of the lateral vehicle guidance control error signals is often approximative and assumes linear interpolation between the data points.

For overcoming these problems, an advanced algorithm for spline-based reference path generation and map matching is presented in the following. Section A.1 introduces a regression spline for the optimal piece-wise cubic polynomial fitting of recorded track data. The polynomial coefficients of the spline provide a memory-efficient representation of the reference track that is further processed by the map matching algorithm presented in section A.2. The map matching algorithm performs an online optimization to search for the minimum distance between the vehicle and spline. At the minimum distance point, exact computations of the lateral deviation and reference path curvature are performed. The resulting control error signals are optimal at any point in time and thus excellently suited as input for lateral vehicle guidance control. Simulation analyses and vehicle tests confirm the effectiveness of the approach.

A.1 Spline-based Reference Path Generation

The reference path is recorded offline using a DGPS measurement system. The DGPS measures the vehicle position in geodetic coordinates, which are expressed by longitude and latitude in decimal degrees (refer to Figure 71). These spherical coordinates are converted to local East, North, Up (ENU) cartesian coordinates given by x and y in meters. The local ENU coordinates are formed from a plane tangent to the Earth's surface that is fixed to a specific location (here the starting point of the reference path). By convention, the east axis is labeled x and the north axis y.

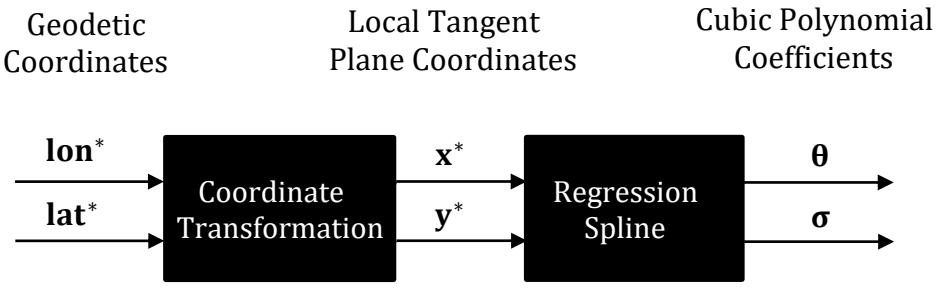

Figure 71: Schematic Diagram of the Reference Path Generation

The x, y coordinates are used as an input to the regression spline algorithm, which performs a piece-wise fit of cubic polynomial functions to the data. Thereby, a smooth analytical representation of the reference path is obtained in x, y plane. In the following, the mathematical problem formulation, solution, and an application example for the regression spline are detailed.

Mathematical Problem Formulation:
Given the time and measurement data (t_i, x_i) for $i = 1 \dots N$ samples, perform a piece-wise fit of j cubic polynomials

$$P(t) = \begin{cases} p_1(t) = \theta_1 + \theta_2 t + \theta_3 t^2 + \theta_4 t^3 & \text{for } 0 < t \leq a \\ p_2(t) = \theta_1 + \theta_2 t + \theta_3 t^2 + \theta_4 t^3 & \text{for } a < t \leq b \\ \vdots \end{cases} \quad \text{(A.1)}$$

such that the sum of the squared errors is minimal and continuity constraints at the transition points are enforced. Ensure smoothness of the curvature by penalizing high order polynomial coefficients. For the time and measurement data (t_i, y_i), the proceeding is analogous.

This can be formulated as a constrained least squares optimization problem with regularization (CLS Reg)

$$\text{minimize} \quad \|\mathbf{A\theta} - \mathbf{b}\|^2 + \mu^2 \boldsymbol{\theta}^T \mathbf{R\theta} \quad \text{(sum of squared errors and coefficient penalty)} \quad \text{(A.2)}$$

$$\text{subject to} \quad \mathbf{C\theta} = \mathbf{d} \quad \text{(continuity constraints)}$$

with

$\mathbf{A\theta} - \mathbf{b}$	error vector (composed of the error vectors for each polynomial, i.e. model – data)
$\boldsymbol{\theta}$	coefficient vector (composed of the coefficients of each polynomial)
$\mathbf{C}, \mathbf{d}$	constraint matrix/constraint vector (continuity at the transition points)
$\mu^2, \mathbf{R}$	regularization (penalty for large 3rd order polynomial coefficients)

The regularized constrained least squares problem can be thought of as a tri-objective least squares problem, with the primary objective $\|\mathbf{A\theta} - \mathbf{b}\|^2$, secondary objective $\mu^2 \boldsymbol{\theta}^T \mathbf{R\theta}$, and tertiary objective $\|\mathbf{C\theta} - \mathbf{d}\|^2$. Roughly speaking, infinite weight is put on the tertiary objective (i.e. enforcing continuity constraints) while a balancing between primary and secondary objective (i.e. sum of the squared errors and coefficient penalty) is done [Boy+18].

Solution:
The optimal polynomial coefficients $\boldsymbol{\theta}$ are found by solving the following linear system of equations [Gav15]

$$\begin{bmatrix} (\mathbf{A}^\mathrm{T}\mathbf{A} + \mu^2 \mathbf{R}) & \frac{1}{2}\mathbf{C}^\mathrm{T} \\ \mathbf{C} & \mathbf{0} \end{bmatrix} \begin{bmatrix} \boldsymbol{\theta} \\ \boldsymbol{\lambda} \end{bmatrix} = \begin{bmatrix} \mathbf{A}^\mathrm{T}\mathbf{b} \\ \mathbf{d} \end{bmatrix}. \quad \text{Optimality Condition} \quad \text{(A.3)}$$

A solution only exists if the left matrix is invertible (see [Van19] for necessary conditions). In the Appendix B, a short derivation of the solution to the constrained least-squares problem with regularization is given.

Application Example:
As an example, the regularized constrained least squares method shall be used to fit a piecewise cubic polynomial function $P(t)$ to a set of points (t_i, x_i) shown in Figure 72. With this respect, $P(t)$ is defined as

$$P(t) = \begin{cases} p_1(t) = \theta_1 + \theta_2 t + \theta_3 t^2 + \theta_4 t^3 & \text{for } t \leq a \\ p_2(t) = \theta_1' + \theta_2' t + \theta_3' t^2 + \theta_4' t^3 & \text{for } t > a \end{cases} \quad \text{(A.4)}$$

with a given. To achieve continuity of the first and second derivative at the point a (i.e. gradient and curvature), the following conditions are imposed

$$\begin{aligned} p_1(a) &= p_2(a), \\ \dot{p}_1(a) &= \dot{p}_2(a), \\ \ddot{p}_1(a) &= \ddot{p}_2(a). \end{aligned} \tag{A.5}$$

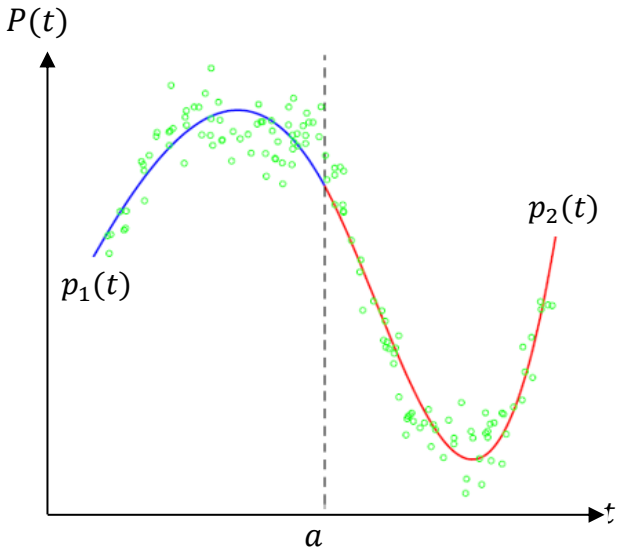

Figure 72: Least Squares Fit of Two Cubic Polynomials to a Set of Points with Continuity Constraints at Transition Point a [Van19]

Suppose the data points (t_i, x_i) are subdivided into two groups so that

$$t_1, \dots, t_K \leq a \quad \text{and} \quad t_{K+1}, \dots, t_L > a. \tag{A.6}$$

Under the application of translation, the time data of the second group is shifted to t_1. This improves the numerical robustness of the computations. For fitting the first polynomial to the data points of group one and the second to the data points of group two, the design matrix $\mathbf{A}$ and vector $\mathbf{b}$ for the least squares fit are defined as [Boy+18]

$$\mathbf{A} = \begin{bmatrix} 1 & t_1 & t_1^2 & t_1^3 & 0 & 0 & 0 & 0 \\ 1 & t_2 & t_2^2 & t_2^3 & 0 & 0 & 0 & 0 \\ \vdots & \vdots & \vdots & \vdots & \vdots & \vdots & \vdots & \vdots \\ 1 & t_K & t_K^2 & t_K^3 & 0 & 0 & 0 & 0 \\ 0 & 0 & 0 & 0 & 1 & t_1 & t_1^2 & t_1^3 \\ 0 & 0 & 0 & 0 & 1 & t_2 & t_2^2 & t_2^3 \\ \vdots & \vdots & \vdots & \vdots & \vdots & \vdots & \vdots & \vdots \\ 0 & 0 & 0 & 0 & 1 & t_K & t_K^2 & t_K^3 \end{bmatrix}, \quad \boldsymbol{\theta} = \begin{bmatrix} \theta_1 \\ \theta_2 \\ \theta_3 \\ \theta_4 \\ \theta_1' \\ \theta_2' \\ \theta_3' \\ \theta_4' \end{bmatrix} \quad \text{and} \quad \mathbf{b} = \begin{bmatrix} x_1 \\ x_2 \\ \vdots \\ x_K \\ x_{K+1} \\ x_{K+2} \\ \vdots \\ x_L \end{bmatrix}. \tag{A.7}$$

Thereby, $\mathbf{A\theta} - \mathbf{b}$ reflects the lumped error vector that is composed of the error vectors for each polynomial.
The continuity conditions $p_1(a) - p_2(0) = 0$, $\dot{p}_1(a) - \dot{p}_2(0) = 0$ and $\ddot{p}_1(a) - \ddot{p}_2(0) = 0$ give three equations that are defined in the constraint matrix $\mathbf{C}$ and vector $\mathbf{d}$ as

$$\mathbf{C} = \begin{bmatrix} 1 & a & a^2 & a^3 & -1 & 0 & 0 & 0 \\ 0 & 1 & 2a & 3a^2 & 0 & -1 & 0 & 0 \\ 0 & 0 & 2 & 6a & 0 & 0 & -2 & 0 \end{bmatrix}, \quad \mathbf{d} = \begin{bmatrix} 0 \\ 0 \\ 0 \end{bmatrix}. \tag{A.8}$$

As a last step, the regularization matrix **R** is specified. In order to penalize large variations in curvature, it is defined as

$$\mathbf{R} = \mathrm{diag}(0, 0, 0, 1, 0, 0, 0, 1). \tag{A.9}$$

Thus, only the third-order polynomial coefficients are subject to regularization.
This application example illustrated how the CLS Reg method is applied for piece-wise polynomial fitting. The approach is easily extended to piece-wise polynomial functions with more than two segments (spline functions) and for multi-dimensional data fitting (curves). In the next section, both is demonstrated by practically applying the algorithm to real measurement data of the reference track.

Application of the CLS Reg Algorithm to Reference Track Data:
After having explained the mathematical basics, the CLS Reg method is now applied to real reference track data that was recorded using a DGPS system. Figure 73 shows a satellite image of the track and the recorded track data converted to local coordinates in x, y plane.

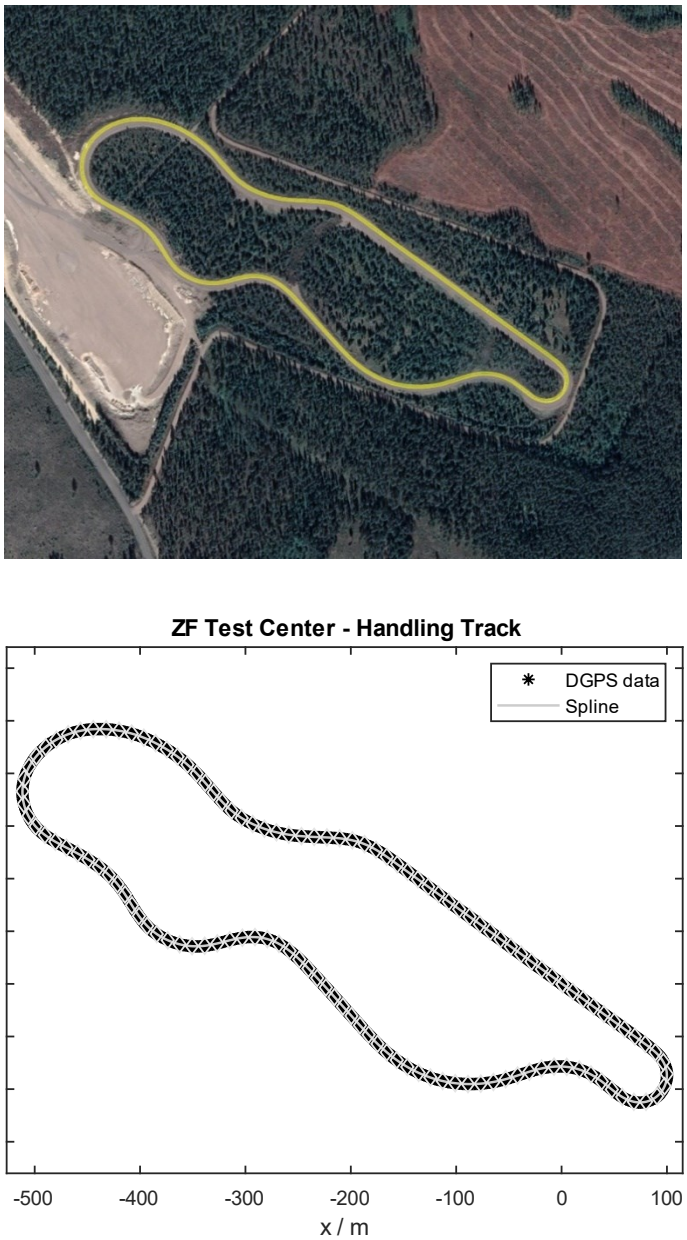

Figure 73: Satellite Image of the Reference Track and Recorded DGPS Data fitted by Spline

The data set comprises 970 points and is fitted by a piece-wise cubic polynomial function with 125 segments. Thereby, an accurate fit was achieved while ensuring a sufficient smoothing effect of the regression. The transition points between the polynomial pieces are continuous in slope and curvature (C2 continuity), due to the enforced continuity constraints.

As the reference track data (x_i, y_i) is 2-dimensional, separate piece-wise polynomial fitting was performed. This yields two spline functions, which are parametric equations of a curve parametrized in time t

$$X(t) = \begin{cases} X_1(t) = \theta_1 + \theta_2 t + \theta_3 t^2 + \theta_4 t^3 & \text{for } 0 < t \leq a \\ X_2(t) = \theta_1 + \theta_2 t + \theta_3 t^2 + \theta_4 t^3 & \text{for } a < t \leq b \\ \vdots \end{cases} \tag{A.10}$$

$$Y(t) = \begin{cases} Y_1(t) = \sigma_1 + \sigma_2 t + \sigma_3 t^2 + \sigma_4 t^3 & \text{for } 0 < t \leq a \\ Y_2(t) = \sigma_1 + \sigma_2 t + \sigma_3 t^2 + \sigma_4 t^3 & \text{for } a < t \leq b \\ \vdots \end{cases}$$

From the component functions of $X(t)$ and $Y(t)$ and their first and second derivatives, the signed curvature (κ_{ref}) of the reference track is analytically calculated. In this context, the signed curvature is obtained from

$$\kappa_{\text{ref}}(t) = \frac{\dot{X}(t)\ddot{Y}(t) - \ddot{X}(t)\dot{Y}(t)}{\left(\dot{X}(t)^2 + \dot{Y}(t)^2\right)^{3/2}}. \tag{A.11}$$

Figure 74 shows the computed reference path curvature for the track being traversed once. Due to regularization, the curvature is very smooth over the entire parameter range t. This is important as the reference path curvature is used for feedforward control inside the lateral vehicle guidance controller and therefore has a direct effect on the control actions.

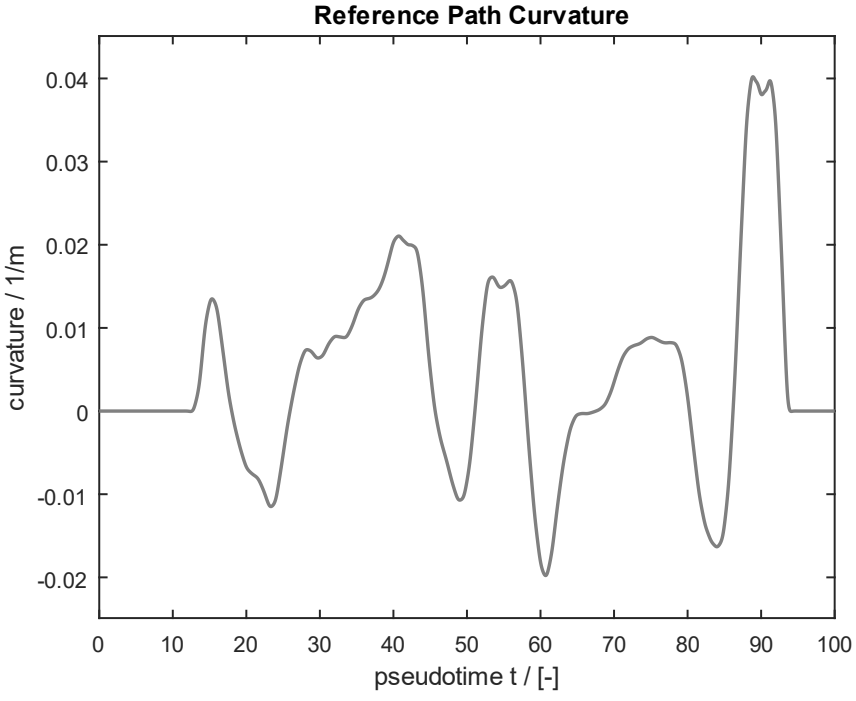

Figure 74: Reference Path Curvature as a Function of Parameter t

In practice, for each reference track, a separate regression spline is generated. The polynomial coefficients of each regression spline are stored in a database and can be loaded before the test drive. This memory-efficient representation of the reference track is further processed in the map matching algorithm, as explained in the next section.

A.2 Spline-based Map Matching

The regression spline described in the previous section provides a mathematical model for the reference path. Under the utilization of this model, map matching is employed to search for the minimum distance between vehicle position and reference path. At the minimum distance point, exact computations of the lateral deviation and reference path curvature are performed, which are the control signals for lateral vehicle guidance control. Figure 75 shows a schematic illustration of the map matching.

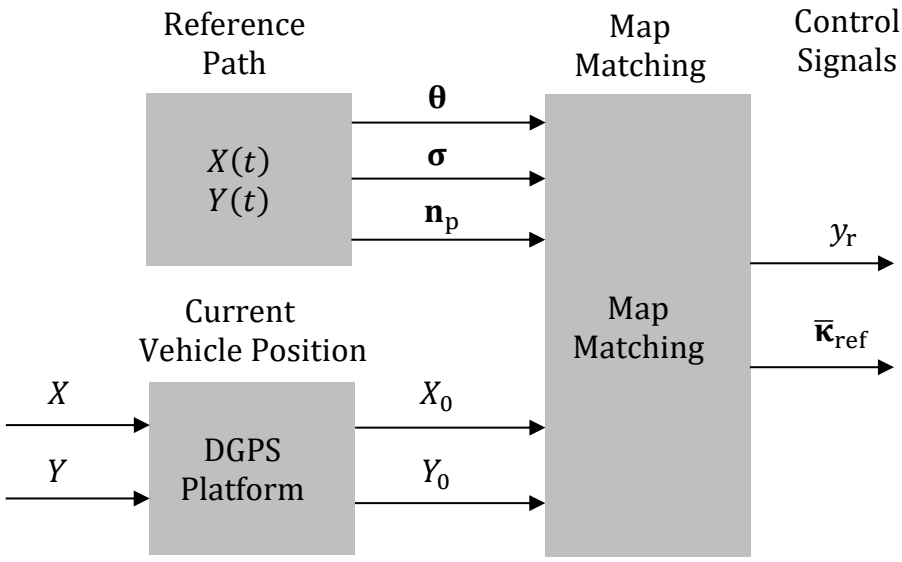

Figure 75: Schematic Illustration of Map Matching

The current vehicle position is measured by a DGPS-based inertial sensor platform at a sampling rate of 20 Hz and with an accuracy of 0.02 meters. Thereby, an accurate localization of the vehicle is obtained. The stored polynomial coefficients and knot points of the regression spline (reference track model) and the vehicle position measurement are input to the map matching algorithm. In the following, the mathematical problem formulation, solution, and an application example for the map matching algorithm are described in detail.

Mathematical Problem Formulation:
Given the current vehicle position

$$X_0, Y_0,$$

and the regression spline with $j = 1 \ldots n$ segments

$$X_j(t) = \theta_1 + \theta_2 t + \theta_3 t^2 + \theta_4 t^3 \quad \text{for} \quad t_j < t \leq t_{j+1}$$
$$Y_j(t) = \sigma_1 + \sigma_2 t + \sigma_3 t^2 + \sigma_4 t^3 \quad \text{for} \quad t_j < t \leq t_{j+1}$$

we want to find the minimum Euclidean distance between the vehicle and spline. This is subject to an online optimization problem, i.e.

$$\begin{aligned} \text{minimize} \quad & D(t) = \sqrt{(X_j(t) - X_0)^2 + (Y_j(t) - Y_0)^2} \\ \text{subject to} \quad & X_j(t) = \theta_1 + \theta_2 t + \theta_3 t^2 + \theta_4 t^3 \\ & Y_j(t) = \sigma_1 + \sigma_2 t + \sigma_3 t^2 + \sigma_4 t^3 \\ & t \in [t_j, t_{j+1}]. \end{aligned} \tag{A.12}$$

Solution:

The solution to the minimization problem is found by

1. Inserting the constraints $X_j(t)$ and $Y_j(t)$ into the objective function $D(t)$
2. Computing the first derivative of $D(t)$, setting it to zero and solving for t
3. Excluding solutions outside the segment or those with imaginary parts
4. Calculating the minimum distance $D(t_E)$ for the remaining solutions t_E

for each spline segment. This shall now be exemplarily demonstrated.

For avoiding the square root in the mathematical derivation, it is reasonable to minimize the squared distance $DS(t)$ (index j omitted for readability), which results in

$$DS(t) = (X(t) - X_0)^2 + (Y(t) - Y_0)^2. \tag{A.13}$$

Inserting $X(t)$ and $Y(t)$ gives an expression for the squared distance as a function of t

$$DS(t) = (\theta_4 t^3 + \theta_3 t^2 + \theta_2 t + \theta_1 - X_0)^2 + (\sigma_4 t^3 + \sigma_3 t^2 + \sigma_2 t + \sigma_1 - Y_0)^2. \tag{A.14}$$

For minimizing $DS(t)$, we expand the expression, compute the first derivative, and set it to zero. This gives a fifth order polynomial function of the general form

$$P(t) = t^5 + a_1 t^4 + a_2 t^3 + a_3 t^2 + a_4 t + a_5 = 0. \tag{A.15}$$

An efficient method for calculating the solutions of the polynomial online is to consider it as a characteristic equation, which can be transferred to matrix representation using the Controllable Canonical form

$$\mathbf{A} = \begin{bmatrix} 0 & 1 & 0 & 0 & 0 \\ 0 & 0 & 1 & 0 & 0 \\ 0 & 0 & 0 & 1 & 0 \\ 0 & 0 & 0 & 0 & 1 \\ -a_5 & -a_4 & -a_3 & -a_2 & -a_1 \end{bmatrix}. \tag{A.16}$$

The eigenvalues of the $\mathbf{A}$ matrix can be efficiently calculated using standard MATLAB routines. They reflect the extreme values t_E of the squared distance function $DS(t)$. The minimum distance search must be restricted to the interval of a spline segment. Thus, extreme values t_E where

- $t_E < t_j$ (start of segment)
- $t_E > t_{j+1}$ (end of segment)
- t_E has an imaginary part

must be discarded. For the remaining t_E, the minimum distance $D(t_E)$ is computed, and the t_E with the shortest distance saved. This distance reflects the control error that is forwarded to lateral vehicle guidance control. After having found the extreme value t_E, the reference path curvature is analytically calculated using the formula from the previous section. The reference path curvature is needed for feedforward control.

For avoiding an iteration over all segments, a simple initialization routine is implemented ("track search") that is executed at the start of the piloted driving mode. This routine searches for the closest knot on the spline to the vehicle. For the online optimization, only the segment before and after this knot is considered. The segment where the minimum was found is used as the starting point for the next iteration (moving segment method). Consequently, during runtime, only two polynomial pieces are considered for the optimization problem, which saves computational complexity.

Application Example:
The map matching algorithm is first tested in an offline simulation assuming a current vehicle position at $P(X_0, Y_0)$ and using the regression spline from the previous section. Figure 76 shows the simulation results.

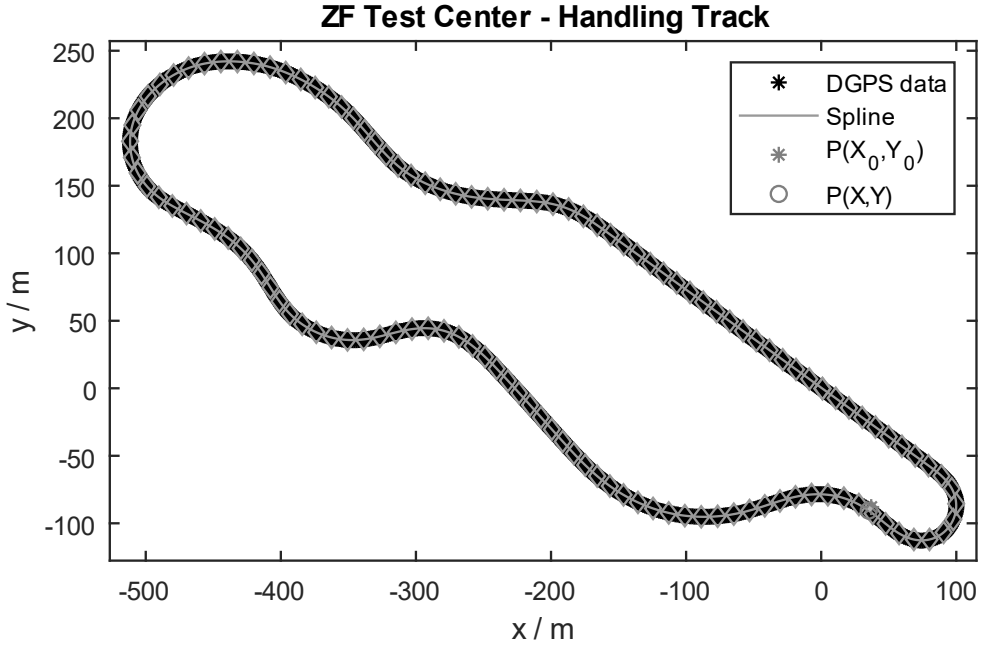

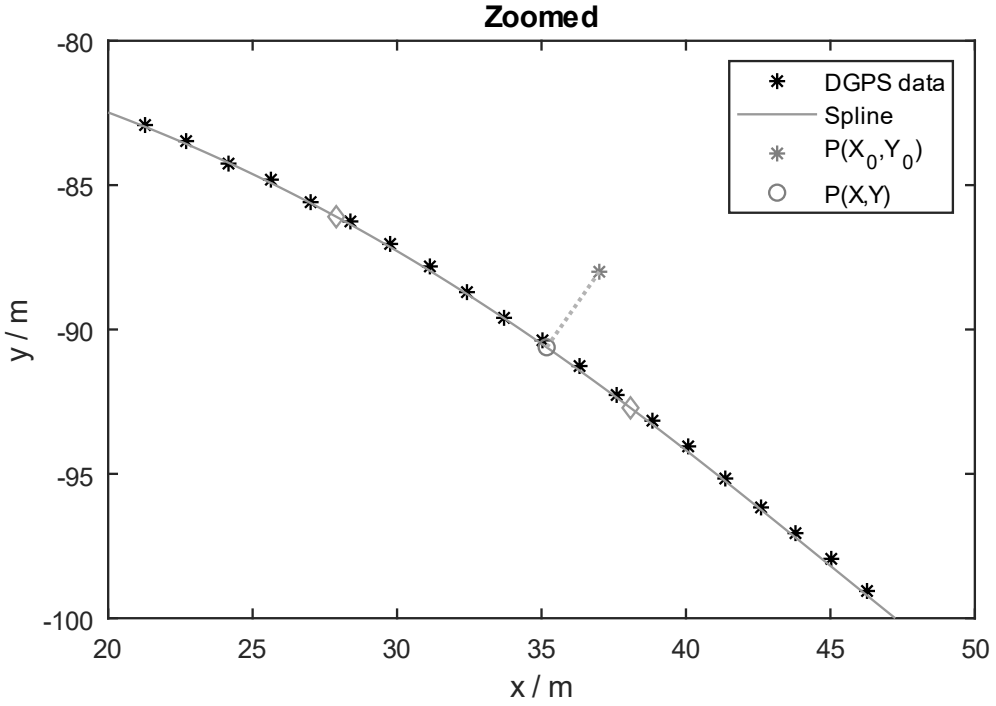

Figure 76: Simulation Analysis of the Map Matching Algorithm

The algorithm correctly finds the minimum distance between the vehicle and regression spline. At the minimum distance point $P(X, Y)$, an exact computation of the reference path curvature is performed. The following table summarizes the computed results:

Extremum:	$t_E = 85.37$
Lateral deviation:	$y_\mathrm{r} = 3.19$ m
Reference path curvature:	$\kappa_\mathrm{ref} = -0.0107$ 1/m

Further testing in simulation was performed using a detailed closed-loop simulation environment of controller and plant, as shown in Figure 70. The algorithm successfully guided the vehicle along the desired reference track. The control signals computed by the map matching algorithm are optimal at any point in time and are thus excellently suited as an input to lateral vehicle guidance control.

As the results obtained in simulation are promising, the spline-based reference path generation and map matching algorithm was practically realized and experimentally validated in the Steer-by-Wire VW Golf 7 prototype vehicle. Vehicle testing confirmed that the algorithm works as expected and reliably provides the required control signals for lateral vehicle guidance. At each sampling instant, the online optimization correctly finds the minimum distance between the vehicle and reference path and performs exact computations of the lateral deviation and reference path curvature. Thereby, an accurate and smooth path tracking is achieved, and the vehicle is correctly guided along the desired reference path.

B

Regularized Constrained Least-Squares Optimization

In this section, a compact derivation of the solution to the constrained least-squares optimization problem with regularization is provided. For deriving the solution, the objective function $J(\boldsymbol{\theta})$ is defined as a Lagrangian function, in which the error function $(\|\mathbf{A}\boldsymbol{\theta}-\mathbf{b}\|^2+\mu^2\boldsymbol{\theta}^{\mathrm{T}}\mathbf{R}\boldsymbol{\theta})$ as well as the continuity constraints $(\mathbf{C}\boldsymbol{\theta}-\mathbf{d}=\mathbf{0})$ are inserted. This gives

$$\begin{aligned} J(\boldsymbol{\theta}) &= \|\mathbf{A}\boldsymbol{\theta}-\mathbf{b}\|^2+\boldsymbol{\lambda}^T(\mathbf{C}\boldsymbol{\theta}-\mathbf{d})+\mu^2\boldsymbol{\theta}^{\mathrm{T}}\mathbf{R}\boldsymbol{\theta} \\ &= (\mathbf{A}\boldsymbol{\theta}-\mathbf{b})^{\mathrm{T}}(\mathbf{A}\boldsymbol{\theta}-\mathbf{b})+\boldsymbol{\lambda}^{\mathrm{T}}(\mathbf{C}\boldsymbol{\theta}-\mathbf{d})+\mu^2\boldsymbol{\theta}^{\mathrm{T}}\mathbf{R}\boldsymbol{\theta} \\ &= (\boldsymbol{\theta}^{\mathrm{T}}\mathbf{A}^{\mathrm{T}}-\mathbf{b}^{\mathrm{T}})(\mathbf{A}\boldsymbol{\theta}-\mathbf{b})+\boldsymbol{\lambda}^{\mathrm{T}}(\mathbf{C}\boldsymbol{\theta}-\mathbf{d})+\mu^2\boldsymbol{\theta}^{\mathrm{T}}\mathbf{R}\boldsymbol{\theta} \\ &= \boldsymbol{\theta}^{\mathrm{T}}\mathbf{A}^{\mathrm{T}}\mathbf{A}\boldsymbol{\theta}-\mathbf{b}^{\mathrm{T}}\mathbf{A}\boldsymbol{\theta}-\boldsymbol{\theta}^{\mathrm{T}}\mathbf{A}^{\mathrm{T}}\mathbf{b}+\mathbf{b}^{\mathrm{T}}\mathbf{b}+\boldsymbol{\lambda}^{\mathrm{T}}(\mathbf{C}\boldsymbol{\theta}-\mathbf{d})+\mu^2\boldsymbol{\theta}^{\mathrm{T}}\mathbf{R}\boldsymbol{\theta} \\ &= \boldsymbol{\theta}^{\mathrm{T}}\mathbf{A}^{\mathrm{T}}\mathbf{A}\boldsymbol{\theta}-2\mathbf{b}^{\mathrm{T}}\mathbf{A}\boldsymbol{\theta}+\mathbf{b}^{\mathrm{T}}\mathbf{b}+\boldsymbol{\lambda}^{\mathrm{T}}(\mathbf{C}\boldsymbol{\theta}-\mathbf{d})+\mu^2\boldsymbol{\theta}^{\mathrm{T}}\mathbf{R}\boldsymbol{\theta}. \end{aligned} \tag{B.1}$$

Note that the two terms in the last row were lumped as these are representing scalars and the transpose of a scalar does not change its value (refer to [Föl22]). For minimizing the Lagrangian function, the gradient must be computed and set to zero, which leads to

$$\begin{aligned} \frac{dJ(\boldsymbol{\theta},\boldsymbol{\lambda})}{d\boldsymbol{\theta}} &= 2\boldsymbol{\theta}^{\mathrm{T}}\mathbf{A}^{\mathrm{T}}\mathbf{A}-2\mathbf{b}^{\mathrm{T}}\mathbf{A}+\boldsymbol{\lambda}^{\mathrm{T}}\mathbf{C}+2\mu^2\boldsymbol{\theta}^{\mathrm{T}}\mathbf{R}=\mathbf{0} \\ &= 2\mathbf{A}^{\mathrm{T}}\mathbf{A}\,\boldsymbol{\theta}-2\mathbf{A}^{\mathrm{T}}\mathbf{b}+\mathbf{C}^{\mathrm{T}}\boldsymbol{\lambda}+2\mu^2\mathbf{R}\boldsymbol{\theta}=\mathbf{0} \\ &= (2\mathbf{A}^{\mathrm{T}}\mathbf{A}\ +2\mu^2\mathbf{R})\boldsymbol{\theta}-2\mathbf{A}^{\mathrm{T}}\mathbf{b}+\mathbf{C}^{\mathrm{T}}\boldsymbol{\lambda}=\mathbf{0} \\ &= (\mathbf{A}^{\mathrm{T}}\mathbf{A}\ +\mu^2\mathbf{R})\boldsymbol{\theta}-\mathbf{A}^{\mathrm{T}}\mathbf{b}+\tfrac{1}{2}\mathbf{C}^{\mathrm{T}}\boldsymbol{\lambda}=\mathbf{0} \end{aligned} \tag{B.2}$$

and

$$\frac{dJ(\boldsymbol{\theta},\boldsymbol{\lambda})}{d\boldsymbol{\lambda}}=\mathbf{C}\boldsymbol{\theta}-\mathbf{d}=\mathbf{0}. \tag{B.3}$$

This gives the following linear system of equations

$$\begin{bmatrix} (\mathbf{A}^{\mathrm{T}}\mathbf{A}+\mu^2\mathbf{R}) & \frac{1}{2}\mathbf{C}^{\mathrm{T}} \\ \mathbf{C} & \mathbf{0} \end{bmatrix}\begin{bmatrix}\boldsymbol{\theta}\\ \boldsymbol{\lambda}\end{bmatrix}=\begin{bmatrix}\mathbf{A}^{\mathrm{T}}\mathbf{b}\\ \mathbf{d}\end{bmatrix} \tag{B.4}$$

whose solution yields the optimal polynomial coefficients $\boldsymbol{\theta}$ and the Lagrange multipliers $\boldsymbol{\lambda}$.

Bibliography

[Abe15] Abe, M. 2015. Vehicle Handling Dynamics - Theory and Application. Second Edition, Amsterdam: Elsevier Science.

[Ack+93] Ackermann, J. 1993. Robust Control - The Parameter Space Approach. London: Springer Verlag.

[Ack+95] Ackermann, J., Guldner, J., Sienel, W., Steinhauser, R. and Utkin, V. I. 1995. "Linear and nonlinear controller design for robust automatic steering." IEEE Transactions on Control Systems Technology 1: 132-143.

[Ada22] Adamy, J. 2022. Nonlinear Systems and Controls. Darmstadt: Springer Verlag.

[Ant+07] Antsaklis, P. J. and Michel, A. N. 2007. A Linear Systems Primer. Boston, USA: Birkhäuser.

[Baj+05a] Bajcinca, N., Schürmann, N. and Bals, J. 2005. "Two degree of freedom motion control of an energy optimized aircraft ram air inlet actuator." Institute of Robotics and Mechatronics, German Aerospace Center, DLR, Oberpfaffenhofen.

[Baj+05b] Bajcinca, N. and Bünte, T. 2005. "A Novel Control Structure for Dynamic Inversion and Tracking Tasks." IFAC.

[Boy+18] Boyd, S. and Vandenberghe, L. 2018. Introduction to Applied Linear Algebra - Vectors, Matrices and Least Squares. Stanford/Los Angeles, California, USA: Cambridge University Press.

[Bru+19] Brunton, S. and Kutz, J. N. 2019. Data-Driven Science and Engineering – Machine Learning, Dynamical Systems, and Control. Washington: Cambridge University Press.

[Buc+08] Buchholz, J. J. and von Grünhagen, W. 2008. Inversion Impossible? Hochschule Bremen.

[Bün+05] Bünte, T., Sahin, A. and Bajcinca, N. 2005. "Inversion of Vehicle Steering Dynamics with Modelica/Dymola." International Modelica Conference.

[Cam+13] Camacho, E. F. and Bordons Alba, C. 2013. Model Predictive Control. Springer-Verlag.

[Coe+00] Coelingh, H. J., Schrijver, E., de Vries, T. J. A. and van Dijk, J. 2000. "Design of Disturbance Observers for the Compensation of low-frequency Disturbances." Proceedings of the 5th International Conference on Motion and Vibration Control (MoViC). Sidney, Australia.

[Deu12] Deutscher, J. 2012. The state space approach to the two-degree-of-freedom control of linear distributed-parameter systems. Berlin: Springer Verlag.

[Deu+14] Deutscher, J. and Roppenecker, G. 2014. "Robust asymptotic disturbance rejection using observer-based disturbance feedforward." at - Automatisierungstechnik 62 (8): 1-13.

[Dor+11] Dorf, R. C. and Bishop, R. H. 2011. Modern Control Systems. New Jersey, USA: Pearson Education.

[Doy+79] Doyle, J. C. and Stein, G. 1979. "Robustness with Observers." IEEE Transactions on Automatic Control AC-24 (4): 607-611.

[Dut+97] Dutton, K., Thompson, S. and Barraclough, B. 1997. The Art of Control Engineering. Sheffield: Prentice Hall.

[Erl15] Erlien, S. M. 2015. "Shared vehicle control using safe driving envelopes for obstacle avoidance and stability." Dissertation, Stanford University.

[Ers+11] Ersoy, M. and Gies, S. 2011. Chassis Handbook - Fundamentals, Driving Dynamics, Components, Mechatronics, Perspectives. Wiesbaden: Vieweg+ Teubner Verlag.

[Fan+14] Fankem, S. and Müller, S. 2014. "Steering feel generation in steer-by-wire vehicles - modular steering torque computation and requirements for the hand wheel actuator." 5th International Munich Chassis Symposium. Wiesbaden.

[Föl22] Föllinger, O. 2022. Regelungstechnik: Einführung in die Methoden und ihre Anwendung. Berlin: VDE Verlag.

[Fra+14] Franklin, G. F., Powell, J. D. and Emami-Naeini, A. 2014. Feedback Control of Dynamic Systems. 7th. Boston: Pearson Education Limited.

[Fra+98] Franklin, G. F., Powell, J. D. and Work, M. L. 1998. Digital Control of Dynamic Systems. California : Addison-Wesley.

[Fri05] Friedland, B. 2005. Control System Design - An Introduction to State-Space Methods. New York: Dover Publications Inc.

[Fuc+19] Fuchs, R., Tamura, T. and Moreillon, M. 2019. "Lenkfunktionen für automatisiertes Fahren." ATZ - Automobiltechnische Zeitschrift 6.

[Gal+17] Gallep, J., Govender, V. and Müller, S. 2017. "Model Predictive Lateral Vehicle Guidance Using a Position Controlled EPS System." IFAC-Papers-OnLine 50 (2): 265-270.

[Gal21] Gallep, J. 2021. "Modellprädiktive, kinetosearme Längs- und Querführung automatisiert fahrender Kraftfahrzeuge." Dissertation, TU Berlin.

[Gao+10] Gao, Y., Lin, T., Borrelli, F., Tseng, E. and Hrovat, D. 2010. "Predictive control of autonomous ground vehicles with obstacle avoidance on slippery roads." Dynamic Systems and Control Conference.

[Gav15] Gavin, H. 2015. Constrained Linear Least Squares – Uncertainty, Design, and Optimization. Durham, North Carolina, USA: Department of Civil and Environmental Engineering, Duke University.

[Gon18] Gonschorek, R. 2018. "State-Space Control of the Force Feedback Actuator for a Steer-by-Wire System." Master Thesis, Technical University Georg Agricola Bochum (Technical University Georg Agricola), Bochum.

[Gon+19] Gonschorek, R., Heitzer, H.-D. and de Moll, A. 2019. "Steer-by-Wire Handwheel Actuator - At the Transition from Manual to Autonomous Driving," Aachener Kolloquium Fahrzeug- und Motorentechnik, Aachen.

[Gon+20] Gonschorek, R., Münch, E. and Bertram, T. 2020. "Reference Track Generation and Map Matching for the Demonstration of Lateral Vehicle Guidance Control Functions," Aachener Kolloquium Fahrzeug- und Motorentechnik, Aachen.

[Gon+21] Gonschorek, R. and Bertram, T. 2021. "Linear-Quadratic-Gaussian Position Control of the Hand Wheel Actuator for a Steer-by-Wire Steering System," VDI Mechatronikfachtagung, Darmstadt.

[Gon+22] Gonschorek, R. and Bertram, T. 2022. "Synthesis of a 2DOF Linear Quadratic Gaussian Position Control for a Steer-by-Wire System in Highly Automated Driving Applications." IEEE Intelligent Vehicles Symposium (IV), Aachen.

[Gon+23a] Gonschorek, R. and Bertram, T. 2023. "Robust Two-Degrees of Freedom Linear Quadratic Gaussian Position Control for the Front Axle Actuator of a Steer-by-Wire System," Springer Nature, Forschung im Ingenieurwesen.

[Gon+23b] Gonschorek, R. and Bertram, T. 2023. "Cooperative Control Concept for the Handwheel Actuator of a Steer-by-Wire System," chassis.tech plus 2023, 14th International Munich Chassis Symposium, Munich. (accepted)

[Grü+17] Grüne, L. and Pannek, J. 2017. Nonlinear Model Predictive Control. 2nd edition, London: Springer Verlag.

[Hei+02] Heinzel, G., Rüdiger, A. and Schilling, R. 2002. "Spectrum and spectral density estimation by the Discrete Fourier Transform (DFT), including a comprehensive list of window functions and some new flat-top windows," Max-Planck-Institut für Gravitationsphysik, Hannover.

[Hen97] Henrichfreise, H. 1997. "Prototyping of a LQG Compensator for a Compliant Positioning System with Friction." Transmechatronik, HNI-Verlagsschriftenreihe 23.

[Irm+20] Irmer, M. and Henrichfreise, H. 2020. "Design of a robust LQG Compensator for an Electric Power Steering." IFAC PapersOnLine 53 (2): 6624–6630.

[Ise+10] Isermann, R. and Münchhof, M. 2010. Identification of Dynamic Systems - An Introduction with Applications. Heidelberg: Springer Verlag.

[Ise22] Isermann, R. 2022. Automotive Control - Modeling and Control of Vehicles. Berlin: Springer Verlag.

[Ise89] Isermann, R. 1989. Digital Control Systems Volume 1 - Fundamentals, Deterministic Control. Berlin: Springer Verlag.

[Isi95] Isidori, A. 1995. Nonlinear Control Systems, Communications and Control Engineering Series. London: Springer.

[Jeo+19] Jeon, S., Lee, K., Kim, H. and Ku, D. 2019. "Path Tracking Control of Autonomous Vehicles Using Augmented LQG with Curvature Disturbance Model." 19th International Conference on Control, Automation and Systems (ICCAS). Jeju, Korea (South).

[Kal60] Kalman, R. E. 1960. "A New Approach to Linear Filtering and Prediction Problems". Journal of Basic Engineering. 82: 35–45.

[Kat+11] Katriniok, A. and Abel, D. 2011. "LTV-MPC Approach for Lateral Vehicle Guidance by Front Steering at the Limits of Vehicle Dynamics." IEEE Conference on Decision and Control and European Control Conference. Orlando, FL, USA.

[Kat+13] Katriniok, A., Maschuw, J. P., Christen, F., Eckstein, L. and Abel, D. 2013. "Optimal vehicle dynamics control for combined longitudinal and lateral autonomous vehicle guidance." IEEE European Control Conference (ECC) 974-979.

[Keh07] Kehl, S. 2007. "Lateral control of a test vehicle along predefined paths." Dissertation, University of Stuttgart.

[Kel+15] Keller, M., Haß, C., Seewald, A. and Bertram, T. 2015. "A Vehicle Lateral Control Approach for Collision Avoidance by Emergency Steering Maneuvers," In: 6th International Munich Chassis Symposium, published by Pfeffer, P. E. Wiesbaden: Springer Vieweg.

[Kel17] Keller, M. 2017. "Trajektorienplanung zur Kollisionsvermeidung im Straßenverkehr." Dissertation, TU Dortmund University.

[Kha14] Khalil, H. K. 2014. Nonlinear Control. East Lansing, Michigan, USA: Pearson Education.

[Koc10] Koch, T. 2010. "Untersuchungen zum Lenkgefühl von Steer-by-Wire Lenksystemen." Dissertation, TU München.

[Kon+15] Kong, J., Pfeiffer, M., Schildbach, G. and Borrelli, F. 2015. "Kinematic and dynamic vehicle models for autonomous driving control design." IEEE Intelligent Vehicles Symposium (IV) 1094–1099.

[Kön+07] König, L., Neubeck, J. and Wiedemann, J. 2007. "Nonlinear Steering Controllers for the Lateral Dynamics Stability Limit." at Automatisierungstechnik 55 (6).

[Kön09] König, L. 2009. "Ein virtueller Testfahrer für den querdynamischen Grenzbereich." Dissertation, University of Stuttgart.

[Kor+19] Korus, J.-D., Karg, P., Ramos, P. G., Schütz, C., Zimmermann, M. and Müller, S. 2019. "Robust Design of a Complex, Perturbed Lateral Control System for Automated Driving." IFAC PapersOnLine 52 (8): 1–6.

[Kra+16] Kranz, T., Hahn, S. and Zindler, K. 2016. "Nonlinear lateral vehicle control in combined emergency steering and braking maneuvers." IEEE Intelligent Vehicles Symposium (IV): 603–610.

[Kre99] Kreisselmeier, G. 1999. "Two-Degree-of-Freedom Control Structure." at Automatisierungstechnik 47 (6): 266-269.

[Kri12] Kritayakirana, K. 2012. "Autonomous vehicle control at the limits of handling." Dissertation, Standford University.

[Kwa+05] Kwakernaak, H., Bosgra, O. H. and Meinsma, G. 2005. Design Methods for Control Systems. Enschede: University of Twente.

[Lew+08] Lewis, F. L., Xie, L. and Popa, D. 2008. Optimal and Robust Estimation - With an Introduction to Stochastic Control Theory. Arlington, Texas, USA: CRC Press, Taylor & Francis.

[Lew+12] Lewis, F. L., Vrabie, D. L. and Syrmos, V. L. 2012. Optimal Control. Hoboken, New Jersey, USA: John Wiley & Sons.

[Liu+20] Liu, Z., Zheng, L. and Li, G. 2020. "Longitudinal motion control for high-speed trimaran based on computational fluid dynamics and predictive control." International Journal of Advanced Robotic Systems 1-14.

[Lu+18] Lu, Z., Shyrokau, B., Boulkroune, B., Van Aalst, S., Happee, R. 2018. Performance benchmark of state-of-the-art lateral path-following controllers. Proceedings - 2018 IEEE 15th International Workshop on Advanced Motion Control (AMC).

[Lug19] Lugner, P. 2019. Vehicle Dynamics of Modern Passenger Cars. Vienna: Springer Cham.

[Mac00] Maciejowski, J. M. 2000. Predictive Control with Constraints. Harlow, England: Pearson Education.

[Mei+04] Meier, G., Roppenecker, G. and Wurmthaler, C. 2004. "Automatic lateral vehicle guidance using tracking control - a modular approach to separate driver- and vehicle-dependent dynamics." IEEE Intelligent Vehicles Symposium (IV) 145-149.

[Men+14] Menhour, L., d'Andréa-Novel, B., Fliess, M. and Mounier, H. 2014. "Coupled nonlinear vehicle control: Flatness-based setting with algebraic estimation techniques." Control Engineering Practice 22: 135-146.

[Mou+97] Mouri, H. and Furusho, H. 1997. "Automatic path tracking using linear quadratic control theory." IEEE Conference on Intelligent Transportation System. Boston, MA, USA.

[Pac12] Pacejka, H. B. 2012. Tyre and Vehicle Dynamics. Amsterdam: Butterworth-Heinemann.

[Pfe+17] Pfeffer, P. and Harrer, M. 2017. Steering Handbook. Wiesbaden: Springer Cham.

[Raj12] Rajamani, R. 2012. Vehicle Dynamics and Control. New York: Springer.

[Rat+14] Rathgeber, C., Winkler, F., Odenthal, D. and Müller, S. 2014. "Lateral Trajectory Tracking Control for Autonomous Vehicles." European Control Conference (ECC).

[Rat+15] Rathgeber, C., Winkler, F., Odenthal, D. and Müller, S. 2015. "Disturbance Observer for Lateral Trajectory Tracking Control for Autonomous and Cooperative Driving." International Journal of Mechanical and Mechatronics Engineering 9 (6): 921-928.

[Rat16] Rathgeber, C. 2016. "Trajectory planning and trajectory tracking control for assisted and highly automated driving." Dissertation, TU Berlin.

[Rop09] Roppenecker, G. 2009. "State Feedback Control of Linear Systems - a Renewed Approach." Automatisierungstechnik 57 (10): 491-498.

[Sch+16] Schramm, D., Hiller, M. and Bardini, R. 2016. Vehicle Dynamics: Modeling and Simulation. Berlin: Springer Vieweg.

[Sch+17] Schucker, J. and Hoffmann, P. 2017. "Nonlinear control methods for combined lateral and longitudinal control." AmE - Automotive meets Electronics, 8th GMM-Symposium. Berlin, Offenbach: VDE Verlag GmbH.

[Sch19] Schacher, S. 2019. "Das Mentorensystem - Race Trainer Konzept für ein semi-automatisches Fahrertraining." Dissertation, TU Berlin.

[Sko+05] Skogestad, S. and Postlethwaite, I. 2005. Multivariable Feedback Control: Analysis and Design. Chichester: John Wiley & Sons Inc.

[Slo+91] Slotine, J. J. E. and Li, W. 1991. Applied Nonlinear Control. New Jersey: Prentice Hall.

[Sni09] Snider, J. M. 2009. "Automatic steering methods for autonomous automobile path tracking." Robotics Institute, Carnegie Mellon University, Pittsburgh, Pennsylvania.

[Sva06] Svaricek, F. 2006. "Zero Dynamics of Linear and Nonlinear Systems: Definitions, Properties and Applications." at - Automatisierungstechnik 54 (7): 310-322.

[Tal+11] Talvala, K. L., Kritayakirana, K. and Gerdes, J. C. 2011. "Pushing the limits: From lanekeeping to autonomous racing." Annual Reviews in Control 35 (1): 137-148.

[Tot+10] Toth, R., Heuberger, P. S. C. and Van den Hof, P. M. J. 2010. "On The Discretization of LPV State-Space Representations." Delft Center for Systems and Control, Delft University of Technology.

[Van19] Vandenberghe, L. 2019. Applied Numerical Computing, Constrained Linear Least Squares. Los Angeles, California, USA: University of California.

[Wal+14] Walter, M., Nitzsche, N., Odenthal, D. and Müller, S. 2014. "Lateral vehicle guidance control for autonomous and cooperative driving." European Control Conference (ECC), Strasbourg, France.

[Wer+12] Werling, M., Gröll, L. and Bretthauer, G. 2012. "Trajectory Tracking of Time-Critical Driving Maneuvers." at Automatisierungstechnik, 60 (1): 28-37.

[Wer11] Werling, M. (2011). "A New Concept for Trajectory Generation and Stabilization in Time-Critical Traffic Scenarios." Karlsruher Institut für Technologie (KIT), Scientific Publishin.

[Wur+09] Wurmthaler, C. and Kühnlein, A. 2009. "Model Based Feed Forward Control for Measurable Disturbances." at Automatisierungstechnik 57 (7): 328-331.

[Yan+15] Yang, J., Xing Zheng, W., Li, S., Wu, B. and Cheng, M. 2015. "Design of A Prediction Accuracy Enhanced Continuous-Time MPC for Disturbed Systems Via A Disturbance Observer." IEEE Transactions on Industrial Electronics 1-10.

[Yos+08] Yoshida, H., Shinohara, S. and Nagai, M. 2008. "Lane change steering manoeuvre using model predictive control theory." Vehicle System Dynamics S1 (46): 669-681.

[Zei12] Zeitz, M. 2012. "Feedforward Control Design in the Frequency Domain: Offline or Online." at Automatisierungstechnik 60 (7): 375-383.

[Zin+12] Zindler, K., Hahn, S., Zecha, S. and Jürgens, G. 2012. "Lateral Vehicle Control for Reproducible Tests of Safety Systems." 60 (2): 61–73.

Related Peer-Reviewed Publications

[1] Gonschorek, R., Heitzer, H.-D. and de Moll, A. 2019. "Steer-by-Wire Handwheel Actuator - At the Transition from Manual to Autonomous Driving," Aachener Kolloquium Fahrzeug- und Motorentechnik, Aachen.

[2] Gonschorek, R., Münch, E. and Bertram, T. 2020. "Reference Track Generation and Map Matching for the Demonstration of Lateral Vehicle Guidance Control Functions," Aachener Kolloquium Fahrzeug- und Motorentechnik, Aachen.

[3] Gonschorek, R. and Bertram, T. 2021. "Linear-Quadratic-Gaussian Position Control of the Hand Wheel Actuator for a Steer-by-Wire Steering System," VDI Mechatronikfachtagung, Darmstadt.

[4] Gonschorek, R. and Bertram, T. 2022. "Synthesis of a 2DOF Linear Quadratic Gaussian Position Control for a Steer-by-Wire System in Highly Automated Driving Applications," IEEE Intelligent Vehicles Symposium (IV), Aachen.

[5] Gonschorek, R. and Bertram, T. 2023. "Robust Two-Degrees of Freedom Linear Quadratic Gaussian Position Control for the Front Axle Actuator of a Steer-by-Wire System," Springer Nature, Forschung im Ingenieurwesen.

[6] Gonschorek, R. and Bertram, T. 2023. "Cooperative Control Concept for the Handwheel Actuator of a Steer-by-Wire System," chassis.tech plus 2023, 14th International Munich Chassis Symposium, Munich.